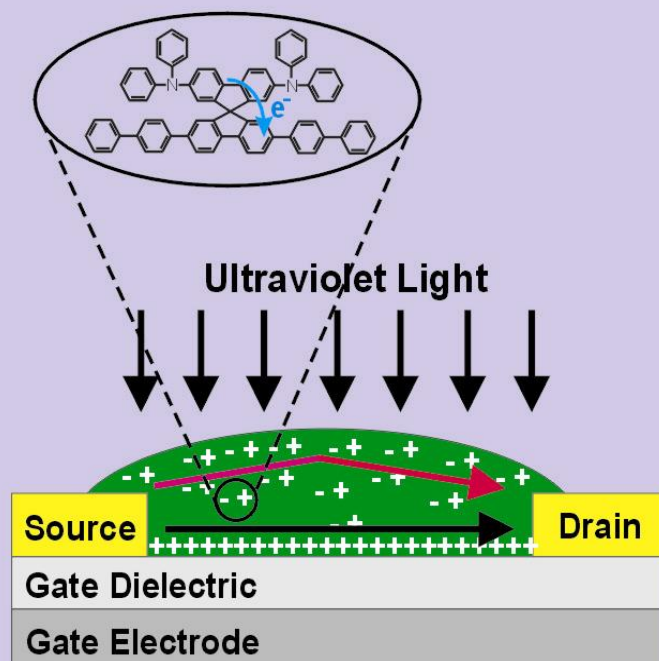
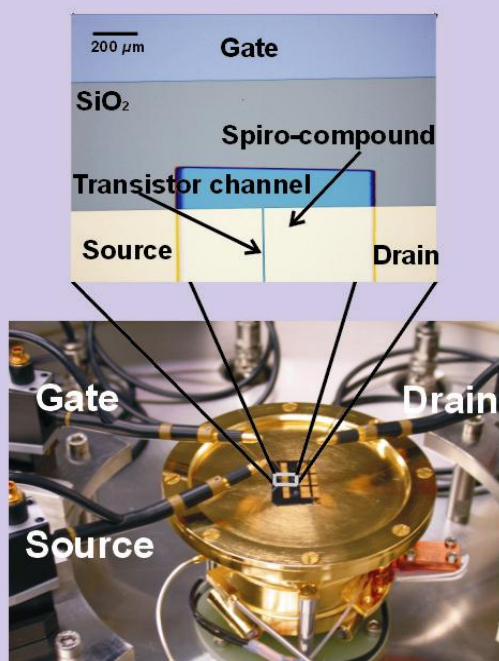


# Organic Field-Effect Transistors and Phototransistors Based on Amorphous Materials

An Inaugural Dissertation for Obtaining the Degree  
Doctor of Natural Sciences (Dr. rer. nat.)  
Presented at Fachbereich 18 Universität Kassel

by

Tobat Parasian Irianto Saragi  
from Serui, Indonesia



Kassel  
2004

*“I herewith certify that I made this thesis independently, without any disallowed assistance and I did not use others than the aid as indicated in this thesis. I marked all place, which are literally or in a general manner taken out of published or unpublished books or articles. No part of this thesis has been previously submitted in support of an application for any other degree or qualification in this or other university.”*

*“Hiermit versichere ich, dass ich die vorliegende Dissertation selbständig und ohne unerlaubte Hilfe angefertigt und andere als die in der Dissertation angegebenen Hilfsmittel nicht benutzt habe. Alle Stellen, die wörtlich oder sinngemäß aus veröffentlichten oder unveröffentlichten Schriften entnommen sind, habe ich als solche kenntlich gemacht. Kein Teil dieser Arbeit ist in einem anderen Promotions- oder Habilitationsverfahren verwendet worden.“*

Accepted as dissertation by Fachbereich 18 Universität Kassel

Advisor : Prof. Dr. J. Salbeck  
First Referee : Prof. Dr. J. Salbeck  
Second Referee : Prof. Dr. H. von Seggern (TU Darmstadt, Germany)  
Day of the oral examination : 10 December 2004

Cover:

Top-view of the sample holder bearing an organic field-effect transistor based on spiro-compound (*left*) and illustration of the mechanism of organic phototransistor based on intramolecular charge transfer in a bifunctional spiro-compound (*right*).

*“Gedruckt mit Unterstützung des Deutschen Akademischen Austauschdienstes”*

*The fear of the LORD is the beginning of knowledge*  
*Proverbs 1:7a*

# Table of Contents

<b>1</b>	<b>Introduction</b>	<b>1</b>
<b>2</b>	<b>Organic Field-Effect Transistors</b>	<b>5</b>
2.1.	Principles Operation of Organic Field-Effect Transistors	5
2.2.	State of the Art	14
2.3.	Charge Transport Properties of Amorphous Molecular Glasses Materials	19
2.3.1.	Gaussian Disorder Model	20
2.3.2.	Activation Energy Model	23
<b>3</b>	<b>Investigated Low Molecular Amorphous Materials</b>	<b>27</b>
3.1.	Classical Hole Transport Material	27
3.2.	Hole Transport Materials based on the Spiro Concept	28
<b>4</b>	<b>Experimental</b>	<b>37</b>
4.1.	Fabrication of Organic Field-Effect Transistors	37
4.1.1.	Preparation of Pre-defined Substrates	37
4.1.2.	Thermal Evaporation	43
4.1.3.	Atomic Force Microscopy and Optical Microscopy	44
4.2.	Electrical Characterization of Organic Field-Effect Transistors	45
4.2.1.	Set-up of Measurement System	45
4.2.2.	Measurement Parameter and Condition	47

<b>5</b>	<b>Surface Morphology of Low Molecular Glasses</b>	<b>53</b>
5.1.	<i>N,N,N',N'</i> -Tetraphenylbenzidine (TAD)	54
5.2.	2,2',7,7'-Tetrakis-(diphenylamino)-9,9'-spirobifluorene (Spiro-TAD)	57
5.3.	<i>N,N'</i> -Bis(3-methylphenyl)-(1,1'-biphenyl)-4,4'-diamine (TPD)	60
5.4.	2,2',7,7'-Tetra-( <i>m</i> -tolyl-phenylamino)-9,9'-spirobifluorene (Spiro-TPD)	63
5.5.	<i>N,N,N',N'</i> -Tetrakis(4-methylphenyl)benzidine (TTB)	66
5.6.	2,2',7,7'-Tetrakis-( <i>N,N'</i> -di- <i>p</i> -methylphenylamino)-9,9'-spirobifluorene (Spiro-TTB)	69
5.7.	<i>N,N'</i> -Diphenyl- <i>N,N'</i> -bis(1-naphthyl)-1,1'-biphenyl-4,4'-diamine ( $\alpha$ -NPB)	71
5.8.	2,2',7,7'-Tetra-( <i>N</i> -phenyl-1-naphtylamine)-9,9'-spirobifluorene (Spiro $\alpha$ -NPB)	75
5.9.	Summary of chapter 5	77
<b>6</b>	<b>Field-Effect Mobility of Charge Carriers in Thin Films of Low Molecular Amorphous Materials</b>	<b>79</b>
6.1.	<i>N,N,N',N'</i> -Tetraphenylbenzidine (TAD)	79
6.2.	2,2',7,7'-Tetrakis-(diphenylamino)-9,9'-spirobifluorene (Spiro-TAD)	83
6.3.	<i>N,N'</i> -Bis(3-methylphenyl)-(1,1'-biphenyl)-4,4'-diamine (TPD)	91
6.4.	2,2',7,7'-Tetra-( <i>m</i> -tolyl-phenylamino)-9,9'-spirobifluorene (Spiro-TPD)	97
6.5.	<i>N,N,N',N'</i> -Tetrakis(4-methylphenyl)benzidine (TTB)	105
6.6.	2,2',7,7'-Tetrakis-( <i>N,N'</i> -di- <i>p</i> -methylphenylamino)-9,9'-spirobifluorene (Spiro-TTB)	108
6.7.	<i>N,N'</i> -Diphenyl- <i>N,N'</i> -bis(1-naphthyl)-1,1'-biphenyl-4,4'-diamine ( $\alpha$ -NPB)	114
6.8.	2,2',7,7'-Tetra-( <i>N</i> -phenyl-1-naphtylamine)-9,9'-spirobifluorene (Spiro $\alpha$ -NPB)	117
6.9.	The influence of a methyl group in symmetrically spiro-linked compounds	121
6.10.	Summary of chapter 6	123

<b>7</b>	<b>Temperature-Dependence in Low Molecular Amorphous Thin Films</b>	<b>125</b>
7.1.	<i>N,N,N',N'</i> -Tetraphenylbenzidine (TAD)	126
7.2.	2,2',7,7'-Tetrakis-(diphenylamino)-9,9'-spirobifluorene (Spiro-TAD)	129
7.3.	<i>N,N'</i> -Bis(3-methylphenyl)-(1,1'-biphenyl)-4,4'-diamine (TPD)	133
7.4.	2,2',7,7'-Tetra-( <i>m</i> -tolyl-phenylamino)-9,9'-spirobifluorene (Spiro-TPD)	135
7.5.	<i>N,N,N',N'</i> -Tetrakis(4-methylphenyl)benzidine (TTB)	139
7.6.	2,2',7,7'-Tetrakis-( <i>N,N'</i> -di- <i>p</i> -methylphenylamino)-9,9'-spirobifluorene (Spiro-TTB)	142
7.7.	<i>N,N'</i> -Diphenyl- <i>N,N'</i> -bis(1-naphthyl)-1,1'-biphenyl-4,4'-diamine ( $\alpha$ -NPB)	145
7.8.	2,2',7,7'-Tetra-( <i>N</i> -phenyl-1-naphtylamine)-9,9'-spirobifluorene (Spiro $\alpha$ -NPB)	147
7.9.	Summary of chapter 7	150
<b>8</b>	<b>Asymmetrically Spiro-Linked Compounds</b>	<b>153</b>
8.1.	Transistor Characteristics Measured in the Dark and Surface Morphology	154
8.2.	Influence of Light Exposure on Asymmetrically Spiro-Linked Compounds Field-Effect Transistors	158
8.2.1.	Device Fabrication and Characterization	158
8.2.2.	2,7-bis-( <i>N,N'</i> -diphenylamino)-2',7'-bis(biphenyl-4-yl)-9,9'-spirobifluorene (Spiro-DPSP)	160
8.2.3.	2,7-bis-( <i>N,N'</i> -diphenylamino)-2',7'-bis(spirobifluorene-2-yl)-9,9'-spirobifluorene (Spiro-DPSP <sup>2</sup> )	172
8.3.	Summary of chapter 8	178
	<b>Conclusions</b>	<b>179</b>
	<b>References</b>	<b>181</b>

# Chapter 1

## Introduction

Electronic devices based on organic semiconductors have been developed over two decades. It is not a dream, that one day organic electronic devices become a mainstay of our technological existence. Indeed, products based on organic semiconductors are already in the market, for instance as displays of several mobile electronic appliances. In the context of electronic devices, organic semiconductors are interesting due to the ability to deposit organic films on a variety of low-cost substrates such as glass and plastic. Moreover, organic thin films can be prepared by various methods like spin-coating, printing, or thermal sublimation.

Business Communications Company reported that the market of optoelectronic devices based on organic semiconductors in 2001 reached \$4500 Million [1]. They predicted it will grow at an average annual rate of over 50% to \$38400 Million by 2006. Organic-based displays make up just over 50 % of the organic optoelectronics market, and the market is expected to grow at a rate of 52 % over the next five years. Digital TV is cited as being one of the largest shares of products. Major electronic firms such as Philips and Pioneer, and smaller companies such as Cambridge Display Technology and Universal Display, are betting that the future holds tremendous opportunity for low-cost production with surprisingly high performance offered by organic optoelectronic devices. OLED full-colour display may eventually replace liquid-crystal displays (LCD) for use with notebooks and even desktop computers. Such a display can be fabricated on a flexible plastic substrate at a moderate temperature, eliminating the fragile and heavy glass substrate used in LCD. Furthermore, it can emit bright light without the pronounced directionality inherent in LCD viewing.

Electroluminescence is the basic effect, which plays the key role of the processes involved in display applications. It was first demonstrated in the 1960s on crystals of anthracene, an organic aromatic hydrocarbon, by Pope and co-workers [2]. Unfortunately, no practical application emerged, since the organic crystal used was too thick and the working voltage was too large (~ 400 V). In 1987 a breakthrough was made by Tang and Van Slyke at Eastman Kodak Co., Rochester, N. Y., who have successfully shown the first efficient light emission (~ 1 %) from a two-layer organic (~ 100 nm) structure, resembling a *p-n* junction, by means of thermal sublimation [3]. The operating voltage of the OLED was dramatically

reduced and the quantum efficiency was significantly improved. In 1990 Friend and co-workers, at Cambridge University in England, reported a similar effect in a conjugated polymer film consisting of poly(para-phenylene vinylene) [4]. Unlike conjugated molecules, conjugated polymers or their precursors are typically cast from solution onto an appropriate substrate such as indium tin-oxide (ITO). Efficiency, drive voltage, and color selection had attained adequate levels for commercialization after the introduction of OLED. Some important requirements for market issues are the luminance of  $100 \text{ cd/m}^2$  and device lifetime of 50000 hours ( $\sim 5.7$  years). The first requirement is fulfilled, but the devices lifetimes were far away from sufficient. The reliability issue is dominated by the morphological stability of the active material and the corresponding cathode materials. Basically, an OLED consists of hole transport, emission, and electron transport layers. The morphological stability of either hole or electron transport materials can be quantified by their glass transition temperatures  $T_g$ . Some examples of active materials are tris(8-hydroxy-quinolate)aluminium (III) ( $\text{Alq}_3$ ) as emitter and  $N,N'$ -bis(3-methylphenyl)-(1,1'-biphenyl) - 4,4'-diamine (TPD) as hole transporter. However, amorphous TPD ( $T_g = 62 \text{ }^\circ\text{C}$ ) thin films easily crystallize [5,6].

Organic field-effect transistors (OFETs), one promising application of organic semiconductors, allow the fabrication of integrated circuits and active-matrix display on a variety of substrates, such as silicon, polyimide, and glass. Moreover, there has been a tremendous progress in OFETs performance during the last decade. The point has recently been reached at which it can be seriously considered for commercial application. Furthermore, the OFET method has been used as a powerful tool for characterizing the charge transport properties in organic conjugated materials. Recently, high performance integrated circuits based on organic transistors have been successfully demonstrated which are interesting for low-cost electronic applications such as identification tags, smart cards, and electronic paper [7,8]. The two most important material parameters that control the OFET characteristics are the charge carrier mobility and the *ON/OFF* current ratio. Especially for applications in digital circuits and pixel switches for electronic ink and liquid crystal displays, a high *ON/OFF* ratio is crucial [8,9].

In order to hinder crystallization of hole or electron transport materials, in 1996 Salbeck introduced the spiro concept in order to improve the morphological stability of chromophores while retaining their functionality [10,11,12,13]. Joining two charge transport moieties (for instance two identical TPD molecules) with a spiro carbon atom center achieves the task of raising  $T_g$ , because the increased steric demand of the resulting spiro-compound 2,2',7,7'-tetra-(*m*-tolyl-phenylamino)-9,9'-spirobifluorene (Spiro-TPD) effectively hinders



crystallization. Basically, two TPD molecules are linked with a spiro carbon center and are thus forced into a perpendicular arrangement. This arrangement gives only relative weak electronic interaction of the molecular halves. The  $T_g$  of the resulting Spiro-TPD is 115 °C.

Generally, spiro-linked compounds are known as glass-forming materials with high glass transition temperatures and a good morphological stability, which makes them well suitable for organic devices. Spiro compounds have been successfully applied in organic solar cells [11], organic light emitting devices [12,13], field-effect transistors [14], phototransistors [15], and lasers [16]. The stability of the device and thin films based on spiro-linked compounds and their corresponding parent compounds grown on different substrates are compared and discussed as well. Despite its potential applications the influence of spiro atom center to the electrical or optical properties of resulting spiro-compound is in abeyance. Therefore, this thesis encompasses a complete electrical characterization of several hole transport materials and their corresponding spiro-linked compounds. The method used in this study is field-effect transistor measurement. The design of a transistor, fabrication of the pre-defined substrates, and fabrication of organic transistors are reported as well. The field-effect transistor method is used for extracting physical parameters such as field-effect mobility of charge carriers, *ON/OFF* ratios, and stability. Besides symmetrically spiro-linked compounds, asymmetrically spiro-linked compounds are already synthesized. A preliminary experiment has shown an intramolecular charge transfer between two constituent moieties [17]. However, the optoelectronic properties of these materials have not been elucidated. Therefore, the realization of an organic transistor using asymmetrically spiro-linked compounds is reported. The effect of illumination on the device performance is also reported and discussed as well. This experiment may open a new aspect on the devices based on organic semiconductors.



## Chapter 2

# Organic Field-Effect Transistors

### 2.1. Principles Operation of Organic Field-Effect Transistors

A schematic structure of a field-effect transistor (FET) is shown in Figure 2.1. An output current in a FET flows between the drain and the source electrodes. This current is controlled by the gate bias. Depending on the gate bias, a FET can be either in the *OFF* state, with very few free charge carriers in the transistor channel between the source and the drain, or in the *ON* state, when free charge carriers enter the transistor channel from the source and may flow to the drain [18,19]. In the *ON* state, the free charge carriers in the transistor channel are capacitively coupled with the gate electrode, which effectively forms a parallel plate capacitor with the transistor channel. The gate-to-channel voltage controls the free carrier charge induced into the transistor channel and, hence, the drain current. In this case, the gate electrode is isolated from the transistor channel by the gate insulator. If the gate insulator is an oxide, it is so-called Metal Oxide Semiconductor Field Effect Transistor (MOSFET). In a MOSFET, a  $\text{SiO}_2$  is used as a gate insulator [18,19].

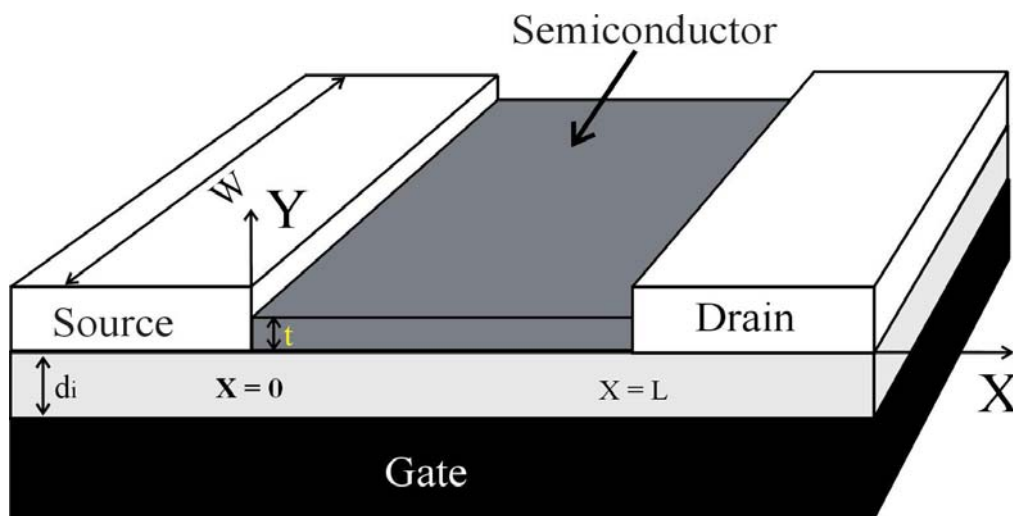


Figure 2.1. Schematic view of a FET, where  $d_i$  is the thickness of the gate insulator,  $t$  is the thickness of the semiconductor,  $W$  is the channel width, and  $L$  is the channel length.

For simplicity, a MOSFET structure based on amorphous silicon is considered [20,21]. A constant mobility is assumed, even though this is not exact for organic semiconductors. The active material is  $p$ -type for the following discussion. The drain-to-source current  $I_d$  in the channel can be approximated as

$$I_d = -q\mu n E_x W \quad (2.1)$$

where  $q$  is the electronic charge,  $\mu$  the band mobility,  $W$  the channel width,  $E_x$  the electric field in  $x$ -direction, and  $n$  the concentration of charge carriers per unit area. Here, the electric field in  $x$ -direction can be written as

$$E_x = -\frac{dV}{dx} \quad (2.2)$$

where  $V$  is the channel potential. Gradual channel approximation provides the basis for the analytical transistor characteristic. This approximation is valid when

$$|E_x| \ll |E_y| \quad (2.3)$$

which means that the channel length should be larger than the gate insulator thickness ( $L \gg d_i$ ).  $E_x$  and  $E_y$  are the components of the electric field in the channel in the  $x$ -direction from the source to the drain and in the perpendicular  $y$ -direction, respectively.

According to the gradual channel approximation, the number of the charge carriers in the channel per unit area  $n_{ind}$ , which is a function of position  $x$  along the channel, can be written as

$$n_{ind} \approx n_{indS} - \left( \frac{\epsilon_i V}{qd_i} \right) \quad (2.4)$$

where  $\epsilon_i$  is the dielectric permittivity of the insulator,  $d_i$  the dielectric thickness, and  $n_{indS}$  the number of the charge carriers in the channel at the source side of the channel per unit area. The concentration of free-conduction-band electrons in the channel  $n$  can be related to the induced charge concentration introducing the field-effect mobility  $\mu_{FET}$ :

$$n = \left( \frac{\mu_{FET}}{\mu} \right) n_{ind} \quad (2.5)$$

In organic semiconductor, the field-effect mobility of charge carrier is not constant as modeled in MOSFET since the field-effect mobility is gate bias dependent due to localized states of charge carriers and not delocalized charge carriers (band model) as in inorganic crystalline semiconductors such as silicon and gallium arsenide. In other words, the charge carrier distribution in the active channel is not uniform. Furthermore, the field-effect mobility  $\mu_{FET}$  is a function of the induced charge and, hence, the gate bias. Substituting Equation 2.2 and 2.5 into Equation 2.1 and integrating along the channel with respect to  $x$  from 0 to  $L$  and with respect to  $V$  from 0 to  $V_D$ , we obtain

$$I_d = \frac{qW}{L} \int_0^{V_D} \mu_{FET}(n_{ind}) n_{ind} dV \quad (2.6)$$

by using Equation 2.4, Equation 2.6 can be rewritten as

$$I_d = \frac{q^2 W d_i}{\epsilon_i L} \int_{n_{indD}}^{n_{indS}} \mu_{FET}(n_{ind}) n_{ind} dn_{ind} \quad (2.7)$$

where  $n_{indD}$  is the number of electron per unit area at the drain side of the channel. Equation 2.7 can be simplified by substituting Equation 2.4 and approximation for  $n_{indS}$ :

$$n_{indS} \approx \frac{\epsilon_i}{q d_i} (V_G - V_T) \quad (2.8)$$

We obtain a typical drain current

$$I_d = \frac{W}{L} C_i \mu_{FET} \left[ (V_G - V_T) V_D - \frac{1}{2} V_D^2 \right] \quad (2.9)$$

The field-effect mobility  $\mu_{FET}$  in the linear regime ( $-V_D \ll -(V_G - V_T)$ ) can be extracted from the transconductance  $g_m$ . The transconductance is calculated by taking the derivative of the channel current with the gate voltage at a constant gate potential.

$$g_m = \left. \frac{\partial I_d}{\partial V_G} \right|_{V_D = \text{Const}} = \frac{W}{L} C_i \mu_{FET} V_D \quad (2.10)$$

By plotting  $I_d$  versus  $V_G$  at a constant low  $V_D$  (in this case  $V_D = -20$  V) with  $-V_D \ll -(V_G - V_T)$ , and equating the value of the slope of this plot to  $g_m$ , we can extract the field-effect mobility in the linear regime. In the saturation regime where  $-V_D > -(V_G - V_T)$  (in this case  $V_D = -60$  V), the drain current can be rewritten as

$$I_d = \frac{W}{2L} C_i \mu_{FET} (V_G - V_T)^2 \quad (2.11)$$

In the saturation regime,  $\mu_{FET}$  can be calculated from the slope of the plot of  $\sqrt{|I_d|}$  versus  $V_G$ . The field-effect mobility of charge carriers calculated in the saturation regime is usually larger than that in the linear regime. In the experimental data and discussion, the field-effect mobility of charge carriers is extracted by using Equation 2.10 and 2.11. In conventional MOSFET, the threshold voltage manifests the transition from the accumulation regime to the inversion regime of the active channel. Therefore, it is a material-specific parameter. However, the threshold voltage determined by Equation 2.10 or 2.11 is a *fitted* parameter in organic transistors and does not directly refer to the already mentioned parameter since no inversion regime has been observed in our organic transistors. Therefore, the threshold voltage, which is later called as *the fitted threshold voltage*, cannot be regarded in this case as a material-specific parameter. As mentioned previously, inversion mode has not been observed in organic FET (OFET) and so the concept of threshold voltage has no physical meaning in OFET. Meijer *et al.* [22] recently have introduced a switch-on voltage ( $V_{so}$ ) based on the variable range hopping model. The switch-on voltage  $V_{so}$  describes the gate bias at which there is no “band” bending in the semiconductor or flat “band” condition. If the absolute gate bias is smaller than  $V_{so}$ , the variation of the channel current with the gate bias is zero. On the contrary, the channel current increases with absolute gate bias higher than  $V_{so}$ . The switch-on voltage  $V_{so}$  can be directly observed in transfer characteristics. In this thesis two types of threshold voltage are used, namely the fitted threshold voltage  $V_T$  derived from the standard conventional semiconductor formulism and the switch-on voltage  $V_{so}$  as described above.

The drain conductance  $g_d$  and transconductance  $g_m$  at low drain bias are also estimated, which are defined by Equation 2.12 and 2.13, respectively,

$$g_d = \frac{\partial I_d}{\partial V_D} = \frac{I_d}{V_D} \quad (2.12)$$

$$g_m = \frac{\partial I_d}{\partial V_G} \quad (2.13)$$

To eliminate the series resistance, Horowitz *et.al* [23] divides Equation 2.12 by the square root of Equation 2.13 and after some manipulation, they obtained Equation 2.14:

$$\frac{g_d}{\sqrt{g_m}} \sqrt{\frac{LV_D}{WC_i}} = \sqrt{\mu} (V_G - V_T) \quad (2.14)$$

In practice, the transfer characteristic of the transistors at low drain bias ( $V_D = -10$  V) is measured, where the charge distribution is practically constant along the channel, and performed a numerical derivation of Equation 2.14. Finally, Equation 2.14 shows that the field-effect mobility of charge carriers depends on the gate voltages.

An interface between a metal and an organic solid can be classified into two characteristics: energy level alignment at the interface and band bending in the organic layer [24]. Energy level alignment at the interface shows the behavior of two vacuum levels, a metal and an organic solid, when they come into real contact. In this case, two situations were reported. First, the organic solid comes into contact with the metal without rearrangement of the electric charge. It means that the vacuum level of the metal and the organic solid lay at the same level. Second, there is an interfacial dipole formation when the organic solid comes into contact with the metal. A dipole layer may be formed right at the interface due to, for instance, charge transfer across the interface [25, 26]. With such interfacial dipole formation, there will be an abrupt shift of the potential across the dipole layer, leading to a shift of virtual vacuum level at the interface. In other words, the vacuum levels of the metal and the organic solid do not lie anymore at the same level. There is a shift between both vacuum levels as they are in contact. The value of the shift is determined by the magnitude of the dipole. Furthermore, a band bending in the organic layer is considered for an interface with a thick organic layer.

Figure 2.2 shows a sketch of an *energy “band” diagram* for a *p*-channel organic field-effect transistor. In this case, we employ organic semiconductor Spiro-TAD as example. At zero gate bias, there is no charge transfer between electrode and active materials. Indeed, the energy difference between the metal work function and the organic materials work function is

zero, or the work function difference is zero. In other words, the “band” is flat (flat “band” condition), as shown in Figure 2.2(a). When a negative gate bias is applied to the gate metal as shown in Figure 2.2(b), the top of the HOMO level bends upward. Since the charge carrier density depends exponentially on the energy difference of HOMO and LUMO level, this “band” bending causes an accumulation of holes near the semiconductor/insulator interfaces. The thickness of the accumulation layer of holes is ca. 5 nm. This is the case in the accumulation mode. When the applied gate bias is positive, the HOMO level bends downward as shown in Figure 2.2(c), and holes as the majority of charge carriers are depleted. This is the depletion case.

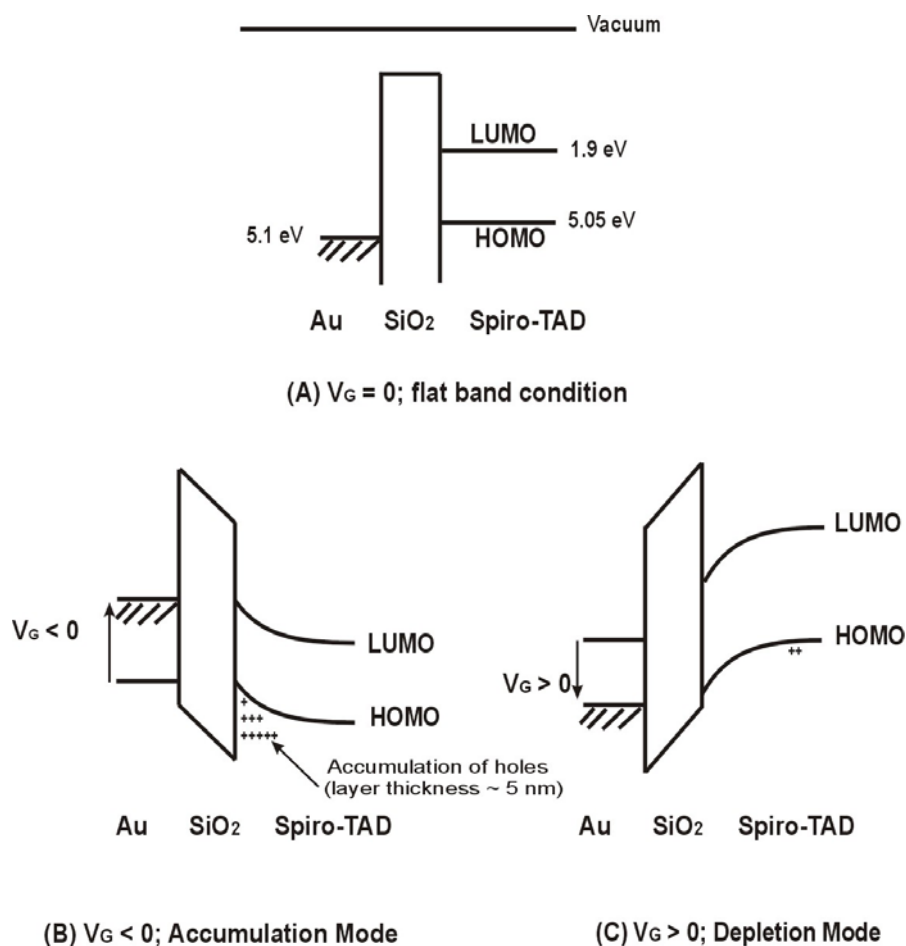


Figure 2.2. Energy “band” diagram for *p*-channel organic field-effect transistor. (a)  $V_G = 0$ , Flat “band” condition, (b)  $V_G < 0$ , Accumulation mode, and (c)  $V_G > 0$ , Depletion mode.

We have already discussed the transistor operation in the context of “band” bending which was adopted from the well-established inorganic MOSFET formalism. However, this formalism has a drawback if applied to organic transistors because of the absence of the



inversion regime. Moreover, we only consider the gate bias and for the time being, ignore the effect of the drain bias. In the following overview, we will discuss in more detail the device operation of *p*-type semiconductors used as active layer in organic field-effect transistors [27]. The major charge carrier in *p*-type is considered to be a positive charge, which forms a radical cation when sitting on a molecule. Figure 2.3(a) shows a schematic view of transistor with all three contacts held at zero bias. The organic semiconductor is dominated by neutral molecules. The neutral molecules are indicated by circles. If a negative bias  $V_G$ , is applied to the gate electrode, the potential is dropped over the insulator and over the semiconductor near the insulator/semiconductor interface, as shown in Figure 2.3(b). It gives rise to “band” bending in the semiconductor, the accumulation region in which the schematic view is shown in Figure 2.2(b). If the insulator has a capacitance per unit area  $C_i$ , then the accumulated charge per unit area is simply  $V_G C_i$ , assuming that a negligible small potential is dropped across the semiconductor and the charge carriers are uniformly distributed. An equal magnitude of compensating negative charge carriers is stored on the gate at the gate/insulator interface. The organic semiconductor now contains radical cation which created the accumulation layer. A current between source and drain will flow if a small bias is applied to the drain contact and the charges are mobile and not trapped, as shown in Figure 2.3(c). In contrast, if a positive gate bias is applied, then the opposite “band” bending occurs (see also Figure 2.2(c)) in the semiconductor at the insulator/semiconductor interface, which leads to a depletion of charges, as shown in Figure 2.3(e). The depletion layer width  $W_d$  in an organic semiconductor is given by [28]

$$W_d = \frac{\epsilon_o \epsilon_{semi}}{C_i} \left[ \sqrt{1 + \frac{2 C_i^2 (V_G - V_{so})}{q N_B \epsilon_o \epsilon_{semi}}} - 1 \right] \quad (2.15)$$

where  $\epsilon_o$  is the permittivity of vacuum,  $\epsilon_{semi}$  the relative dielectric constant of the semiconductor,  $C_i$  the capacitance of the gate dielectric per unit area,  $N_B$  the charge carrier density,  $V_{so}$  the switch-on voltage,  $V_G$  the gate bias,  $C_i$  the capacitance of insulator per unit area, and  $q$  the elementary charge.

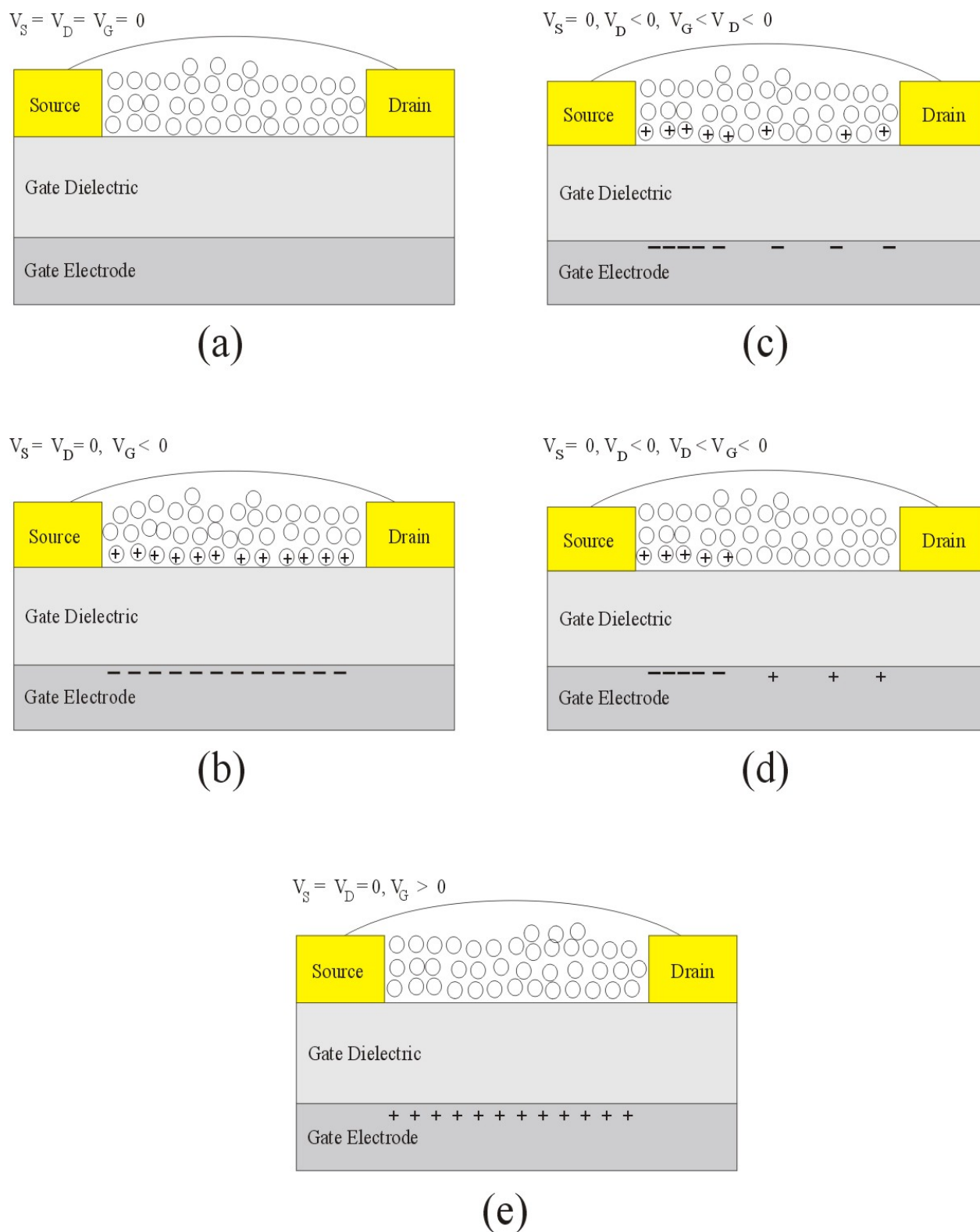


Figure 2.3. Schematic view of operation of an OFET. The circle indicates a neutral molecule and the circle containing sign + indicates a radical cation.

At large negative gate bias and low drain bias, there will be a uniform distribution of charge carriers throughout the transistor channel. However, as the drain bias becomes

increasingly negative, consequently the voltage drop over the insulator/semiconductor will become a function of the position in the channel. At the source contact, the voltage drop and the number of accumulated charge carriers will remain the same. At the drain contact, the voltage drop will decrease, giving lower concentration of charge carriers. Thus, the accumulation of charge carriers will decrease from the source to drain contact. If the drain becomes more negative than the gate then a depletion zone will begin to appear and grow from the drain contact (Figure 2.3(d)).

Generally, OFET device structure is adopted from amorphous or crystalline silicon transistor and the key parameters in characterizing an OFET are the field-effect mobility and the *ON/OFF* ratio. The field-effect mobility quantifies the average of charge carrier drift velocity per unit electric field, whereas the *ON/OFF* ratio is defined as the drain current ratio between the *ON* and *OFF* states. The *ON/OFF* ratio strongly depends on the gate bias used for calculation. Therefore, the comparison of *ON/OFF* ratios between two devices can be made only when the same gate voltage are used for both *ON* and *OFF* states. For the driving circuits in liquid crystal displays high performance OFETs are required, i.e. field-effect mobility of greater than  $0.1 \text{ cm}^2/\text{Vs}$  and *ON/OFF* ratio greater than  $10^6$ . Moreover, the conductivity of thin films can be obtained by plotting the curve of the drain current against the drain voltage at gate bias lower than  $V_{so}$  or at zero gate bias. The zero gate bias used for calculation of the conductivity does not necessarily imply that the switch-on voltage  $V_{so}$  is zero since many materials used in OFET structure have shown an accumulation of charge carriers below or higher than zero gate bias.

Two widespread device configurations of OFET are namely top-contact device and bottom-contact device (Figure 2.4). A top-contact device employs source and drain electrodes evaporated onto the organic semiconductor layer through a shadow mask. In contrast, in a bottom-contact device the organic semiconductor is deposited onto the gate insulator with prefabricated source and drain electrodes. The field-effect mobilities of charge carriers in OFETs utilizing a top-contact structure show higher values than those in bottom-contact structures. It is assumed that this is because during OFET operation of top-contact devices the migration of source/drain atoms actively takes place in the active transistor channel. At the moment, the difference in both methods is not understood yet. The major advantage of bottom-contact structures is that the organic active material can be processed as the last step by means of vacuum sublimation or wet processing such as spin-coating which helps to prevent the organic thin films from reacting with moisture in following steps.

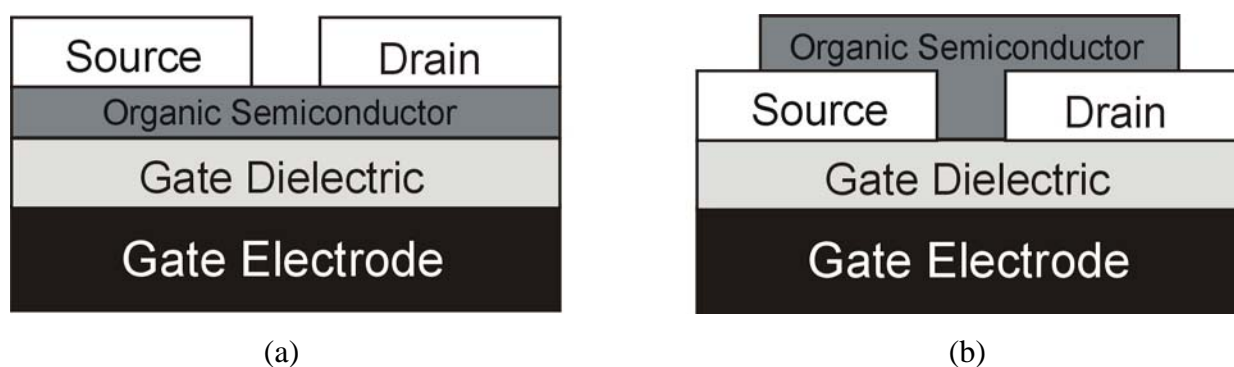
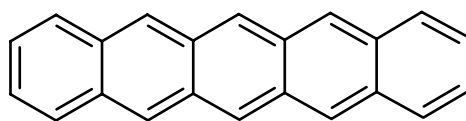


Figure 2.4. Two OFET configurations: (a) Top-contact structure, and (b) Bottom-contact structure. The gate electrodes are silicon, chromium, or other metal-like materials including organic semiconductor. Gate dielectrics are  $\text{SiO}_2$ ,  $\text{Si}_3\text{N}_4$ ,  $\text{SiO}_x$ , and polymeric materials such as poly(vinyl phenol) or poly(vinyl alcohol). The source and drain electrode are Gold with Titanium or Chromium as adhesion layer.

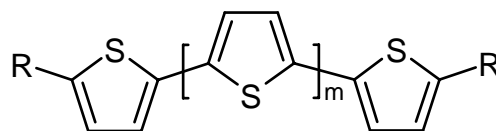
## 2.2. State of the Art

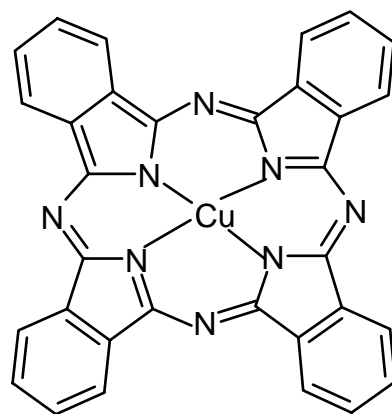
There has been a tremendous progress in Organic Field-Effect Transistors (OFET) performance during the last decade. The point has recently been reached at which it can be seriously considered for commercial application. Scheme 2.1 and 2.2 show typical chemical structures of some *p*-type and *n*-type organic semiconductors which are usually employed in OFET. Pentacene is a widely-known small molecule with one of the highest hole mobilities of  $1.5 \text{ cm}^2/\text{Vs}$  and an *ON/OFF* ratio of  $10^8$  [29]. However, the polycrystalline state in pentacene thin film transistors is a major drawback due to limitation of charge carrier mobility by grain boundaries. Indeed, the performance of pentacene transistor also suffers due to absorption of water molecules. The surface morphology and physical properties can strongly be influenced by surface pre-treatment of the gate dielectric and variation of deposition parameters such as substrate temperature and/or deposition rate [30,31,32,33]. Furthermore, the performance of bottom-contact pentacene transistors is inferior to that of devices with the top-contact structure. On the other hand, solution processability in OFET manufacture is strongly desirable for low-cost production. One excellent example is regioregular poly(3-hexylthiophene), P3HT, consisting of 98% head-to-tail (HT) linkage which exhibits hole mobilities of up to  $0.045 \text{ cm}^2/\text{Vs}$  [34]. However, the mobility of charge carriers in P3HT thin films has been found to vary by two orders of magnitude depending on the solvent used, with chloroform giving the highest charge carriers mobility. The other parameter controlling the charge carriers mobility is the pre-treatment of the gate dielectric surfaces [35]. Hole mobilities as high as  $0.1 \text{ cm}^2/\text{Vs}$  in P3HT thin films can be obtained via treatment of the gate

dielectric SiO<sub>2</sub> with hexamethyldisilazane (HMDS) [36]. On the contrary, exposure of P3HT films to air causes an increase in conductivity and subsequently the *ON/OFF* ratios fall off caused by the presence of trapped oxygen. Another *p*-type material is oligothiophene. For example an  $\alpha,\omega$ -dihexylquaterthiophene (DH $\alpha$ -4T) transistor has been shown to exhibit a field-effect mobility of 0.06 cm<sup>2</sup>/Vs for films deposited at 50 °C of substrate temperature [37]. A classical metallophthalocyanine such as copper phthalocyanine (CuPc) has also shown a high mobility of 0.02 cm<sup>2</sup>/Vs and an *ON/OFF* ratio of  $4 \times 10^5$  when the substrate temperature was kept constant at 125 °C during thermal sublimation [38]. A recent result of polycrystalline  $\alpha,\alpha'$ -bis(dithieno[3,2-b:2',3'-d]dithiophene) (BDT) showed an exceptionally high *ON/OFF* ratio of 10<sup>8</sup>, mobility of 0.05 cm<sup>2</sup>/Vs, and subthreshold voltage of 0.6 V/decade for a bottom-contact OFET. The high performance is attributed to the closely packed face-to-face stacking and the wide highest occupied molecular orbital (HOMO)-lowest unoccupied molecular orbital (LUMO) gap of the materials [39,40].

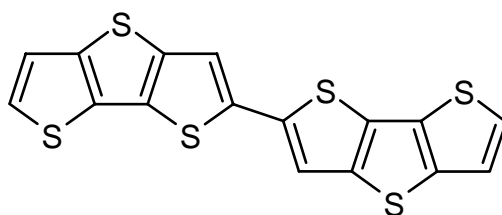


Pentacene

HT-poly(3-alkyl)thiophene, R = C<sub>n</sub>H<sub>2n+1</sub> ; n = 6 $\alpha,\omega$ -Oligothiophene (m = 4), R = C<sub>n</sub>H<sub>2n+1</sub> ; n = 0-8

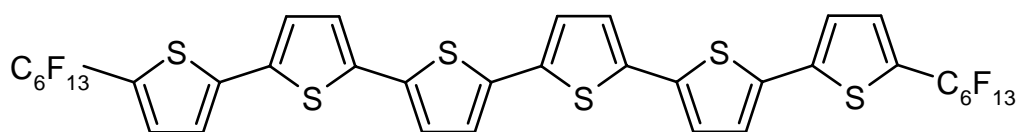


Copper phthalocyanine (CuPc)

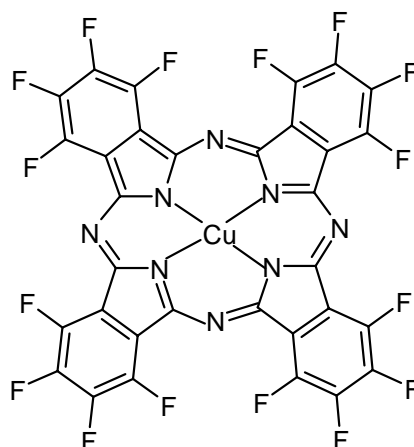
 $\alpha, \alpha'$ -Bis(dithieno[3,2-b:2',3'-d]dithiophene) (BDT)Scheme 2.1. Typical chemical structures of *p*-type organic semiconductors for OFET applications.

High performance *n*-type materials will enable the fabrication of *p-n* junctions, as well as complementary logic devices. However, the *n*-type OFET shows an inferior performance with respect to *p*-type OFET. These results can be attributed to the inherent instability of organic anions that react with oxygen and water under operating condition, thus providing unstable devices. Scheme 2.2 shows typical chemical structures of some *n*-type materials used in OFET. An electron mobility of  $0.02 \text{ cm}^2/\text{Vs}$  and an *ON/OFF* ratio of  $10^5$  can be achieved by utilizing  $\alpha, \omega$ -diperfluorohexylsexithiophene (DHT-6T) [41]. However, all measurements were performed under nitrogen. An appropriate substitution on metallophthalocyanines allowed the fine-tuning of the energy gap levels thus altering the majority charge carriers of the materials. A device made of perfluorinated copperphthalocyanine ( $\text{F}_{16}\text{CuPc}$ ) exhibited a mobility of  $0.03 \text{ cm}^2/\text{Vs}$  and an *ON/OFF* ratio of  $10^5$  when the substrate temperature was kept constant at  $125^\circ\text{C}$  during thermal sublimation [42]. Remarkably, these devices were air stable even if the samples were stored in air for half a year. No decrease in mobility and *ON/OFF* ratios was observed. On the other hand, the widely known  $\text{C}_{60}$  or fullerene has shown an electron mobility of  $0.08 \text{ cm}^2/\text{Vs}$  [43] which is slightly higher than the electron mobility in  $\text{F}_{16}\text{CuPc}$  or DFH-6T. However, OFET based on  $\text{C}_{60}$  can not be operated in air since their

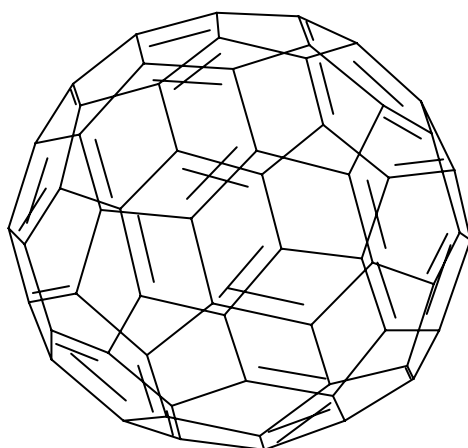
resistivity quickly increased by five orders of magnitude. This indicates that oxygen acts as an electron trap within the  $C_{60}$  lattice. Therefore, design rules for  $n$ -type materials require high chemical stability. For instance incorporating hydrophobic functionalities into the chemical structure could prevent the penetration of moistures. On the other hand, the electron affinity has to be optimized such that the LUMO level offset with respect to the Fermi level of the source and drain electrodes does not limit the injection of electrons from the source into the semiconductor and from the semiconductor to the drain [44]. Other excellent examples of  $n$ -type materials are  $N$ -substituted naphthalene-1,4,5,8-tetracarboxylic diimide (NTCDI) derivatives and  $N,N'$ -dioctyl-3,4,9,10-perylenetetracarboxylic diimide (PTCDI-C8). NTCDI-derivative transistors show a mobility of  $0.16 \text{ cm}^2/\text{Vs}$  when the measurement performed under vacuum [45]. PTCDI-C8 transistors show a mobility of  $0.6 \text{ cm}^2/\text{Vs}$  and an  $ON/OFF$  ratio of larger than  $10^5$  [46]. However, a high fitted threshold voltage of 75 V was observed, which can be attributed to the formation of traps related to structural defects.



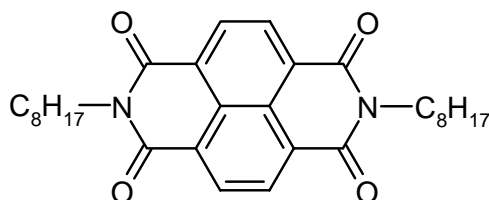
$\alpha,\omega$ -Diperfluorohexylsexithiophene (DFH-6T)



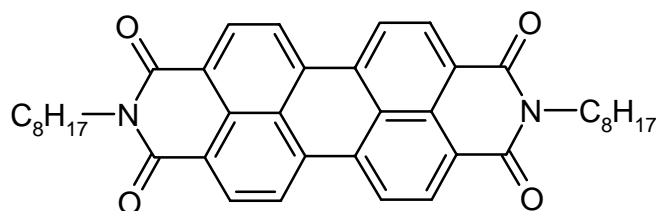
Fluorinated copper phthalocyanine ( $F_{16}CuPc$ )



C<sub>60</sub> or Fullerene



*N*-substituted naphthalene-1,4,5,8-tetracarboxylic diimide derivatives (NTCDI-C8H)



*N,N'*-Dioctyl-3,4,9,10-perylenetetracarboxylic diimide (PTCDI-C8)

Scheme 2.2. Typical chemical structures of *n*-type organic semiconductor for OFET applications.

Several important points have to be considered in the context of device fabrication and interpretation of the data: (i) The mobilities of charge carriers in the active materials have to be considered in the conception of the device geometry. The prediction of the mobility is important in order to get a reasonable ratio of the channel width ( $W$ ) to the channel length ( $L$ ) which exhibits field-effect transistor effect. (ii) Two device configurations can be fabricated, either top-contact devices or bottom contact devices. If the active material is very sensitive to moisture, the bottom-contact structure is preferred. (iii) An appropriate source and drain electrode material have to be carefully chosen with respect to the HOMO or LUMO level of the active materials. The HOMO and LUMO level of the organic semiconductor can be



measured by utilizing ultraviolet photoelectron spectroscopy (UPS). Gold is a well-established electrode material for both types, but LiF/Al can be also used for electron injection in *n*-type OFET with top-contact structure. (iv) Pre-treatment of the gate dielectric surface is important to prevent hydrophilic tendency of the gate dielectric surface. The difference in mobility between with and without pre-treatment of the gate dielectric surface has reached three orders of magnitude. (v) Fabrication process parameters such as evaporation rate, background pressure, and surface treatment have to be recorded carefully in order to avoid misinterpretation of the output data. (vi) Device characterization should be statistically analyzed which reflects the distribution and reproducibility of the physical properties of the active materials. Therefore, simultaneous fabrication and characterization of many identical devices is preferred. In the following text, the charge transport mechanism in organic semiconductors is described.

### 2.3. Charge Transport Properties of Amorphous Molecular Glasses Materials

The weak intermolecular interaction in organic semiconductors may be responsible for limiting the charge carrier mobility. A typical Van-der-Waals interaction energy is smaller than 42 kJ/mol. By contrast, in inorganic semiconductors such as silicon and germanium, the atoms are held together by strong covalent bonds, which in the case of silicon have energies of 318 kJ/mol. The charge carriers move as highly delocalized plane waves in wide bands and have very high mobility up to 1000 cm<sup>2</sup>/Vs at room temperature. The mobility is limited by lattice vibrations or phonons that scatter the carriers and thus it is reduced as the temperature increases. Therefore, band transport is not applicable to amorphous molecular glasses, where charge carrier transport takes place by hopping processes between localized states and charge carriers are scattered at every step. The hopping process is assisted by phonons and the charge carrier mobility is thermally activated. Nevertheless, the charge carriers mobility remains very low ( $\mu_{FET} \ll 1$  cm<sup>2</sup>/Vs). In the following discussion, three models to explain the charge transport mechanism in amorphous organic semiconductor are considered. The first model is the Gaussian Disorder Model proposed by Bässler and co-worker, which has successfully explained time of flight (TOF) data. The second is the activation energy model following Arrhenius behavior. Finally, the Variable Range Hopping theory proposed by Vissenberg and Matters will be discussed as well.

### 2.3.1. Gaussian Disorder Model

A fundamental assumption of the Gaussian disorder model (GDM) is that upon abandoning long-range order, the transport manifold of a molecular crystal is split into a Gaussian distribution of localized states. This assumption is based on the observation that the absorption profiles of polymers and organic glasses feature inhomogeneously broadened Gaussian profiles [47,48,49,50]. The distribution arises from fluctuations of the dipole-dipole and ion-dipole intermolecular potentials and is described as diagonal disorder. Basically, the hopping transport mechanism in organic solids is modeled such that the charge transporting elements are identified as sites where the energies of their hole or electron transporting states are governed by a Gaussian distribution of energies:

$$g(\varepsilon) = \frac{1}{\sqrt{2\pi\sigma^2}} \exp\left[-\frac{\varepsilon^2}{2\sigma^2}\right] \quad (2.16)$$

It implies that all states are completely localized with relatively weak intermolecular interaction. The energy  $\varepsilon$  is measured relative to the center of the density of states (DOS), and  $\sigma$  describes the Gaussian width. The origin of the energetic (diagonal) disorder is the fluctuation of the lattice polarization energies. The Gaussian shape of the DOS is suggested by the Gaussian profile of the absorption band and by the recognition that the polarization energy is determined by a large number of internal coordinates each varying randomly by small amounts. On the other hand, the hopping is assumed to be controlled by jump rates among sites  $i$  and  $j$  is assumed to be of the Miller-Abrahams type [51]

$$v_{ij} = v_o \exp\left(-2\gamma a \frac{\Delta R_{ij}}{a}\right) \exp\left[-\left(\frac{\varepsilon_j - \varepsilon_i}{k_B T}\right)\right], \quad \varepsilon_j > \varepsilon_i \quad (2.17a)$$

$$v_{ij} = v_o \exp\left(-2\gamma a \frac{\Delta R_{ij}}{a}\right), \quad \varepsilon_j < \varepsilon_i \quad (2.17b)$$

where  $v_{ij}$  is the jump rate,  $v_o$  the frequency factor,  $\gamma$  the overlap parameter,  $\Delta R_{ij} = |R_i - R_j|$  the intersite distance between sites  $i$  and  $j$ ,  $\varepsilon_i$  and  $\varepsilon_j$  the energy sites  $i$  and  $j$ ,  $T$  the temperature,  $a$  the average lattice distance, and  $k_B$  the Boltzmann's constant. In Equation 2.17, it is assumed that the Boltzmann jump probability is unity for  $\varepsilon_j < \varepsilon_i$ . Hops down in energy are not impeded by an energy matching condition for dissipating the difference in electronic energy. The

Miller-Abrahams formulism is based on a single phonon approximation and implies that downward jumps in energy are not accelerated by the electric field. Finally, the polaronic effect was assumed to be negligible which means that electron-phonon coupling is weak enough.

However, the Gaussian form of the DOS in random organic system prevents closed form analytical solutions of the hopping transport problem. Therefore, a Monte Carlo simulation was considered as an alternative approach to solve the problem with various degrees of complexity [52,53]. The Gaussian distribution with  $\sigma$  width was assigned to the sites of a cubic lattice. The geometrical disorder (off-diagonal disorder) was attributed to random fluctuation of the wave function overlap parameter  $\Gamma_{ij} = 2\gamma a$ . Thus, it can be obtained by splitting it into two sites contribution  $\Gamma_{ij} = \Gamma_i + \Gamma_j$  with a variance of  $\Sigma = 2(\sigma_T)^{0.5}$ . Based on the simulation, a universal law is established relating  $\mu$  to the degree of both diagonal and off-diagonal disorder in the high field limit ( $10^6$  V/cm) and  $T < T_g$ ,  $T_g$  being the glass transition temperature [54]

$$\mu = \mu_o \exp \left[ - \left( \frac{2\sigma}{3k_B T} \right)^2 \right] \exp \left\{ C \sqrt{E} \left[ \left( \frac{\sigma}{k_B T} \right)^2 - \Sigma^2 \right] \right\} \quad (2.18)$$

where  $\mu_o$  is the prefactor mobility relating to the overlap between the molecular orbital and can be viewed as the mobility in the absence of energetic disorder or infinite temperature. Furthermore,  $C$  is an empirical constant of  $2.9 \times 10^{-4}$  (cm/V)<sup>1/2</sup>, assuming the intersite distance of 0.6 nm and it contains no adjustable parameter. Variance  $\sigma$  represents the width of the Gaussian DOS and  $E$  denotes the electric field.  $\Sigma$  is a parameter which describes the degree of off-diagonal disorder. It accounts for the variation of intersite coupling due to variations of both intersite distances and wave function overlaps. The simulation also indicates that diagonal and off-diagonal disorder contribute independently. Equation 2.18 has been found to be useful in describing TOF data. However, Employing Equation 2.18 to describe temperature- and field-dependence in OFET may be opened to question since the OFET is a two-dimensional device, which is in contrast to one-dimensional TOF. In the case of OFET, the second term of Equation 2.18 can be neglected due to the low electric field ( $E_D = 6 \times 10^4$  V/cm for  $V_D = -60$  V and  $L = 10$   $\mu$ m). Therefore, the data will be evaluated by simplifying Equation 2.18,

$$\mu = \mu_o \exp \left[ - \left( \frac{2 \sigma}{3 k_B T} \right)^2 \right] \quad (2.19)$$

Equation 2.19 can be rewritten as

$$\mu = \mu_o \exp \left[ - \left( \frac{T_o}{T} \right)^2 \right] \quad (2.20)$$

where  $T_o$  is a characteristic temperature proportional to the width of the distribution,  $T_o = 2\sigma/(3k_B)$ . Other parameter such as activation energy  $\Delta E_a$  can be deduced from following equation [52]

$$\Delta E_a = \frac{8 \sigma^2}{9 k_B T} \quad (2.21)$$

Therefore, a consequence of hopping in a Gaussian DOS is the non-Arrhenius behavior of the mobility. However, within the temperature range studied it is not possible to distinguish between Arrhenius behavior and non-Arrhenius behavior. As mentioned above, the simulation has to take into account the electric field in a narrow field range, at relatively high fields ( $10^6$  V/cm). The agreement with the experiment has to be improved by taking into account the presence of long-range energy correlation [55,56] which can possibly arise from charge-dipole interactions in the material. Novikov *et al.* [55] proposed a correlated Gaussian disorder model (CDM) following the empirical relation,

$$\mu = \mu_o \exp \left[ - \left( \frac{3 \sigma}{5 k_B T} \right)^2 + 0.78 \left( \left( \frac{\sigma}{k_B T} \right)^{3/2} - 2 \right) \sqrt{\frac{qaE}{\sigma}} \right] \quad (2.22)$$

with  $a$  being the intersite spacing. The main difference between the GDM and CDM formulism is the predicted temperature dependence of the field activation factor  $\gamma$ , which can be written as

$$\gamma = \frac{\beta}{k_B} \left( \frac{1}{T} - \frac{1}{T_o} \right) \quad (2.23)$$

where  $\beta = 2.7 \times 10^{-5} \text{ eV}(\text{V/m})^{-0.5}$ . Blom and Vissenberg observed that the temperature dependence of the mobility in the inhomogeneous model follows that of the CDM rather than the GDM [57].

### 2.3.2. Activation Energy Model

In 1972 Gill described the transport mechanism in poly-*n*-vinylcarbazole, PVK [58]. He observed that the temperature behavior of the charge carrier mobility was thermally activated with a large activation energy. The three main features of the data he presented were: (i) mobility is an activated process; (ii) the activation energy is electric field dependent, decreasing with increasing electric field; and (iii) the data extrapolate to a common intersection at a finite temperature  $T_o$ . The hopping mechanism in organic materials can be viewed as hopping due to a single level of traps or an activation energy arising from polaron relaxation. The general expression of the Activation Energy model can be written as

$$\mu = \mu_o \exp\left[-\frac{\Delta E_a}{k_B T}\right] \exp\left[\beta \sqrt{E} \left(\frac{1}{k_B T} - \frac{1}{k_B T_o}\right)\right] \quad (2.24)$$

where  $\mu_o$  is the prefactor mobility,  $\Delta E_a$  is the activation energy,  $\beta$  is the factor of the field dependence ( $\beta = 2.7 \times 10^{-5} \text{ eV}(\text{V/m})^{-0.5}$ ),  $E$  the electric field,  $T$  the temperature,  $k_B$  the Boltzmann's constant, and  $T_o$  is the temperature at which the field dependence vanishes. The major objection to the Arrhenius model is the unreasonable value of  $\mu_o$  ( $\mu_o$  is too large for low molecular glasses or polymer, for instance  $\mu_o \approx 10 \text{ cm}^2/\text{Vs}$ ), if the data is obtained from TOF measurements. However, Gill obtained a prefactor mobility in the range of  $10^{-4} \text{ cm}^2/\text{Vs}$  and  $10^{-2} \text{ cm}^2/\text{Vs}$  for a different composition of 2,4,7-trinitro-9-fluorenone (TNF) with PVK.

The field and temperature dependence expressed in Equation 2.24 is similar to the field dependence of the mobility as described by Poole-Frenkel (PF) effects [59]. In the one dimensional case the mobility can be written as  $\exp\left(\beta_{PF} \sqrt{E} / k_B T\right)$ , where  $\beta_{PF} = \sqrt{(q^3 / \pi \epsilon \epsilon_o)}$ . Here,  $E$  is the electric field,  $q$  is the electronic charge, and  $\epsilon$  is the dielectric constant at high frequency. Basically, the PF model describes the reduction in ionization energy of a carrier in a coulomb potential by an electric field. Thus the applied electric field increases the free-carriers density. Despite predicting the field dependence of mobility, the discrepancy to the PF model is apparent. First, it assumes delocalization of the

charge carriers, which contradicts to the fact that most organic semiconductors are governed by an energy distribution of localized states. The second obvious discrepancy is the requirement of a relatively high density of charged coulombic centers, which in these insulating systems can only be compensated by oppositely charged centers. Ionized centers of this kind are not expected to occur in organic semiconductor system. Therefore, the PF model is not applicable for organic semiconductor system.

Vissenberg and Matters proposed the concept of variable-range hopping (VRH) as the charge transport mechanism in amorphous organic transistors, where the charge is governed by hopping [60,61]. This theory preferred the thermally activated tunneling of charge carriers between localized states rather than by the activation of carriers to a transport level. The charge carriers may either hop over a small distance with a high activation energy or hop over a long distance with a low activation energy. Their model is based on the following exponential DOS:

$$g(\varepsilon) = \frac{N_t}{k_B T_0} \exp\left(\frac{\varepsilon}{k_B T_0}\right) \quad (2.25)$$

where  $N_t$  is the number of states per unit volume,  $k_B$  is the Boltzmann's constant, and  $T_0$  is a parameter that indicates the width of the exponential distribution. The transport properties were determined by the tail of the DOS which was assumed for low carrier densities and low  $T$ . The influence of temperature and the influence of filling of states on the conductivity of a VRH system with an exponential distribution of DOS can be expressed by incorporating percolation theory. As a result, the field-effect mobility can be expressed in the following equation

$$\mu_{FET} = \frac{\sigma_0}{e} \left( \frac{\pi(T_0/T)^3}{(2\alpha)^3 B_c \Gamma(1-T/T_0) \Gamma(1+T/T_0)} \right)^{T_0/T} \left[ \frac{(C_i V_G)^2}{2k_B T_0 \varepsilon_s} \right]^{T_0/T-1} \quad (2.26)$$

where  $B_c$  is critical number of bonds in percolation theory, which is  $B_c = 2.8$  for three dimensional amorphous system [62],  $k_B$  is the Boltzmann's constant,  $V_G$  is the gate bias,  $e$  is the elementary charge,  $\sigma_0$  is the preexponential factor of the conductivity,  $\alpha^{-1}$  is the overlap parameter, and  $\varepsilon_s$  is the dielectric constant of the semiconductor.

Furthermore, Vissenberg and Matters reported that the temperature dependence of  $\mu_{FET}$  in experimental data follows a simple Arrhenius behavior  $\sim \exp[-E_d/(k_B T)]$ , where the

activation energy  $E_a$  depends on gate voltage  $V_G$ . They also showed that the decrease of  $E_a$  with increasing gate voltage is the direct result of accumulated charges filling the lower-lying states. As a result, any additional charge carriers in the system will occupy sites with a higher energy and less energy will be required for the activated jumps to neighboring sites. This results in a higher mobility with increasing gate voltage. This theory has been applied for pentacene and polythienylene vinylene (PTV) field-effect transistors. They obtained a preexponential prefactor  $\sigma_0$  of  $1.6 \times 10^{10}$  S/m for pentacene and  $7 \times 10^9$  S/m for PTV. The overlap parameter  $\alpha^{-1}$  was 0.22 nm for pentacene and 0.08 nm for PTV and the width of the exponential distribution of localized state  $T_0$  was 385 K for pentacene and 380 K for PTV [60].





## Chapter 3

# Investigated Low Molecular Amorphous Materials

In this chapter the characteristic features of the widely-known low molecular amorphous, which are used as hole transporter in OLEDs, are compared with hole transport materials based on the spiro concept. Low molecular-weight organic compounds readily form stable amorphous glasses above room temperature, which we refer to as *amorphous molecular materials* or *molecular glasses*. Amorphous molecular materials are of interested because of the following aspects. They are endowed with interesting features, for instance, they are characterized by disorder both in intermolecular distance and in orientation, by the presence of free volume and they exhibit isotropic properties [63]. They have well-defined molecular structures and definite molar masses, which cannot be found in polymeric materials. Moreover, they also may form homogeneous amorphous thin films by vapor deposition or spin-coating methods.

### 3.1. Classical Hole Transport Material

Generally, most hole transport materials for OLEDs are based on aromatic amine groups or contains these groups. *N,N'*-Bis(3-methylphenyl)-(1,1'-biphenyl) - 4,4'-diamine or TPD, as shown in Figure 3.1(a), is a widely-known hole transport material for electroluminescent devices. Amorphous TPD thin films can be easily obtained by means of thermal evaporation, but they exhibit glass transition temperatures ( $T_g$ ) of 60 °C. Unfortunately, the morphological stability of TPD thin films is very poor. Shirota *et al.* [5], Qiu *et al.* [6], and Fujihara *et al.* [64,65] observed that TPD thin films were easily crystallized at room temperature after the film was stored for less than one week. Smith *et al.* [66] gave the first evidence of spherulitic crystallization of TPD thin films in the degradation of organic electroluminescent devices. During operation the appearance of nonemissive dark spots, which was attributed to the formation of spherulits, was observed. These spherulits cause the delamination of the device, and thus lead to the failure of the device. The presence of moisture and oxygen were believed enhanced the formation of dark spots.

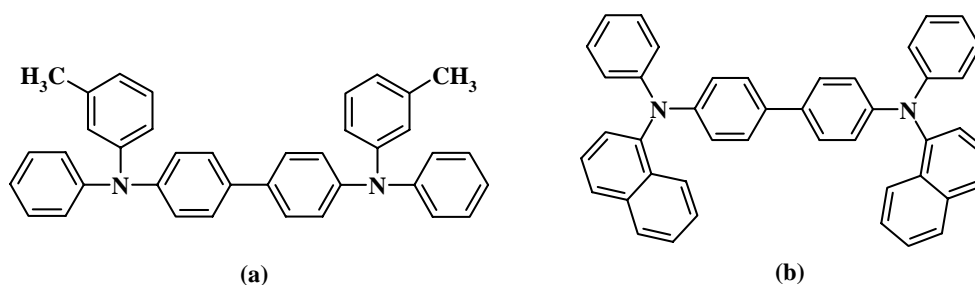


Figure 3.1 A widely-known hole transport materials for OLED. (a) TPD, (b)  $\alpha$ -NPB.

In contrast to TPD, the naphthyl-substituted benzidine derivative  $\alpha$ -NPB (Figure 3.1(b)), *N,N'*-diphenyl-*N,N'*-bis(1-naphthyl)-1,1'-biphenyl-4,4'-diamine, exhibits a relative high  $T_g$  of 96 °C. Kodak group reported for the first time an OLED based on  $\alpha$ -NPB as the hole transport layer, which was sandwiched between the emitter Tris(8-hydroxyquinoline)aluminium, Alq3 and the hole blocking layer copper phthalocyanine, CuPc. They demonstrated a highly stable organic electroluminescent device with an initial luminance of 510 cd/m<sup>2</sup> and the half-lifetime of 4000 hours [67]. Moreover, Thompson *et al.* [68] also demonstrated that an OLED employing CuPc as the hole blocking layer,  $\alpha$ -NPB as the hole transporter and Alq3 as the emitting layer, sandwiched between an ITO and a Mg:Ag, exhibited a quantum efficiency of 0.85 %, and a maximum luminance of 15700 cd/m<sup>2</sup> at 5 mA. However, we observed that  $\alpha$ -NPB thin films were crystallized after the samples were stored in ambient atmosphere for three days. This observation will be presented and discussed in chapter 5.

### 3.2. Hole Transport Materials based on the Spiro Concept

The glass transition temperature of molecular glasses can be increased by the incorporation of structurally rigid moieties and by increasing molecular size and weight, as well as by enhancing intermolecular interaction. In 1996, Salbeck [10] introduced the spiro concept for charge transporting or emitter materials. The schematic view of the spiro concept is presented in Figure 3.2(a). Joining two  $\pi$ -systems (in this case two identical  $\alpha$ -NPB or TPD molecules) with a spiro center achieves the task of raising the glass transition temperature  $T_g$ , because of the increased steric demand of the resulting spiro-compound (Spiro  $\alpha$ -NPB or Spiro-TPD), which effectively hinders crystallization. Even though the spiro atom links two identical charge transport molecules, the electronic properties are retained. The chemical structure of 2,2',7,7'-Tetra-(*m*-tolyl-phenylamino)-9,9'-spirobifluorene (Spiro-TPD) and

2,2',7,7'-Tetra-(*N*-phenyl-1-naphtylamine)-9,9'-spirobifluorene (Spiro  $\alpha$ -NPB) are shown in Figure 3.2(b) and Figure 3.2(c). The resulting spiro-compound has a higher  $T_g$  than its corresponding parent compounds as shown in Table 3.1.

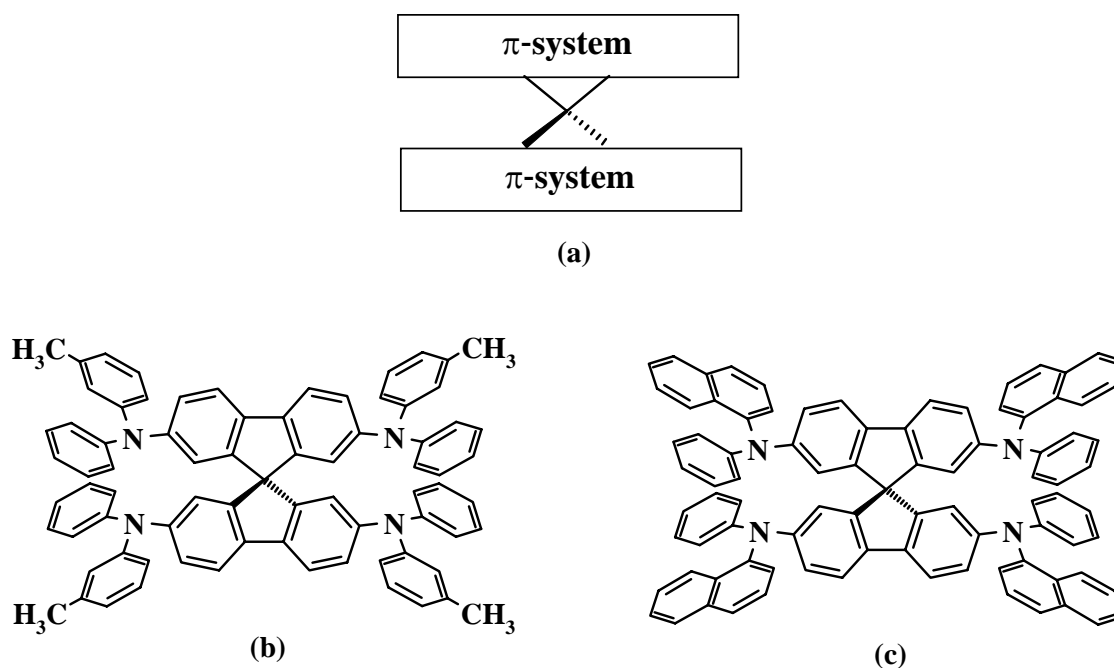


Figure 3.2. Schematic view of the spiro concept (a) and hole transport materials based on the spiro-concept, Spiro-TPD (b), and Spiro  $\alpha$ -NPB (c).

Table 3.1. Glass temperature of spiro-compounds and the corresponding parent compounds.

Material	$T_g$ ( $^{\circ}\text{C}$ )	Ref.	Material	$T_g$ ( $^{\circ}\text{C}$ )	Ref.
TPD	62	[5]	Spiro-TPD	115	[70]
$\alpha$ -NPB	95	[69]	Spiro $\alpha$ -NPB	147	[70]

The interesting question arising from this thesis concerns the electronic properties of spiro-compounds and their corresponding parent compounds. In the following explanation, we will discuss the blue emitters sexiphenyl and spiro-sexiphenyl. Their chemical structures are shown in Figure 3.3.

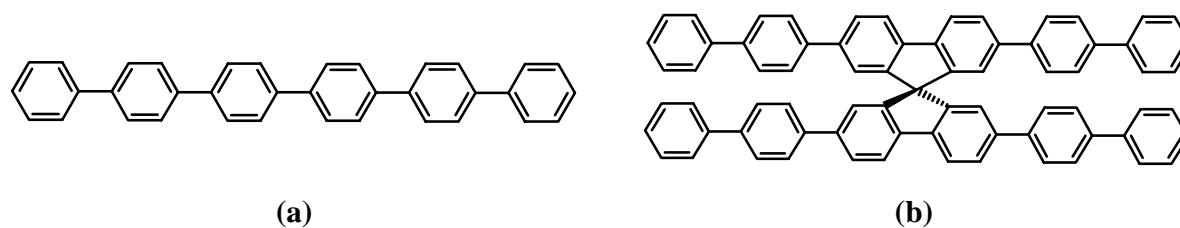


Figure 3.3. Blue emitter sexiphenyl (a) and its spiro-compound, Spiro-sexiphenyl (b).

The photoelectron spectroscopy measurement showed that the position of the highest occupied molecular orbital (HOMO) level of Spiro-sexiphenyl is  $5.9 \pm 0.1$  eV [71]. Furthermore, the experimental determination of the HOMO level in Spiro-sexiphenyl shows the same value as in sexiphenyl [72], which is consistent with the general idea of considering the global  $\pi$ -system of spiro molecules as a result from two weakly interacting  $\pi$ -system of the perpendicular molecular halves. In other words, most of the electronic properties of symmetric spiro-compounds may be deduced from the consideration of a molecule half and thus these properties are similar for the spiro and its parent molecules. It should be stressed that, although the molecular halves of the spiro molecules are perpendicular to each other, there is a finite interaction at the spiro-center between the two  $\pi$ -electron systems of the two molecular halves, which leads to a splitting of some of the orbitals. Moreover, Time of Flight (TOF) measurements [73] showed that the hole mobility in spiro-compounds thin films is in the same order of magnitude as that of its parent compound. Therefore, we conclude that linking two charge transport moieties in a perpendicular arrangement via a spiro carbon atom strongly improves the thermal stability of the amorphous state without significantly changing their charge-transport properties. This is consistent with the idea that Salbeck previously introduced [10].

The active materials used in this study can be divided into three classes, namely Spiro-linked compounds (symmetrically spiro-linked compounds), the corresponding parent-compounds, and photosensitive spiro-linked compounds (asymmetrically spiro-linked compounds). Some of symmetrically spiro-linked compounds used in this study were

- 2,2',7,7'-Tetrakis-(diphenylamino)-9,9'-spirobifluorene (Spiro-TAD),
- 2,2',7,7'-Tetrakis-(*N,N'*-di-*p*-methylphenylamino)-9,9'-spirobifluorene (Spiro-TTB),
- 2,2',7,7'-Tetra-(*m*-tolyl-phenylamino)-9,9'-spirobifluorene (Spiro-TPD), and
- 2,2',7,7'-Tetra-(*N*-phenyl-1-naphtylamine)-9,9'-spirobifluorene (Spiro  $\alpha$ -NPB).

Related parent compounds of the symmetrically spiro-linked compound used in this study were

- *N,N,N',N'*-Tetraphenylbenzidine (TAD),
- *N,N,N',N'*-Tetrakis(4-methylphenyl)benzidine (TTB),
- *N,N'*-Bis(3-methylphenyl)-(1,1'-biphenyl)-4,4'-diamine (TPD), and
- *N,N'*-Diphenyl-*N,N'*-bis(1-naphthyl)-1,1'-biphenyl-4,4'-diamine ( $\alpha$ -NPB).

The photosensitive asymmetrically spiro-linked compounds used in this study were

- 2,7-bis-(*N,N'*-diphenylamino)-2',7'-bis(biphenyl-4-yl)-9,9'-spirobifluorene (Spiro-DPSP), and
- 2,7-bis-(*N,N'*-diphenylamino)-2',7'-bis(spirobifluorene-2-yl)-9,9'-spirobifluorene (Spiro-DPSP<sup>2</sup>).

The photoresponsive materials based on asymmetrically spiro-linked compounds belong to the class of asymmetric spiro-linked compounds in which two different functional chromophores are linked together by a central spiro atom [17]. In this case, the functional moiety consists of a sexiphenyl chain and a bis(diphenyl-amino)biphenyl unit. Generally, spiro compounds are known as glass-forming materials with high glass transition temperatures and a good morphological stability, which makes them well suitable for organic devices. The symmetrically substituted parent compounds of Spiro-DPSP and Spiro-DPSP<sup>2</sup>, 2,2',7,7'-tetrakis(diphenylamino)-9,9'-spirobifluorene (Spiro-TAD) and 2,2',7,7'-tetrakis(biphenyl-4-yl)-9,9'-spirobifluorene (Spiro-6 $\Phi$ ), and 2,2',7,7'-tetrakis(9,9'-spirobifluorene-2-yl)-9,9'-spirobifluorene (4-Spiro<sup>2</sup>), have been successfully applied in organic solar cells [11], light-emitting diodes [12,13], field-effect transistors [14] and lasers[16], respectively. The glass transition temperature of Spiro-DPSP and Spiro-DPSP<sup>2</sup> are 159 °C and 210 °C which lie between the glass transition temperatures of Spiro-TAD (133°C) and 4-Spiro<sup>2</sup> (273 °C). Figure 3.4 shows the chemical structure of every compound used in this study and Figure 3.5 shows that the resulting spiro-compound has a higher  $T_g$  than their corresponding parent compounds.

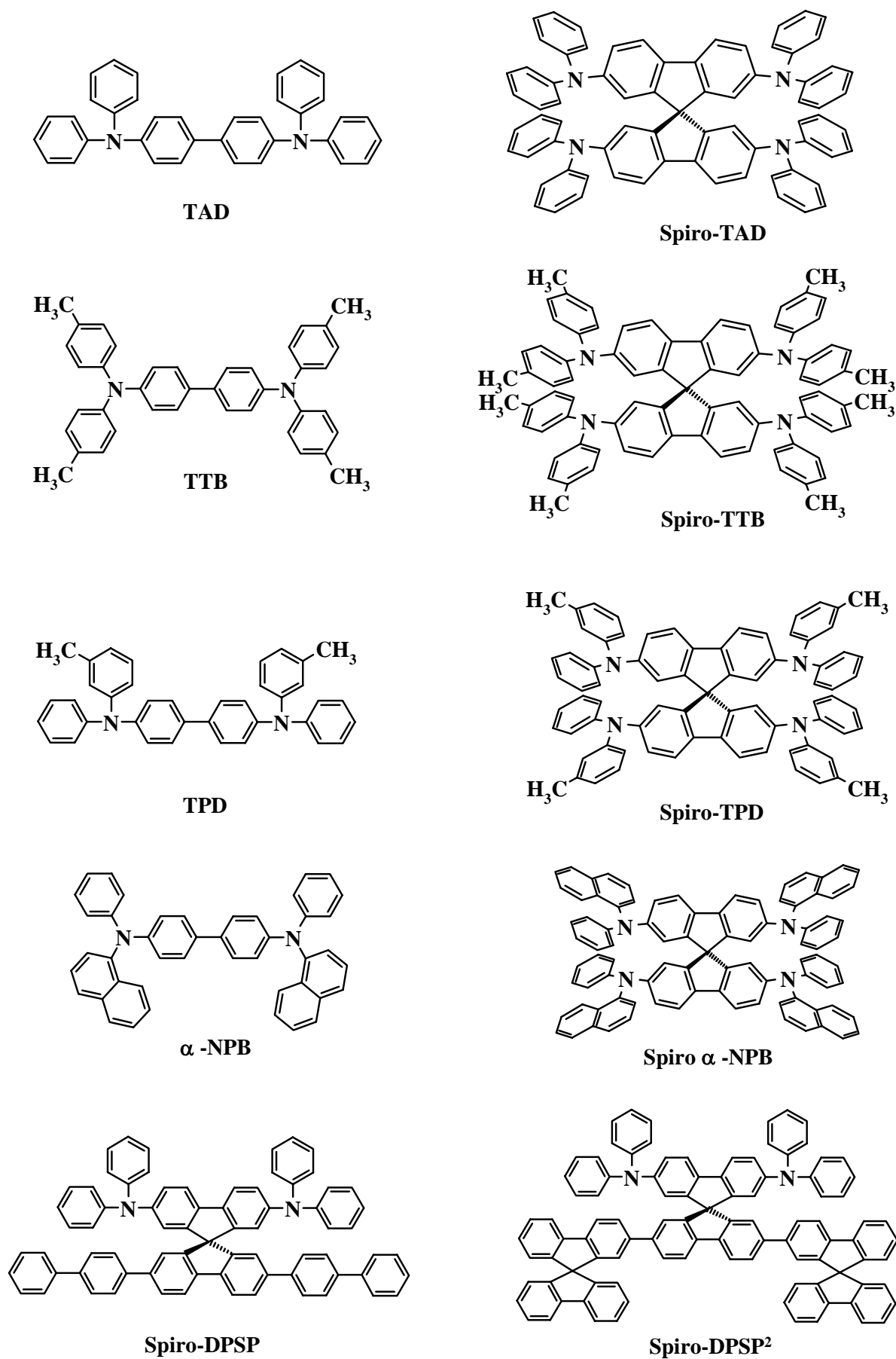


Figure 3.4. The chemical structures of active materials used in this study.

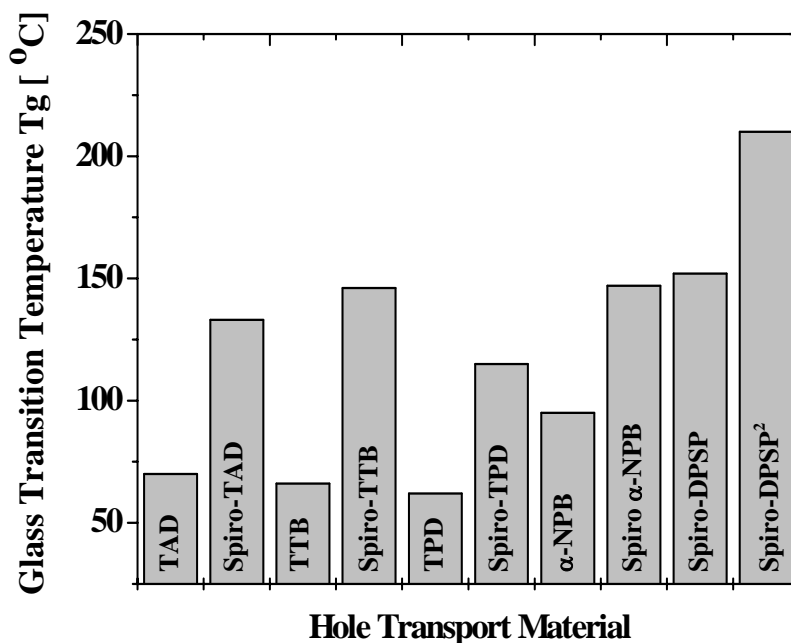


Figure 3.5. The glass temperatures ( $T_g$ ) of the active materials used in this study.

As described previously in chapter 2, the charge injection between the gold electrode and the HOMO level of the active material is a crucial point in organic transistors. The energy level HOMO or lowest unoccupied molecular orbital (LUMO) of the active materials can be investigated by utilizing photoelectron spectroscopy (PES). However, the organic materials are usually characterized by cyclic voltammetry [74]. From this point, the values can be extrapolated to the gas phase by choosing an appropriate reference and neglecting the influence of the polarity of the solvent in which the measurements are taken [75]. The ionization energy of ferrocene is assumed to be 4.8 eV, thus linking the electrochemical potential to the work function scale of the electrode [76]. Therefore, the energy of the molecular orbital is the negative value, that is,

$$E_{MO} = -(4.8 + E_{1/2}) \quad (3.1)$$

$E_{1/2}$  being the reversible half-wave potential of the electron-transfer reaction with respect to ferrocene. Figure 3.6 shows the work function of the gold electrode and the HOMO level of the active materials used in this study. The HOMO level is extracted by substituting the value of  $E_{1/2}$  in equation 3.1, which is obtained from cyclic voltammetry measurements [77].

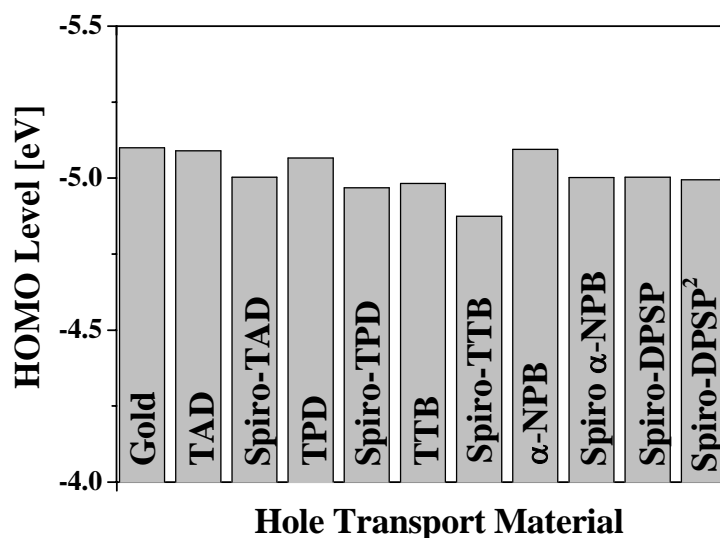


Figure 3.6. The work function of gold electrode and the HOMO level of the hole transport materials used in this study.

Table 3.2. Potential barrier for charge injection from the gold electrodes to the spiro-linked compounds and the corresponding parent compounds.

Material	Potential Barrier $\phi_B$ (eV)
TAD	0.010
Spiro-TAD	0.097
TPD	0.034
Spiro-TPD	0.132
TTB	0.117
Spiro-TTB	0.225
$\alpha$ -NPB	0.005
Spiro $\alpha$ -NPB	0.098
Spiro-DPSP	0.097
Spiro-DPSP <sup>2</sup>	0.106

The output characteristic of organic transistor strongly depends on the contact properties between the gold electrodes and the spiro-linked compounds or their corresponding parent compounds. An ohmic contact in organic transistor is required, which is defined as a metal-semiconductor contact that has a negligible contact resistance relative to the bulk or



spreading resistance of the semiconductor [18]. Therefore, the contact properties are highly dependent on both the metal work function and the HOMO level of the active materials. Table 3.2 shows that the HOMO level of the TAD and  $\alpha$ -NPB exhibits a small potential barrier and, thus, the contact is ohmic. On the contrary, the HOMO level of Spiro-TTB exhibits a large potential barrier with the gold electrodes. This barrier can probably cause a nonlinear behavior on the transistor characteristics. The behaviors of the transistor characteristics will be presented in chapter 6.



## Chapter 4

# Experimental

The details of the experimental procedures will be described in this chapter. It encompasses the fabrication of organic field-effect transistors (OFET) and electrical characterization. Furthermore, a design of a transistor, fabrication of pre-defined substrates, and fabrication of organic transistors are presented. OFETs were fabricated by means of optical lithography. Electrical characterization was performed by using a well-established semiconductor parameter analyzer. Furthermore, electrical characterization was performed in different environmental conditions.

### 4.1. Fabrication of Organic Field-Effect Transistors

#### 4.1.1. Preparation of Pre-defined Substrates

The fabrication of OFETs can be divided into two parts: (i) the fabrication of the substrates with a pre-defined field-effect transistor (FET) structure which is similar to the conventional Metal-Oxide-Semiconductor Field-Effect Transistor (MOSFET) structure [78] and (ii) the growth of organic thin films by means of thermal evaporation. The whole fabrication was carried out in a clean room. The schematic view of the OFET structure used in this study is shown in Figure 4.1 and the details of device fabrication are displayed in Figure 4.2.

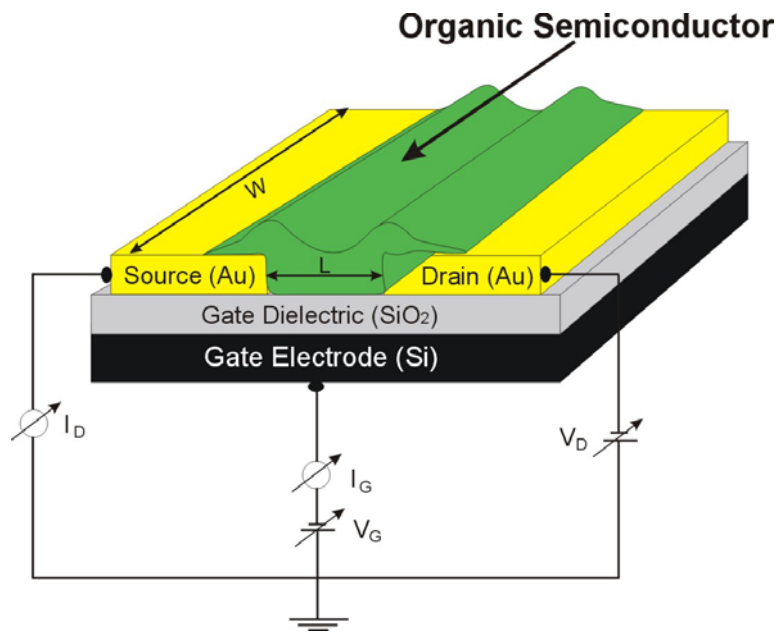
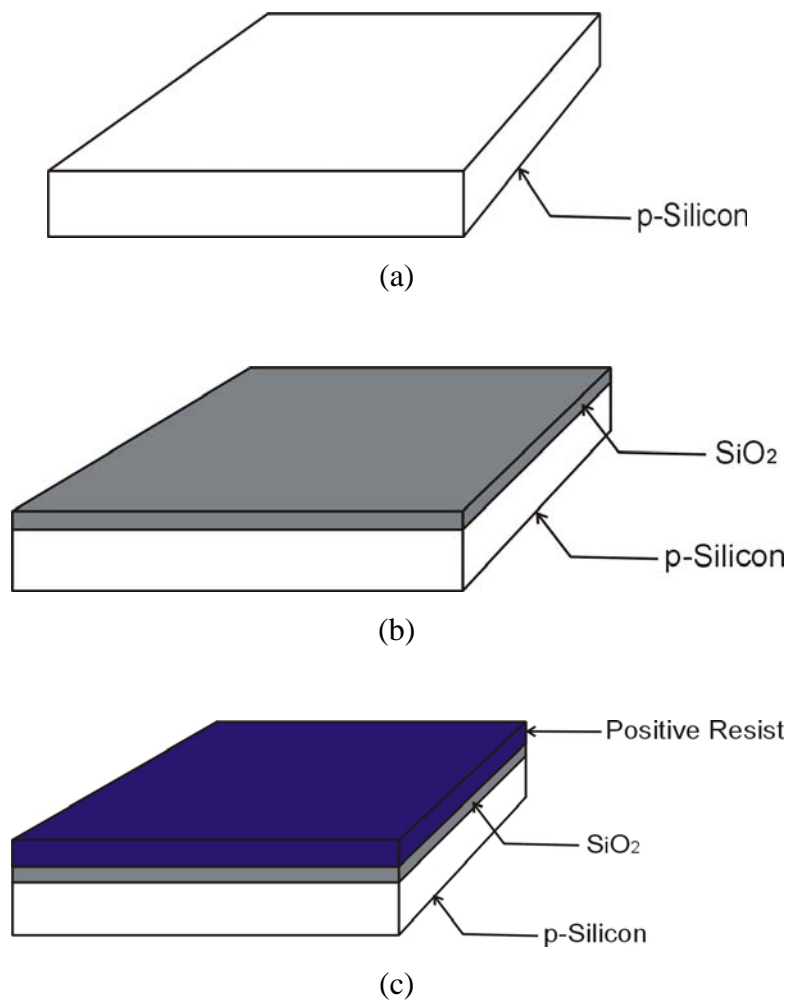
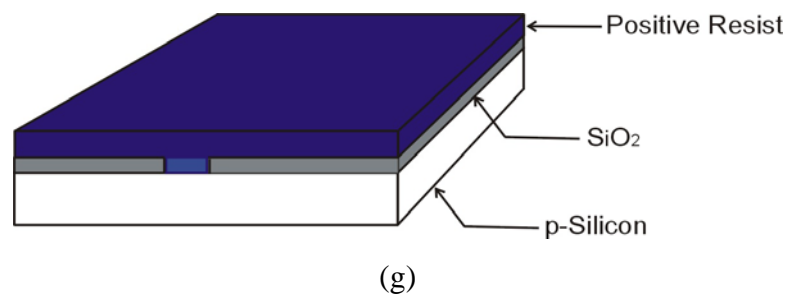
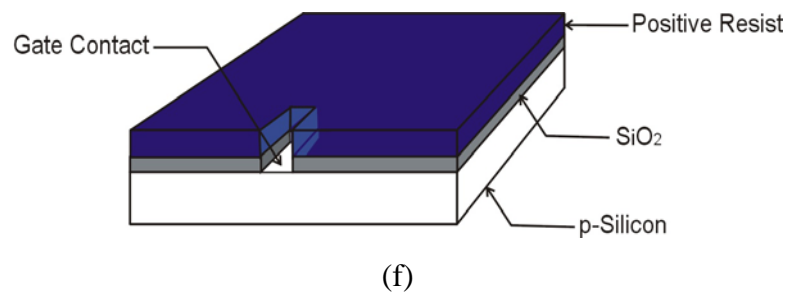
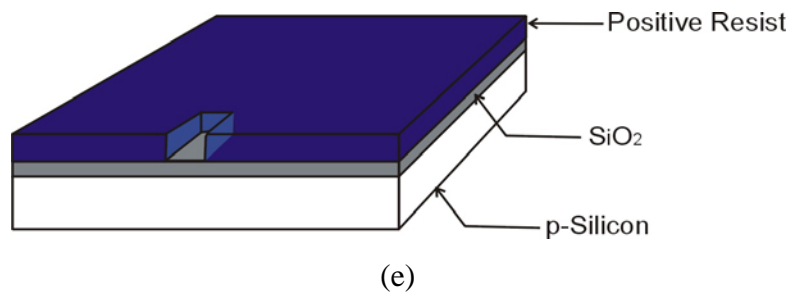
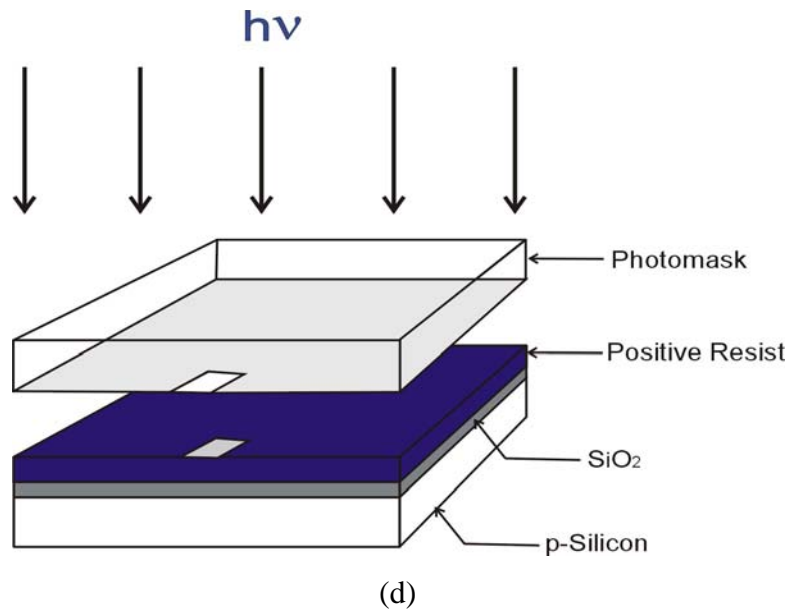
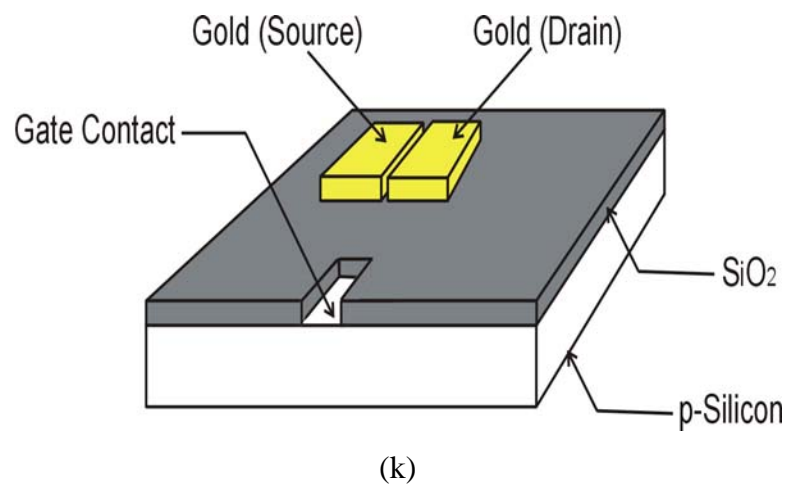
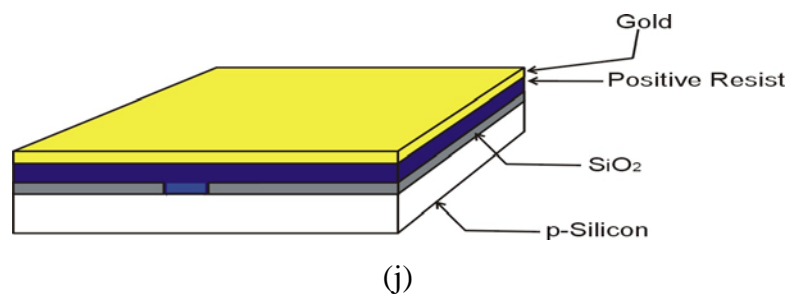
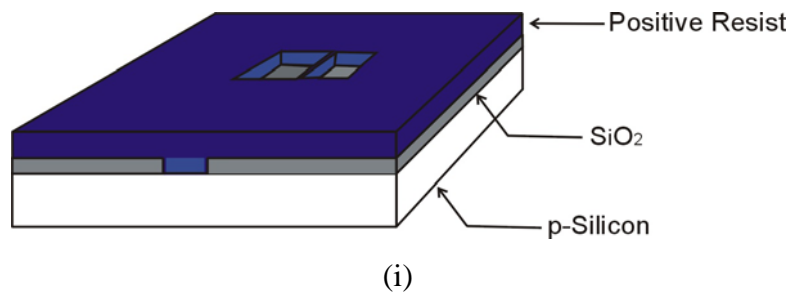
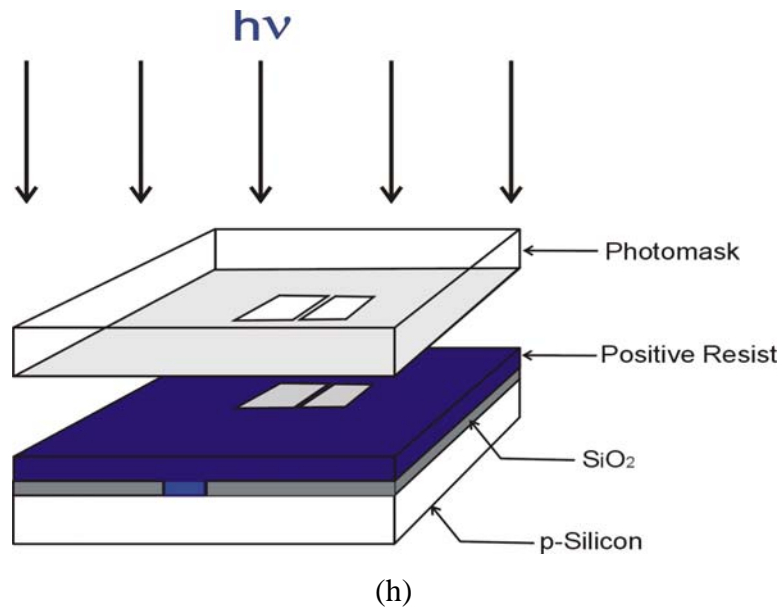


Figure 4.1. Schematic view of an organic field-effect transistor (OFET).







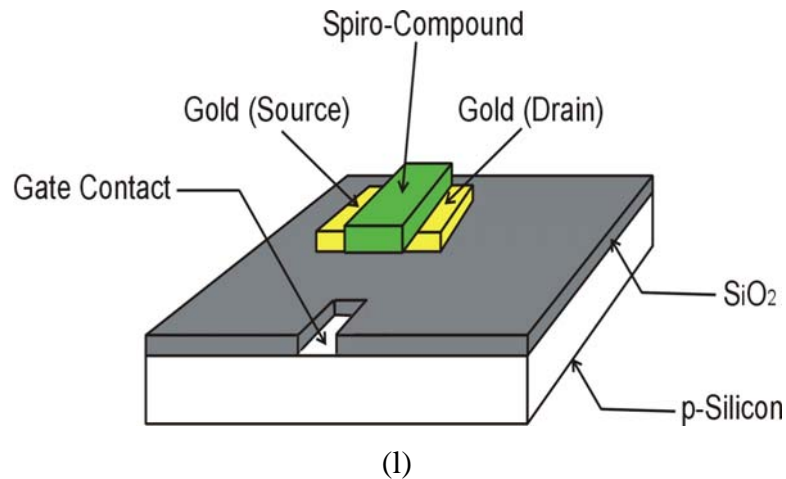


Figure 4.2. The details of organic field-effect transistor (OFET) fabrication.

The details of OFET fabrication are described in the following:

- a. A highly doped *p*-Silicon wafer (resistivity of 0.005 – 0.02 Ohm cm, (100)) was used as the substrate. First, the wafer was cleaned in  $\text{H}_2\text{SO}_4 : \text{H}_2\text{O}_2$  (3:1) solution at 90 °C for at least 30 minutes. Then the wafer was dried with a spin-coater (3000 rpm for 13 s), followed by baking on a hotplate (at 120 °C for 60 s).
- b. Gate dielectric silicon dioxide  $\text{SiO}_2$  was prepared by thermal oxidation in a dry oxygen atmosphere (thickness of  $\text{SiO}_2$  was in the range of 150 nm and 200 nm, i.e. capacitance per unit area is between 17 nF/cm<sup>2</sup> and 23 nF/cm<sup>2</sup>). This process was carried out in a furnace at 950 °C for 10 hours. The thickness of the gate dielectric  $\text{SiO}_2$  was measured with an Ellipsometer (J.A. Woollam, Co., USA).
- c. The *p*-silicon will serve as a common gate electrode. Therefore, the  $\text{SiO}_2$  layer should be patterned. Like usual the wafer was cleaned in  $\text{H}_2\text{SO}_4 : \text{H}_2\text{O}_2$  (3:1) solution at 90 °C for 30 minutes. Then, the wafer was dried and treated with hexamethyldisilazane (HMDS) for 2 minutes. HMDS was used in order to improve photoresist adhesion to oxides. The HMDS reacts with the oxide surface in a process known as silylation, forming a strong bond to the surface. At the same time free bonds are left which readily react with the photoresist, enhancing the photoresist adhesion. The process works not only on silicon dioxide, but also with other oxides (e.g.  $\text{Al}_2\text{O}_3$ ) as well. The AZ 1518 positive photoresist [79] was spin-coated on the entire wafer at 4000 rpm for 40 s. The thickness of photoresist was 1.8  $\mu\text{m}$ . Subsequently, the wafer was baked at 90 °C for 15 – 30 minutes in order to remove the solvent from the photoresist film and increase resist adhesion. Finally, the wafer was kept at room temperature for at least 20 minutes.

- d. The patterning of the gate electrodes was performed with a photomask (the first photomask) by means of optical lithography. The wafer was aligned with respect to the mask in an optical lithographic system, and the resist was exposed to UV light for 9 s.
- e. Photoresist development was done by flooding the wafer with the developer (0.8 % KOH solution) for ca. 50 s. Since positive photoresist was used, the exposed resist was dissolved in the developer. Then the wafer was subsequently dried and baked at 120 °C for 30 minutes.
- f. The SiO<sub>2</sub> was etched with *Buffered-HF* solution (NH<sub>4</sub>F : HF = 7:1) for ca. 4 minutes. The etching rate of SiO<sub>2</sub> in *Buffered-HF* solution is 45 – 70 nm/minute. Finally, the resist was stripped with oxygen plasma or solvent, leaving behind an insulator image that is the same as the opaque image on the mask.
- g. The next step is patterning the source and drain electrodes. First, the wafer was cleaned in H<sub>2</sub>SO<sub>4</sub> : H<sub>2</sub>O<sub>2</sub> (3 :1) solution at 90 °C for at least 30 minutes. Subsequently the wafer was dried and treated with HMDS for 2 minutes. The AZ 1518 positive photoresist was spin-coated on the entire wafer at 4000 rpm for 40 s. The thickness of photoresist was 1.8 μm. Afterward the wafer was baked at 90 °C for 15 – 30 minutes. The wafer then was kept at room temperature for at least 20 minutes.
- h. Patterning source and drain electrodes were performed with photomask (the second photomask) by means of optical lithography with exposed time of 9 s.
- i. After that the wafer was developed in KOH 0.8 % solution for ca. 50 s. The wafer was subsequently baked at 120 °C for 30 minutes.
- j. The source and drain electrodes were fabricated by means of a lift-off process. They consisted of 10 nm titanium and 100 nm gold deposited by thermal evaporation (at a background pressure of  $2 \times 10^{-6}$  mbar). The titanium was used to improve the adhesion between gold and SiO<sub>2</sub>.
- k. Lift-off process was performed with acetone. Finally, the pre-defined substrate containing 48 independent devices is obtained as shown in Figure 4.3.



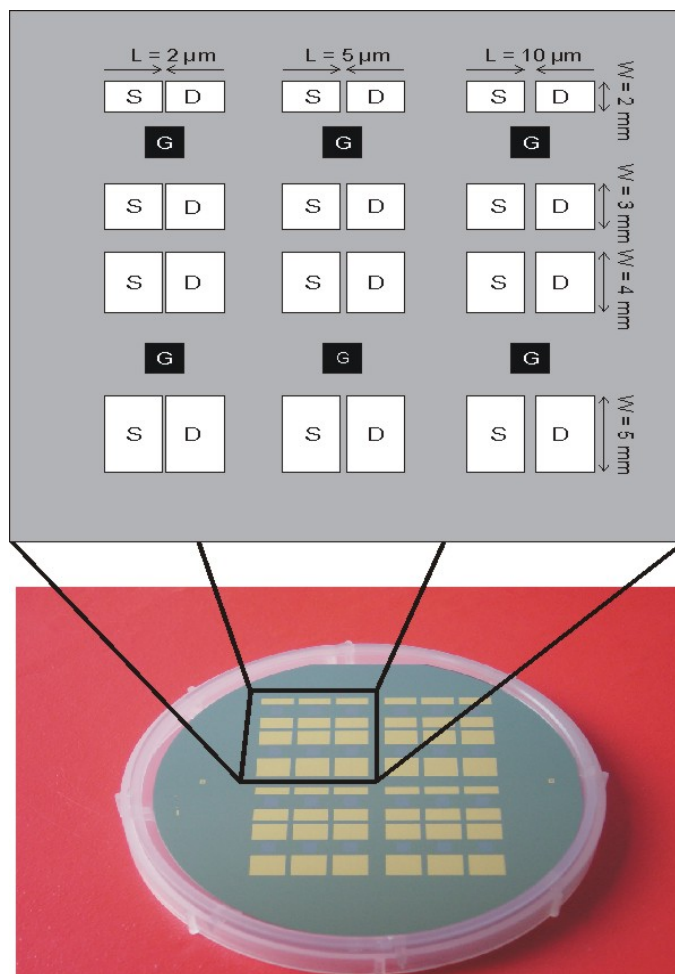


Figure 4.3. Pre-defined substrate of Organic Field-Effect Transistor (OFET). S, D, G, L, and W denote Source, Drain, Gate, Channel Length, and Channel Width.

#### 4.1.2. Thermal Evaporation

Prior to the deposition of the organic material, the pre-defined substrates were cleaned with acetone and then treated with oxygen plasma (0.7 mbar, 250 watt, for 30 minutes). This step will remove residual of photoresist from the gold contacts and the channel. To promote the structural order at the interface it has been found to be beneficial to chemically modify the hydrophilic surface of the silicon dioxide prior to the deposition of the organic materials [7, 80]. The pre-defined substrate was placed in a furnace containing HMDS for ca. 2 minutes to replace the natural hydroxyl end-group from the  $\text{SiO}_2$  substrate with an apolar methyl group. Although the atomic interface structure is not known, this is believed to attract the molecules toward the interface. Subsequently, the organic materials were deposited by means of thermal evaporation at a vacuum of  $2 \times 10^{-6}$  mbar ( $T_{\text{Substrate}} = 295$  K and a rate of 0.04 nm/s –

0.1 nm/s) with a typical thickness of 100 – 150 nm, as shown in Figure 4.2(1). The thermal evaporation system used to grow organic thin films is shown in Figure 4.4 (BESTEC GmbH, Berlin).

All spiro-linked compounds used in this study were synthesized in the group of Macromolecular Chemistry and Molecular Materials (MMCMM), The University of Kassel. TPD (Product Number: 44,326-3, 99 %) was purchased from Aldrich Co., whereas TAD (ST 16/5-04990.03), TTB (ST 16/3-03541.01), and  $\alpha$ -NPB (ST 16/7-04264.02) were purchased from Sensient Imaging Technologies GmbH (Wolfen, Germany) and their purity was specified as higher than 99 %. These materials were used without further purification.

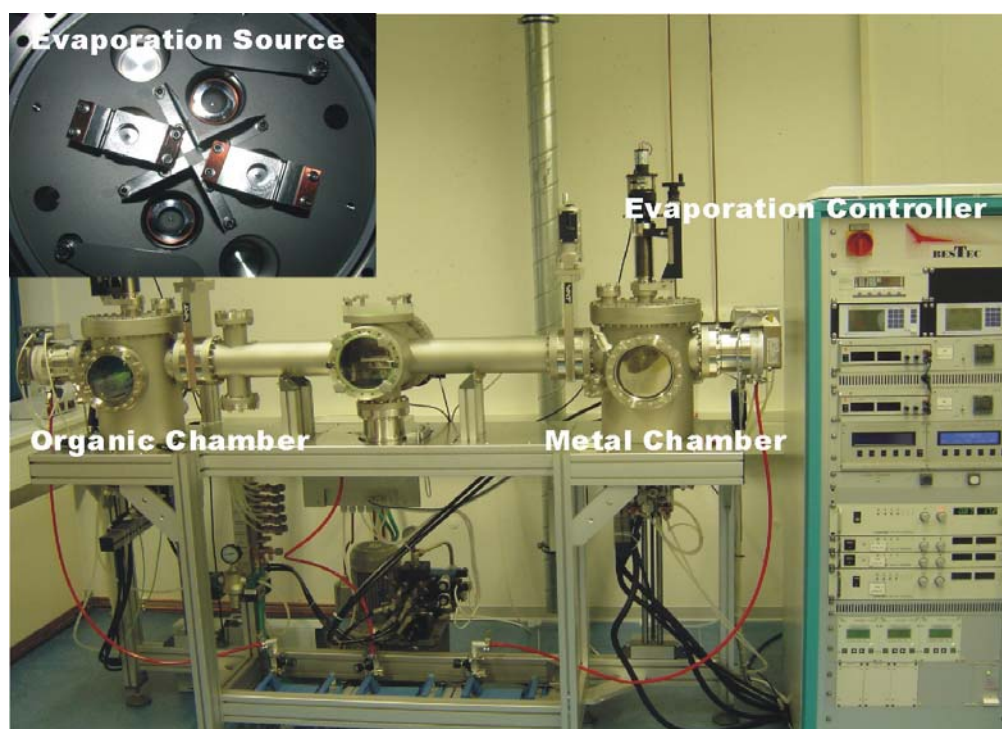


Figure 4.4. Thermal evaporation system used to grow organic thin films.

### 4.1.3. Atomic Force Microscopy and Optical Microscopy

The images of vacuum-deposited low molecular glasses thin films were performed with Digital Instruments Nanoscope Multimode III with a scan frequency of between 0.5 and 2.0 Hz. Conducting silicon cantilevers (Nanosensors GmbH and NASCATEC GmbH) with a spring constant of 41 – 46 N/m and a resonant frequency of 340 – 390 kHz were used. All

measurements were carried out under ambient atmosphere. AFM images were performed twice for each organic thin film. First, the Atomic Force Microscopy (AFM) images were obtained subsequently after the evaporation process and the second measurement was carried out after a certain time. This provides us with qualitative information about the changing of surface morphology in time. All AFM images presented in this thesis were obtained from films grown on SiO<sub>2</sub> substrates. One additional AFM image is for Spiro-TAD, which the AFM image of films grown on a mica substrate was also reported. For large area observation, an optical microscopy method is used. The observations were carried out for field-effect transistor samples and thin films on SiO<sub>2</sub>, silicon, and glass substrates.

## **4.2. Electrical Characterization of Organic Field-Effect Transistors**

### **4.2.1. Set-up of Measurement System**

The electrical characterization of the OFET-devices has been performed using a Keithley 4200-SCS Semiconductor Characterization System, supplied with a remote preamplifier for improving low current measurements (Figure 4.5). Two Keithley 4200-PA Preamplifiers have been used in our measurement. The transistor measurements were performed in air and in a vacuum utilizing a Konti-Kryostat. The Konti-Kryostat, supported by a SUSS VIT 800 Vibration Isolating Table, was also used for temperature dependent measurements. The temperature was controlled by a TIC 304-MA Temperature Control Unit in the range of 80 K to 500 K. During the temperature dependent measurements the sample was kept under a vacuum ( $\sim 2 \times 10^{-3}$  mbar). The Konti-Kryostat and the SMU-4200 SCS unit were connected with a triax cable. The triax cables were used in order to optimize both low current and high impedance measurement. This cable may be used down to femtoampere (fA) levels when properly equipped with a guarded probe. This guard voltage tracks the force voltage exactly, so that no voltage drop can exist between guard and force. This eliminates the capacitive loading that would otherwise limit low current measurements. Finally, each electrode was connected with a SUSS PH100 Probe Station (Figure 4.6) provided with a 0.020" Tungsten Probe (American Probe and Technologies, Model # 72T-J3/200, and a radius of 20  $\mu\text{m}$ ).

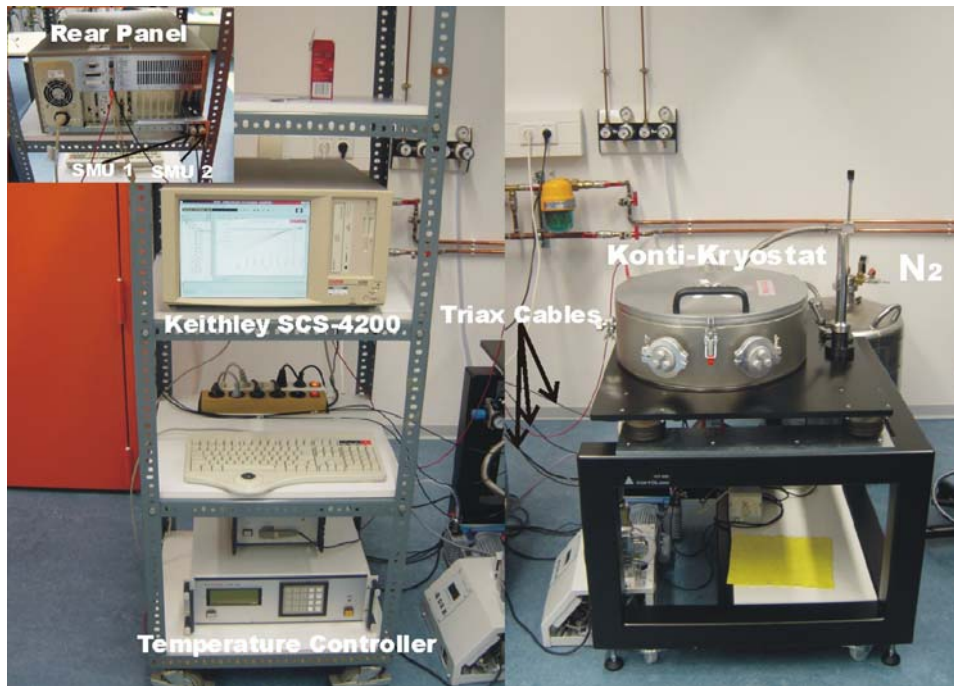


Figure 4.5. Set-up of measurement system utilizing a Keithley SCS-4200 Semiconductor Characterization System.

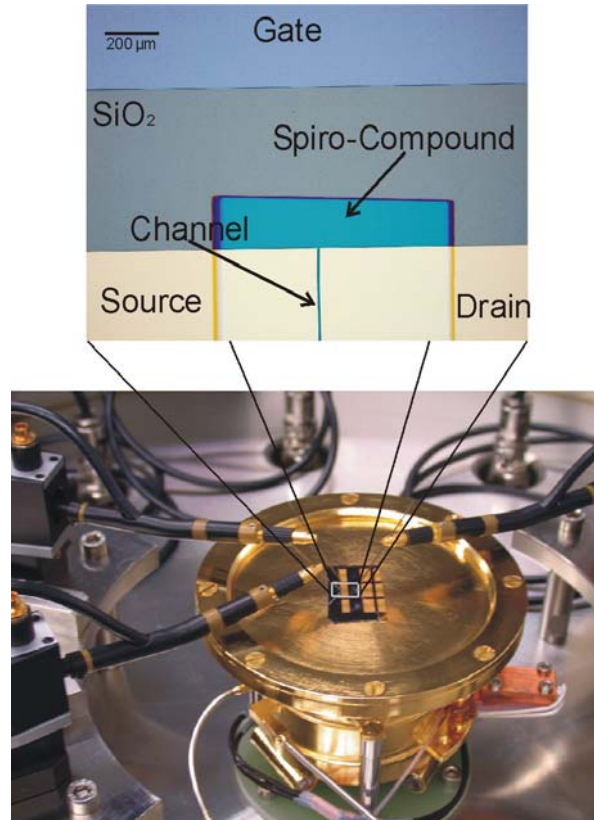


Figure 4.6. Top-view of the sample holder bearing an Organic Field-Effect Transistor based on Spiro-Compound.

### 4.2.2. Measurement Parameter and Condition

Prior to the measurements the Keithley 4200-SCS Semiconductor characterization System should be allowed to warm up for at least 30 minutes to achieve rated measurement accuracy. Re-calibration (auto calibration mode) for Keithley SCS-4200 is required according to the instrument manufacturer's recommendations or when the instrument is moved or when the testing conditions change significantly (*e.g.*, temperature change greater than 10 °C, relative humidity change greater than 30%, etc.) [81]. Characterization of the organic transistors requires four primary sets of measurements:

1. The transfer characteristics ( $V_{GS}$  vs.  $I_{DS}$ ) measurements are necessary for the characterization of field-effect mobility  $\mu$ , *fitted* threshold voltage,  $V_T$  and *ON/OFF* ratios. These data are typically necessary for characterization of the semiconductor transport properties. Transconductance is also derived from this measurement.
2. Output characteristics ( $V_{DS}$  vs.  $I_{DS}$ ) measurements provide the most data on device performance from a single measurement. While not generally of direct use for characterization of the semiconductor transport properties, it is necessary for the development of device models for circuit simulation and design. Circuit models also generally require at least one transfer curve in addition to the output curve.
3. Gate leakage ( $V_{GS}$  vs.  $I_{GS}$ ) measurements are strongly recommended due to the electrical isolation required between the gate electrode and semiconductor channel. Those results represent the gate dielectric quality and quantify the leakage current from the gate to the channel that might interfere with transistor performance. This measurement requires that both the drain and source electrodes are grounded ( $V_{DS} = 0$  V).  $V_{GS}$  is then swept from +10 V to -60 V (for *p*-channel devices), while  $I_{GS}$  is measured. On the other hand, the gate bias is swept from -10 to +60 V for *n*-channel devices. Ideally, zero current flow should be measured from the gate to the channel, but in practical devices,  $I_{GS}$  should be sufficiently lower than  $I_{DS}$  while the device is in operation, *i.e.*,  $I_{GS} < 0.001 I_{DS}$ .
4. Due to stray capacitance effects, potential bias stress phenomena, mobile ionic impurities, and other mechanism, the direction of voltage bias stepping (*i.e.*, towards more positive values versus more negative values) have been shown to give slightly different electrical data. This effect typically manifests in a shift of the data (*e.g.*, differing threshold voltages). However, such effects should not

affect determination of field effect mobility or *ON/OFF* ratios. In order to determine the severity of hysteresis resulting from the above effects, it is recommended to:

- a. Perform each measurement twice, first from *OFF state* (the voltage range at the device is most likely off) to *ON state*. A second measurement is performed from the *ON state* to the *OFF state*. This measurement was performed for transfer characteristic.
- b. Devices are to sit idle, unbiased for a minimum of 10 minutes before any measurement. This is to minimize both long-lifetime electro-optical effects when the device is inserted into the measurement system, and stray capacitance-charging effects from previous measurements.

Several sets of measurements with different conditions for each set were performed in order to compare their physical characteristics. Four primary sets of measurements were:

1. *Ambient air* (25 °C, 1013 mbar, 24 % Relative Humidity, in the dark).
2. *Vacuum* (25 °C,  $2 \times 10^{-3}$  mbar, in the dark).
3. *Temperature Dependence* ( $2 \times 10^{-3}$  mbar, in the dark, measured with a resolution of 0.1 K). The measurement was carried out at a rate of 1 K/minute.
4. *Time dependence measurement*. Every device was characterized twice. First, it was characterized shortly after the preparation of organic thin films and the second measurement was performed after the sample was left in ambient atmosphere for a certain time. The sample was left in the dark. The effect of moisture on the transistor characteristics of Spiro-TPD was characterized.

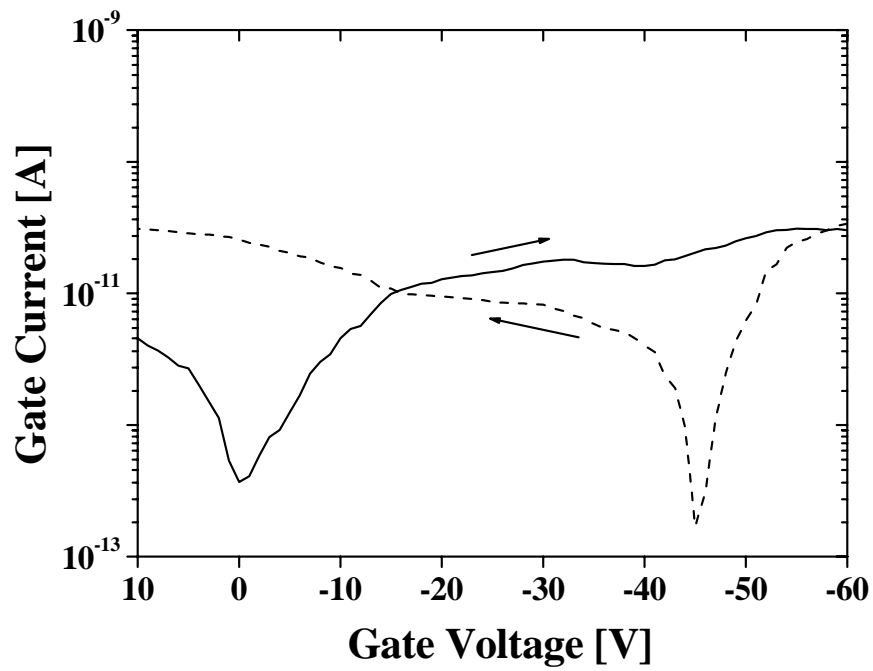


Figure 4.7. Gate leakage currents at  $V_D = 0$  V. The arrows show the direction of the gate bias being swept.

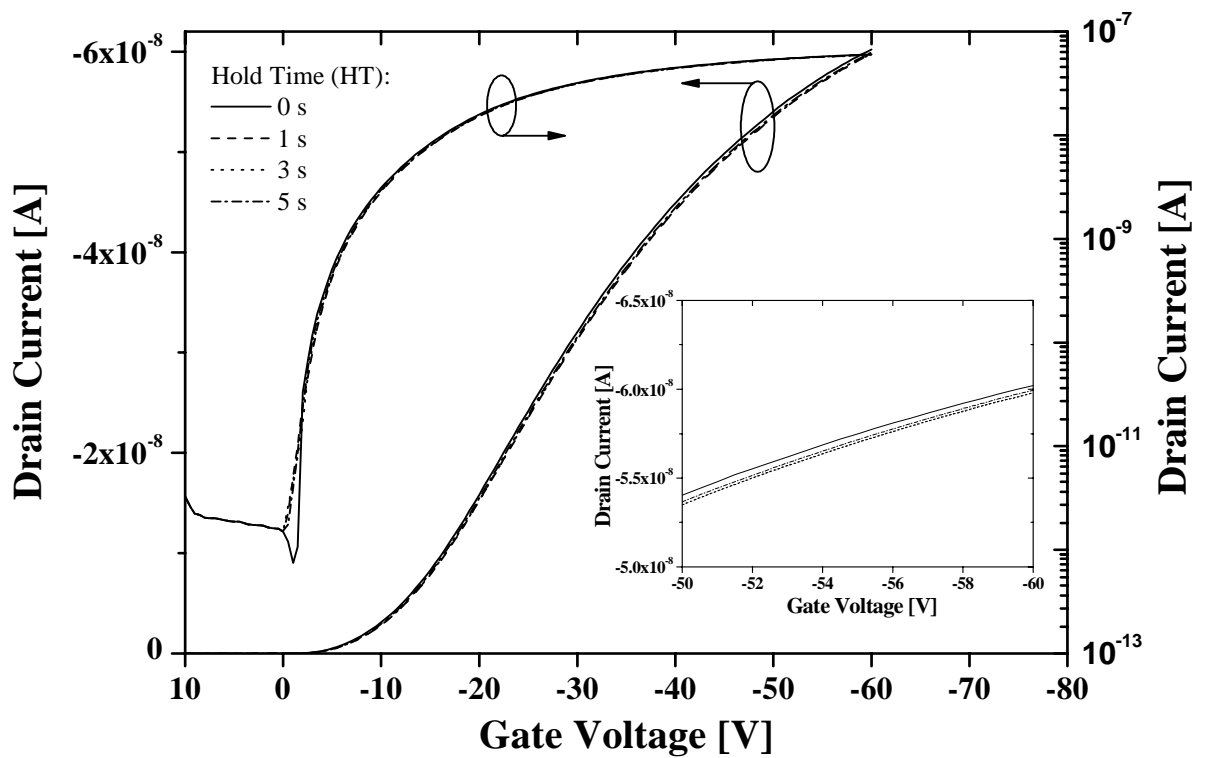


Figure 4.8. Transfer characteristics performed in air at  $V_D = -20$  V for different values of the hold time (HT).

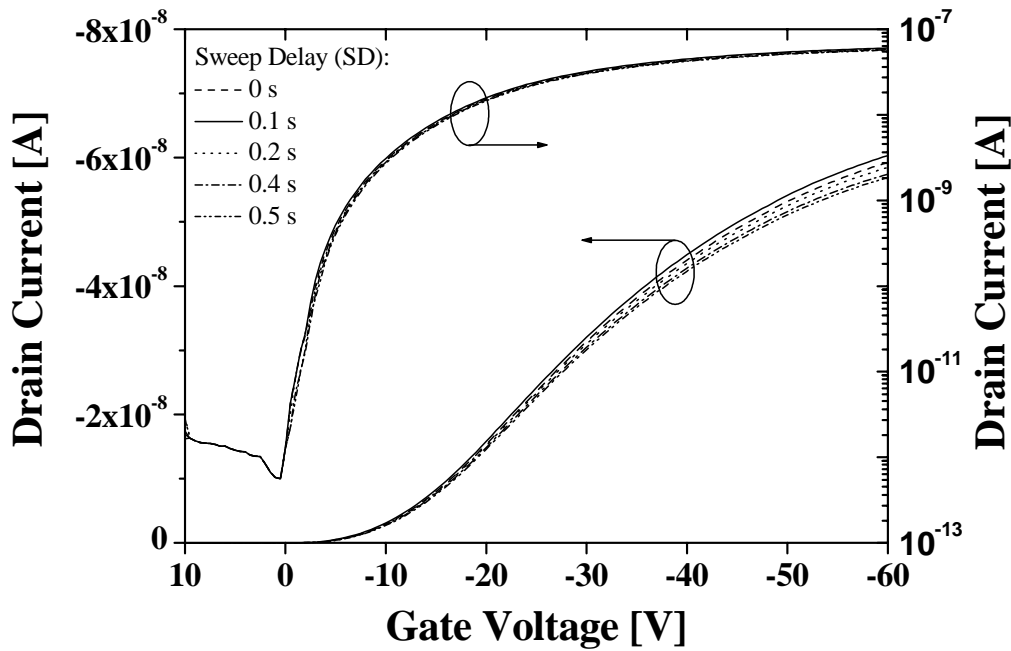


Figure 4.9. Transfer characteristics performed in air at  $V_D = -20$  V for different values of the sweep delay (SD).

Figure 4.7 shows a plot of gate leakage current against gate bias at zero drain bias. The gate current behavior depends on the direction in which the gate bias is being swept. However, the gate leakage can be neglected with respect to drain current ( $I_{GS} \ll 0.001 I_{DS}$ ). Transfer characteristic measurements were also performed at a different value of hold time (HT) and sweep delay (SD). Basically, the gate bias is set to its initial value and after waiting for a certain time (hold time, HT), the gate bias sweep begins. Each gate bias step (in this case 0.5 V) is followed by a sweep delay (SD) before the drain current is measured. The time needed for drain current measurement is therefore affected by the hold time and sweep delay. Both parameters affected the establishment of the steady-state regime and device aging. The last effect should be minimized. Since the hold time affects just before the measurement, this parameter should be kept to a minimum. Figure 4.8 shows that the drain current has an optimum value at a hold time of 0 s. On the other hand, the optimum value for sweep delay is 100 ms (Figure 4.9). The sweep delay affects the drain current in the entire transfer characteristics. When the transistor is no longer in the strong accumulation regime, the sweep delay is the time needed to reach the equilibrium regime. If the sweep delay is 0 s, the drain current is not at optimum value as shown in Figure 4.9, since between two adjacent gate bias measurements there is not enough time to reach its permanent regime. However, very long sweep delay lengthens the measurement duration and can affect the device aging. As a result, measurement system was set-up with a hold time of 0 s and sweep delay of 100 ms. These



---

results match very well with results obtained using other equipment, namely the HP 4156A Semiconductor Parameter Analyzer [82].



## Chapter 5

# Surface Morphology of Low Molecular Glasses

In this chapter, a systematic study of the surface morphology of vacuum-deposited low-molecular glasses thin film grown on SiO<sub>2</sub>/p-Si substrates is presented by means of tapping-mode atomic force microscopy (TM-AFM) and optical microscopy. In principle, the AFM technique measures the physical properties, namely the interaction forces between a sharp conical tip and the sample surface. Moreover, it allows investigations to be performed on conductors as well as on semiconductor and organic materials. TM-AFM operates as following: the cantilever-tip is vibrated close to its resonance frequency by a piezo element [83]. Then, the signal obtained by the deflection sensor is analyzed by the lock-in techniques. A subsequent feedback circuit regulates on a constant phase shift between signal of the deflection sensor and the original driving signal or on constant amplitude of the modulated deflection sensor signal. Both methods keep the resonance frequency constant. Tapping-mode has several characteristics. First, lines of constant force gradient are recorded since the resonance frequency, not the deflection of the cantilever, is kept constant. Second, the cantilever tip does not touch the sample during measurement. Therefore, surface deformations and lateral forces are minimized. Third, since a surface can be traced not only for a distance of a few nanometers, but also for more than ten nanometers, long range forces such as electrostatic, or magnetic forces can be imaged separately from the surface topography.

AFM method is utilized for a quantitative investigation of the surface morphology of thin films since the morphological features together with the roughness can be acquired simultaneously on a wide range of scale lengths. The surface roughness  $R_a$  is defined as the standard deviation of the topographical height:

$$R_a = \frac{1}{N} \sum_{j=1}^N |Z_j| \quad (5.1)$$

where  $N$  is the number of points within the book cursor, and  $Z_j$  is the height of  $j$ th pixel. Another parameter is the root-mean-square roughness  $R_q$  which is defined as:

$$R_q = \sqrt{\frac{\sum (z_j - \langle z \rangle)^2}{N}} \quad (5.2)$$

where  $\langle z \rangle$  is the mean height. The roughness is a function of the image size due to the anisotropic growth of organic thin films. Another analysis performed in the experiment is a cross-section analysis of an AFM image. The cross-section analysis describes the peak-to-valley height of a selected line of an AFM image. The selected line of the corresponding AFM image denotes by dotted lines across the image.

### 5.1. *N,N,N',N'*-Tetraphenylbenzidine (TAD)

Figure 5.1, 5.2, and 5.3 show the morphological change of TAD thin films. TAD thin films were grown on different substrates with the following deposition parameters: vacuum of  $2 \times 10^{-6}$  mbar, deposition rate of  $1.7 \text{ \AA/s}$ , and a final thickness of 160 nm. Figure 5.1 shows typical  $4 \mu\text{m} \times 4 \mu\text{m}$  images of as-deposited TAD thin films grown on a  $\text{SiO}_2/p\text{-Si}$  substrate, which exhibited an entirely amorphous and relatively flat surface with a mean roughness of 1.06 nm.

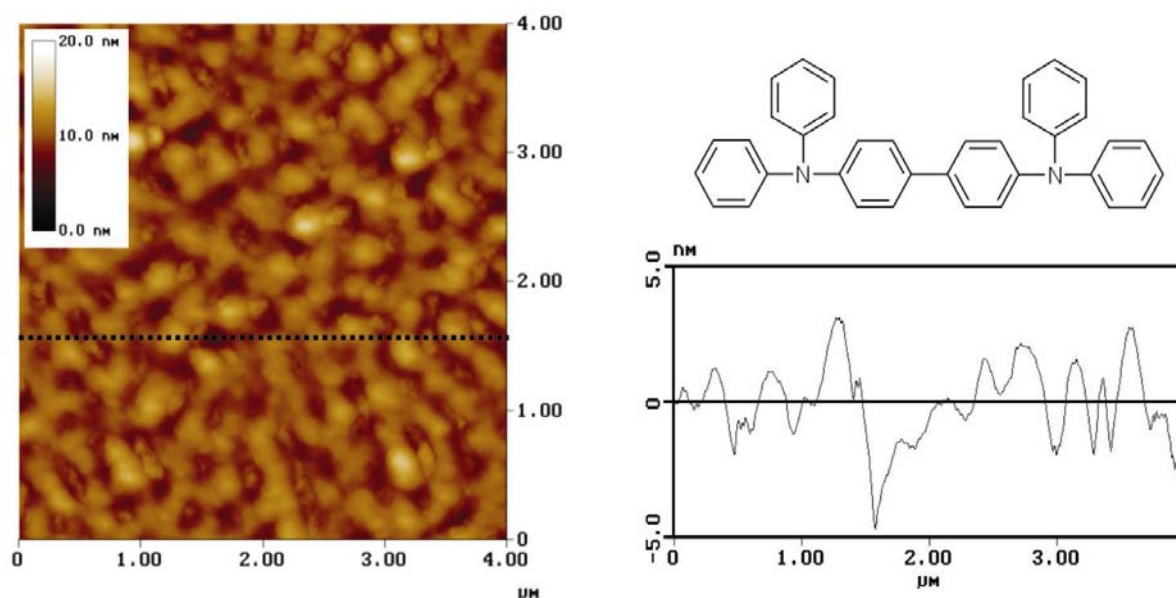


Figure 5.1. AFM topographical image of a TAD thin film as deposited on a  $\text{SiO}_2/p\text{-Si}$  substrate. Left side:  $4 \times 4 \mu\text{m}^2$  AFM images, and Right side: Surface height of AFM images and the chemical structure of TAD. The mean roughness  $R_a$  was 1.06 nm and the root-mean square roughness  $R_q$  was 1.35 nm.

After the sample was stored under an ambient atmosphere and at room temperature (RT) for 3 days, the surface profile of TAD thin films was measured again by means of AFM and optical microscopy. The films of TAD underwent a distinctive change in morphology with the surface roughness greatly increased, as shown in Figure 5.2. The cross-section analysis of the corresponding AFM images showed that the surface of TAD thin films was crystallized after the sample has been stored in ambient atmosphere and at RT for 3 days. Moreover, the mean roughness value was increased by a factor of 36 and the peak-to-valley height was increased by a factor of 33, as shown in the cross-section analysis of Figure 5.2. Peak-to-valley heights of 7 nm and 233 nm were obtained for a fresh sample and after the sample was stored in ambient atmosphere and at RT for 3 days, respectively. Along with the crystallization of TAD films, it has been shown in the cross-section analysis (in Figure 5.2) that the peak-to-valley formations were also created between crystals. The valley formation was necessary, because the heights of the resulting crystals were much higher than the peak-to-valley heights of as-deposited films themselves. Hence, the depth of the lowest valleys from the highest peaks is much higher than the thickness of the as-deposited TAD films itself. It implies that the substrate surface was revealed by the crystallization.

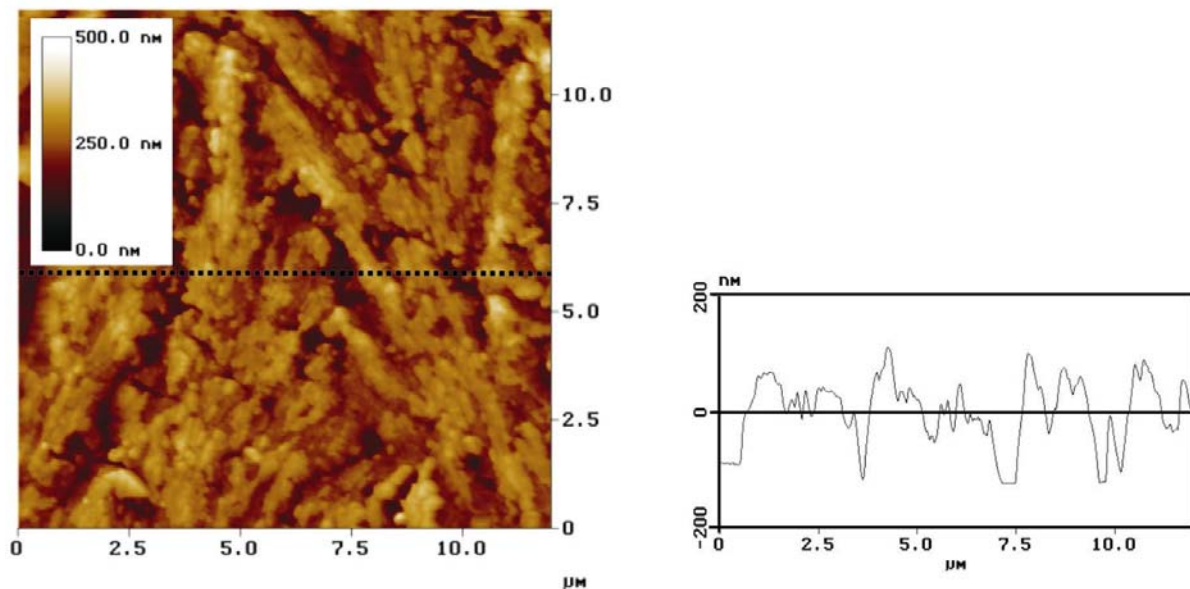


Figure 5.2. AFM topographical image of a TAD thin film after the sample was stored in ambient atmosphere and at RT for 3 days. Left side:  $12 \times 12 \mu\text{m}^2$  AFM images, and Right side: Surface height of AFM images. The mean roughness  $R_a$  was 38.6 nm and the root-mean square roughness  $R_q$  was 48.6 nm.

Figure 5.3 shows the optical micrographs of TAD thin films grown on *p*-Si substrate,  $\text{SiO}_2$  substrate, glass substrate and field-effect transistor. The images were obtained after the

samples were left in an ambient atmosphere and at RT for 3 days. The films grown on *p*-Si substrate, SiO<sub>2</sub> substrate and glass substrate showed a rounded shape of crystal and large voids. This indicates that the substrates were revealed by crystallization as observed previously in the corresponding AFM images. The crystals with a radius of varying between 500 μm and 900 μm were observed. Figure 5.3(d) show a field-effect transistor with TAD as active materials. The films of TAD crystallized in entire substrates, on the gold electrodes and in the active channel. The resulting crystals of TAD films indicate that the films are not morphologically stable in ambient atmosphere and at RT. This is the main cause why the field-effect characteristic with TAD as active materials vanished even if the sample was stored for more than 150 hours in a dynamic continuously evacuated chamber. To the best of my knowledge, there is no publication yet, having reported on the surface morphology of TAD thin films.

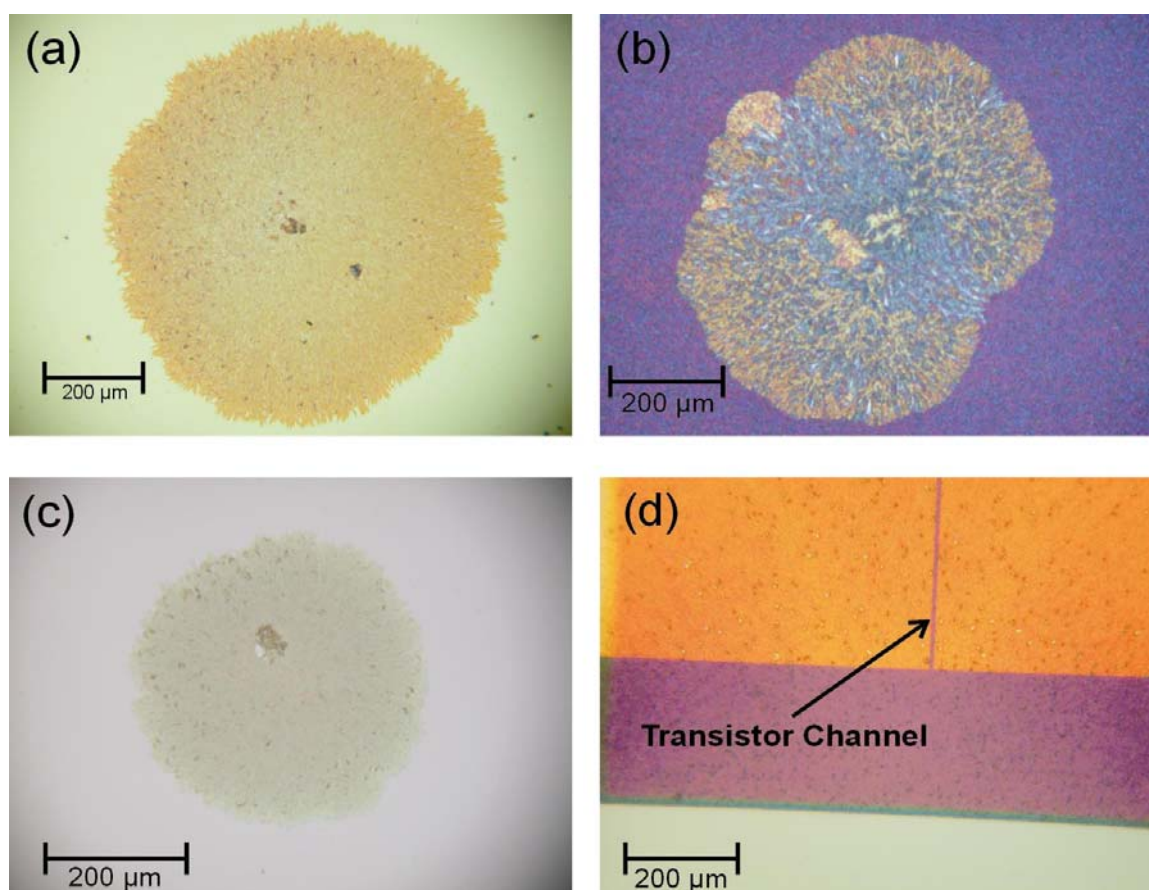


Figure 5.3. The optical microscopy images of TAD thin films after the samples were stored in ambient atmosphere and at RT for 3 days. TAD thin films were grown on (a) *p*-Si substrate, (b) SiO<sub>2</sub> substrate, (c) Glass substrate, and (d) Field-effect transistor.

## 5.2. 2,2',7,7'-Tetrakis-(diphenylamino)-9,9'-spirobifluorene (Spiro-TAD)

Figure 5.4, 5.5, and 5.6 show the surface morphology change of Spiro-TAD thin films, the corresponding parent compound of TAD, grown on SiO<sub>2</sub> substrate, *p*-Si substrate, field-effect transistor and mica substrates. Spiro-TAD was thermally evaporated with deposition parameters: background pressure of  $2 \times 10^{-6}$  mbar, deposition rate of 4.5 Å/s and a final thickness of 90 nm. Figure 5.4(a) and Figure 5.5(a) show the surface morphology of Spiro-TAD thin films grown on a SiO<sub>2</sub> substrate and a mica substrate directly after deposition. The AFM images of both films showed very flat surfaces having a mean roughness of 1.56 nm for films grown on a SiO<sub>2</sub> substrate and 0.21 nm for films grown on a mica substrate. However, the surface of Spiro-TAD thin films grown on mica substrate was smoother than that grown on SiO<sub>2</sub> substrate. Furthermore, the peak-to-valley height of Spiro-TAD thin films grown on SiO<sub>2</sub> substrate (peak-to-valley height  $\sim 9.8$  nm) was higher than that grown on mica substrate (peak-to-valley height  $\sim 1.4$  nm). This is the case, because the thermally oxidized SiO<sub>2</sub> substrates have larger roughness ( $R_a \sim 1$  nm) than the mica substrates ( $R_a \sim 0.2$  nm) [84,85].

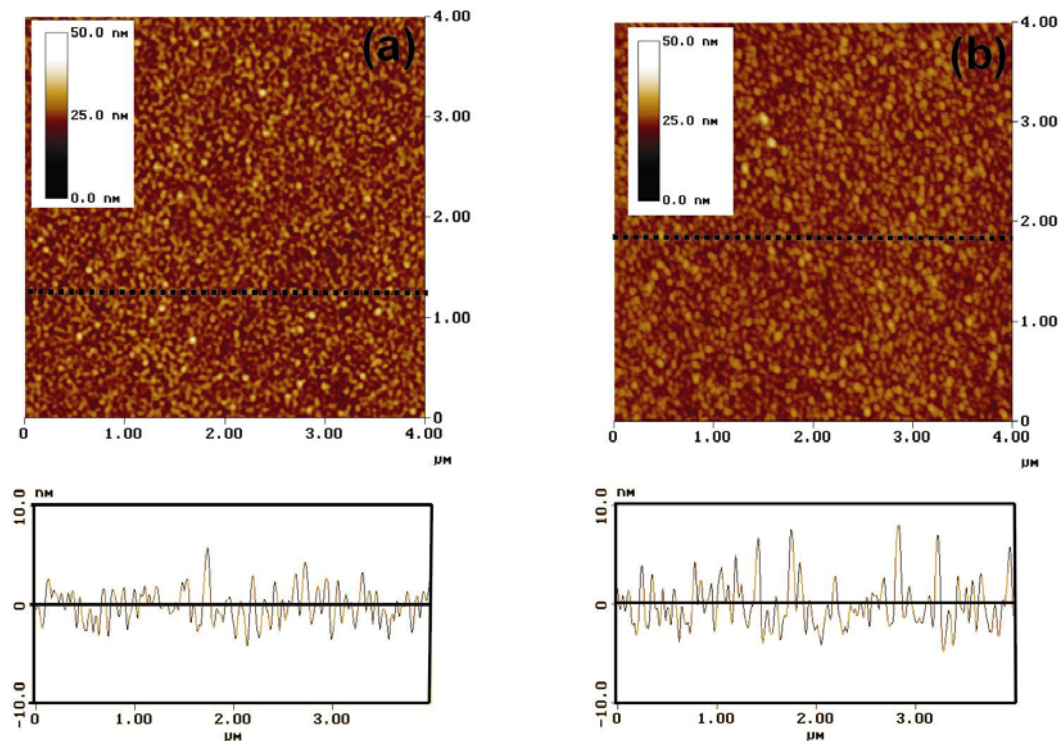


Figure 5.4. AFM topographical images of a Spiro-TAD thin film on a SiO<sub>2</sub>/*p*-Si substrate ( $4 \times 4 \mu\text{m}^2$ ). (a) As deposited; the mean roughness  $R_a$  was 1.56 nm and the root-mean square roughness  $R_q$  was 1.96 nm and (b) After the sample was stored in ambient atmosphere and at RT for 5 weeks; the mean roughness  $R_a$  was 1.89 nm and the root-mean square roughness  $R_q$  was 2.41 nm.

As described previously in sub-chapter 5.1, the mean roughness of as-deposited TAD thin films, the parent compound of Spiro-TAD, grown on a  $\text{SiO}_2$  substrate was 1.06 nm. This value is smaller than that of Spiro-TAD films. However, a similar value of peak-to-valley height for both films was obtained. Peak-to-valley heights of 7 nm and 9.8 nm were obtained for as-deposited TAD and as-deposited Spiro-TAD thin films, respectively. The surface morphology of as-deposited TAD and as-deposited Spiro-TAD thin films grown on  $\text{SiO}_2$  substrate is similar in terms of the peak-to-valley height. Furthermore, it is clear that the as-deposited TAD films exhibited larger grains-like and voids with respect to as-deposited Spiro-TAD films. Moreover, the distance between adjacent grains-like in as-deposited TAD films is longer than that in thin films of as-deposited Spiro-TAD. Therefore, the as-deposited Spiro-TAD films are better than the as-deposited TAD films in terms of the grains-like and void sizes.

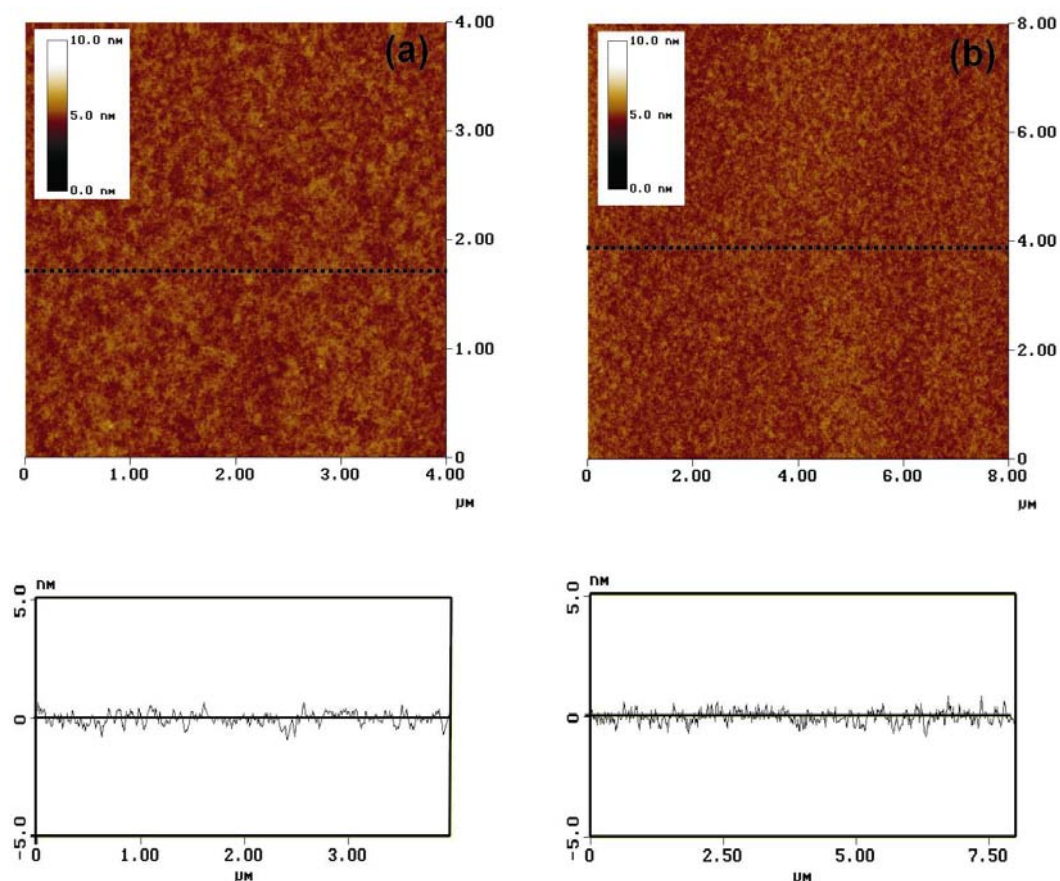


Figure 5.5. AFM topographical images of a Spiro-TAD thin film on a mica substrate ( $4 \times 4 \mu\text{m}^2$  and  $8 \times 8 \mu\text{m}^2$ ). (a) As deposited; the mean roughness  $R_a$  was 0.21 nm and the root-mean square roughness  $R_q$  was 0.27 nm and (b) After the sample was stored in ambient atmosphere and at RT for 5 weeks; the mean roughness  $R_a$  was 0.23 nm and the root-mean square roughness  $R_q$  was 0.29 nm.



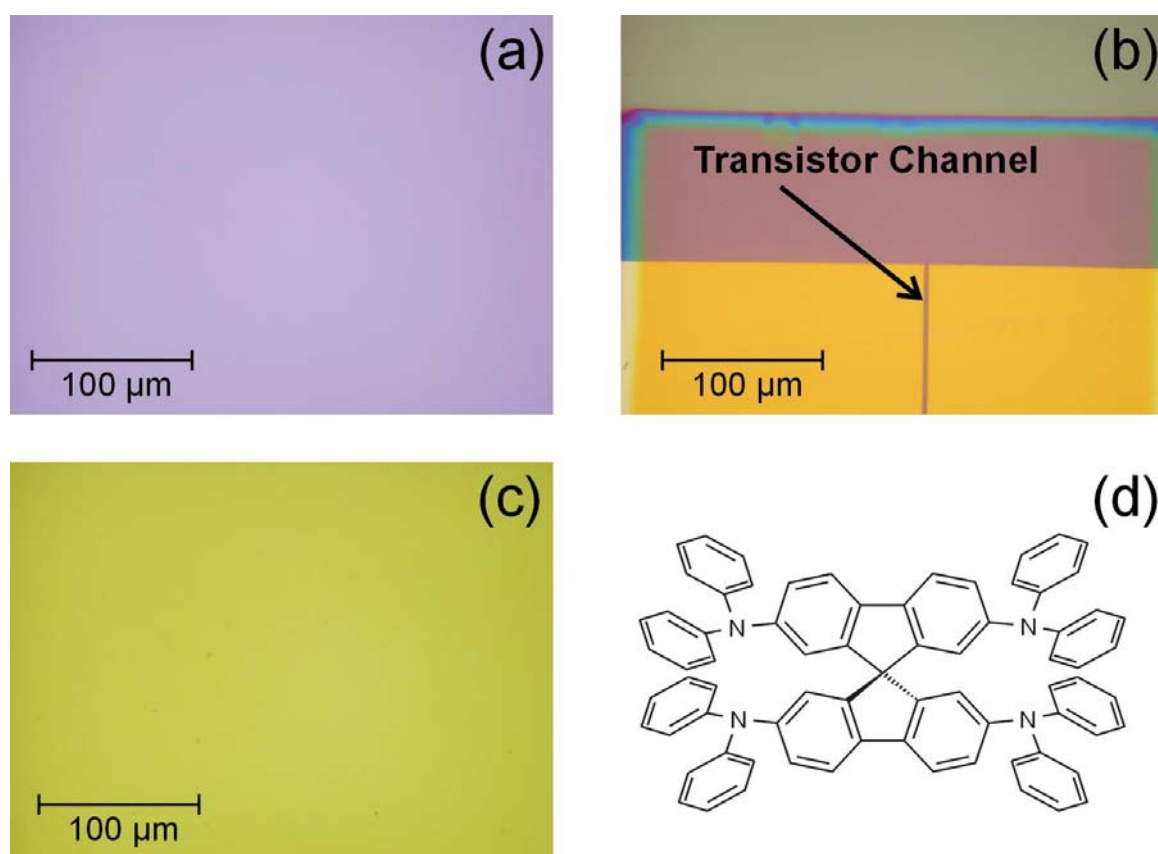


Figure 5.6. The optical microscopy images of Spiro-TAD thin films after the samples were stored in ambient atmosphere and at RT for 9 months. Spiro-TAD thin films were grown on (a) SiO<sub>2</sub> substrate, (b) Field-effect transistor, and (c) *p*-Si substrate. (d) The chemical structure of Spiro-TAD.

After Spiro-TAD thin films were stored for 5 weeks in an ambient atmosphere and at RT, the surface images of thin films were measured again. The as-deposited film underwent a negligible change, the mean roughness level slightly changed from 1.56 nm to 1.89 nm for films grown on SiO<sub>2</sub> substrates and from 0.21 nm to 0.23 nm for films grown on mica substrates. The peak-to-valley heights of films after the samples have been stored for 5 weeks were 12.1 nm for films grown on SiO<sub>2</sub> substrates and 1.7 nm for films grown on mica substrates. Time dependent measurements of the surface morphology also showed that the films of Spiro-TAD did not change significantly after the samples were exposed to ambient atmosphere and at RT for 5 weeks. The roughness values and peak-to-valley heights on average did not significantly change as well. In contrast, the roughness and peak-to-valley height of TAD thin films after the sample has been stored for 3 days in ambient atmosphere and at RT were increased by a factor of 36 and 33, respectively. Therefore, the films of Spiro-TAD are more morphologically stable at RT and in ambient atmosphere than that of TAD.

Figure 5.6 provides the large area scale of Spiro-TAD thin films, after the samples have been stored for 9 months at RT and in ambient atmosphere. The surfaces of Spiro-TAD thin films grown on SiO<sub>2</sub> substrate, *p*-Si substrate, and field-effect transistor have remained flat and smooth. Moreover, Figure 5.6(b) also shows that Spiro-TAD thin films do not crystallize and the active channel of field-effect transistor is still clean and smooth. Exposure the field-effect transistor to ambient atmosphere also does not significantly influence the transistor characteristics of Spiro-TAD, which will be described in chapter 6.

### 5.3. *N,N'*-Bis(3-methylphenyl)-(1,1'-biphenyl)-4,4'-diamine (TPD)

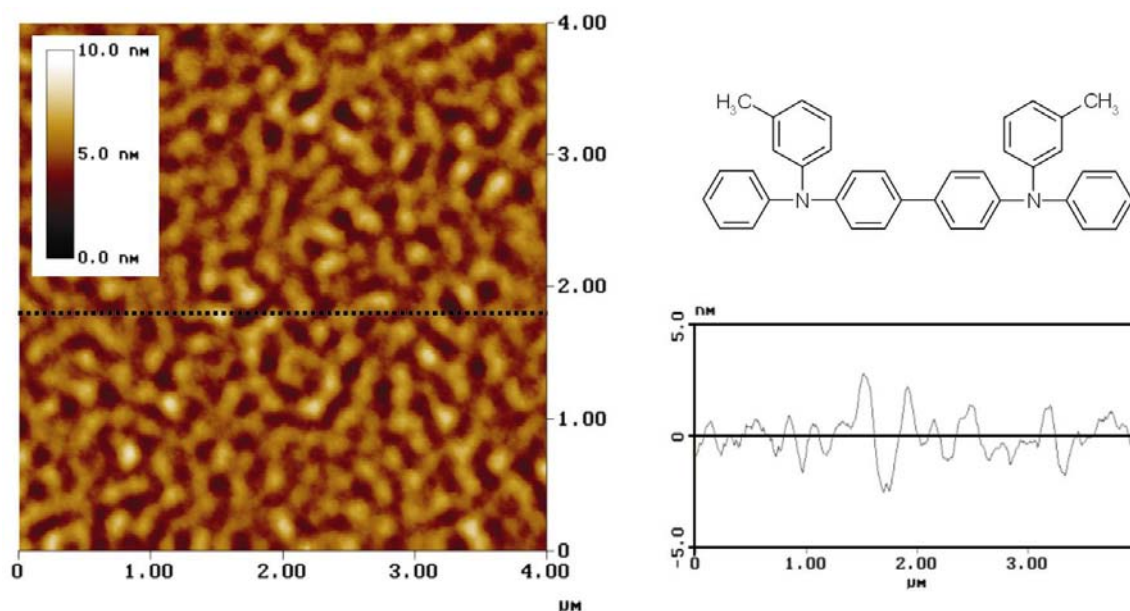


Figure 5.7. AFM topographical image of a TPD thin film as deposited on a SiO<sub>2</sub>/*p*-Si substrate. Left side:  $4 \times 4 \mu\text{m}^2$  AFM images, and Right side: Surface height of AFM images and the chemical structure of TPD. The mean roughness  $R_a$  was 0.7 nm and the root-mean square roughness  $R_q$  was 0.87 nm.

TPD has been widely used as hole transport materials in many studies. In this experiment, TPD thin films were grown on silicon, silicon dioxide, and glass substrate. Deposition parameters of TPD thin films were: vacuum of  $2 \times 10^{-6}$  mbar, deposition rate of 0.8 Å/s, and a final thickness of 130 nm. Figure 5.7 shows an AFM image and a cross-section analysis of an as-deposited TPD film. The scan range is  $4 \times 4 \mu\text{m}^2$ . The surfaces of as-deposited TPD film were flat with a mean roughness of 0.7 nm and a peak-to-valley of 5.4 nm. The surface of as-deposited TPD films was smoother than those of as-deposited thin

films of TAD and Spiro-TAD. The peak-to-valley height of as-deposited TPD films was also lower than those of as-deposited thin films of TAD and Spiro-TAD. However, the as-deposited TPD films exhibited lamellae-like structures with sharp edges separated by large voids, which was also observed on as-deposited TAD films. This is in contrast with the as-deposited Spiro-TAD films, as described previously in sub-chapter 5.2.

The surface of TPD films was measured again after the sample was stored in ambient atmosphere and at RT for 12 days. The corresponding AFM image is shown in Figure 5.8. The surface of TPD films underwent a morphological change from relatively flat surface to lamellae-like structure separated by large voids. After 12 days, the mean roughness of TPD thin films increased from 0.7 nm for as-deposited films to 27.9 nm and the peak-to-valley also increased from 5.4 nm for as-deposited films to 175 nm. The heights of the resulting crystals were much higher than the film thicknesses themselves. However, the height of the resulting crystals of TPD films was lower than that of TAD films even though the height of the resulting crystals of TPD film was measured after the sample has been left in ambient atmosphere and at RT for 12 days. It implies that the film of TPD is more stable in ambient atmosphere and at RT than that of TAD. However, TPD films are easier to crystallize with respect to Spiro-TAD films.

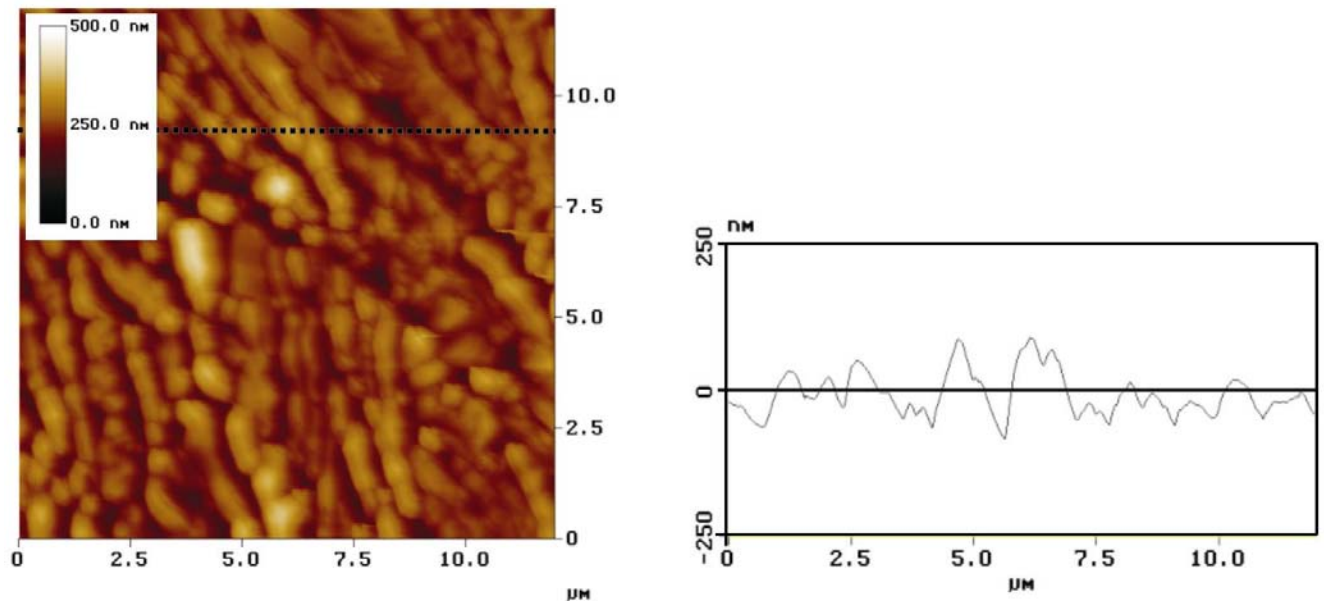


Figure 5.8. AFM topographical image of a TPD thin film after the sample was stored in ambient atmosphere and at RT for 12 days. Left side:  $12 \times 12 \mu\text{m}^2$  AFM images, and Right side: Surface height of AFM images. The mean roughness  $R_a$  was 27.9 nm and the root-mean square roughness  $R_q$  was 36.4 nm.

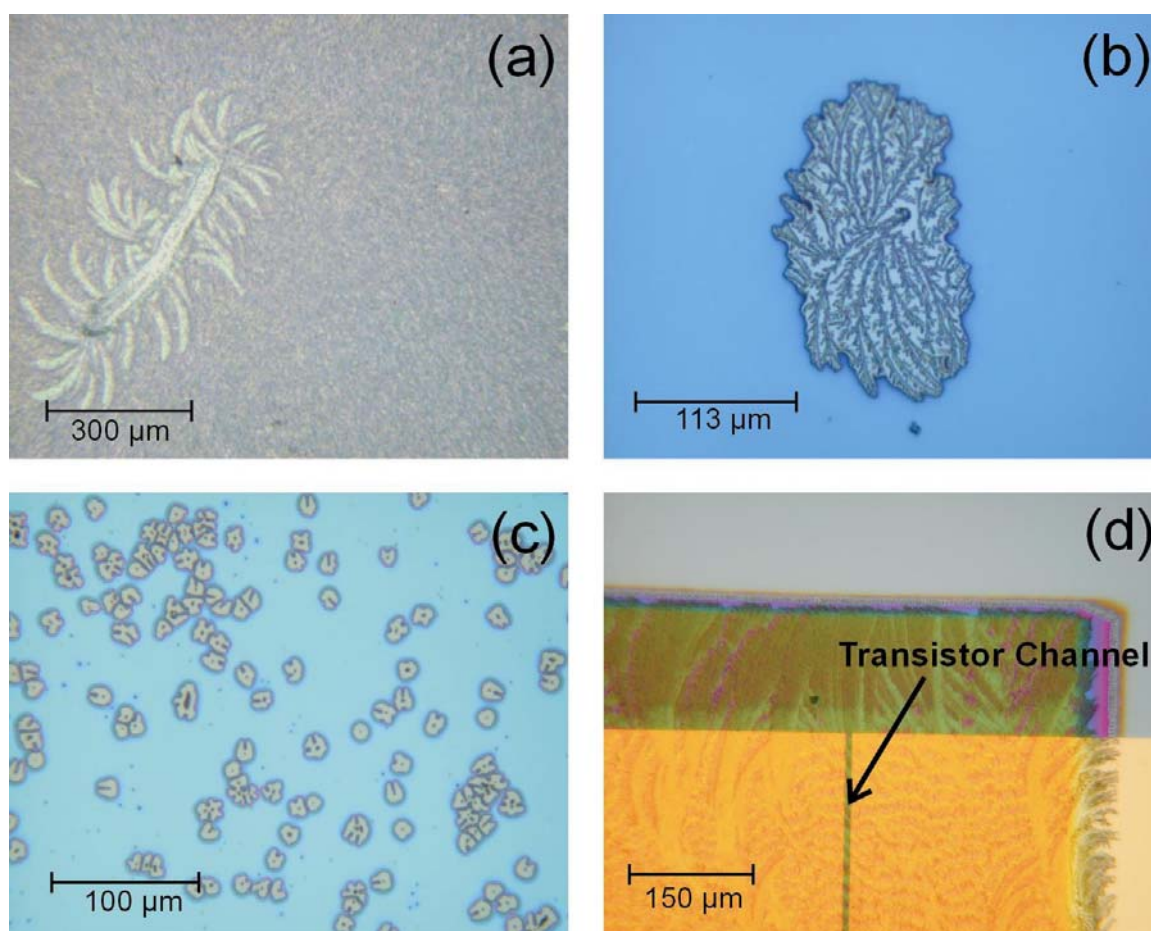


Figure 5.9. The optical microscopy images of TPD thin films after the samples were stored in ambient atmosphere and at RT for 12 days. TPD thin films were grown on (a) *p*-Si substrate, (b) SiO<sub>2</sub> substrate, (c) Glass substrate, and (d) Field-effect transistor.

Qiu and Qiao reported that the roughness of a TPD thin film was 2.85 nm directly after deposition and increased to 15.25 nm after the sample was left in air for 15 days [6]. In contrast, Han *et al.* reported that the roughness of TPD thin films as deposited was 0.3 nm [5]. The films of TPD were grown at a background pressure of  $10^{-6}$  Torr, a deposition rate of 2 – 3 Å/s and a final thickness of 50 nm. However, the films were partially crystallized after one week and completely crystallized after 3 months [65]. They also reported that the peak-to-valley height was less than 10 nm for samples after deposition and was ca.250 nm after the same sample was stored in ambient atmosphere for 3 months. These results agree very well with the data showed in Figure 5.7 and 5.8. On the other hand, Mori *et al.* reported that the crystallization of TPD could be successfully suppressed by plasma modification at least for 30 days, but the operating lifetime of OLED could not be improved [86]. Another evidence of the drawbacks of TPD thin films was provided by Smith *et al.* [66]. They observed that the degradation of an electroluminescent device can be attributed in part to the crystallization of

the hole transport layer, in this case TPD thin films. The crystallization appears to be nucleated from a defect present in the anode, which is indicated by the radial growth of dendritic structure from a  $\mu\text{m}$  defect.

Figure 5.9 shows the optical micrographs of TPD films after the samples were left in ambient atmosphere and at RT for 12 days. The size of crystals of TPD films grown on a *p*-Si substrate was larger than those grown on  $\text{SiO}_2$  substrate and glass substrate. For example, the crystal sizes of  $330 \times 500 \mu\text{m}^2$  and  $125 \times 225 \mu\text{m}^2$  were obtained for films grown on *p*-Si substrates and  $\text{SiO}_2$  substrates, respectively. On the other hand, the size of crystal of  $20 \times 25 \mu\text{m}^2$  was obtained for film grown on glass substrates. However, the size of the resulting crystals of TPD films was smaller than that of TAD films, as shown in Figure 5.3. Finally, Figure 5.9(d) shows an organic field-effect transistor with TPD as active materials. The TPD films easily crystallized, as shown by crystal-like structure in entire areas of the device. Such crystal-like structure was also observed in organic field-effect transistor with TAD as active materials, as showed previously in Figure 5.3(d). The crystallization of TAD and TPD films was mainly caused by lack of morphological stability. The glass transition temperature ( $T_g$ ) is regarded as a mainly factor that influences the organic film stability. The  $T_g$  of TAD and TPD are  $70^\circ\text{C}$  and  $62^\circ\text{C}$ , respectively.

#### 5.4. 2,2',7,7'-Tetra-(*m*-tolyl-phenylamino)-9,9'-spirobifluorene (Spiro-TPD)

Figure 5.10 and 5.11 show the surface morphology change of Spiro-TPD thin films. The thin films of Spiro-TPD were grown on different substrates with following deposition parameters: background pressure of  $2 \times 10^{-6}$  mbar, deposition rate of  $0.7 \text{ \AA}/\text{s}$ , and a final thickness of 140 nm. The thin films of as-deposited Spiro-TPD were very smooth with a mean of roughness of 0.28 nm and a peak-to-valley height of 1.9 nm (Figure 5.10(a)). The surface of as-deposited Spiro-TPD film was also smoother than those of TPD and TAD films. Moreover, the variation of peak-to-valley height of as-deposited Spiro-TPD films was around three times lower than those of as-deposited TPD and TAD films. The surface roughness of as-deposited Spiro-TPD films was also five times lower than that of as-deposited Spiro-TAD films. The surface roughness of as-deposited Spiro-TAD, as-deposited Spiro-TPD, as-deposited TAD, and as-deposited TPD films were compared as well. It was found that the surface of as-deposited Spiro-TPD films was the smoothest among the films mentioned above.

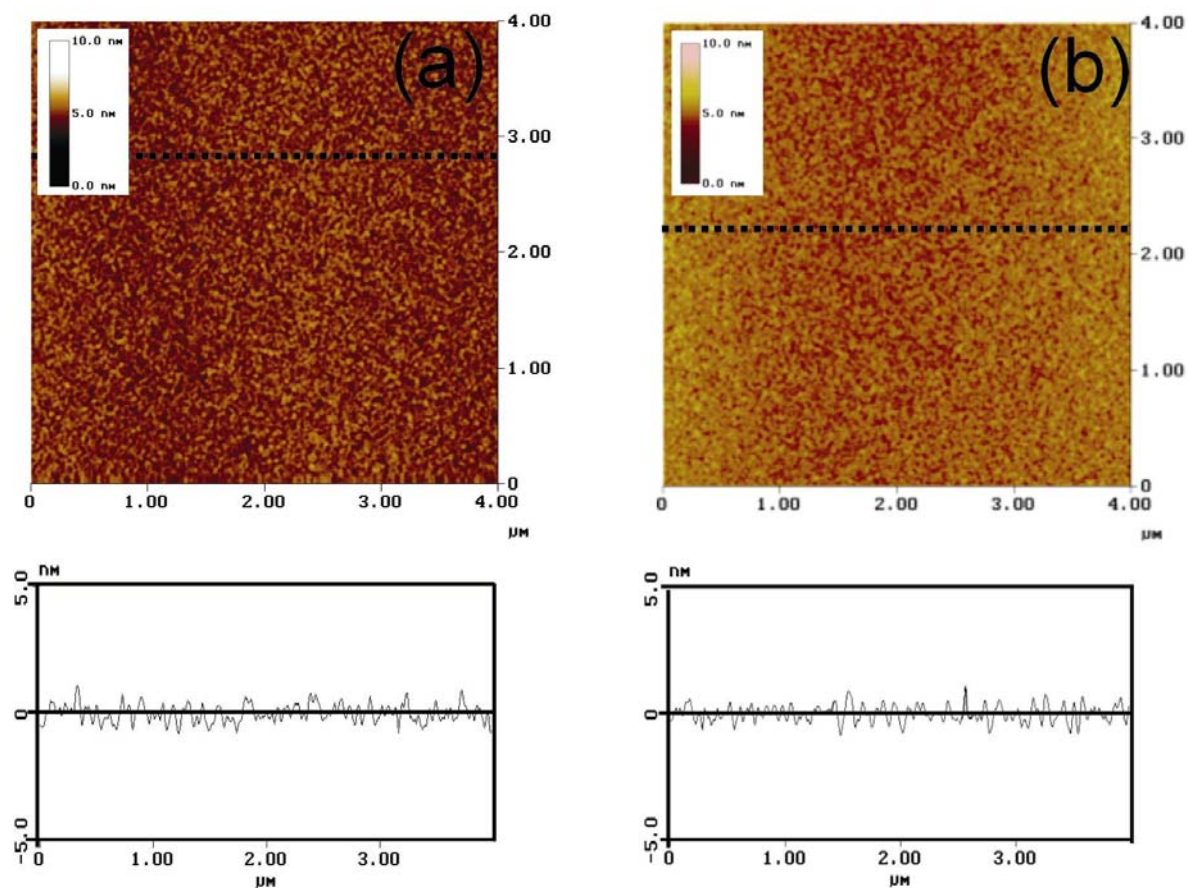


Figure 5.10. AFM topographical image of a Spiro-TPD thin film on a  $\text{SiO}_2/p\text{-Si}$  substrate ( $4 \times 4 \mu\text{m}^2$ ). (a) As deposited; the mean roughness  $R_a$  was 0.28 nm and the root-mean square roughness  $R_q$  was 0.36 nm and (b) After the sample was stored in ambient atmosphere and at RT for 2 months; the mean roughness  $R_a$  was 0.38 nm and the root-mean square roughness  $R_q$  was 0.46 nm.

After the first measurements, the sample was stored in ambient atmosphere and at RT for two months. Subsequently, the surface of films was measured again. The AFM image of Spiro-TPD films did not change significantly, as shown in Figure 5.10(b). A mean roughness of 0.38 nm and a peak-to-valley height of 2.2 nm were reported. These values were relatively unchanged from the initial values, the as-deposited Spiro-TPD film. Therefore, the surface morphology of Spiro-TPD films does not change as the films have been stored for 2 months in an ambient atmosphere and at RT. In contrast, the films of TPD or TAD were easily crystallized after the samples were exposed to ambient atmosphere for a few days. The mean roughness of Spiro-TPD films after the sample is being left for 2 months was increased by a factor of 1.4. This value is the same as the value obtained for Spiro-TAD films after the sample has been stored in ambient atmosphere and at RT for 5 weeks. Finally, the mean roughness value of Spiro-TPD films is the smallest values among the thin films of spiro-linked compounds and their parent compounds.

Figure 5.11 shows the optical microscopy images of Spiro-TPD thin films grown on SiO<sub>2</sub> substrate, *p*-Si substrate and field-effect transistor, which the samples were measured after the samples have been stored in ambient atmosphere and at RT for 15 months. The surfaces of Spiro-TPD thin films did not change and were as smooth as the initial films. A similar result was also observed on Spiro-TAD films, as shown previously in Figure 5.6. Moreover, it will be proved later by transistor measurements that the transistor characteristics of Spiro-TPD did not significantly change over 9 months as the samples were left under an ambient atmosphere. Finally, Spiro-TPD thin films form an entirely amorphous and flat surface. So far, no crystallization was observed in thin films of Spiro-TAD and Spiro-TPD, which is in contrast with their corresponding parent compounds, TAD and TPD.

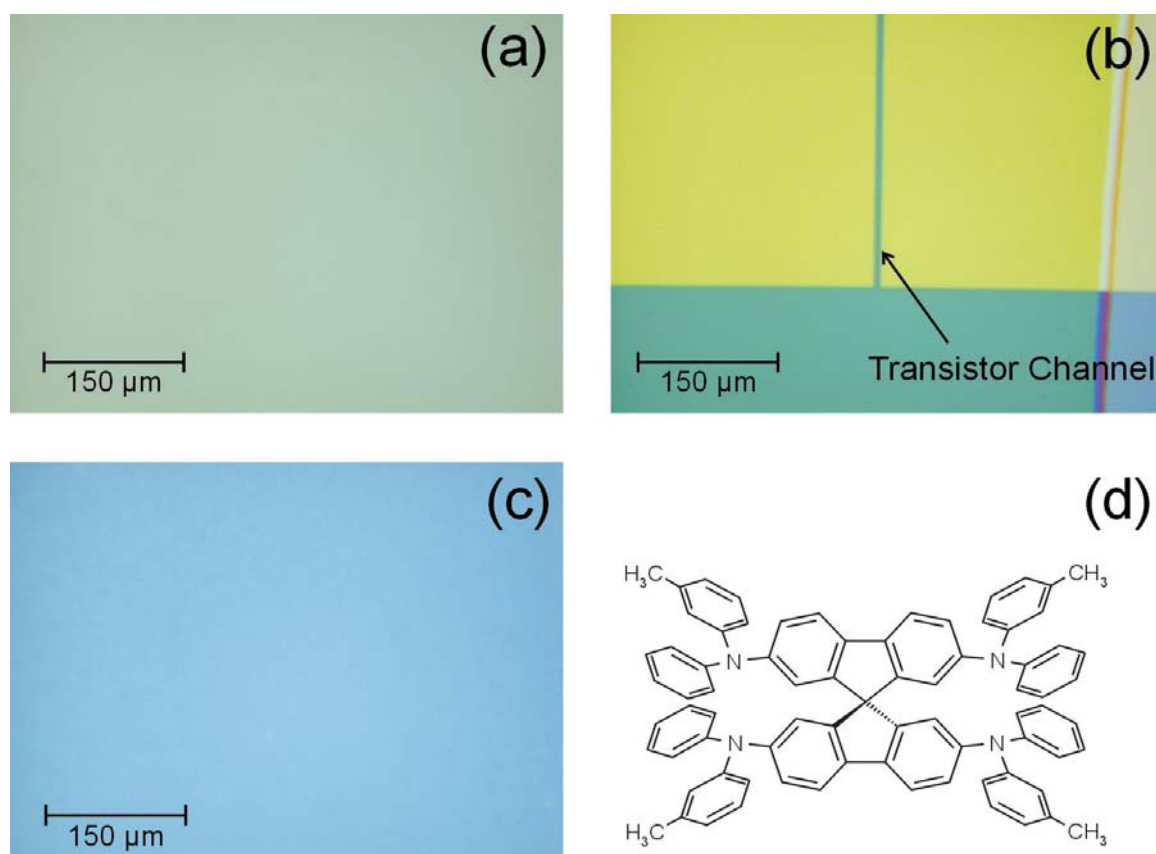


Figure 5.11. The optical microscopy images of Spiro-TPD thin films after the samples were stored in ambient atmosphere and at RT for 15 months. Spiro-TTB thin films were grown on (a) SiO<sub>2</sub> substrate, (b) Field-effect transistor, and (c) *p*-Si substrate. (d) The chemical structure of Spiro-TPD.

### 5.5. *N,N,N',N'*-Tetrakis(4-methylphenyl)benzidine (TTB)

Figure 5.12, 5.13, and 5.14 show the surface morphology change of TTB films (growth parameters: vacuum of  $2 \times 10^{-6}$  mbar, deposition rate of  $0.8 \text{ \AA/s}$  and a final thickness of 100 nm). Figure 5.12 shows the AFM image of an as-deposited TTB film. The surface was relative smooth with a mean roughness of 0.69 nm. This value is the same as the value of the as-deposited TPD film but smaller than those of as-deposited TAD and as-deposited Spiro-TAD films. However, the surface roughness of as-deposited TTB films is much lower than that of as-deposited Spiro-TPD films. The variation of the peak-to-valley height of as-deposited TTB films was 5.6 nm, which is the same as that of as-deposited TPD films but lower than that of as-deposited TAD films. In addition, the peak-to-valley height of as-deposited TTB films was lower than that of as-deposited Spiro-TAD films but higher than that of as-deposited Spiro-TPD films. However, it is clear that as-deposited TTB films exhibited large voids on the surface, as shown in Figure 5.12. Similar results were also reported for thin films of as-deposited TAD and TPD, as described in sub-chapter 5.1 and 5.3.

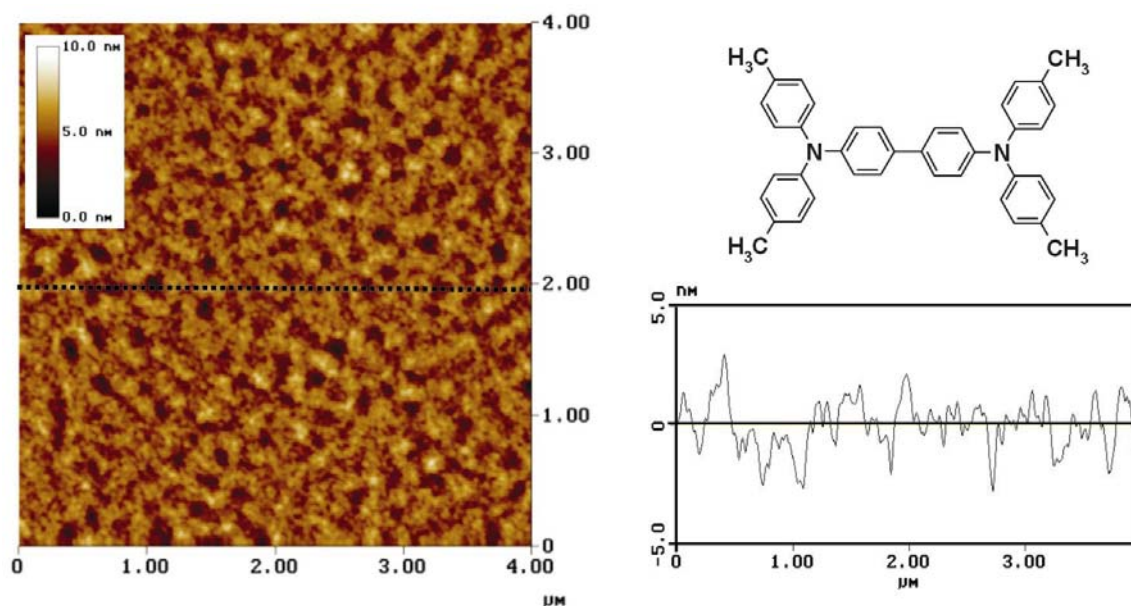


Figure 5.12. AFM topographical image of a TTB thin film as deposited on a  $\text{SiO}_2/p\text{-Si}$  substrate. Left side:  $4 \times 4 \mu\text{m}^2$  AFM images, and Right side: Surface height of AFM images and the chemical structure of TTB. The mean roughness  $R_a$  was 0.69 nm and the root-mean square roughness  $R_q$  was 0.87 nm.

For the quantitative analysis of the surface, a second measurement was carried out after a certain time. The TTB films were found to be crystallized as the samples were left in



ambient atmosphere and at RT for 5 days. The transition is accompanied by a change in the film corrugation. The mean roughness was increased by a factor of 30 over 5 days, as shown in Figure 5.13. Similar results were also reported for thin films of TAD and TPD. The mean roughness of TAD and TPD films was increased by a factor 36 and 40, respectively. However, those values were obtained after the samples have been left in ambient atmosphere for 3 days for TAD films and 12 days for TPD films. The peak-to-valley height of TTB films obtained from the cross-section analysis was 155 nm after the sample has been left for 5 days. The height of the resulting crystals was lower than those of TAD and TPD films. In addition, the height of the resulting crystals was higher than the thickness of the as-deposited film itself. The main caused of the crystallization is due to lack of the morphology stability, the  $T_g$  of TTB is 66 °C, and probably due to the oxidation product of TTB films as well.

Heun and Borsenberger qualitatively reported that the films of TTB showed no tendency to crystallize over a period of several months [87]. The TTB thin films were grown on nickel coated with a polyethyleneterephthalate substrate with a deposition rate of 120 Å/s and a final thickness in the range of 11.0  $\mu\text{m}$  and 12.1  $\mu\text{m}$ . The discrepancy of the surface morphology of TTB thin films can be ascribed to different substrates are being used in each experiment and probably also caused by different deposition parameters. Indeed, they used very thick films so that the crystallization process could have occurred in a different way.

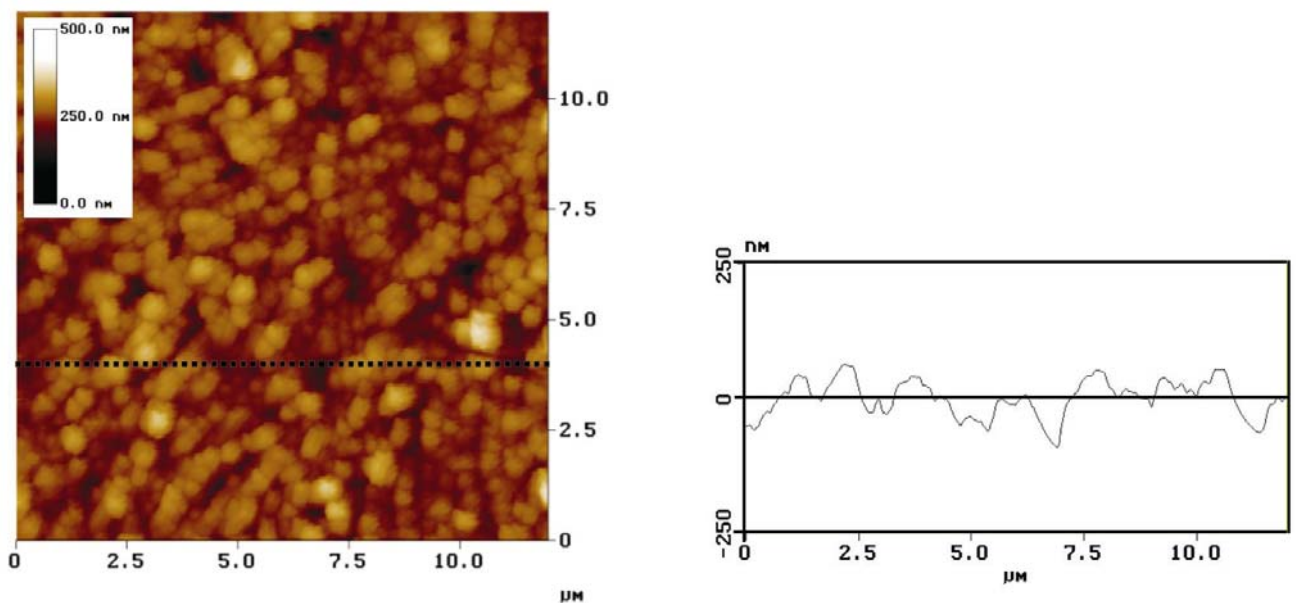


Figure 5.13. AFM topographical image of a TTB thin film after the sample was stored in ambient atmosphere and at RT for 5 days. Left side:  $12 \times 12 \mu\text{m}^2$  AFM images, and Right side: Surface height of AFM images. The mean roughness  $R_a$  was 20.6 nm and the root-mean square roughness  $R_q$  was 26.7 nm.

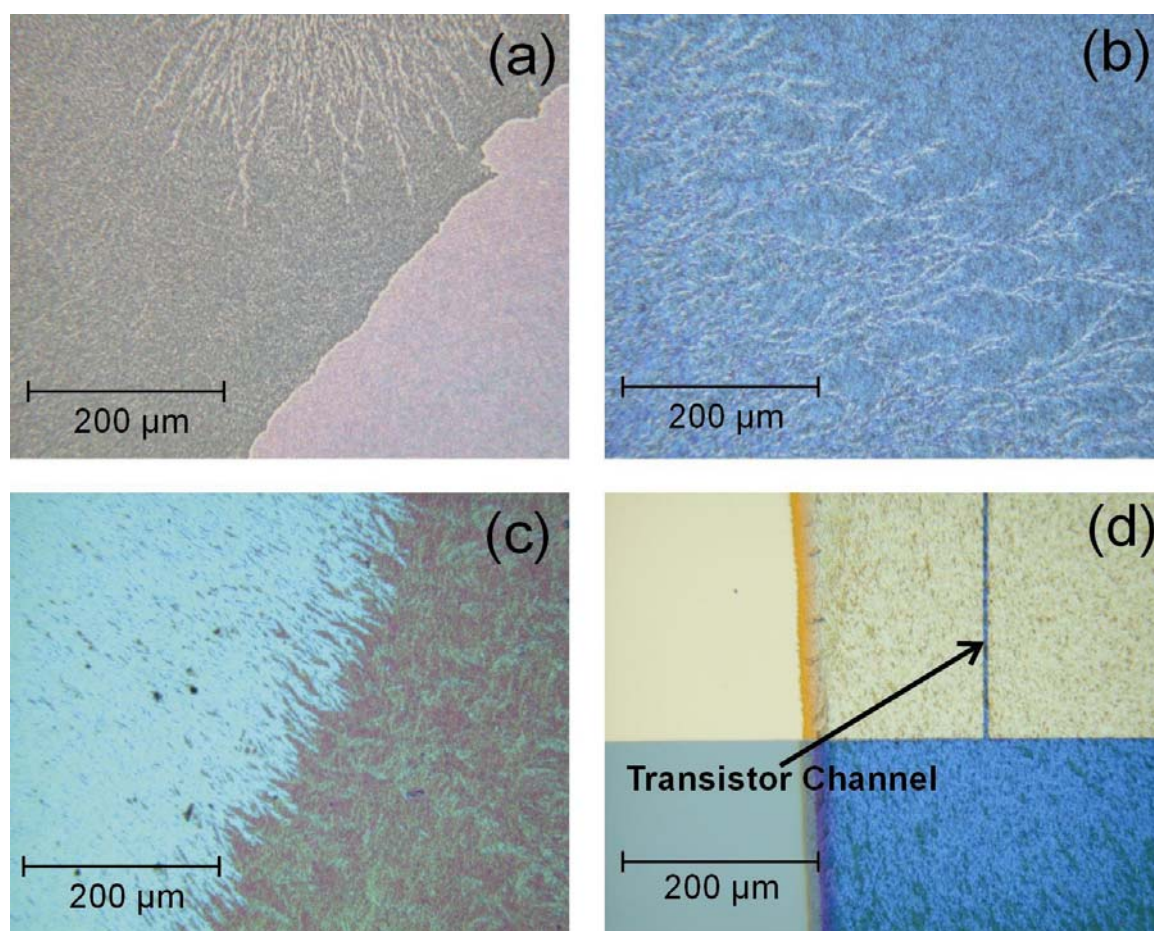


Figure 5.14. The optical microscopy images of TTB thin films after the samples were stored in ambient atmosphere and at RT for 5 days. TTB thin films were grown on (a) *p*-Si substrate, (b) SiO<sub>2</sub> substrate, (c) Glass substrate, and (d) Field-effect transistor.

Figure 5.14 shows the optical micrographs of TTB films after the samples have been stored under an ambient atmosphere and at RT for 5 days. The films grown on *p*-Si substrate, SiO<sub>2</sub> substrate, glass substrate and an organic field-effect transistor were crystallized. Moreover, the resulting crystals covered the whole substrates. This is in contrast with the films of TAD and TPD, as shown in Figure 5.3 and 5.9. The resulting crystals of TAD and TPD films were found to be circularly grown, which is not the case of TTB films. For instance, the TPD films grown on glass substrates have a crystal size of  $20 \times 25 \mu\text{m}^2$  after the samples were left for 12 days in ambient atmosphere. In contrast, the TTB films crystallized in most areas of the glass substrate, as shown in Figure 5.14(c). This indicates that TTB films have larger tendency to crystallize than TPD films. Field-effect transistors characterization of both films will be presented in chapter 6, which support the argument that TPD film is more stable under operation in ambient atmosphere than TTB film. However, a comparison of the

morphology of TTB and TAD films can not be directly performed since both films show the same tendency to crystallize.

#### **5.6. 2,2',7,7'-Tetrakis-(*N,N'*-di-*p*-methylphenylamino)-9,9'-spirobifluorene (Spiro-TTB)**

Figure 5.15(a) shows topographic AFM images of as-deposited Spiro-TTB films grown on SiO<sub>2</sub>/*p*-Si substrate. The thermal evaporation parameters were: background pressure of  $2 \times 10^{-6}$  mbar, deposition rate of 1.2 Å/s, and a final thickness of 130 nm. The surface of as-deposited Spiro-TTB thin films was smooth with a mean roughness of 0.74 nm, which is the same as those of TPD and TTB films. In addition, a peak-to-valley height of 5.7 nm was obtained as well. These values are the same as that of TTB films, as described previously in sub-chapter 5.5. The surface roughness of as-deposited Spiro-TTB films was higher than that of Spiro-TPD films and was lower than that of Spiro-TAD films. The as-deposited Spiro-TTB films contained no voids, which is in contrast with TTB films.

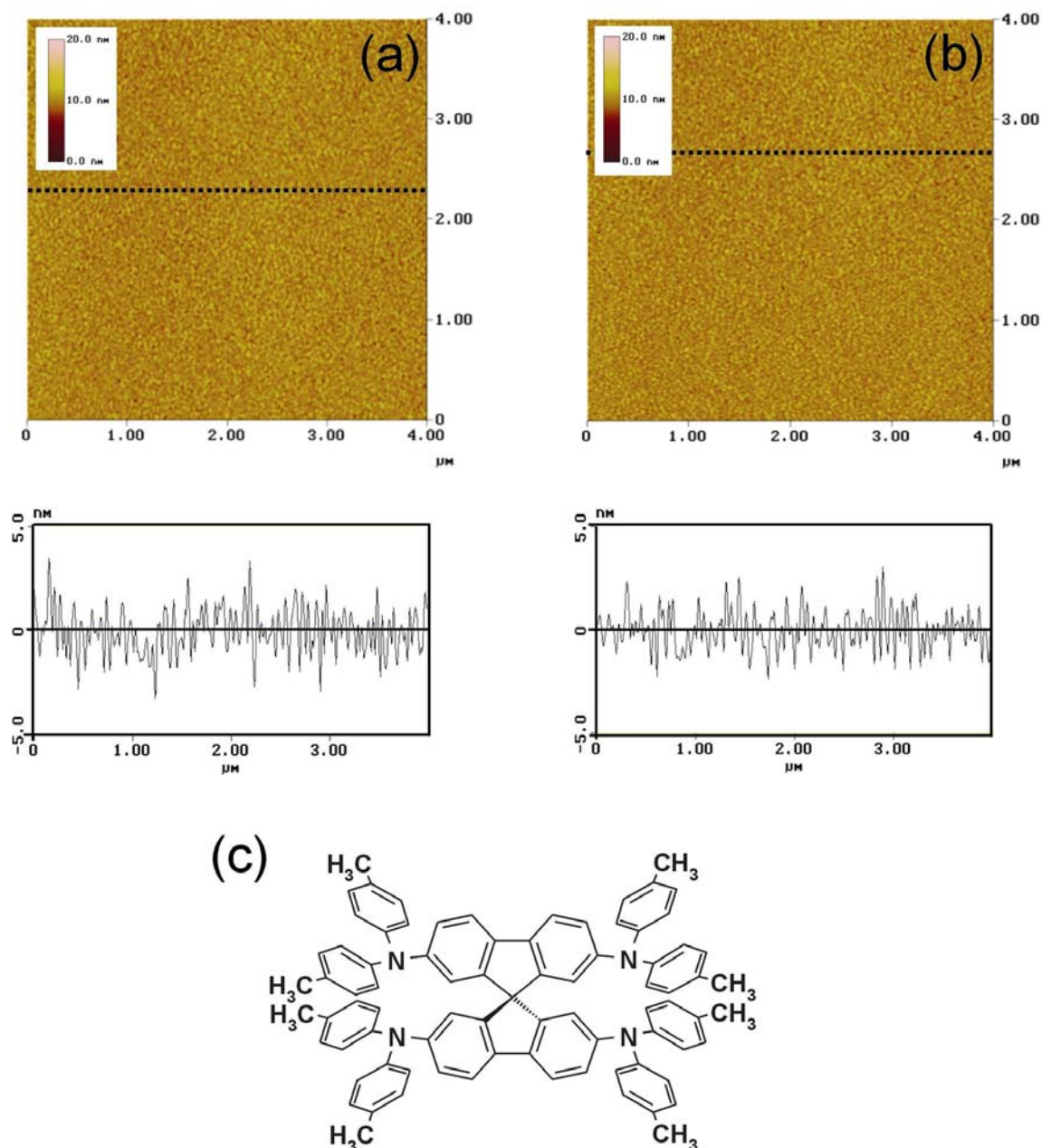


Figure 5.15. AFM topographical image of a Spiro-TTB thin film on a  $\text{SiO}_2/p\text{-Si}$  substrate ( $4 \times 4 \mu\text{m}^2$ ). (a) As deposited; the mean roughness  $R_a$  was 0.74 nm and the root-mean square roughness  $R_q$  was 0.93 nm and (b) After the sample was stored in ambient atmosphere and at RT for 2 months; the mean roughness  $R_a$  was 0.75 nm and the root-mean square roughness  $R_q$  was 0.95 nm. (c) The chemical structure of Spiro-TTB.

After the sample was left in ambient atmosphere and at RT for two months, the surface morphology was measured again and the result is shown in Figure 5.15(b). The mean roughness value is slightly increased and, by contrast, the peak-to-valley height decreased from 5.7 nm to 5 nm. The change in surface roughness ( $\sim 0.1$  nm) of Spiro-TTB films was the smallest among the materials used in this study. This indicates that Spiro-TTB film is extremely stable in air and at RT. This result agrees very well with transistor measurement,

which the output and transfer transistor characteristics do not change significantly over two months as the sample was left in ambient atmosphere and at RT. Figure 5.16 shows the surface morphology of Spiro-TTB films after the sample has been left under an ambient atmosphere and at RT for four months. The surfaces of thin films were still smooth and clean. Moreover, no crystallization was observed in entire the surface.

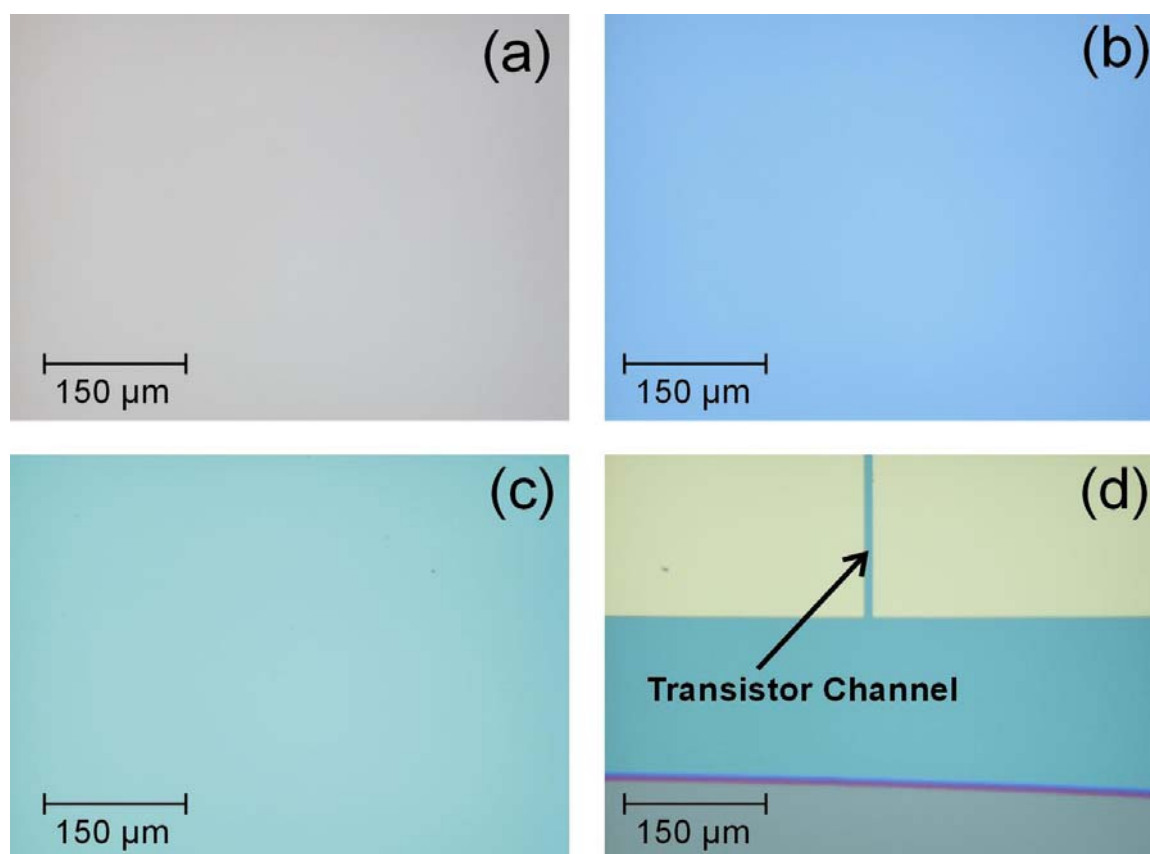


Figure 5.16. The optical microscopy images of Spiro-TTB thin films after the samples were stored in ambient atmosphere and at RT for 4 months. Spiro-TTB thin films were grown on (a) Glass substrate, (b) *p*-Si substrate, (c) SiO<sub>2</sub> substrate, and (d) Field-effect transistor.

### 5.7. *N,N'*-Diphenyl-*N,N'*-bis(1-naphthyl)-1,1'-biphenyl-4,4'-diamine ( $\alpha$ -NPB)

Figure 5.17, 5.18, and 5.19 show the time dependency of the surface morphology of vacuum-deposited 130 nm thick  $\alpha$ -NPB films grown on different substrates at  $2 \times 10^{-6}$  mbar, with a deposition rate of 0.75 Å/s. Figure 5.17 shows that the surface of as-deposited  $\alpha$ -NPB thin films were relatively smooth and flat with a mean roughness of 0.43 nm and a peak-to-

valley of 2.86 nm. The surface of as-deposited  $\alpha$ -NPB films was the smoothest film among the as-deposited films of the parent compounds. In addition, the peak-to-valley height of as-deposited  $\alpha$ -NPB films was the lowest among the as-deposited parent compounds thin films as well. This indicates that  $\alpha$ -NPB films exhibited better film uniformity than other films of parent compounds. However, Spiro-TPD, Spiro-TAD, and Spiro-TTB films are better than  $\alpha$ -NPB in terms of the uniformity of the surface, because the as-deposited  $\alpha$ -NPB films contained large voids.

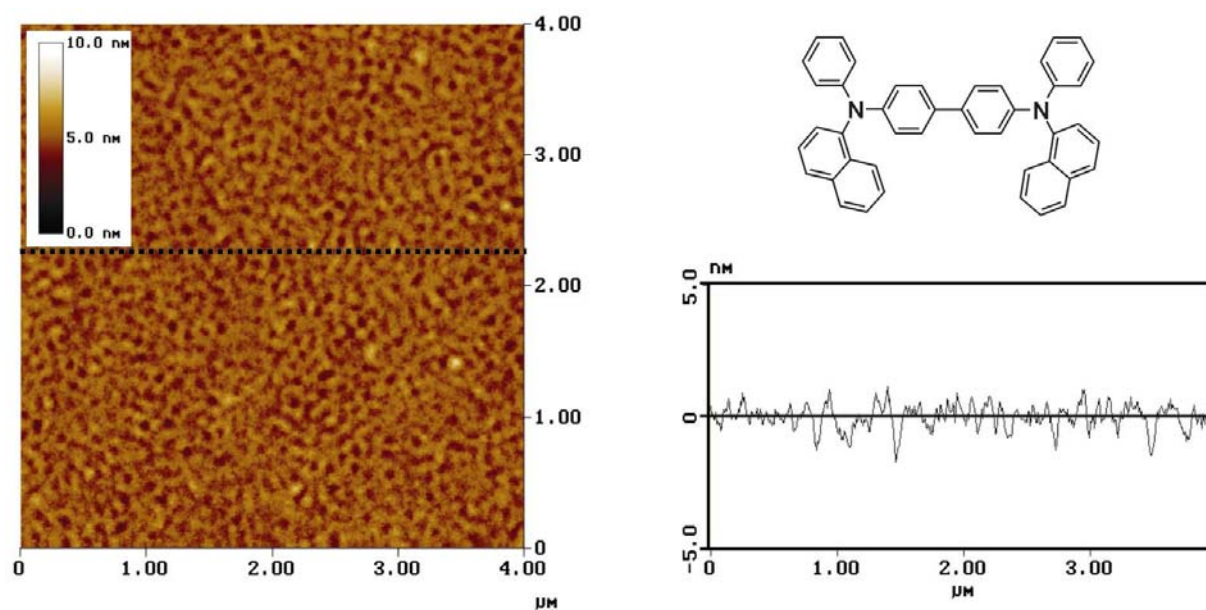


Figure 5.17. AFM Topographical image of an  $\alpha$ -NPB thin film as deposited on a  $\text{SiO}_2/p$ -Si substrate. Left side:  $4 \times 4 \mu\text{m}^2$  AFM images, and Right side: Surface height of AFM images and the chemical structure of  $\alpha$ -NPB. The mean roughness  $R_a$  was 0.43 nm and the root-mean square roughness  $R_q$  was 0.54 nm.

In contrast, thin films of  $\alpha$ -NPB showed different features after the sample was left in ambient atmosphere and at RT for 3 days, as shown in Figure 5.18 and 5.19. The AFM image of  $\alpha$ -NPB films underwent a distinctive change with the mean surface roughness greatly increased. The film morphology undergoes a phase transition from amorphous to oriented lamellae with sharp edges separated by large voids. This indicates that  $\alpha$ -NPB thin films easily crystallized as the samples were left in ambient atmosphere for 3 days. The mean roughness has increased by a factor of 84 and the peak-to-valley was 187 nm (increased by a factor of 67). The change in surface roughness of  $\alpha$ -NPB films was the roughest among the films of the parent compounds. Moreover, the change in the peak-to-valley formation of  $\alpha$ -NPB films was also the highest among the films of the parent compounds. This finding is

very suspicious, because the  $T_g$  (95 °C) of  $\alpha$ -NPB is the highest among the parent compounds. Therefore, the resulting crystal of  $\alpha$ -NPB films is probably not due to crystallization of  $\alpha$ -NPB itself but probably caused by the oxidation product of  $\alpha$ -NPB. However, this phenomenon is not understood yet.

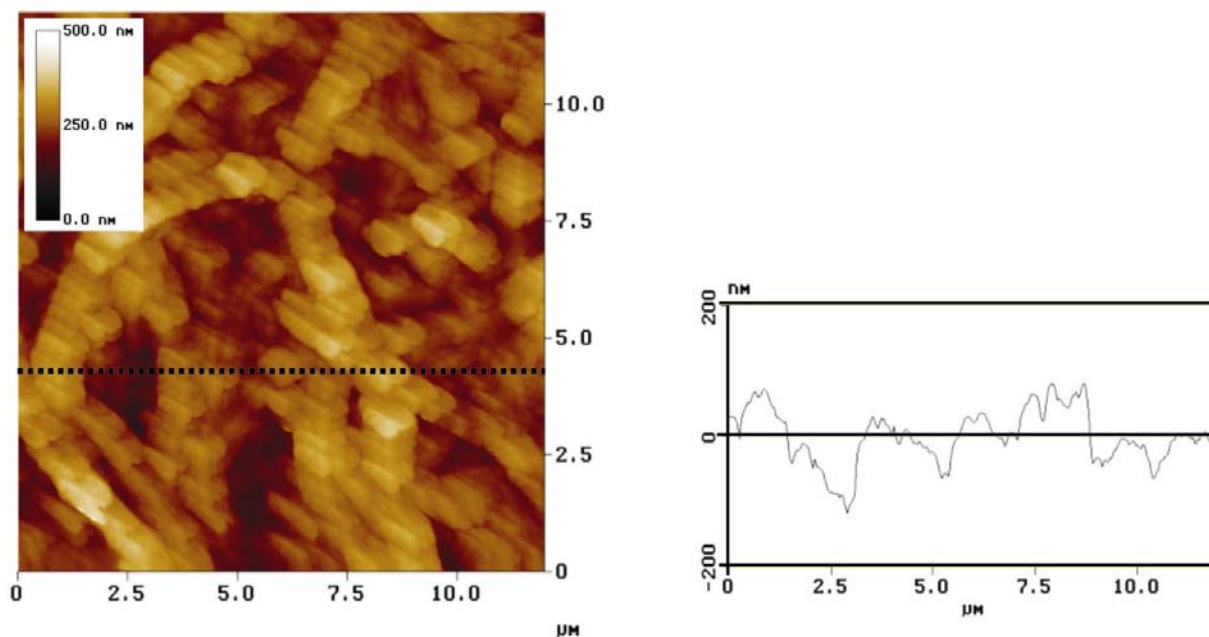


Figure 5.18. AFM topographical image of an  $\alpha$ -NPB thin film after the sample was stored in ambient atmosphere and at RT for 3 days. Left side:  $12 \times 12 \mu\text{m}^2$  AFM images, and Right side: Surface height of AFM images. The mean roughness  $R_a$  was 36.1 nm and the root-mean square roughness  $R_q$  was 45.1 nm.

The resulting crystals of  $\alpha$ -NPB films were also observed in thin films grown on  $p$ -Si substrate,  $\text{SiO}_2$  substrate, glass substrates, and field-effect transistor (see Figure 5.19). For example, a size of crystal of  $360 \times 360 \mu\text{m}^2$  was obtained for films grown on  $p$ -Si substrate and glass substrate. On the other hand, a crystal size of  $880 \times 510 \mu\text{m}^2$  was obtained for film grown on  $\text{SiO}_2$  substrate. A similar crystal size was also reported for TAD films; a radius of crystal is in the range of  $500 \mu\text{m}$  and  $900 \mu\text{m}$ . Figure 5.19(d) shows an organic field-effect transistor with  $\alpha$ -NPB as active materials. The films of  $\alpha$ -NPB easily crystallized as TAD, TPD and TTB films. Such crystal-like structure was also observed in organic field-effect transistor with  $\alpha$ -NPB as active materials. These observations explain the vanishing of FET behavior of  $\alpha$ -NPB transistors after the samples were stored for 3 days in ambient atmosphere and at RT.

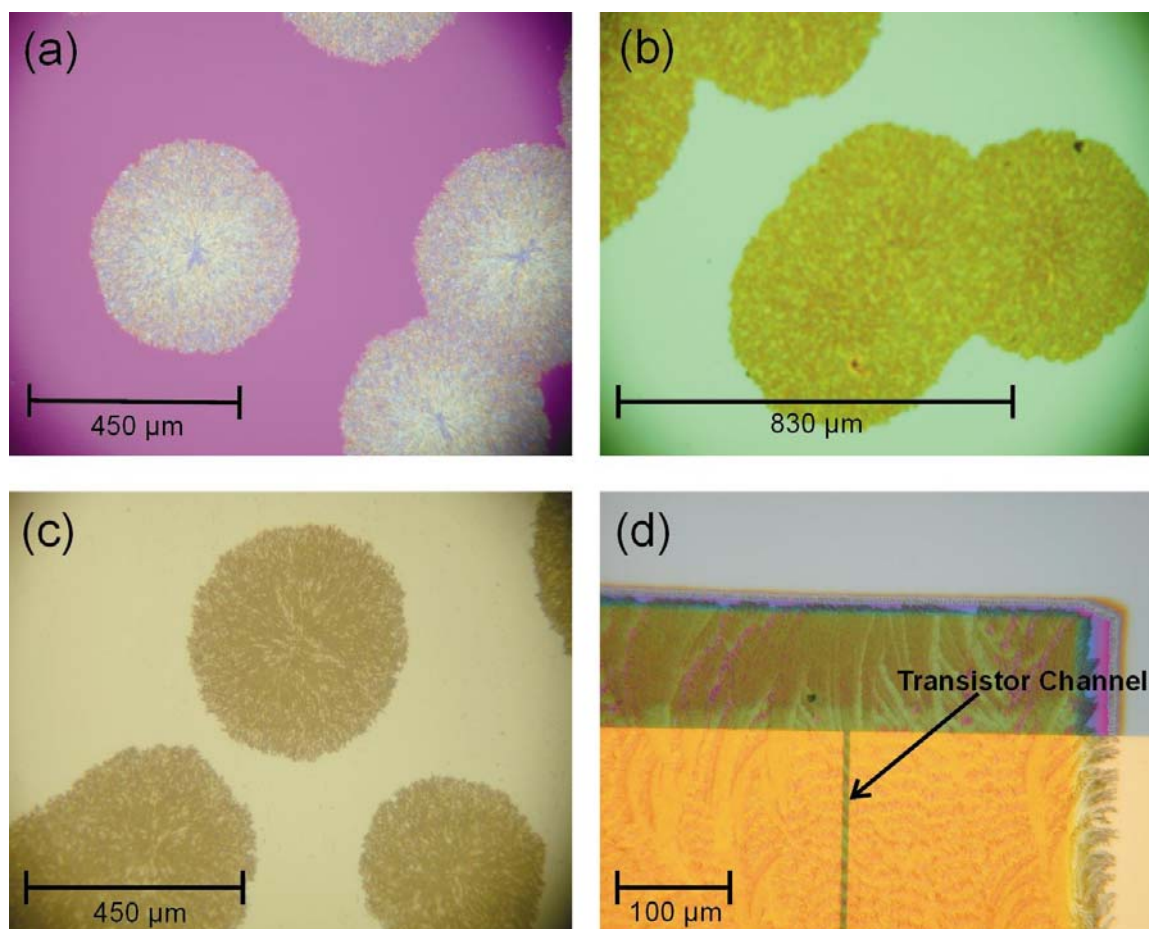


Figure 5.19. The optical microscopy images of  $\alpha$ -NPB thin films after the samples were stored in ambient atmosphere and at RT for 3 days.  $\alpha$ -NPB thin films were grown on (a)  $p$ -Si substrate, (b)  $\text{SiO}_2$  substrate, (c) Glass substrate, and (d) Field-effect transistor.

The surface morphology of  $\alpha$ -NPB thin films was also reported by other groups. Qiu and Qiao reported that the roughness of  $\alpha$ -NPB thin films grown on ITO substrates (at a vacuum of  $10^{-5}$  Torr, a deposition rate of  $4 \text{ \AA/s}$  and a final thickness of 40 nm) has remained relatively smooth over 15 days with a roughness of 0.2 – 0.4 nm [6]. The origin of this discrepancy was not understood yet, but somehow it could be attributed to differences in deposition parameters and/or pre-treatment of the substrate. In contrast, all organic films presented here were thermally evaporated onto HMDS-treated  $\text{SiO}_2/p$ -Si substrate and followed by morphological characterization with a Digital Instruments Nanoscope Multimode III. Moreover, the comparison of the surface morphology between each film will be easier. This step was also taken because all organic field-effect transistors were prepared on HMDS-treated  $\text{SiO}_2$  pre-defined substrates. However, the surface morphology of thin film do not exactly show the morphology of one or two first monolayer of organic films near gate insulator surfaces whereas it plays an important role in organic field-effect transistors.



### 5.8. 2,2',7,7'-Tetra-(*N*-phenyl-1-naphthylamine)-9,9'-spirobifluorene (Spiro $\alpha$ -NPB)

Figure 5.20 and 5.21 show the surface morphology change of thin films of Spiro  $\alpha$ -NPB. The thermal evaporation parameters were: background pressure of  $2 \times 10^{-6}$  mbar, deposition rate of 0.7 Å/s, and a final thickness of 130 nm. Figure 5.20(a) shows the surface morphology of as-deposited Spiro  $\alpha$ -NPB film. The thin film was very smooth and flat with a very small roughness of less than 0.6 nm. This value was higher than that of as-deposited  $\alpha$ -NPB films but lower than those of TAD, TPD, TTB, Spiro-TAD, and Spiro-TTB films. The peak-to-valley height of Spiro  $\alpha$ -NPB films was 3.2 nm, which is higher than those of  $\alpha$ -NPB and Spiro-TPD films but much lower than those of TAD, TPD, TTB, Spiro-TAD and Spiro-TTB films.

The surface of thin films was measured again after the sample was stored at RT and under ambient atmosphere for 2 months. The AFM image is shown in Figure 5.20(b). Generally, the surface of films did not show any change. However, the roughness of surface was slightly increased to 0.8 nm and the peak-to-valley height was increased by a factor of 2. These values were larger than those obtained for Spiro-TPD and Spiro-TTB films but smaller than that obtained for Spiro-TAD films. Finally, Figure 5.21 shows the large areas of the surface morphologies grown on different substrates, after the sample have been stored in ambient atmosphere for 7 months. The films have remained smooth and flat and, indeed, the transistor characteristics did not significantly change, which will be presented in chapter 6.

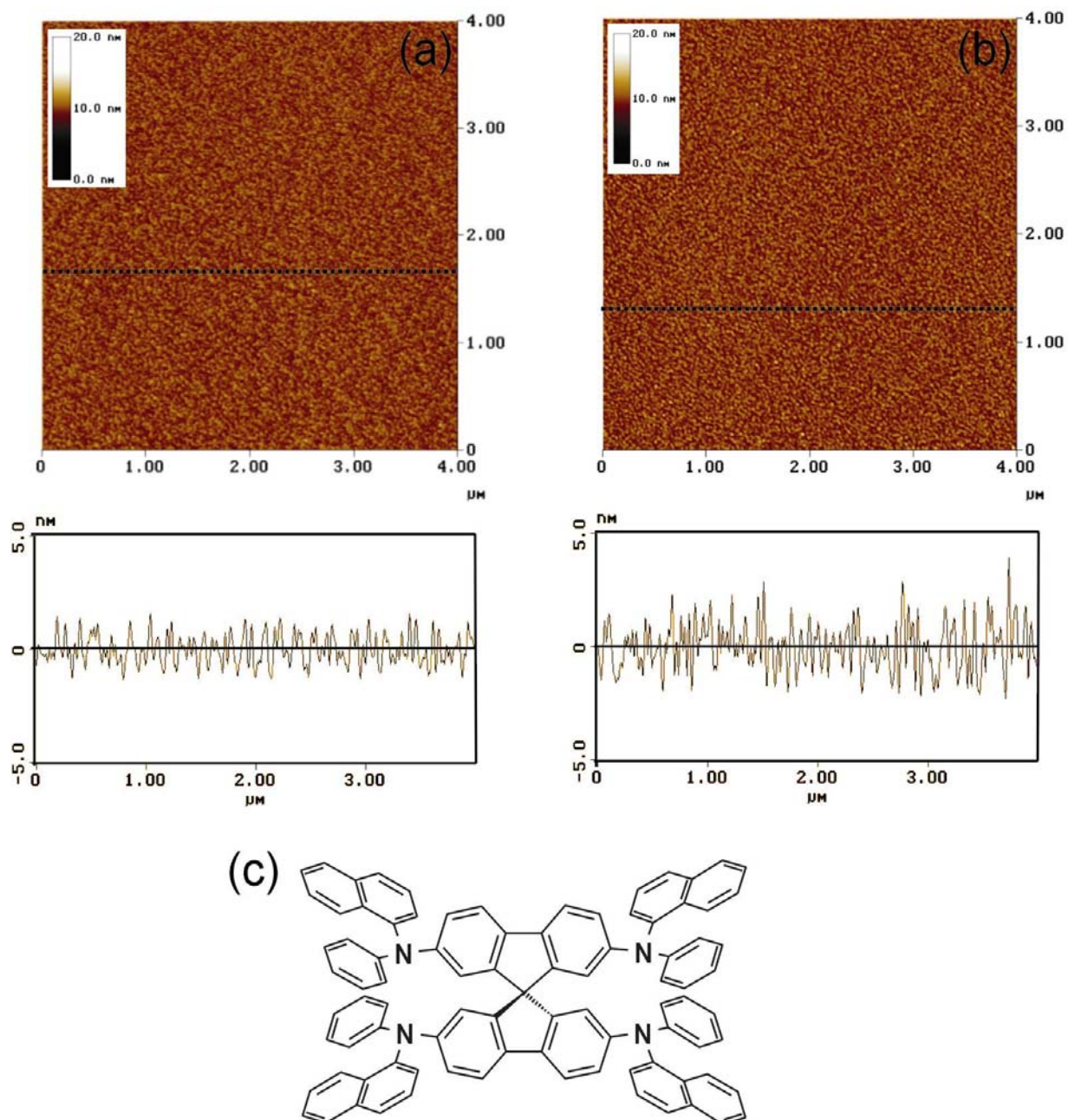


Figure 5.20. AFM topographical image of a Spiro  $\alpha$ -NPB thin film on a  $\text{SiO}_2/p$ -Si substrate ( $4 \times 4 \mu\text{m}^2$ ). (a) As deposited; the mean roughness  $R_a$  was 0.52 nm and the root-mean square roughness  $R_q$  was 0.65 nm and (b) After the sample was stored in ambient atmosphere and at RT for 2 months; the mean roughness  $R_a$  was 0.79 nm and the root-mean square roughness  $R_q$  was 0.99 nm. (c) The chemical structure of Spiro  $\alpha$ -NPB.

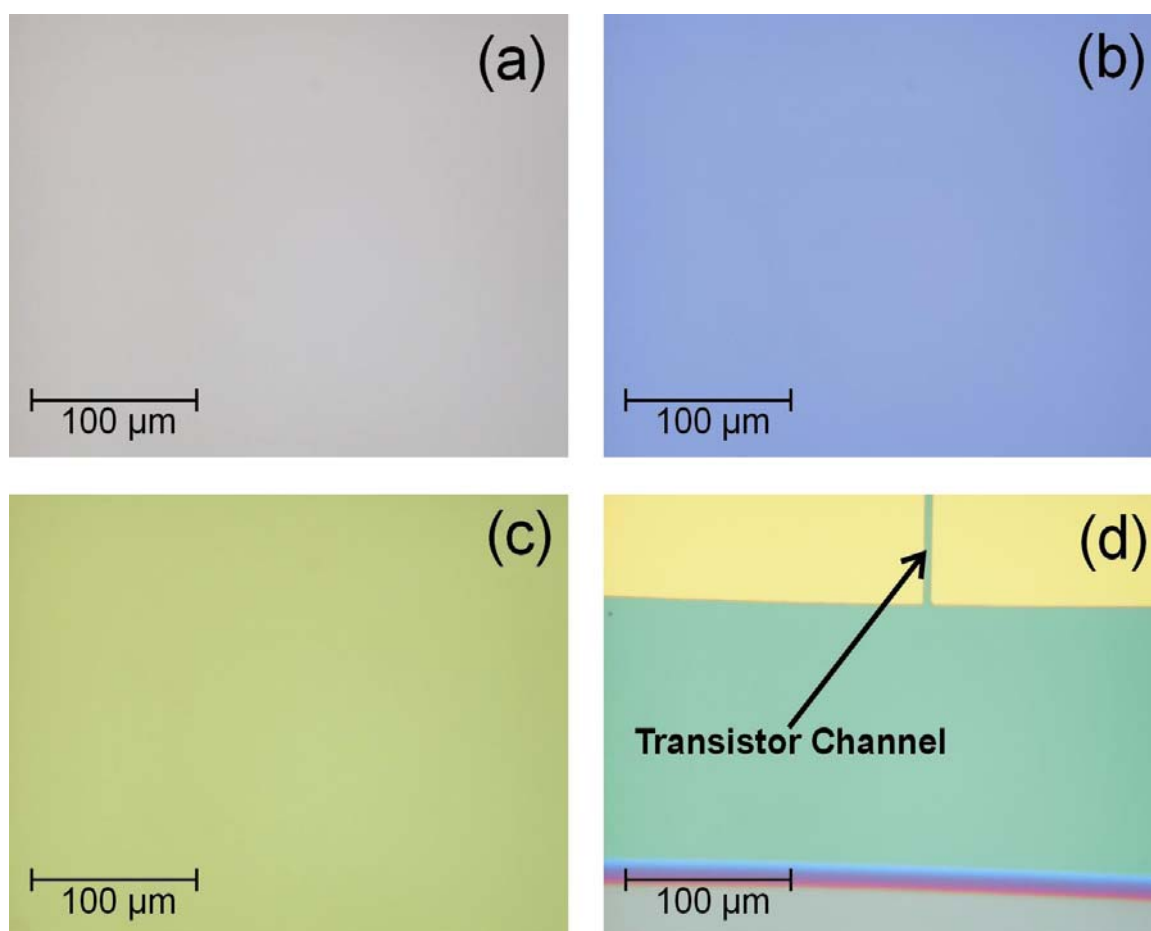


Figure 5.21. The optical microscopy images of Spiro  $\alpha$ -NPB thin films after the samples were stored in ambient atmosphere and at RT for 7 months. Spiro  $\alpha$ -NPB thin films were grown on (a) Glass substrate, (b) *p*-Si substrate, (c) SiO<sub>2</sub> substrate, and (d) Field-effect transistor.

## 5.9. Summary of chapter 5

The surface morphologies of as-deposited TAD, TPD, TTB,  $\alpha$ -NPB, Spiro-TAD, Spiro-TPD, Spiro-TTB, and Spiro  $\alpha$ -NPB thin films grown on HMDS-treated SiO<sub>2</sub>/*p*-Si pre-defined substrates exhibited entirely amorphous and flat surfaces. However, the films of as-deposited parent compounds exhibited lamellae-like structure and large voids, which are not the case of the corresponding spiro-linked compound films. The thin films of as-deposited parent compounds have a maximum mean roughness of 1.06 nm and peak-to-valley heights of less than 7 nm. On the other hand, the as-deposited spiro-linked compound thin films have a maximum mean roughness of 1.56 nm. The peak-to-valley height extracted from the cross-section analysis exhibited a maximum height of 9.8 nm for Spiro-TAD films and a minimum height of 1.9 nm for Spiro-TPD films.

The samples were left in an ambient atmosphere and at RT for a certain time. It was found that the films of the corresponding parent compounds crystallized easily after the samples have been stored under an ambient atmosphere and at RT for several days. As a result, mean roughnesses of films were increased by a factor of larger than 30. The resulting crystals were a rounded shape with a crystal size of larger than  $125 \times 225 \mu\text{m}^2$ , except TPD films grown on glass substrates had a size of crystal of  $20 \times 25 \mu\text{m}^2$ . Moreover, the heights of the resulting crystals were much higher than the thicknesses of films themselves. This indicates that the substrates were revealed by crystallization.

In contrast, the as-deposited spiro-linked compound thin films did not change significantly after the samples have been stored in ambient atmosphere and at RT for several months. The films still formed very flat surfaces with mean roughnesses of less than 1.9 nm and peak-to-valley heights of less than 12 nm. Moreover, the optical micrographs have shown that the films grown on different substrates were also clean and flat. No crystallization has been observed.

Based on AFM and optical microscopy data, TAD, TPD,  $\alpha$ -NPB, and TTB films do not form morphologically stable amorphous films at RT and in an ambient atmosphere. The thin films were easily crystallized after the samples have been exposed in ambient atmosphere and at RT for a certain time. If such materials are used as active layer in devices, for instance OLED, the operating lifetime of the devices will suffer. An example is the hole transport layer easily crystallized and disturb the function of layer. Subsequently, it was followed by aging of the devices. Finally, the devices do not work anymore. Therefore, high morphological and chemical stabilities of organic materials are required. The introduction of a central (spiro-) carbon atom, linking two hole transport moieties, yields materials capable of forming morphologically very stable thin amorphous films. The surface morphologies of Spiro-linked compound thin films were flat and smooth. Moreover, their surface morphologies do not change as the samples were left in ambient atmosphere over several months. This result is sustained by time-dependent measurements of field-effect transistors, which will be presented in chapter 6.

## Chapter 6

# Field-Effect Mobility of Charge Carriers in Thin Films of Low Molecular Amorphous Materials

In this chapter, the field-effect mobility of charge carriers in low molecular amorphous thin films based on bottom-contact organic field-effect transistors (OFET) structures is presented. The charge carrier mobility was extracted from the transfer characteristics as previously described in chapter 2. The hole mobility of charge carrier is presented in two regimes of the transistor characteristics i.e. in the linear regime and in the saturation regime. The electrical measurements, transfer and output characteristics, were measured in air and in a vacuum. Furthermore, the time dependency of the field-effect mobility of the charge carriers is also presented in order to gain a deep insight into the dependency of the device characteristics with increasing time of exposure to ambient atmosphere. Additionally, these results are compared with the results obtained by other groups and with different methods as well. The gate bias in the transfer characteristics was swept both from *ON* states to *OFF* states (dotted lines) and vice versa (solid lines).

### 6.1. *N,N,N',N'*-Tetraphenylbenzidine (TAD)

Figure 6.1(a) shows the output characteristics of a TAD field-effect transistor (FET) measured in air and at room temperature (RT). The channel currents were plotted against the drain voltage for different gate voltages. The drain current increases as the gate voltage is increased towards larger negative voltage, which underwent an effective field-effect modulation caused by the variation of the gate bias. The sign of the field-enhanced current ( $I_D < 0$  with  $V_G < 0$ ) is consistent with an accumulation regime, owing to the *p*-type character of TAD. At low drain biases ( $V_D < 10$  V); however, the output characteristics exhibit some nonlinearities which can be attributed to the non-ohmic contacts between TAD and the gold electrodes. Figure 6.1(b) shows the variation of channel conductivity with gate voltage for a constant drain voltage of -20 V and -60 V. The channel conductivity rises by a factor of 1.65

$\times 10^4$  ( $V_D = -20$  V) and  $5.5 \times 10^4$  ( $V_D = -60$  V) as the gate voltage is being scanned from 0 V to -60 V. Moreover, the channel conductivity does not significantly change as the gate bias is being scanned reversely, from -60 V to 0 V. The device operates between depletion and accumulation for these gate voltages. No evidence for the formation of an inversion layer has been observed. Figure 6.1(b) shows a small hysteresis in the transfer characteristics as well. The origin of this effect could be attributed to charge trapping with gaseous oxygen and/or water vapors. By extrapolating the linear regime ( $V_D = -20$  V) in Figure 6.1(b) to  $V_G$  axis, the fitted threshold voltage is -9.8 V. A carrier mobility of  $1.7 \times 10^{-5}$  cm<sup>2</sup>/Vs is obtained from the slope of the linear regime. In the saturation regime ( $V_D = -60$  V), the mobility can be calculated from the slope of the plot of the square-root of the saturated drain current versus  $V_G$ . A fitted threshold voltage of -3 V and a carrier mobility of  $4.4 \times 10^{-5}$  cm<sup>2</sup>/Vs were obtained.

Figure 6.1(c) shows the output characteristics of a TAD FET measured in vacuum and at RT. The saturated drain current measured in vacuum was 52 % higher than the values measured in air. On the other hand, Figure 6.1(d) shows the variation of channel conductivity with gate bias, measured in vacuum, for a constant drain voltage of -20 V and -60 V. The channel conductivity rises by a factor of  $4 \times 10^4$  ( $V_D = -20$  V) and  $1.4 \times 10^5$  ( $V_D = -60$  V) as the gate voltage is being scanned from +2 V to -60 V. Moreover, the channel conductivity does not significantly change as the gate bias is being scanned from -60 V to +2 V. It also means that the channel conductivity is increased by a factor of 2.5 for both drain voltages ( $V_D = -20$  V and  $V_D = -60$  V) as the device is being measured in vacuum. Nevertheless, the hole mobility measured in vacuum and in air were in the same order of magnitude. The hole mobility was  $2.9 \times 10^{-5}$  cm<sup>2</sup>/Vs for linear regime operation and  $6.7 \times 10^{-5}$  cm<sup>2</sup>/Vs for saturation regime operation. The mobility values calculated from the saturation regime are larger than the corresponding values, calculated from the linear regime by factors of 2.3 and 3.3, for measurements performed under vacuum and in air, respectively. This is something routinely observed in experiments and is ascribed to the fact that oxygen may diffuse in the organic film and act as an acceptor [44,88]. The switch-on voltage  $V_{so}$ , i.e. an onset voltage at accumulation mode, was 0 V measured in air and +2 V measured in vacuum, as shown in Figure 6.1(b) and 6.1(d), respectively. The fitted threshold voltage  $V_T$  was -9 V extracted in the linear regime and -1.4 V extracted in the saturation regime. (To the best of my knowledge, there is no result of the hole mobility of charge carriers in TAD thin films from another group)

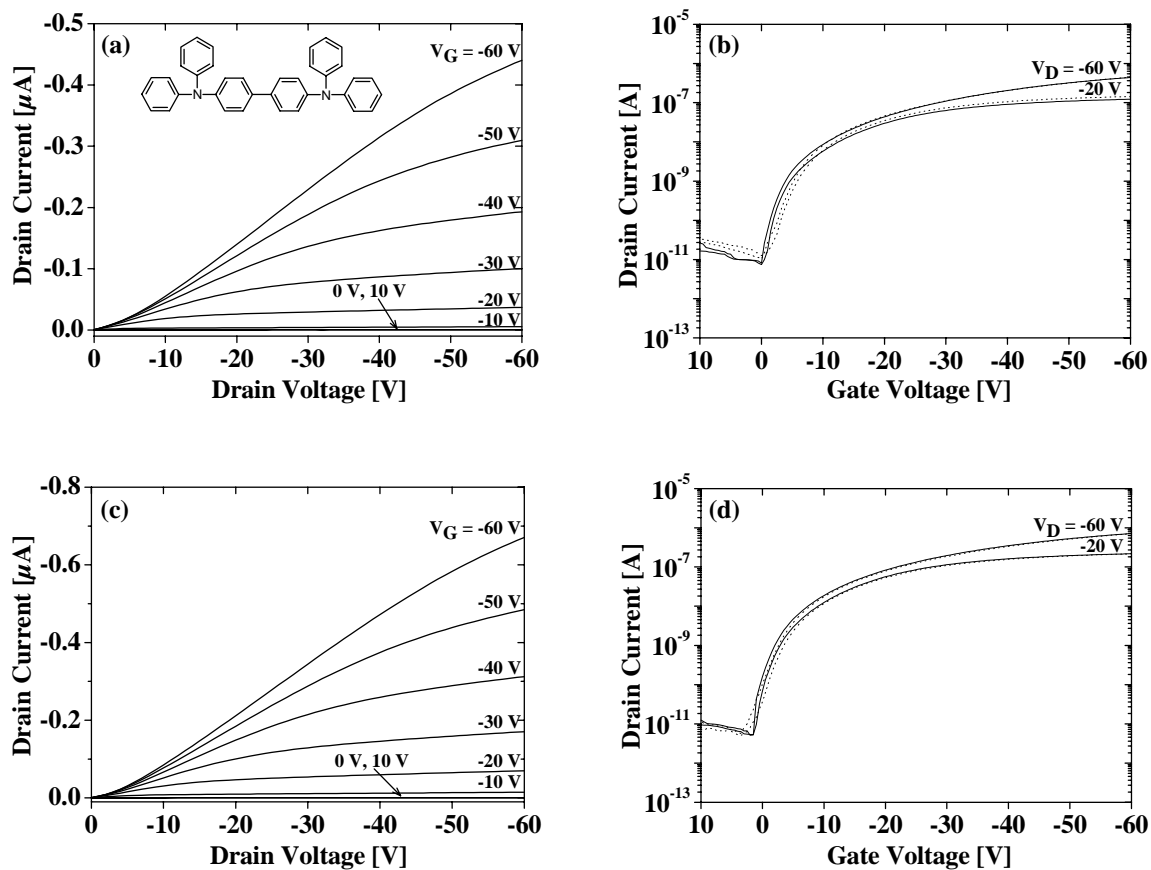
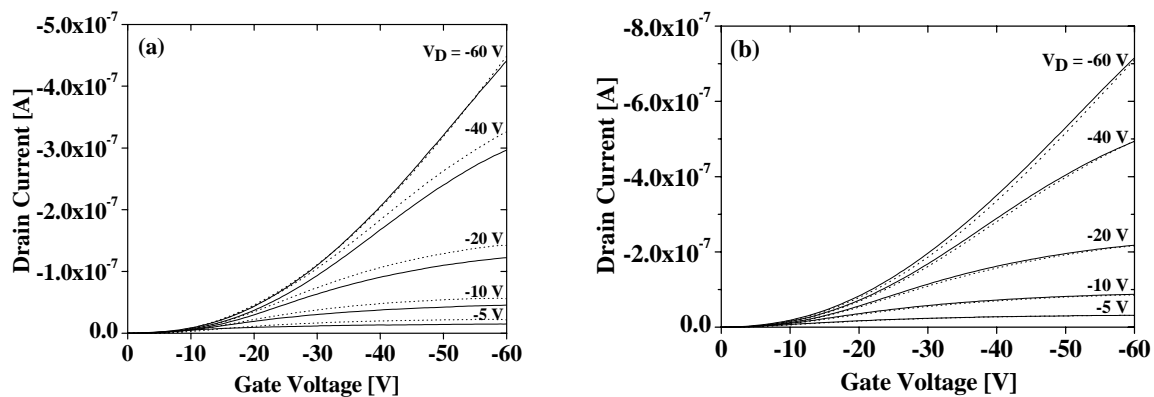


Figure 6.1. Output and transfer characteristics of a TAD FET,  $W = 2 \text{ mm}$ ,  $L = 5 \mu\text{m}$ ,  $C_i = 17.3 \text{ nF/cm}^2$ . (a). Output characteristics measured in air. The inset depicts the chemical structure of TAD. (b). Transfer characteristics measured in air, (c). Output characteristics measured in vacuum and (d). Transfer characteristics measured in vacuum.



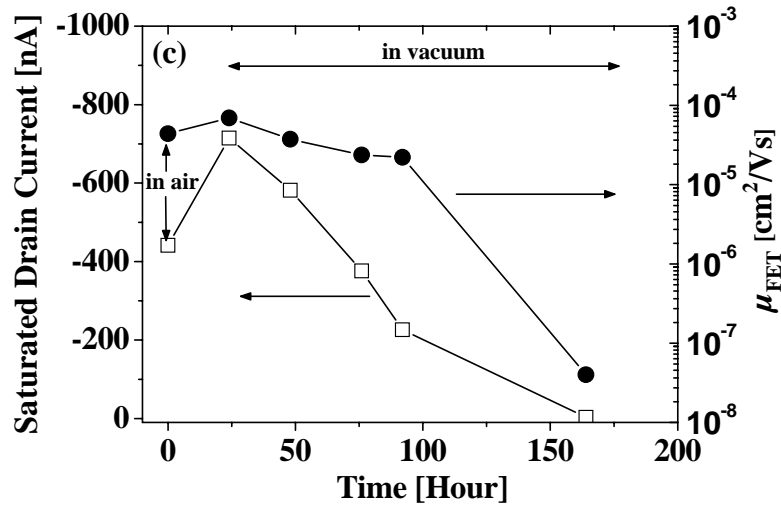


Figure 6.2. Hysteresis characteristics of a TAD FET ( $W = 2 \text{ mm}$ ,  $L = 5 \text{ }\mu\text{m}$ ,  $C_i = 17.3 \text{ nF/cm}^2$ ) measured at RT and in air (a) and in vacuum (b). (c). Drain current of a TAD FET measured in air and in continuously evacuated chamber. The saturated drain current was measured at  $V_D = V_G = -60 \text{ V}$ . The saturated drain current is plotted linearly versus time (left side) and the field-effect mobility is plotted semi-logarithmically versus time (right side).

Figure 6.2(a) and 6.2(b) shows the hysteresis of the transfer characteristics observed in a TAD FET. Moreover, the hysteresis depends on the environment, in which the measurement was taken. The measurements performed in vacuum revealed less hysteresis in the transfer characteristics than those performed in air. Furthermore, the hysteresis was strongly present at low drain biases for measurements performed in air. Therefore, the hysteresis effect can be attributed to the charge trapping effect or gaseous oxygen and water vapor effects. In contrast, the hysteresis measured in vacuum did not significantly show a dependency on the drain bias. This indicates that the environment plays an important role on the device characteristics. Figure 6.2(c) shows the time dependency of the saturated drain current (at  $V_D = V_G = -60 \text{ V}$ ) and field-effect mobility of charge carriers. Initially, the saturated drain current increased substantially, as the device was stored for 24 hours in a continuously evacuated chamber. However, the saturated drain current decreased by 47 % after the chamber was continuously evacuated for 75 hours. Finally, the saturated drain current was nearly zero after the device was stored in vacuum for more than 150 hours and no transistor effect could be observed. This implies that device aging took place even if the sample was placed or stored in a dynamic vacuum. The AFM and optical microscopy images of TAD thin films on various substrates supported this result that TAD thin films crystallized easily after the samples were stored in ambient atmosphere and at RT for a few days, as reported previously in chapter 5.



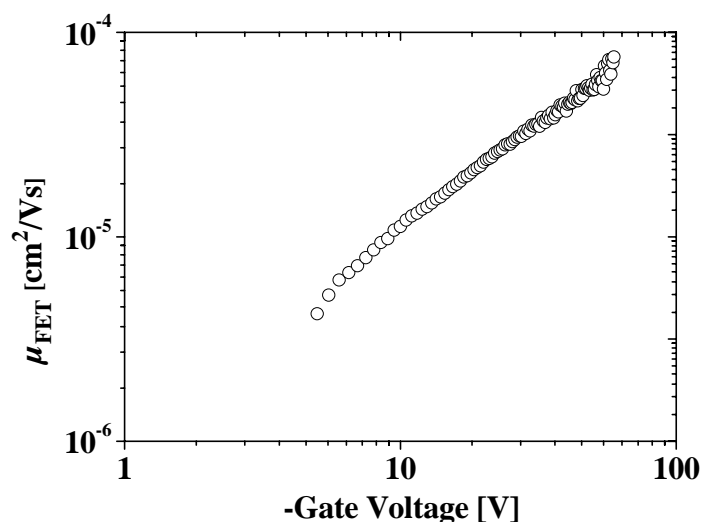


Figure 6.3. Variation of the hole mobility of a TAD film as a function of gate bias. Data were recorded at 294 K and measured in vacuum.

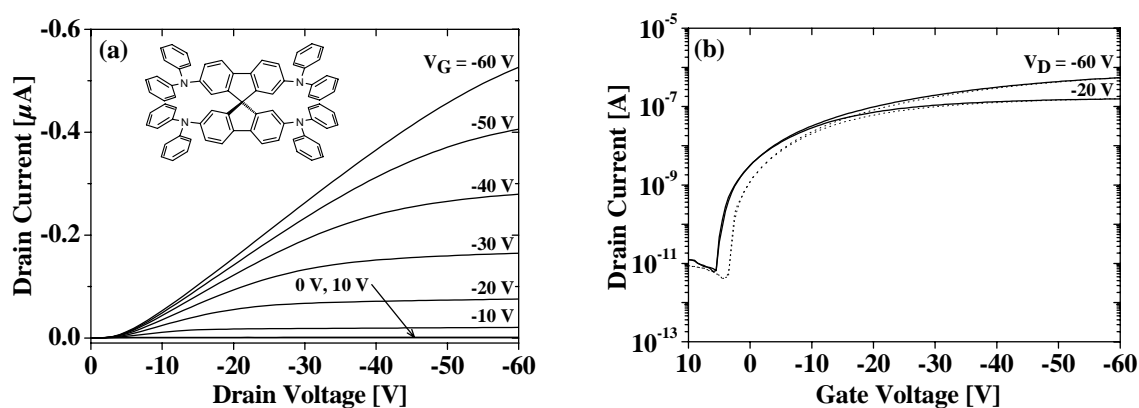
Figure 6.3 shows the variation with gate bias of the field-effect mobility for TAD FETs. The mobilities are obtained by utilizing equation 2.14. The mobility increases from very low values ( $4.2 \times 10^{-6} \text{ cm}^2/\text{Vs}$  at  $-5 \text{ V}$ ) to  $7.6 \times 10^{-5} \text{ cm}^2/\text{Vs}$  at  $-60 \text{ V}$ . The most striking feature revealed by Figure 6.3 is a quasi-linear gate bias dependence of the field-effect mobility. The mobility clearly exhibits strong gate bias dependence. The apparent gate-voltage dependence would in fact be due to the charge concentration, which is mainly confined in the first 5 nm of semiconductor layer away from the insulator/semiconductor interface.

## 6.2. 2,2',7,7'-Tetrakis-(diphenylamino)-9,9'-spirobifluorene (Spiro-TAD)

2,2',7,7'-Tetrakis-(diphenylamino)-9,9'-spirobifluorene or Spiro-TAD is the corresponding spiro-compound of *N,N,N',N'*-Tetraphenylbenzidine (TAD). Figure 6.4(a) shows a typical set of drain current against source-drain voltage curves for different source-gate voltages, measured on a device with a channel length of  $10 \mu\text{m}$  and a channel width of  $4 \text{ mm}$ . The measurement was carried out in air and at RT. Although a clear saturation of the drain current is observed when the drain voltage exceeds the gate voltage, the onset of the curves is far from being linear. At low drain biases, the currents deviate from the expected linear relationship which can be attributed to the non-ohmic contacts between the organic materials

and the gold electrodes. Figure 6.4(b) also shows the transfer characteristics of a typical Spiro-TAD FET measured in air. Spiro-TAD is a *p*-type semiconductor and the device operates in the accumulation mode. A small reverse gate bias of 4 – 6 V is sufficient to turn the channel *OFF* or *ON*. In enhancement mode operation, i.e., between  $V_G = 0$  V and  $V_G = -60$  V, the *ON/OFF* ratio is typically 46 for  $V_D = -20$  V and 140 for  $V_D = -60$  V. However, since the turn-*OFF* voltage is small compared to practical supply voltages the full *ON/OFF* ratio between accumulation and depletion mode can be exploited. *ON/OFF* ratios of typically  $2.4 \times 10^4$  for  $V_D = -20$  V and  $6.6 \times 10^4$  for  $V_D = -60$  V can be obtained when  $V_G$  is being scanned from +6 V to -60 V. The field-effect mobility of charge carriers in Spiro-TAD thin films is  $3.3 \times 10^{-5}$  cm<sup>2</sup>/Vs extracted in the linear regime and  $5.7 \times 10^{-5}$  cm<sup>2</sup>/Vs extracted in the saturation regime. The fitted threshold voltage and the switch-on voltage were +1 V extracted in the saturation regime and +4 V.

Figure 6.4(c) and 6.4(d) show the output and transfer characteristics for the same device measured in vacuum and at RT. The field-effect mobilities of charge carriers in Spiro-TAD thin films were  $4.0 \times 10^{-5}$  cm<sup>2</sup>/Vs for linear regime operation and  $7 \times 10^{-5}$  cm<sup>2</sup>/Vs for saturation regime operation. The fitted threshold voltage and the switch-on voltage were +1.4 V and 0 V, respectively. An *ON/OFF* ratio of  $1.6 \times 10^5$  can be obtained at a drain bias of -20 V and the gate bias is being scanned from 0 V to -60 V. The measurements carried out in air and in vacuum gave the mobility values calculated from the saturation regime of approximately a factor of 1.8 larger than those calculated from the linear regime. In addition, the mobility values measured in a vacuum are approximately a factor of 1.2 larger than those measured in air. This indicates that Spiro-TAD FETs are stable under operation in ambient atmosphere.



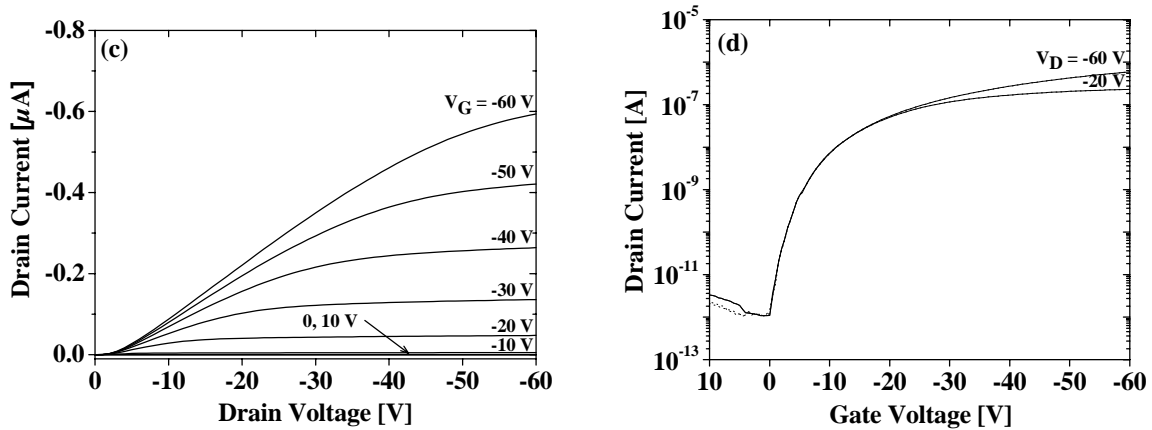
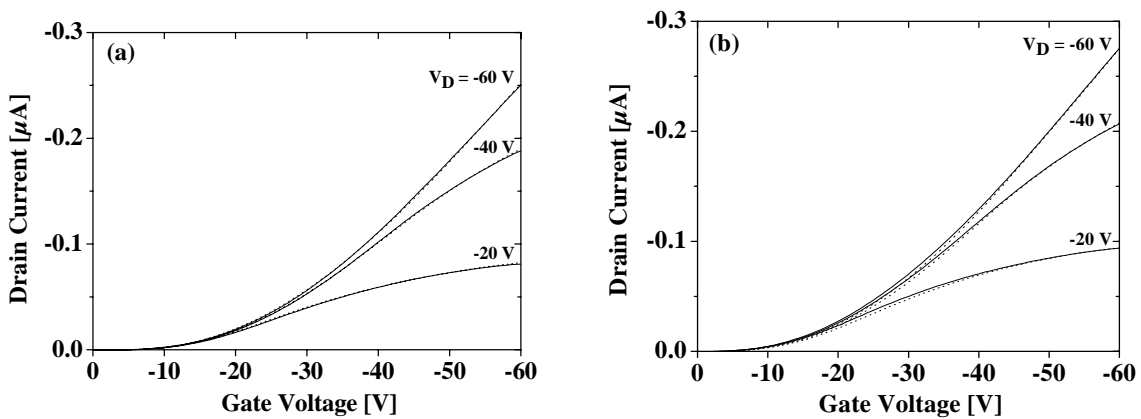


Figure 6.4. Output and transfer characteristics of a Spiro-TAD FET,  $W = 4 \text{ mm}$ ,  $L = 10 \text{ }\mu\text{m}$ ,  $C_i = 19.9 \text{ nF/cm}^2$ . (a). Output characteristics measured in air. The inset depicts the chemical structure of Spiro-TAD, (b). Transfer characteristics measured in air, (c). Output characteristics measured in vacuum and (d). Transfer characteristics measured in vacuum. All measurements were performed after thermal evaporation of Spiro-TAD.

In sub-chapter 6.1 the field-effect mobility of charge carriers in TAD thin films has been described. The measurements performed in air and at RT showed that the mobilities of holes in Spiro-TAD FETs are approximately a factor of 2 (for linear regime operation) and 1.3 (for saturation regime operation) larger than those in TAD FETs. In addition, the mobilities of holes in Spiro-TAD FETs measured in vacuum are approximately a factor of 1.3 (for linear regime operation) and 1.04 (for saturation regime operation) larger than those in TAD FETs. The mobilities obtained in the saturation regime in TAD FETs are the same as the values in Spiro-TAD FETs for measurements having been performed in vacuum. However, the mobilities of holes are different by a factor of 1 – 2 between TAD and Spiro-TAD being measured in air.



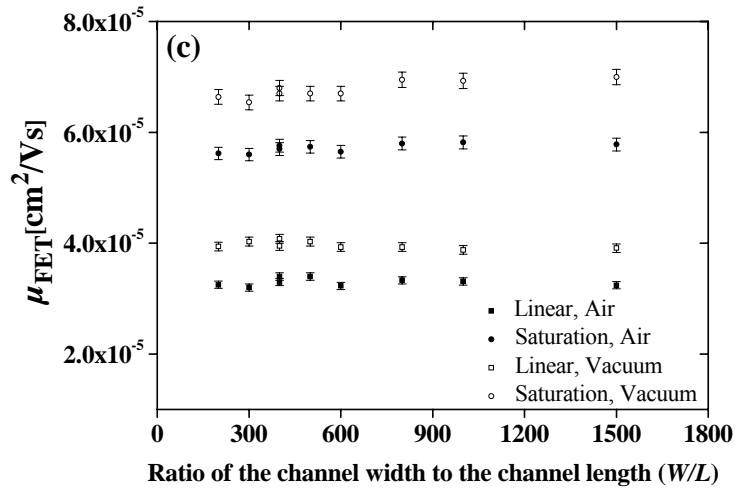


Figure 6.5. Hysteresis characteristics of a Spiro-TAD FET ( $W = 2 \text{ mm}$ ,  $L = 10 \text{ }\mu\text{m}$ ,  $C_i = 19.9 \text{ nF/cm}^2$ ) measured at RT and in air (a) and in vacuum (b). (c). The field-effect mobility of charge carriers in Spiro-TAD thin films at different ratios of the channel width to the channel length ( $W/L$ ).

Figure 6.5(a) and 6.5(b) show the transfer characteristics of a Spiro-TAD FET measured in air and in vacuum at different gate biases. Both measurements performed in vacuum and in air exhibited no hysteresis in the transfer characteristics on the time scale of dc measurements. This indicates that Spiro-TAD thin films were stable in air. The measurement performed in vacuum gives only 10% difference in drain current with respect to the measurement performed in air. The mobility of charge carriers in many devices were found to be independent of the geometry of the devices (the ratios of the channel width to the channel length), as shown in Figure 6.5(c). The hole mobility in Spiro-TAD thin films was also measured by means of time of flight (TOF) techniques by other groups. Bach *et. al* reported that a hole mobility of  $3 \times 10^{-4} \text{ cm}^2/\text{Vs}$  at an electric field of  $1.6 \times 10^5 \text{ V/cm}$  was obtained [73]. They also observed that the transient photocurrent exhibits a pronounced plateau, which is followed by a longer tail indicating non-dispersive transport in Spiro-TAD. The charge transport is then called *non-dispersive* if the photocurrent stays constant while the carriers drift across the device. On the other hand, the charge transport is called *dispersive*, if no constant photocurrent plateau is observed and the current drops monotonically. Another Spiro-compound was also characterized by TOF techniques, namely 2,2',7,7'-tetrakis-(*N,N*-di-4-methoxyphenylamino)-9,9'-spirobifluorene (Spiro-MeOTAD). The hole mobility in this material is  $1.5 \times 10^{-4} \text{ cm}^2/\text{Vs}$  at an electric field of  $2.4 \times 10^5 \text{ V/cm}$  and  $1 \times 10^{-4} \text{ cm}^2/\text{Vs}$  at an electric field of  $1.2 \times 10^5 \text{ V/cm}$  (the thickness of thin films for both conditions was  $1 \text{ }\mu\text{m}$ ) [89].

Below threshold voltages or switch-on voltages, i.e. for higher positive gate biases an *OFF* current as low as 1 pA was measured in all device geometries. Two pathways are possible for the measured *OFF* current: through the channel due to the intrinsic conductivity of the materials and via the insulating layer and the gate electrode. In order to obtain information about the influence of gate leakage on the *OFF* current, gate leakage measurements were performed and it was found that the gate leakage current was lower than the drain current for devices in operation. For details, please take a look at chapter 4, especially in Figure 4.7. The independence of the *OFF* current on geometry parameters such as channel width  $W$  indicates that this value is close to the accuracy limit of the measurement setup. Thus, the determined *ON/OFF* ratios can be regarded as lower limits. The *ON/OFF* ratio at  $V_D = -5$  V was  $2 \times 10^4$ . At  $V_D = -60$  V, the unsaturated *ON/OFF* ratio was  $5 \times 10^5$  for Spiro-TAD. The dependence of the measured *ON/OFF* ratios on the device geometry was also investigated. Since the measured *OFF* current was independent on the device parameters, and the *ON* current is proportional to the ratio  $W/L$  according to equation 2.11, the highest *ON/OFF* values have been obtained for large channel widths and small channel lengths. The highest *ON/OFF* ratios with values of  $1.5 \times 10^6$  was measured for device with  $W = 5$  mm,  $L = 5$   $\mu$ m, and at  $V_D = -60$  V.

In order to investigate the influence of gaseous oxygen and moisture, the sample was stored in ambient atmosphere and at RT for 9 months. After that, the transistor characteristics were measured again. The results are shown in Figure 6.6. The saturated drain current measured in air decreased by 23 % with respect to a fresh device. The drain current measured in vacuum decreased only by 9 %. Nevertheless, the hole mobility measured in vacuum decreased typically 12 % for linear regime operation and 2 % for saturation regime operation (22 °C, a relative humidity of 24 %). In contrast, the hole mobility measured in air decreased typically 52 % for linear regime operation and 28 % for saturation regime operation. The field-effect mobility change was clearly obtained for linear regime operation and under an ambient atmosphere. The origin of this result can be attributed to gaseous oxygen acting as a trap, as the sample is being stored in ambient atmosphere and at RT for 9 months. In addition, the fitted threshold voltage measured in vacuum also shifted from +1.4 V for a fresh device to -5 V after 9 months. It means that more charges were needed to turn on the transistor after the sample has been stored in air and at RT for 9 months. This is in contrast with the result obtained for TAD thin films. The saturated drain current of a TAD FET decreased by 47 % as the sample is being stored in a continuously evacuated chamber for 75 hours. Finally, the saturated drain current was nearly zero after the device was stored in vacuum for more than

150 hours and no transistor effect could be observed. As a result, a Spiro-TAD FET is more stable under operation in air than a TAD FET. The stability of Spiro-TAD FET is in contrast with organic transistors based on the small molecule pentacene. OFET based on pentacene showed a decrease in mobility of typically 30 % after the sample has been stored for 3 months at 25 °C and a relative humidity of 50 % [9].

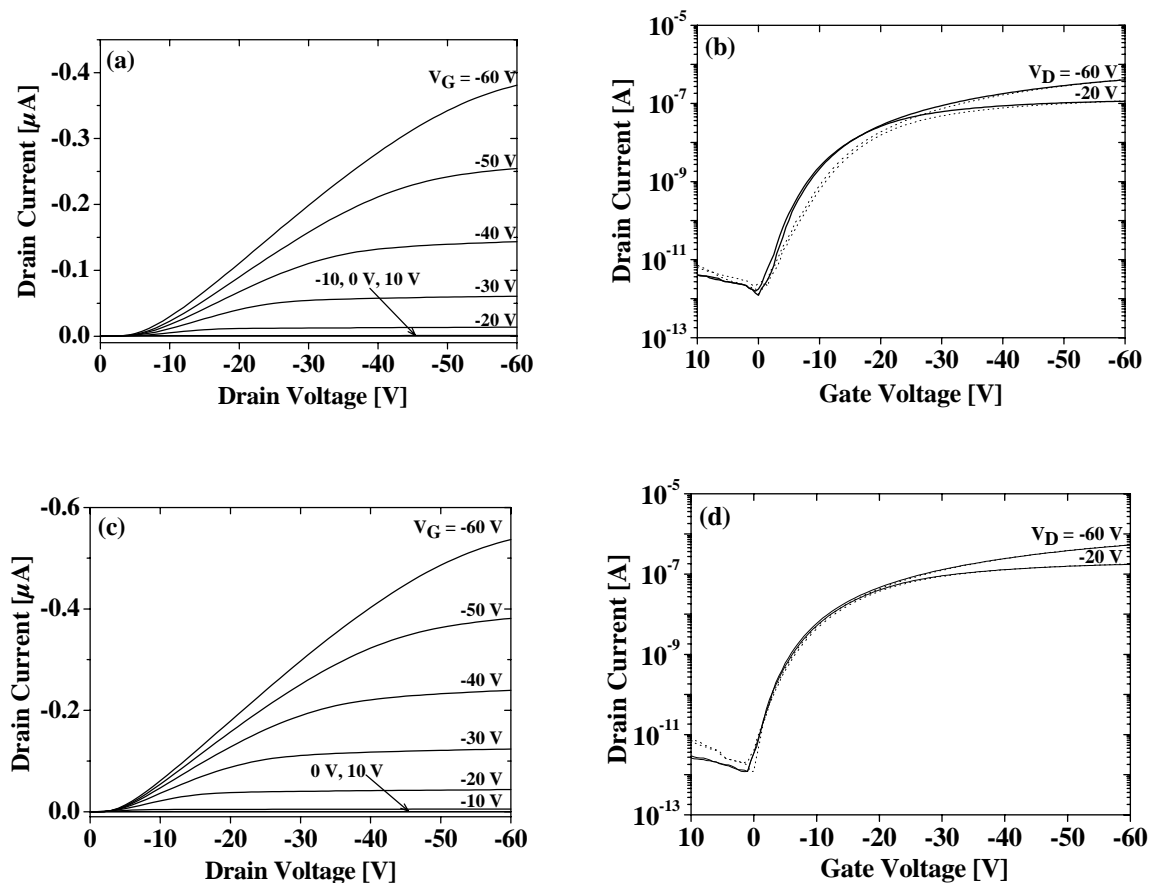


Figure 6.6. Output and transfer characteristics of a Spiro-TAD FET, which was measured after the sample was stored in ambient atmosphere and at RT for 9 months,  $W = 4$  nm,  $L = 10$   $\mu\text{m}$ ,  $C_i = 19.9$  nF/cm<sup>2</sup>. (a). Output characteristics measured in air, (b). Transfer characteristics measured in air, (c). Output characteristics measured in vacuum, and (d). Transfer characteristics measured in vacuum.

Figure 6.7 shows the variation of the field-effect mobility of Spiro-TAD as a function of gate voltage. The variation of the mobility with gate bias is practically linear at a gate bias lower than -50 V. At a gate bias higher than -50 V, the mobility is super-linearly dependent on the gate bias. The origin of this behavior is not fully understood. Moreover, the hole mobility of a TAD and a Spiro-TAD thin film as a function of gate bias are also plotted in the inset of the Figure 6.7. At gate biases lower than -10 V, the hole mobility in a TAD thin film

is smaller than that in a Spiro-TAD thin film. However, in the range of -10 V and -60V the hole mobility of both materials seem to be the same.

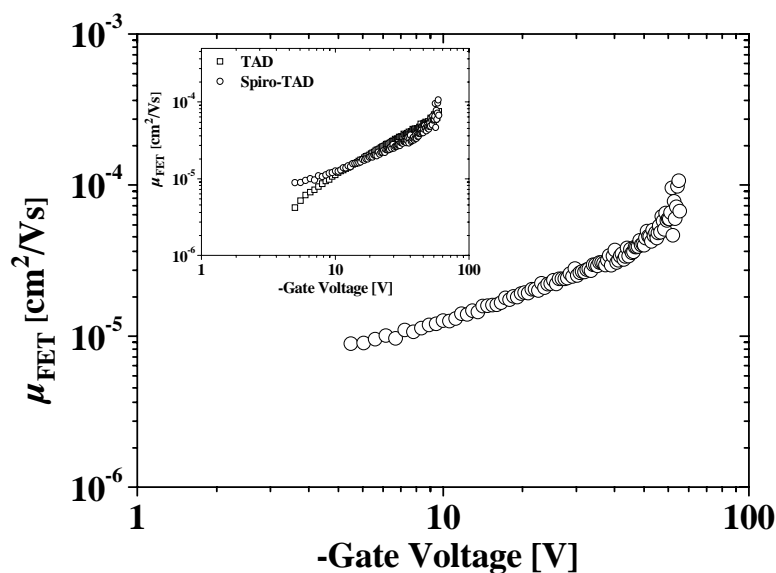


Figure 6.7. Variation of the hole mobility of a Spiro-TAD thin film as a function of gate bias at 294 K. The inset shows gate-voltage dependent mobility of TAD (from Figure 6.3) and Spiro-TAD based-field-effect transistors measured at 294 K.

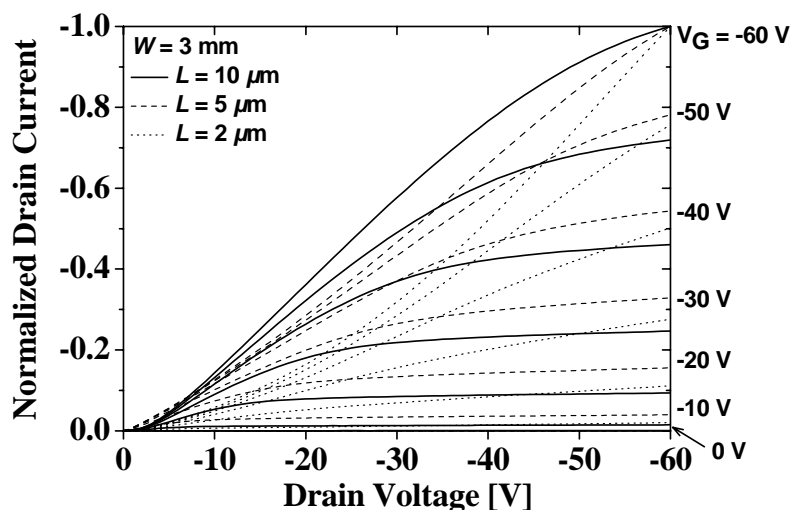


Figure 6.8. The normalized drain current against drain voltage of Spiro-TAD with different channel lengths ( $L = 2 \mu\text{m}$ ,  $5 \mu\text{m}$ ,  $10 \mu\text{m}$ ), while channel width is constant ( $W = 3 \text{ mm}$ ).

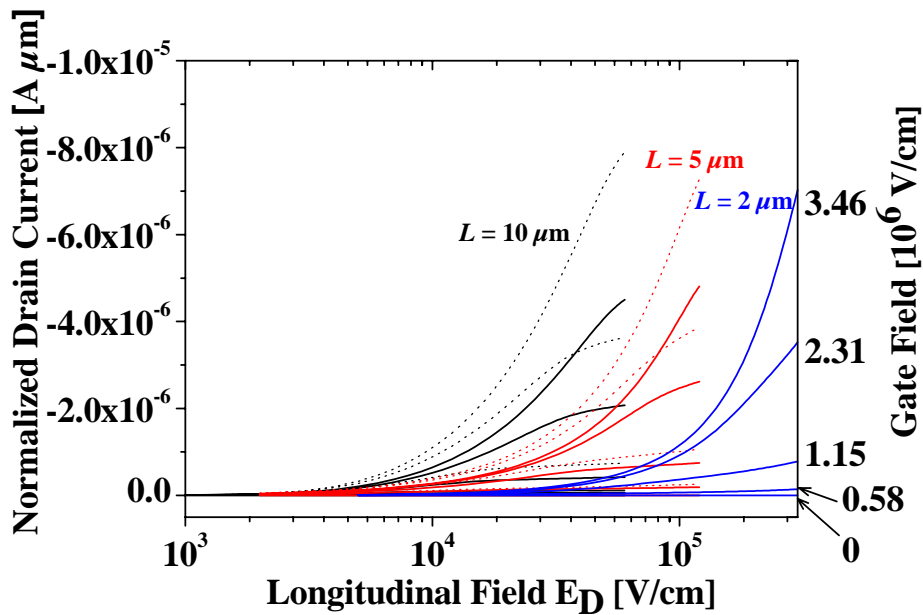


Figure 6.9. Families of normalized drain currents for  $L = 2 \mu\text{m}$ ,  $5 \mu\text{m}$ ,  $10 \mu\text{m}$  at different gate fields as a function of longitudinal field ( $E_D = V_D/L$ ).  $V_D$  ranges for all transistors, from 0 V to -60 V. Solid lines is for channel width 3 mm and dotted lines is for channel width 5 mm.

Figure 6.8 shows the normalized drain current with different channel length (a channel width of 3 mm) against drain bias. At low drain biases, a nonlinear behavior of the drain current was observed. As expected, the behavior of drain current is severely limited by the two dimensional electric field in the active channel. This effect is the so-called short channel effect and shows a sharp increase with increasing drain bias. Short channel conditions are present when the channel length  $L$  is comparable to the sum of the source and drain depletion layer widths [20]. When this happens the potential distribution in the channel region, as well as the electric field becomes two dimensional and the gradual channel approximation ( $E_y \gg E_x$ ) is no longer valid (see Figure 2.1 for details). In Figure 6.9, a family of the drain current for the transistor with different channel lengths at different gate fields is presented as a function of the longitudinal electric fields ( $E_D = V_D/L$ ). The value of drain bias ranges for all transistors, from 0 to -60 V. The drain currents plotted in Figure 6.9 have been normalized by multiplying each of them by the corresponding channel length. The drain currents are ideally identical when the gate field is the same. But this is not the case. Take a look at devices with channel width 3 mm (solid lines) in Figure 6.9. The drain currents increase when the channel length decreases. This effect, which is most evident when  $E_D > 10^5 \text{ V/cm}$ , indicates that at a high electric field an increase of mobility possibly occurs. The short channel effect was also reported for  $\alpha$ -hexathienylene thin film transistors [90]. However, the hole mobilities in



devices with short channel length are still in the same order of magnitude with those with long channel length.

### 6.3. *N-N'*-Bis(3-methylphenyl)-(1,1'-biphenyl)-4,4'-diamine (TPD)

The output and transfer characteristics of a TPD FET measured in air and at RT are shown in Figure 6.10(a) and 6.10(b). A clear saturation of drain current is observed when the drain voltage exceeds the gate voltage; however, the onset of the curves is far from being linear. The drain current at a gate bias of -60 V and drain bias of -60 V was 0.82  $\mu\text{A}$ . Furthermore, Figure 6.10(b) shows the variation of channel conductivity with varying gate bias. The channel conductivity rises by a factor of  $1.7 \times 10^3$  ( $V_D = -20$  V) and  $7 \times 10^3$  ( $V_D = -60$  V) as the gate voltage is being scanned from 0 V to -60 V. The switch-on voltage was between 0 V and -2 V. On the other hand, the fitted threshold voltage extracted in the saturation regime was +2.1 V. The hole mobility extracted in the linear regime was  $5.6 \times 10^{-5}$   $\text{cm}^2/\text{Vs}$ . In addition, the hole mobility measured in the saturation regime was  $7.4 \times 10^{-5}$   $\text{cm}^2/\text{Vs}$ , which is higher than the values measured in the linear regime

Figure 6.10(c) and 6.10(d) show the output and transfer characteristics of a TPD FET measured under a vacuum and at RT. The saturated drain current (at  $V_D = V_G = -60$  V) of TPD-based FETs measured in vacuum was only 2.4 % higher than the values measured in air. In contrast, the saturated drain current in a TAD FET measured in vacuum was 52 % higher than the values measured in air. This result indicates that TPD thin films are more stable under operation in air than TAD thin films. The hole mobility extracted in the linear regime was  $6.3 \times 10^{-5}$   $\text{cm}^2/\text{Vs}$ . On the other hand, the hole mobility in the saturation regime was  $8.5 \times 10^{-5}$   $\text{cm}^2/\text{Vs}$ . The mobility of holes in a TPD film is higher than those in TAD and Spiro-TAD films. Figure 6.10(d) shows the variation of channel conductivity with varying gate bias as the device is being measured in vacuum. The channel conductivity measured in vacuum rises by a factor of  $3.7 \times 10^3$  ( $V_D = -20$  V) and  $1.5 \times 10^4$  ( $V_D = -60$  V) as the gate voltage is being swept from 0 V to -60 V. The fitted threshold voltage extracted in the saturation regime was +2.0 V.

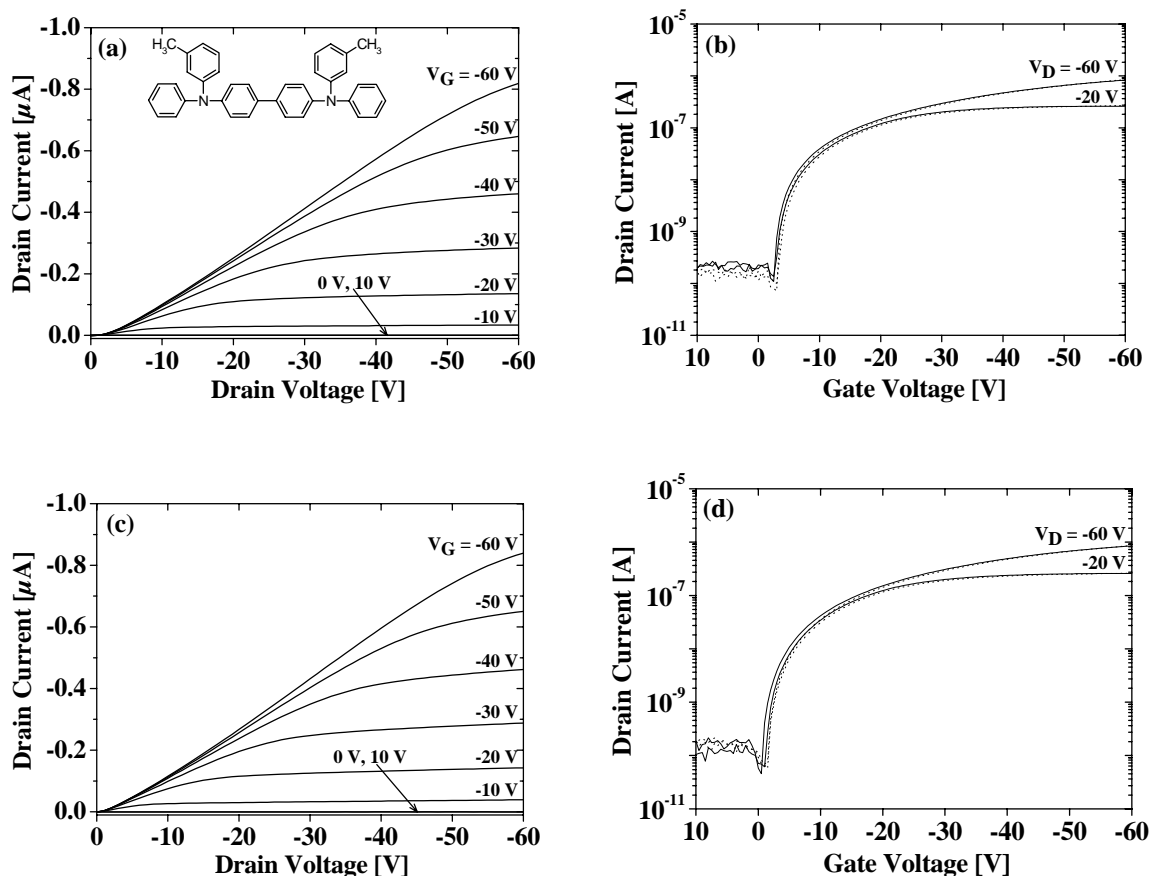


Figure 6.10. Output and transfer characteristics of a TPD FET,  $W = 4 \text{ mm}$ ,  $L = 10 \text{ }\mu\text{m}$ ,  $C_i = 19.9 \text{ nF/cm}^2$ . (a). Output characteristics measured in air. The inset depicts the chemical structure of TPD, (b). Transfer characteristics measured in air, (c). Output characteristics measured in vacuum, and (d). Transfer characteristics measured in vacuum.

Table 6.1. Hole mobilities in TPD thin films extracted from TOF and FET measurements.

Device and Material	Field-effect mobility $\mu$ [ $\text{cm}^2/\text{Vs}$ ]	Reference
TOF TPD	$1 \times 10^{-3}$	87
TOF TPD	$1 \times 10^{-3}$	91
TOF TPD	$(2 - 3) \times 10^{-3}$	92
FET TPD	$8.5 \times 10^{-5}$	This work

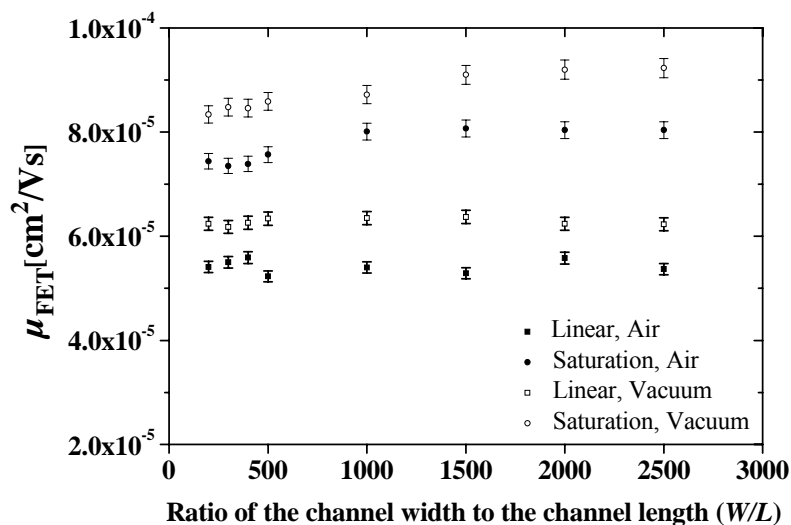


Figure 6.11. The field-effect mobility of charge carriers in TPD thin films at different ratios of the channel width to the channel length ( $W/L$ ).

Figure 6.11 shows the dependency of field-effect mobilities of charge carriers on the geometry of FETs, i.e. the ratio of the channel width ( $W$ ) to the channel length ( $L$ ). The hole mobility measured in vacuum is slightly higher than the values measured in air. Moreover, the hole mobility does not depend significantly on the geometry of FETs. The hole mobility of devices with  $W/L$  smaller than 500 were slightly lower than those in devices with  $W/L$  higher than 1000. As a result, the hole mobilities in TPD thin films measured in air and in vacuum were in the range of  $(7 - 9) \times 10^{-5} \text{ cm}^2/\text{Vs}$ . Determining hole mobility in TPD thin films was also reported by means of TOF techniques. It was found that the hole mobility in TPD thin films was in the range of  $(2 - 3) \times 10^{-3} \text{ cm}^2/\text{Vs}$  at an electric field of  $3 \times 10^5 \text{ V/cm}$  [87,91,92]. The discrepancies in both methods possibly originate from the strong dependence of the hole mobility on the charge carriers density in organic semiconductors [93]. Various methods have been used to characterize the hole mobility in TPD thin films as displayed in Table 6.1. The mobility obtained from TOF measurement was higher than the values obtained from FET measurement. The origin of this result is not fully understood yet.

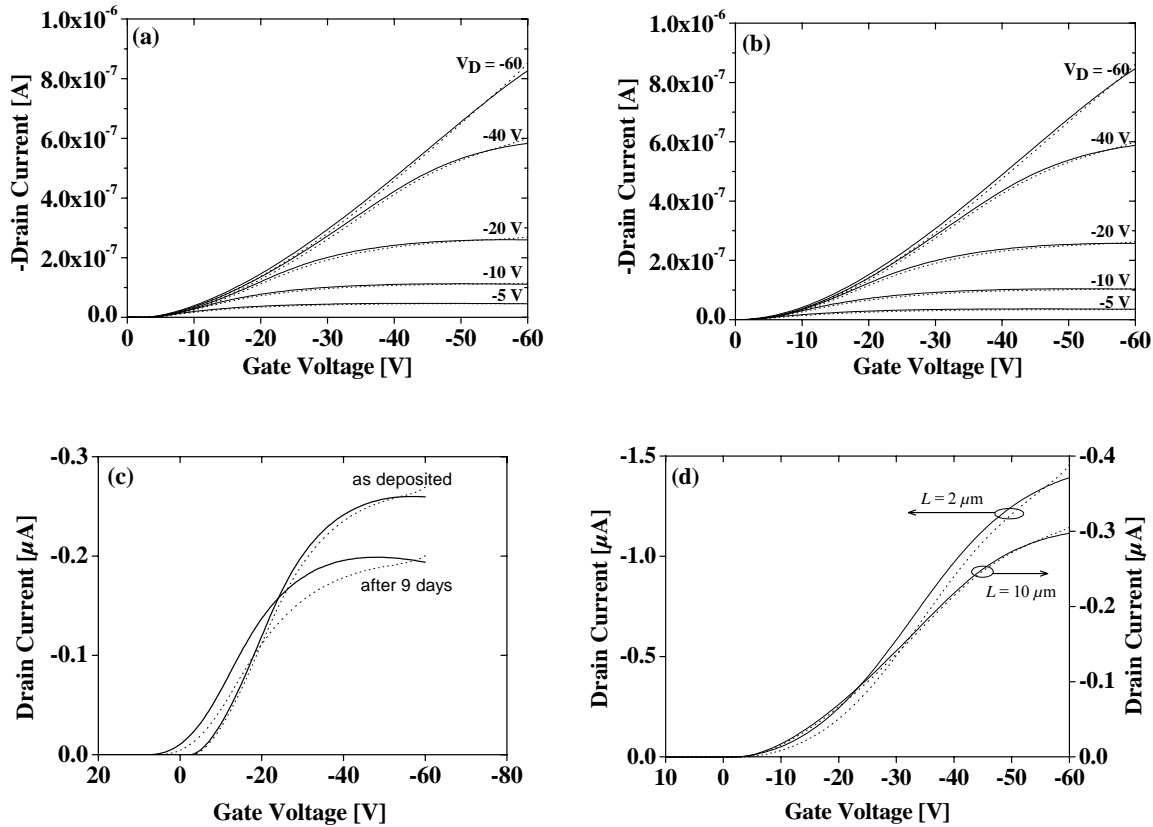


Figure 6.12. Transfer characteristics of a TPD FET ( $L = 10 \mu\text{m}$ ,  $W = 4 \text{ mm}$ ,  $C_i = 19.9 \text{ nF/cm}^2$ ) measured in air (a) and in vacuum (b). (c). Transfer characteristics ( $V_D = -20 \text{ V}$ ) of the FET measured in air for fresh sample and after the sample was stored in ambient atmosphere, in the dark and at RT for 9 days. (d). Hysteresis of the transfer characteristics (at  $V_D = -40 \text{ V}$ ) for devices with different channel lengths ( $L = 2 \mu\text{m}$  and  $10 \mu\text{m}$ ), while the channel width  $W$  was constant ( $W = 2 \text{ mm}$ ). The solid lines denote the advancing curve and the dotted lines denote the receding curve.

Figure 6.12(a) and 6.12(b) show the transfer characteristic of a FET measured first in air and then under a vacuum of  $10^{-3}$  mbar. The transfer characteristic was measured twice. First, the gate bias was swept from an *OFF* state to *ON* state, the advancing curve. Second, the gate bias was swept from an *ON* state to *OFF* state, the receding curve. The measurements performed in air and in vacuum do not give any difference in amount of the hysteresis. Moreover, the hysteresis is not totally absent under vacuum. The hysteresis seems to be present in both conditions. A large amount of the hysteresis is observed after the sample was stored in ambient atmosphere for nine days, as shown in Figure 6.12(c). The hysteresis was also clearly observed in the device with short channel length, for instance the channel length  $L$  of  $2 \mu\text{m}$  as shown in Figure 6.12(d). Therefore, the channel length affects the hysteresis and it is more pronounced for devices with short channel length. Generally, the hysteresis effect in organic FETs could be ascribed to a doping/de-doping with gaseous oxygen [94]. Similar

results are also reported for pentacene and poly(thienylene vinylene)-based FETs [27]. Moreover, the hysteresis effects were also observed on carbon nanotube FETs [95] and FETs comprising semiconducting platinum-based chain structures [96].

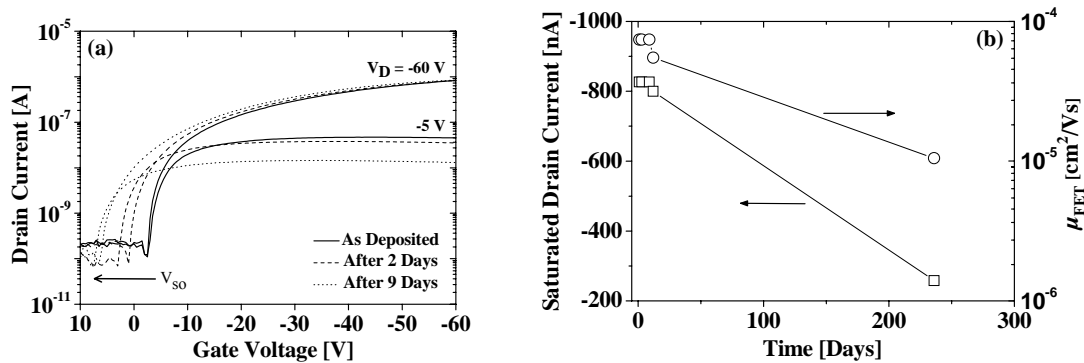


Figure 6.13. Time dependent measurement of a TPD FET. (a). Transfer characteristics of a TPD FET measured in air. The switch-on voltage shifts toward more positive gate bias with increasing time. (b). Saturated drain current (at  $V_D = V_G = -60$  V) is plotted linearly against time (left side) and field-effect mobility is plotted semi-logarithmically against time (right side).

Figure 6.13(a) supports previous results, in which the transfer characteristics were measured after the sample was stored in ambient atmosphere for 2 days and 9 days. The switch-on voltage after 9 days shifts toward more positive gate bias with respect to the initial curve. However, at a drain bias of  $-60$  V and a gate bias of  $-60$  V, the drain current has remained constant after the sample was stored in air and at RT for 9 days. On the contrary, at a drain bias of  $-60$  V and a gate bias of  $-20$  V the drain current is significantly decreased as the sample was stored in ambient atmosphere for 9 days. A deterioration of the material was clearly observed for a measurement performed at a drain bias of  $-5$  V. In this case, the drain current at a gate bias of  $-60$  V significantly decreased after 9 days. Figure 6.13(b) shows that the drain current significantly decreased after the sample was stored in air for more than 10 days. Moreover, the hole mobility in TPD thin films decreased by a factor of eight after the samples were stored in air and at RT for 7 months. It was also found that an aging of the devices characteristics was accompanied by changes in the surface morphology of the corresponding thin films. Moreover, the investigating issue of device stability in the presence of gaseous oxygen and moisture became a primary intention. For examples, it was found that the field-effect mobility in pentacene FETs decreased by 30% after the sample was stored in ambient atmosphere for 500 hours. The adsorption of water molecules on the pentacene layer was the main reason for the degradation [97]. Water molecules caused not only a decrease in

device parameters such as mobility, and *ON/OFF* ratio, but also a hysteresis in the electrical characteristics.

Figure 6.14 shows the variation of the field-effect mobility in a TPD thin film as a function of gate bias. The charge carrier mobilities linearly depend on the gate bias. However, it becomes a super-linear dependency as the gate bias increases ( $V_G < -50$  V). Moreover, the mobility clearly depends on the gate bias. For instance, the mobility was around  $5 \times 10^{-6}$  cm<sup>2</sup>/Vs at a gate bias of -5 V and increased to  $10^{-3}$  cm<sup>2</sup>/Vs at a gate bias of -60 V. This is in contrast with the gate bias dependence of the field-effect mobility in a TAD FET. A mobility of  $4.2 \times 10^{-6}$  cm<sup>2</sup>/Vs was obtained at gate bias -5 V, which is the same as the values for TPD FET. However, a mobility of  $7.6 \times 10^{-5}$  cm<sup>2</sup>/Vs was obtained at a gate bias of -60 V, which is much lower than that obtained for TPD FET. This result implies that the mobility of holes in TPD strongly depends on the gate bias with respect to TAD.

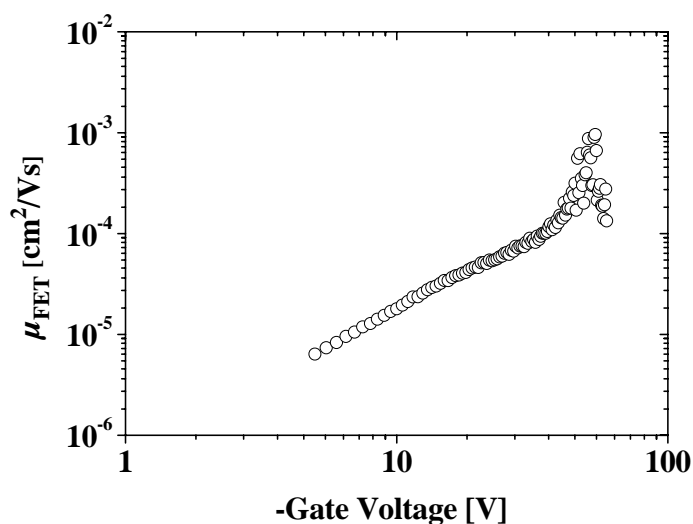
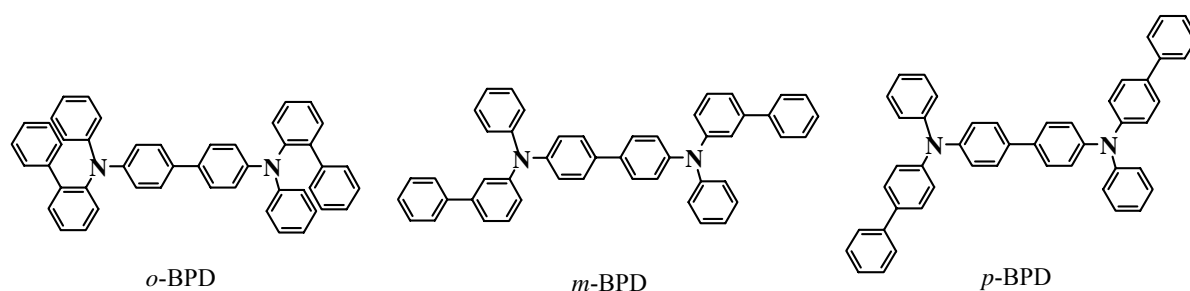


Figure 6.14. Variation of the hole mobility of a TPD film as a function of gate bias. Data were recorded at 294 K and measured in vacuum.

Shirota *et.al* also presented a similar molecule as TPD, but the phenyl chain is connected with another phenyl chain on a different position, namely in *ortho*, *para*, and *meta* positions [98]. The chemical structure of the corresponding material is displayed in the next page. They are *N,N'*-di(biphenyl-2-yl)-*N,N'*-diphenyl-[1,1'-biphenyl]-4,4'-diamine (*o*-BPD), *N,N'*-di(biphenyl-3-yl)-*N,N'*-diphenyl-[1,1'-biphenyl]-4,4'-diamine (*m*-BPD), and *N,N'*-di(diphenyl-4-yl)-*N,N'*-diphenyl-[1,1'-biphenyl]-4,4'-diamine (*p*-BPD). The hole drift mobility was measured by means of TOF techniques. Furthermore, they found that the hole

mobilities were  $6.5 \times 10^{-4} \text{ cm}^2/\text{Vs}$ ,  $5.3 \times 10^{-5} \text{ cm}^2/\text{Vs}$ , and  $1.0 \times 10^{-3} \text{ cm}^2/\text{Vs}$  for *o*-BPD, *m*-BPD, and *p*-BPD, respectively [98]. Especially on *meta* position, the mobility of charge carrier in methyl-substituted diphenylamine is higher than the mobility of charge carrier in phenyl-substituted diphenylamine. However, there is a hint from the result obtained by Shirota *et.al* that a substitution on *para* position with an appropriate substituent gives relative high charge carrier mobility rather than the one on the other positions.



#### 6.4. 2,2',7,7'-Tetra-(*m*-tolyl-phenylamino)-9,9'-spirobifluorene (Spiro-TPD)

Spiro-TPD is the corresponding spiro-compound of the before described and well-known organic hole transport materials, TPD. Figure 6.15(a) shows a typical drain current *vs.* drain bias plot of a Spiro-TPD FET at various gate voltages, where the channel width  $W$  and the channel length  $L$  were 4 mm and 10  $\mu\text{m}$ . The drain current at a gate bias of -60 V and drain bias of -60 V was 0.52  $\mu\text{A}$ . The transistor action is observed for negative gate voltages, i.e., transport are due to positive charges. Moreover, Figure 6.15(b) shows the variation of channel conductivity as a function of gate bias. *ON/OFF* ratios of  $6.9 \times 10^4$  and  $2.4 \times 10^5$  can be obtained at drain biases of -20 V and -60 V as the gate bias is being scanned from +2 V to -60 V. The hole mobilities extracted in the saturation regime and linear regime were  $5.2 \times 10^{-5} \text{ cm}^2/\text{Vs}$  and  $2.5 \times 10^{-5} \text{ cm}^2/\text{Vs}$ , respectively. In addition, the fitted threshold voltages for in air operation were +2.2 V extracted in the saturation regime and -4.5 V extracted in the linear regime, respectively. The device turns on at +2 V.

Figure 6.15(c) shows the output characteristics measured in vacuum and at RT. The saturated drain current was increased by 25 % with respect to the measurement performed in air. Moreover, Figure 6.15(d) shows the transfer characteristics as the gate bias is being scanned from +10 V to -60 V and vice versa. The hole mobilities were  $7 \times 10^{-5} \text{ cm}^2/\text{Vs}$  extracted in the saturation regime and  $3.7 \times 10^{-5} \text{ cm}^2/\text{Vs}$  extracted in the linear regime. *ON/OFF* ratios of  $9 \times 10^4$  and  $2.9 \times 10^5$  can be obtained at drain biases of -20 V and -60 V as

the gate bias is being scanned from +3 V to -60 V. The fitted threshold voltages for operation in vacuum were +1.4 V extracted in the saturation regime and -2.3 V extracted in the linear regime. The switch-on voltage was +3 V for in vacuum operation. In many *p*-type organic FETs, a positive switch-on voltage is observed [99]. This is often caused by unintentional extrinsic doping of the organic film [40]. A positive, reverse gate bias is then required to deplete the bulk of the film. If a negative switch-on voltage is observed, it indicates a low extrinsic doping level of the film. The mobility of holes in TPD films has been described previously in sub-chapter 6.3. It was found that the hole mobility extracted in the linear regime in thin films of TPD is two times higher than the that in thin films of Spiro-TPD as the sample has been measured in air. However, the hole mobility in thin films of TPD, measured in air and extracted in the saturation regime, is 42 % higher than that in thin films of Spiro-TPD.

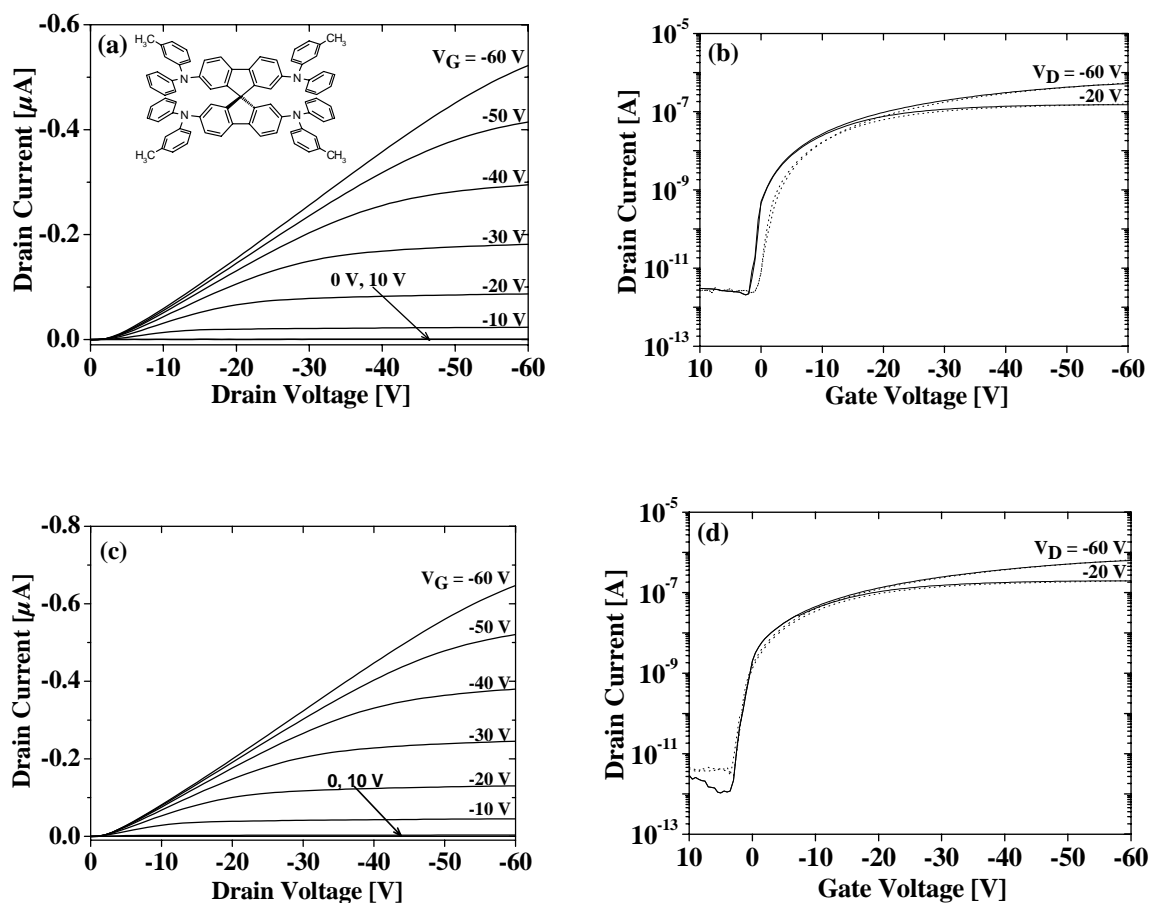


Figure 6.15. Output and transfer characteristics of a Spiro-TPD FET,  $W = 4 \text{ mm}$ ,  $L = 10 \text{ }\mu\text{m}$ ,  $C_i = 19.9 \text{ nF/cm}^2$ . (a). Output characteristics measured in air. The inset depicts the chemical structure of Spiro-TPD, (b). Transfer characteristics measured in air, (c). Output characteristics measured in vacuum and (d). Transfer characteristics measured in vacuum. All measurements were performed after thermal evaporation of Spiro-TPD.



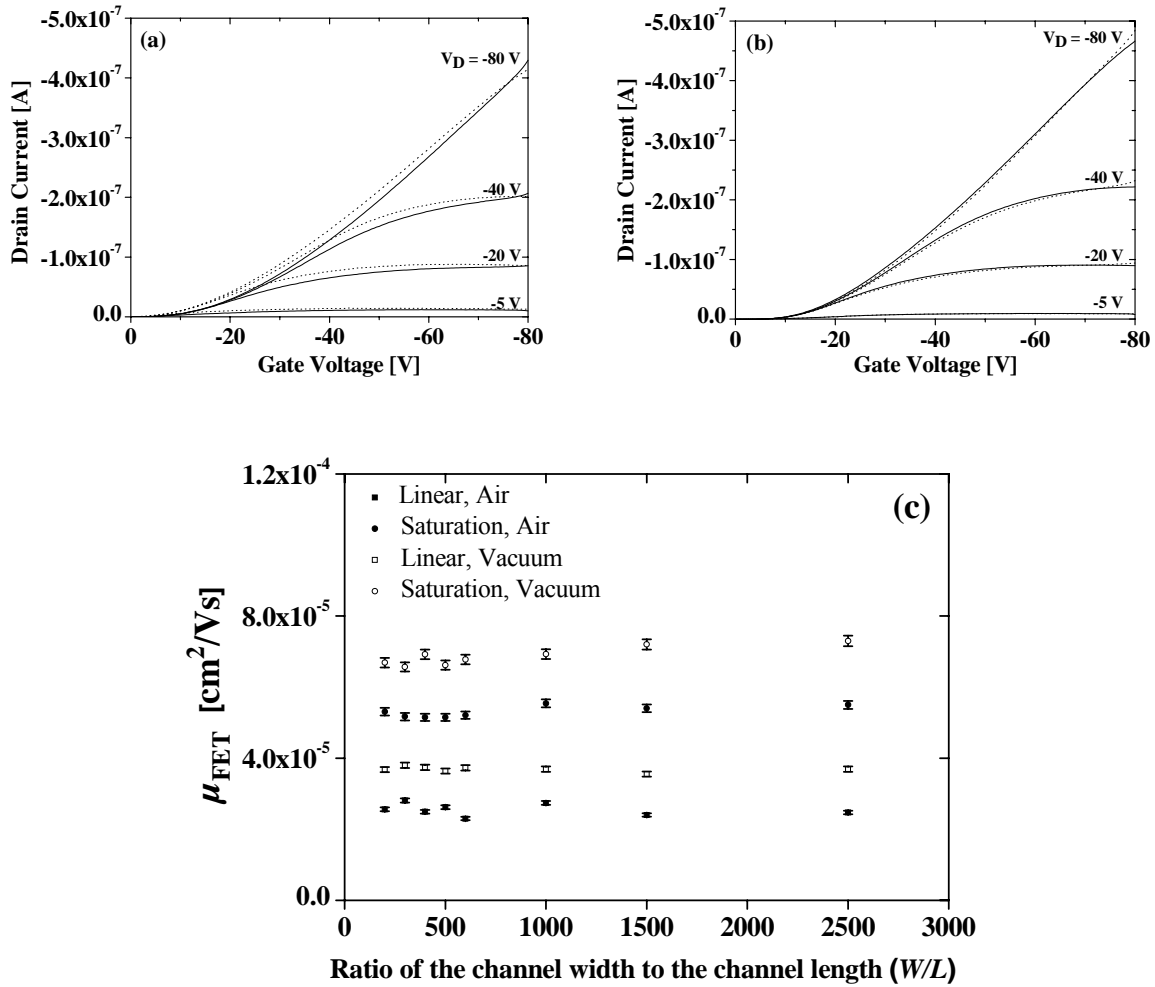


Figure 6.16. Hysteresis characteristics of a Spiro-TPD FET ( $W = 2$  mm,  $L = 10$   $\mu$ m,  $C_i = 19.9$  nF/cm<sup>2</sup>) measured at RT and in air (a) and in vacuum (b). (c). The field-effect mobility of charge carriers in Spiro-TPD thin films at different ratios of the channel width to the channel length ( $W/L$ ).

Figure 6.16(a) and 6.16(b) show the transfer characteristics of a Spiro-TPD FET measured in air and in vacuum, respectively. A clear hysteresis in the transfer characteristics was observed for measurement carried out in air. However, the measurement carried out in vacuum exhibited only a small increase in the drain current with respect to the measurement carried out in air. Furthermore, the variation of mobility with devices geometry such as the ratio of the channel width to the channel length is relative small, as shown in Figure 6.16(c). It implies the high reproducibility of the results, which the mobility of holes does not depend on the geometry of devices. The *ON/OFF* ratio at a drain bias of  $-5$  V was  $2 \times 10^4$  and at a drain bias of  $-60$  V was  $6 \times 10^5$ . The highest *ON/OFF* ratio with a value of  $3.6 \times 10^6$  was measured for a channel length of  $5$   $\mu$ m, a channel width of  $5$  mm, and at a drain bias of  $-60$  V.

The transfer and output characteristics of a FET were also measured after the sample was stored in ambient atmosphere and at RT for 9 months, as shown in Figure 6.17. A nonlinear behavior at low drain biases was also observed, which is attributed to the non-ohmic contacts between the gold electrodes and Spiro-TPD. Moreover, the presence of the hysteresis behavior in the transfer characteristics curve measured in air, for fresh sample and after the sample was stored in ambient atmosphere for 9 months, were observed as well. The origin of this effect is not clear yet, but probably due to oxygen acting as a dopant upon keeping the sample for a certain time in ambient atmosphere.

For fresh device, the saturated drain current decreased by 19 % as the sample was measured in air. After the sample was stored in ambient atmosphere and at RT for 9 months, the saturated drain current for measurement carried out in air decreased by 8 %. In addition, the drain current decreased by 13 % for measurement carried out in vacuum. In contrast, the saturated drain current of a Spiro-TAD FET decreased by 23 % for measurement carried out in air and by 9 % for measurement carried out in vacuum after the sample has been stored for 9 months in air and at RT. It implies that Spiro-TPD is more stable for operation in air than Spiro-TAD. After the device was stored for 9 months in ambient atmosphere and at RT, the mobility of holes extracted in the saturation regime and measured in vacuum was dropped by 3 %, which is similar with the value obtained for Spiro-TAD FETs. However, the hole mobility in thin films of Spiro-TPD measured in vacuum decreased typically by 32 % for linear regime operation. For in air operation, the hole mobilities dropped by 8 % and 11 % for linear regime operation and saturation regime operation, respectively. However, the *OFF* current and the switch-on voltage do not change significantly over 9 months. The fitted threshold voltage measured in vacuum shifted from +1.4 V to -2.4 V after 9 months, which is similar with the values obtained for Spiro-TAD FETs.

Based on these results, the field-effect mobility changes of holes in Spiro-TPD is smaller than that in Spiro-TAD as the devices have been operated under an ambient atmosphere. Moreover, the saturated drain current and field-effect mobility of holes in TPD, the corresponding parent compound of Spiro-TPD, decreased by 86 % and 70 %, respectively, after the sample has been stored in ambient atmosphere for 236 days (ca.8 months). It implies that Spiro-TPD FETs are stable under operation in ambient atmosphere than TPD FETs.

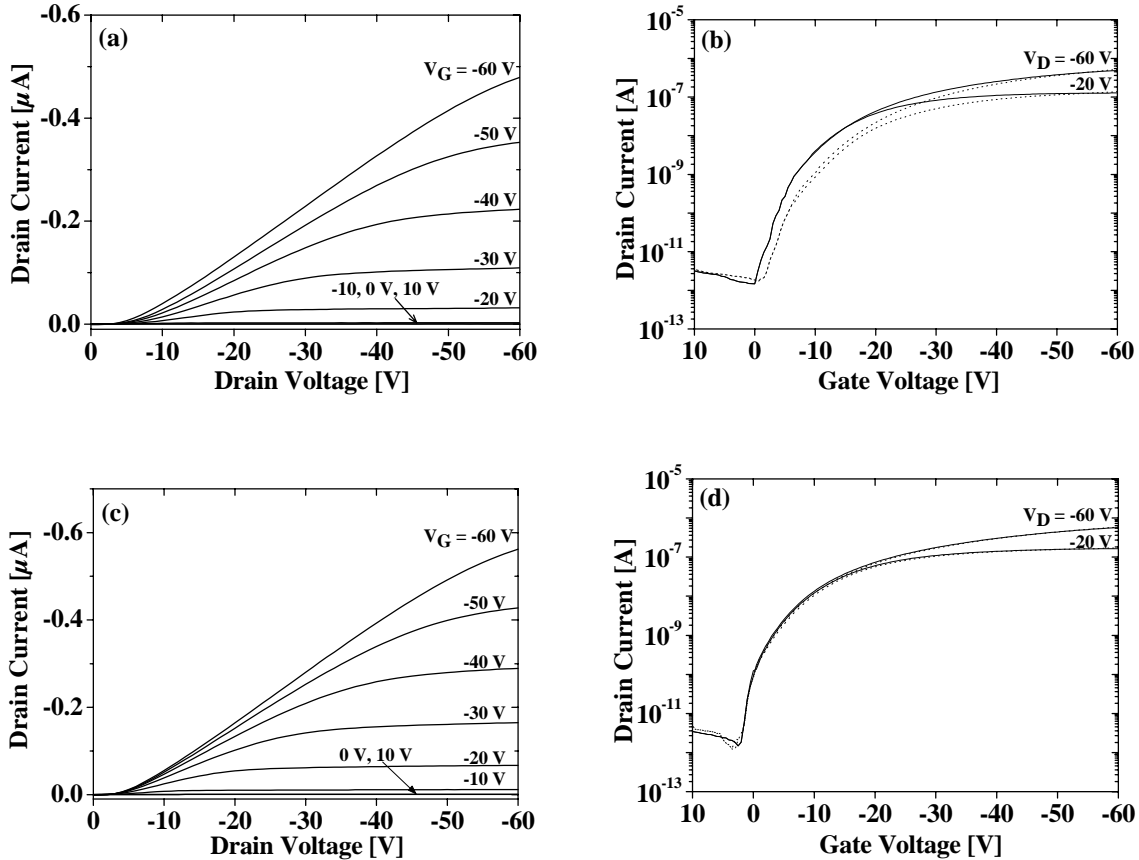


Figure 6.17. Output and transfer characteristics of a Spiro-TPD FET, which was measured after the sample was stored in ambient atmosphere and at RT for 9 months,  $W = 4$  mm,  $L = 10$   $\mu\text{m}$ ,  $C_i = 19.9$  nF/cm<sup>2</sup>. (a). Output characteristics measured in air, (b). Transfer characteristics measured in air, (c). Output characteristics measured in vacuum, and (d). Transfer characteristics measured in vacuum.

Figure 6.18 shows the dependency of the field-effect mobility of charge carriers on the gate bias. The mobility was linearly dependent on the gate bias ( $-50$  V  $< V_G < -5$  V). In contrast, the mobility is super-linearly dependent on the gate bias at  $V_G < -50$  V. This result is not fully understood. In the inset of Figure 6.18, the mobility of holes in thin films of TPD is also plotted with the mobility of holes in thin films of Spiro-TPD. At low gate biases ( $V_G > -15$  V), the mobility of holes in thin films of TPD is smaller than that in thin films of Spiro-TPD. It implies that the mobility of holes in thin films of TPD is strongly dependent on the gate bias, whereas the mobility of holes is weakly dependent on the gate bias in thin films of Spiro-TPD. In a FET, an applied gate voltage gives rise to the accumulation of charge in the region of the semiconducting layer that is close to the insulator (accumulation layer thickness  $< 5$  nm). As these accumulated charge carriers fill the lower-lying states, any additional charges in the accumulation layer will occupy states at relatively high energies. Consequently, the additional charges will require less activation energy to hop away to a neighboring site.

This results in a higher mobility with increasing gate bias [60,61]. However, the mobility first increased linearly with the gate bias and then tends to saturate or decrease at high gate biases. This effect could be attributed to the contact resistance effect as reported for other materials [23]. The contact resistance between source/drain electrode and the semiconductor behaviors are caused by the channel length which is small enough that the contact resistance dominates the overall device resistance.

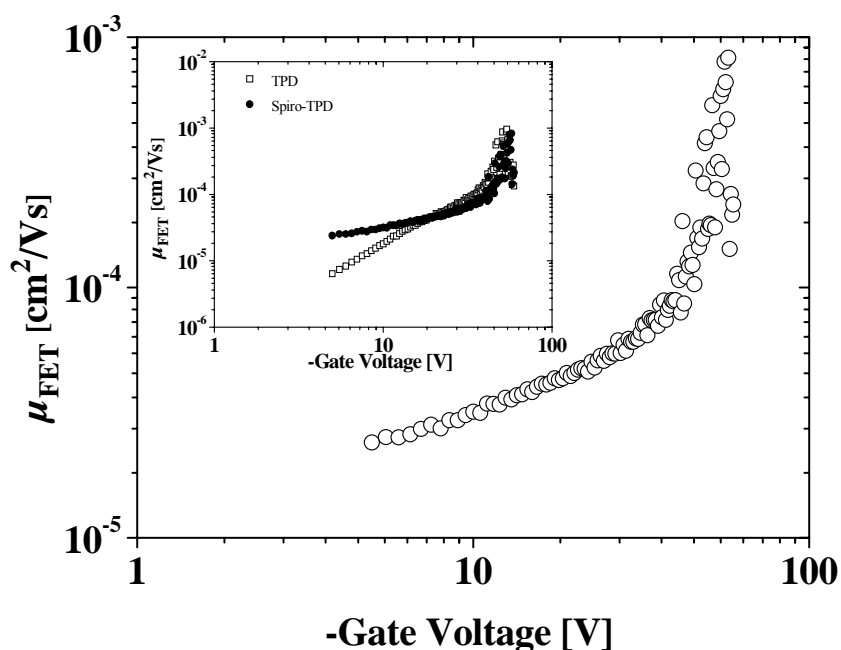
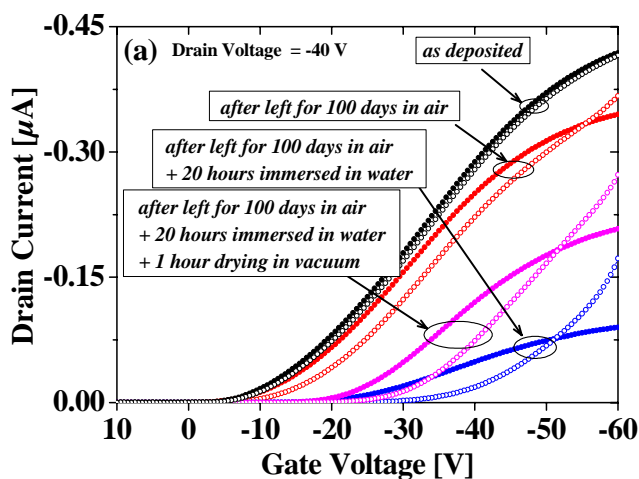


Figure 6.18. Variation of the hole mobility of a Spiro-TPD thin film as a function of gate bias at 294 K. The inset shows gate-voltage dependent mobility of TPD (from Figure 6.14) and Spiro-TPD based-field-effect transistors measured at 294 K.



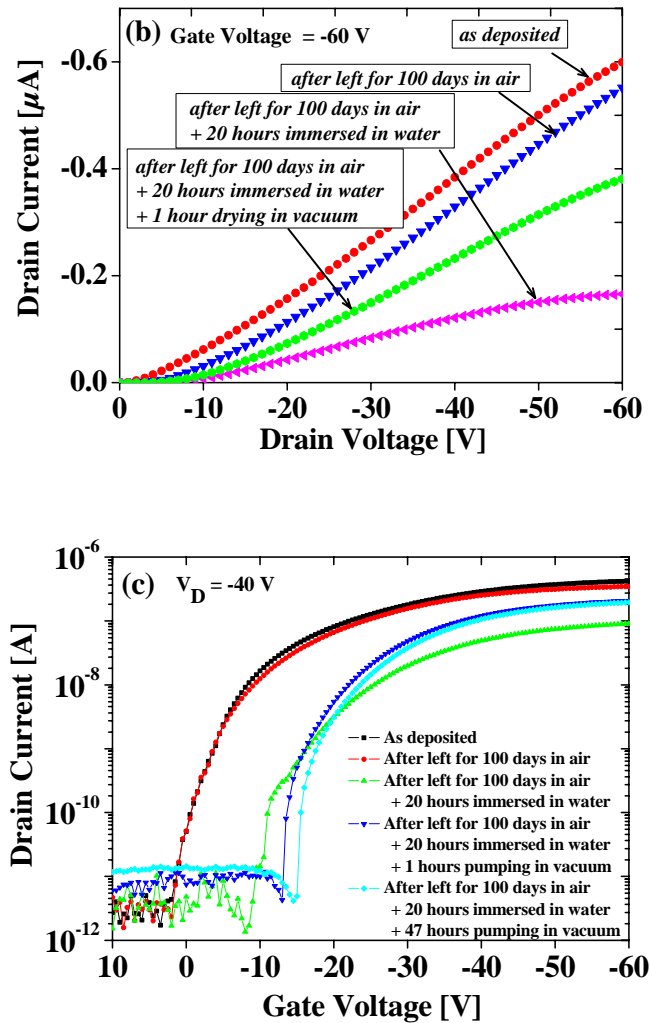


Figure 6.19. Output and transfer characteristics of a Spiro-TPD FET after the device was stored in air for 100 days, following immersed in water and degassing in vacuum. (a). Transfer characteristic at a drain bias of -40 V, filled circles denotes advancing measurement and open circles denotes receding measurement, (b). Output characteristics measured at a gate bias of -60 V, and (c). Transfer characteristics measured at a drain bias of -40 V.

Figure 6.19 shows the transistor characteristics of a Spiro-TPD FET ( $W = 2\text{ mm}$ ,  $L = 5\text{ }\mu\text{m}$ ,  $C_i = 19.9\text{ nF/cm}^2$ ) for different conditions or environments. Figure 6.19(a) shows the hysteresis in the transfer characteristic after the sample was stored in ambient atmosphere and at RT for 100 days. This hysteresis is due to the presence of a trapped mobile charge which probably came from moisture. The trapped mobile charge is more obvious, as the sample was immersed in water for 20 hours ( $T_{\text{water}} = 20\text{ }^\circ\text{C}$ ). The hysteresis in the transfer characteristics was larger and the drain current was substantially lower than before, as shown in Figure 6.19(a). However, if the sample was degassed under vacuum for 1 hour the drain current increased, but the hysteresis effect does not disappear. This implies that the presence of water

in the device is difficult to remove. Figure 6.19(b) shows the output characteristics of a Spiro-TPD FET at a gate bias of -60 V for different conditions. The evolution of the field effect mobility for different conditions is:  $6.8 \times 10^{-5} \text{ cm}^2/\text{Vs}$  after deposition of Spiro-TPD,  $6.6 \times 10^{-5} \text{ cm}^2/\text{Vs}$  after the device was stored in ambient atmosphere for 100 days,  $1.2 \times 10^{-5} \text{ cm}^2/\text{Vs}$  after the sample was stored in ambient atmosphere for 100 days and subsequently the device was immersed in water for 20 hours, and  $3.2 \times 10^{-5} \text{ cm}^2/\text{Vs}$  after the sample was stored in ambient atmosphere for 100 days, subsequently the device was immersed in water for 20 hours, and the device was degassed under vacuum for 1 hour. The corresponding fitted threshold voltages are +1.4 V, -0.9 V, -12.4 V, and -11 V, respectively. Figure 6.19(c) also shows that the switch-on voltage shifts toward positive gate bias. The fitted threshold voltage  $V_T$  for organic FETs in the accumulation regime is given by [100]

$$V_T = -\frac{qn_0d}{C_i} + V_{FB} \quad (6.1)$$

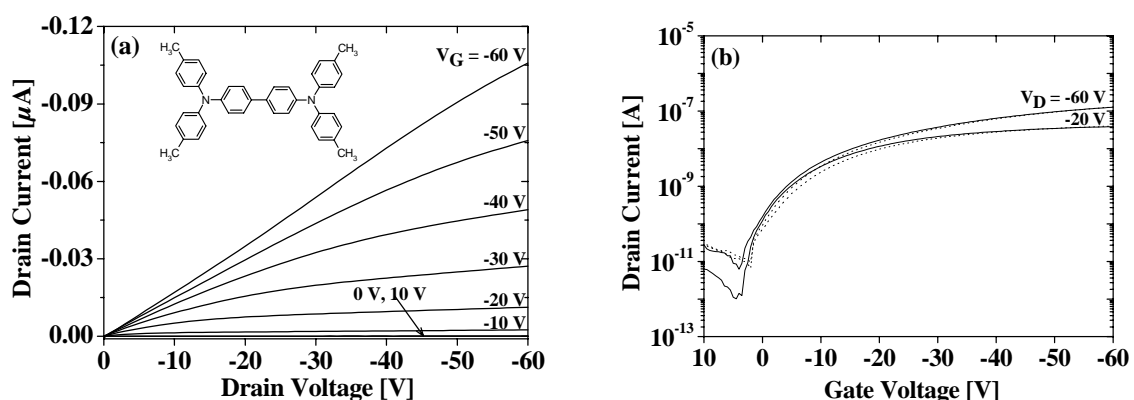
where  $V_{FB}$  is the flat-band potential,  $q$  is the elementary charge,  $d$  is the film thickness, and  $n_0$  is the charge carrier density. Assuming the flat-band voltage to be invariant, the charge carrier density is the only parameter which can be changed. For the following calculation,  $V_{FB}$  was assumed being zero,  $d$  was 140 nm,  $C_i$  was 19.9 nF/cm<sup>2</sup> and  $q$  is  $1.6 \times 10^{-19}$  C. The number of charge carriers was  $8 \times 10^{15} \text{ cm}^{-3}$  after the sample was stored in ambient atmosphere for 100 days. This value increased to  $1.1 \times 10^{17} \text{ cm}^{-3}$  after the sample was stored for 100 days and, subsequently, the sample was immersed in water for 20 hours. However, if the sample was degassed under vacuum for 1 hour, the charge carrier density decreased by 11 %. In contrast, the mobility increased by a factor of 2.7. This indicates that the degassing treatment effectively pull oxygen, water and or moisture out of the sample. The large concentration of charge carriers after the sample has been stored for 100 days and was immersed in water for 20 hours is probably dominated by traps, because the mobility does not increase with increasing the number of charge carriers. Therefore, *the charge carrier density* does not reflect the *free charge carrier* but rather a composition between *free* and *trap charge carrier density* in film.

Similarly, it was also found that the adsorption of H<sub>2</sub>O on pentacene layer was the main reason for the degradation of devices. It was indicated by appearance of a broadband centered at 3443 cm<sup>-1</sup> in infrared spectrum which attributed to incorporated of H<sub>2</sub>O molecules. Without encapsulation, the mobility decreases rapidly by 30 % over 500 hours. In contrast, a small decreasing in mobility of 5 % was found for device encapsulated with ultraviolet curable resin [97]. The mechanism of degradation caused by H<sub>2</sub>O molecules can be explained

by diffusion of H<sub>2</sub>O molecules into devices and interact with the trapped charge. As a result, the concentration of the traps increased. As a result, a high *OFF* current was observed. In contrast, field-effect transistors comprising platinum-based tetrakis(*S*)-1-amino-3,7-dimethyloctane)platinum(II)tetrachloroplatinate(II), as the active layer revealed a remarkably characteristic after the device was immersed in water ( $T_{\text{water}} = 90\text{ }^{\circ}\text{C}$ ) for 12 hours. The device did not deteriorate, but the *ON/OFF* ratio increased by a factor of ten [96]. The origin of this effect was attributed to a removal of ionic impurities by rinsing with water.

### 6.5. *N,N,N',N'*-Tetrakis(4-methylphenyl)-benzidine (TTB)

Figure 6.20(a) shows the output characteristics of a TTB FET measured in air and at RT. A small nonlinearity of the drain current at low drain biases was observed. This could be explained by the presence of a small potential barrier for charge injection at the contacts between TTB and the gold electrodes. Furthermore, Figure 6.20(b) shows the transfer characteristics measured in air as the gate bias is being scanned from +10 V to -60 V and vice versa. The transfer characteristics were measured at drain biases of -20 V and -60 V. The hysteresis in the transfer characteristics was observed as well, which described the difference between the drain current obtained from the advancing and receding curve. The field-effect mobilities of charge carriers were  $6.3 \times 10^{-6}\text{ cm}^2/\text{Vs}$  extracted in the linear regime and  $1.12 \times 10^{-5}\text{ cm}^2/\text{Vs}$  extracted in the saturation regime. The fitted threshold voltages of -6.2 V and +1.1 V were obtained from the linear regime and the saturation regime, respectively. Moreover, the modulation of channel conductivities of  $2 \times 10^4$  ( $V_D = -20\text{ V}$ ) and  $4.1 \times 10^4$  ( $V_D = -60\text{ V}$ ) were obtained as the gate bias is being scanned from -60 V to +2 V.



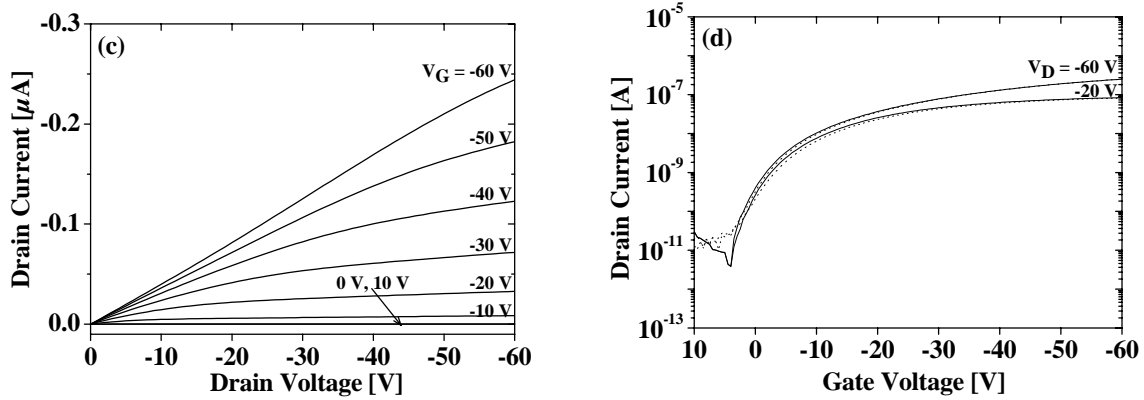


Figure 6.20. Output and transfer characteristics of a TTB FET,  $W = 2 \text{ mm}$ ,  $L = 5 \text{ }\mu\text{m}$ ,  $C_i = 17.3 \text{ nF/cm}^2$ . (a). Output characteristics measured in air. The inset depicts the chemical structure of TTB, (b). Transfer characteristics measured in air, (c). Output characteristics measured in vacuum, and (d). Transfer characteristics measured in vacuum.

Figure 6.20(c) and 6.20(d) show the output and transfer characteristics of the same sample measured in vacuum and at RT. Surprisingly, the saturated drain current substantially increased by 100 % with respect to the values obtained from the measurement carried out in air. The difference in the drain current between measurements carried out in air and in vacuum for TTB FETs is the largest among the FETs based on materials used in this study. In the saturation regime, the field-effect mobility of charge carriers and the fitted threshold voltage for in vacuum operation were  $1.8 \times 10^{-5} \text{ cm}^2/\text{Vs}$  and  $+5.7 \text{ V}$ , respectively. In addition, the field-effect mobility of charge carriers extracted in the linear regime gave lower values than that extracted in the saturation regime. In the linear regime, a field-effect mobility of  $1.4 \times 10^{-5} \text{ cm}^2/\text{Vs}$  and a fitted threshold voltage  $V_T$  of  $-5.9 \text{ V}$  were obtained. Moreover, *ON/OFF* ratios of  $2.1 \times 10^4$  and  $5.2 \times 10^4$  were obtained for  $V_D = -20 \text{ V}$  and  $-60 \text{ V}$ , respectively, as the gate bias is being scanned from  $-60 \text{ V}$  to  $+3 \text{ V}$ . Those values are slightly higher than those obtained from measurement performed in air. In conclusion, the field-effect mobility of holes in thin films of TTB was the lowest value among the materials investigated in this thesis.

Table 6.2. Hole mobilities in TTB thin films extracted from TOF and FET measurements.

Device and Material	Mobility $\mu$ [ $\text{cm}^2/\text{V s}$ ]	Reference
TOF TTB	$7 \times 10^{-4}$	87
TOF TTB	$1 \times 10^{-3}$	101
FET TTB	$1.8 \times 10^{-5}$	This work



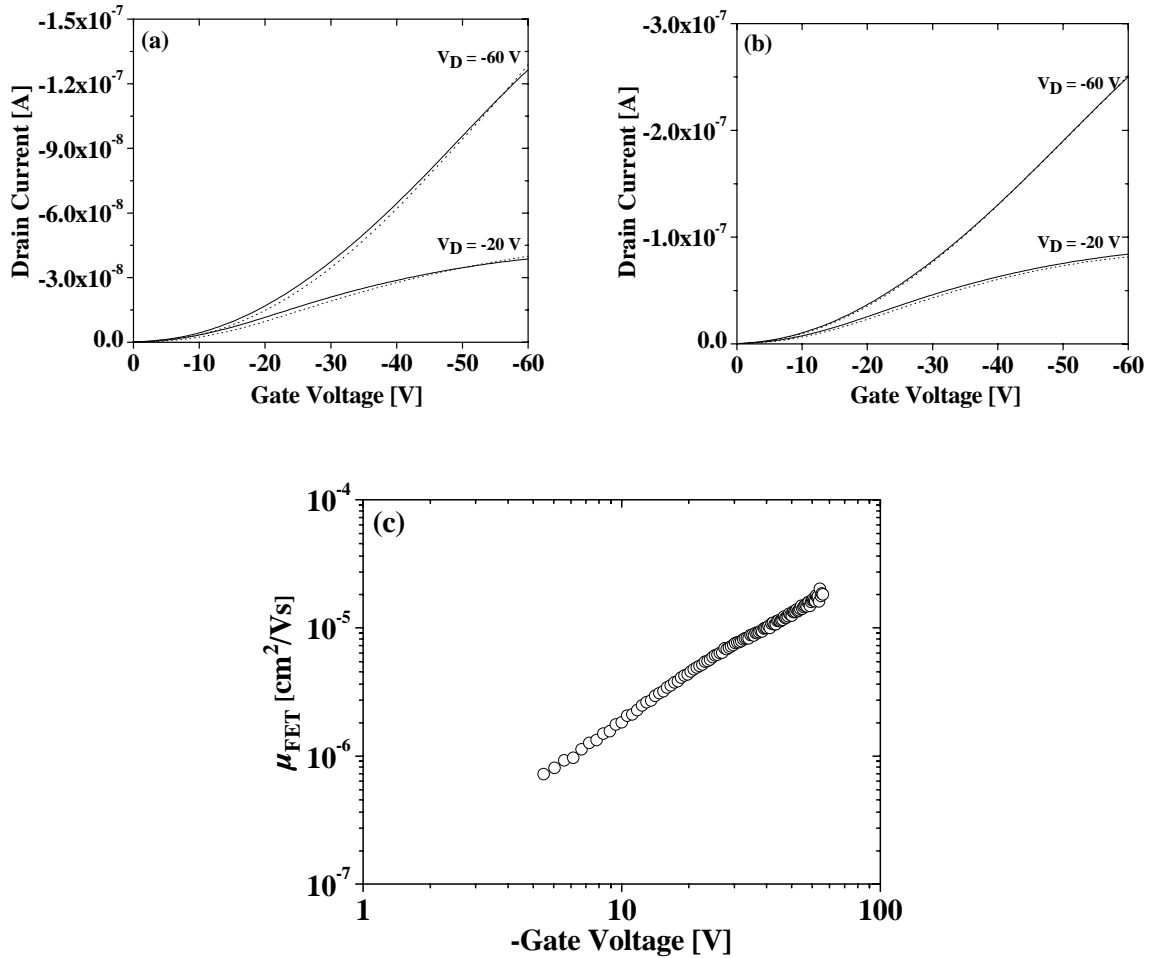


Figure 6.21. Hysteresis characteristics of a TTb FET ( $W = 2 \text{ mm}$ ,  $L = 5 \text{ }\mu\text{m}$ ,  $C_i = 17.3 \text{ nF/cm}^2$ ) measured at RT and in air (a) and in vacuum (b). (c). Variation of the hole mobility of a TTb film as a function of gate bias. Data were recorded at 294 K and measured in vacuum.

The mobilities of charge carrier in TTb thin films investigated by TOF techniques and FET methods are presented in Table 6.2. In 1995, Heun and Borsenberger reported that the charge carrier mobility in TTb thin films was around  $7 \times 10^{-4} \text{ cm}^2/\text{Vs}$  at an electric field of  $1.6 \times 10^5 \text{ V/cm}$  (film thickness was between 11 and 12.1  $\mu\text{m}$ ) [87]. Two years before, they also reported a mobility of  $1 \times 10^{-3} \text{ cm}^2/\text{Vs}$  at an electric field of  $1.45 \times 10^5 \text{ V/cm}$  (film thickness was 5.5  $\mu\text{m}$ ) [101]. As observed during measurement, the TTb FET did not stable as operating in air, even if the sample was stored under vacuum. Moreover, the maximum drain current measured in vacuum is 100 % higher than the values measured in air. A similar result was also revealed in the transfer curves, as shown in Figure 6.21(a) and 6.21(b). The hysteresis in the transfer characteristics measured in vacuum is smaller than that measured in air. However, the transistor effect vanished even if the sample was stored in a continuously evacuated chamber for a few days. Additionally, Figure 6.21(c) shows the variation of the

hole mobility of a TTB film as a function of gate bias. The mobilities were obtained from the transfer characteristics at  $V_D = -10$  V measured in vacuum. As shown in Figure 6.21(c), the mobility is linearly dependent on the gate bias. The mobility increases from very low values ( $7.2 \times 10^{-7}$  cm<sup>2</sup>/Vs at a gate bias of -5 V) to  $1.8 \times 10^{-5}$  cm<sup>2</sup>/Vs at a gate bias of -60 V. This is different with TPD (Figure 6.14), but similar with TAD (Figure 6.3). The most striking feature revealed in Figure 6.21 is a linear gate bias dependence of the field-effect mobility.

### 6.6. 2,2',7,7'-Tetrakis-(*N,N'*-di-*p*-methylphenylamino)-9,9'-spirobifluorene (Spiro-TTB)

Figure 6.22(a) shows the output characteristics of a 2,2',7,7'-tetrakis-(*N,N'*-di-*p*-methylphenylamino)-9,9'-spirobifluorene (Spiro-TTB) FET for a fresh sample measured in ambient atmosphere and at RT. At low drain biases, a nonlinearity in the output characteristics was observed, which can be attributed to the non-ohmic contacts between Spiro-TTB and the gold electrodes. The maximum drain current at  $V_D = V_G = -60$  V was 0.8  $\mu$ A. In addition, Figure 6.22(b) shows the transfer characteristic of the same sample. The hole mobilities measured in air were  $3.2 \times 10^{-5}$  cm<sup>2</sup>/Vs for saturation regime operation and  $2.3 \times 10^{-5}$  cm<sup>2</sup>/Vs for linear regime operation. Along with the mobilities, the fitted threshold voltages of +0.9 V and -7.5 V were obtained for saturation regime operation and for linear regime operation. In contrast, the device turn on or turn off at +4 V. *ON/OFF* ratios of  $1.5 \times 10^5$  ( $V_D = -20$  V) and  $1.8 \times 10^5$  ( $V_D = -60$  V) can be obtained as the gate bias is being scanned from +4 V to -60 V. Those values are one order of magnitude larger than those obtained for TTB FETs, as described in the previous sub-chapter.

Figure 6.22(c) shows a typical set of drain current against drain bias at different gate biases, measured in vacuum and at RT. The saturated drain current measured in vacuum was 38 % higher than that measured in air. In contrast, the saturated drain current of a TTB FET, the corresponding parent compound of Spiro-TTB, increased by 100 % as the device is being measured in vacuum. It is clear that a Spiro-TTB FET is more stable under operation in air than a TTB FET. Moreover, the channel conductivities rise by factors of  $4 \times 10^5$  ( $V_D = -20$  V) and  $1 \times 10^6$  ( $V_D = -60$  V) as the gate voltage is being swept from +7 V to -60 V. The switch-on voltage was +7 V, which is higher than the values obtained for in air operation. The hole mobilities were  $4 \times 10^{-5}$  cm<sup>2</sup>/Vs for linear regime operation and  $5.9 \times 10^{-5}$  cm<sup>2</sup>/Vs for saturation regime operation, which are higher than the values obtained from measurement

performed in air. On the other hand, the fitted threshold voltages extracted in the saturation regime and linear regime were +2.8 V and -5.1 V, respectively.

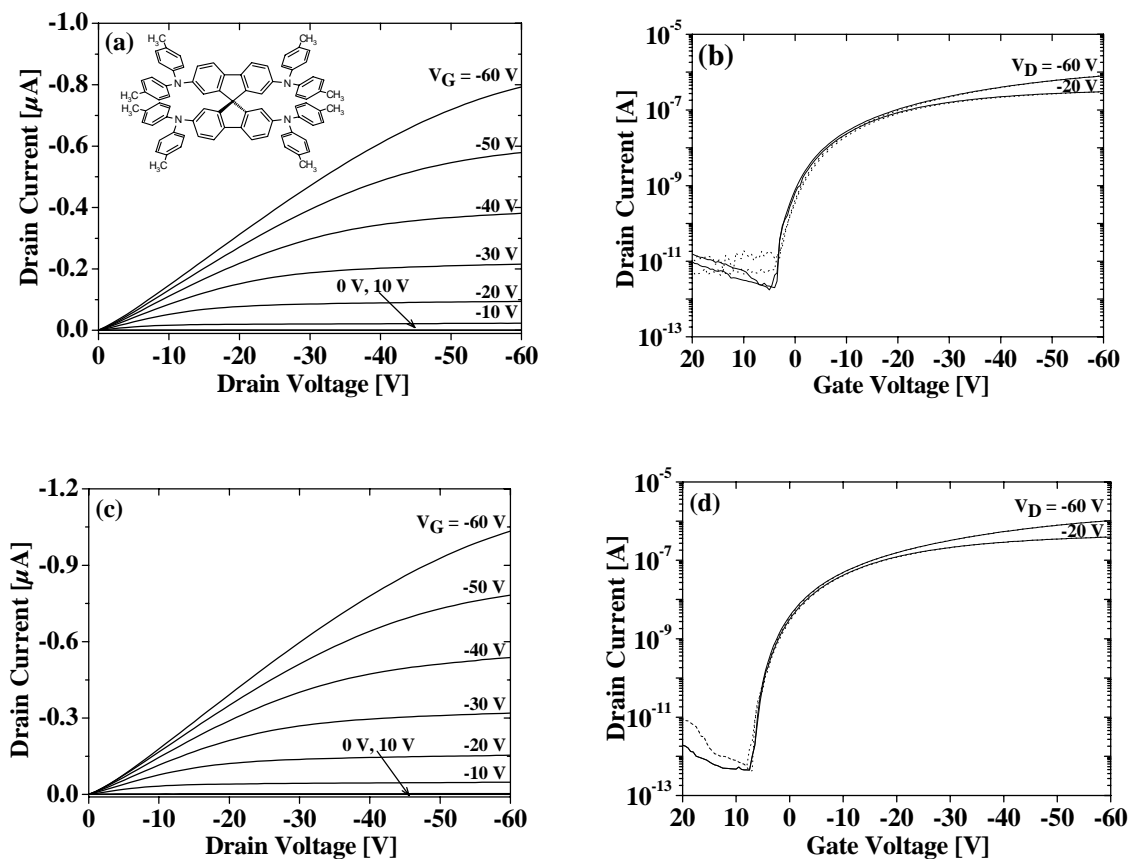


Figure 6.22. Output and transfer characteristics of a Spiro-TTB FET,  $W = 5 \text{ mm}$ ,  $L = 10 \mu\text{m}$ ,  $C_i = 17.3 \text{ nF/cm}^2$ . (a). Output characteristics measured in air. The inset depicts the chemical structure of Spiro-TTB, (b). Transfer characteristics measured in air, (c). Output characteristics measured in vacuum and (d). Transfer characteristics measured in vacuum. All measurements were performed after thermal evaporation of Spiro-TTB.

The mobility of holes in thin films of Spiro-TTB is higher than that in thin films of TTB but lower than those in thin films of Spiro-TAD and Spiro-TPD. Interestingly, the switch-on voltage of Spiro-TTB FETs is the largest among the FETs based on the materials used in this study. This result can be understood from the HOMO level point of view. As described previously in chapter 3, the HOMO level of Spiro-TTB exhibits the largest potential barrier for charge injection among the materials investigated in this thesis with respect to the work function of gold electrodes. Therefore, it was not surprising if Spiro-TTB FETs exhibit large switch-on voltage, which means that large gate bias is then required to deplete the bulk of the film. In other words, a large bias is required in order to bring the HOMO level of Spiro-TTB and the Fermi level of gold electrode into equilibrium. Ideally, the HOMO level of the

active material lies at the value of the work function of the electrode. Hence, zero bias is required to turn the device on. Figure 6.23 shows the variation of field-effect mobility of charge carriers in different devices. Devices with small ratios of the channel width to the channel length ( $W/L$ ) have slightly smaller mobility than ones with a high  $W/L$ . However, this effect is not very pronounced.

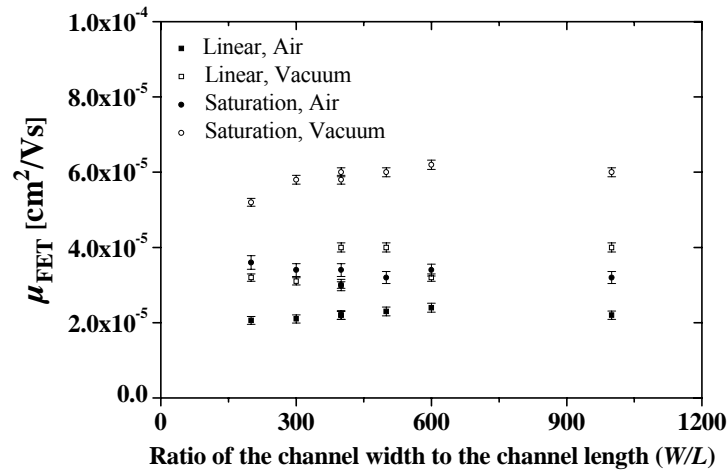


Figure 6.23. The field-effect mobility of charge carriers in Spiro-TTB thin films at different ratios of the channel width to the channel length ( $W/L$ ).

After the same sample was stored in ambient atmosphere and at RT for 4 months, the characteristics of the same device were measured again. The results are shown in Figure 6.24. It was found that the hole mobility decreased by 13 % for in vacuum operation and 21 % for in air operation. The saturated drain current at  $V_G = V_D = -60$  V decreased by 10 % measured in air and 20 % measured in vacuum after the sample was stored at RT and in ambient atmosphere for 4 months. The mobility of hole in Spiro-TTB FET is decreased by 31 % for linear regime operation after the sample has been stored for 4 months. On the other hand, the mobility of hole is decreased by 24 % for saturation regime operation.

The fitted threshold voltages extracted in the linear regime were +0.7 V for in air operation and -5.7 V for in vacuum operation. On the other hand, the fitted threshold voltages extracted in the saturation regime were +6.3 V for in air operation and +3.1 V for in vacuum operation. The switch-on voltage was also shifted after 4 months from +7 V to +14 V for in vacuum operation (Figure 6.24(d)) and from +4 V to +23 V for in air operation (Figure 6.24(b)). It was also found that the  $V_{so}$  of Spiro-TTB is the largest among the investigated

spiro-compounds. This effect could be probably attributed to the large trapped charges concentration in thin films of Spiro-TTB.

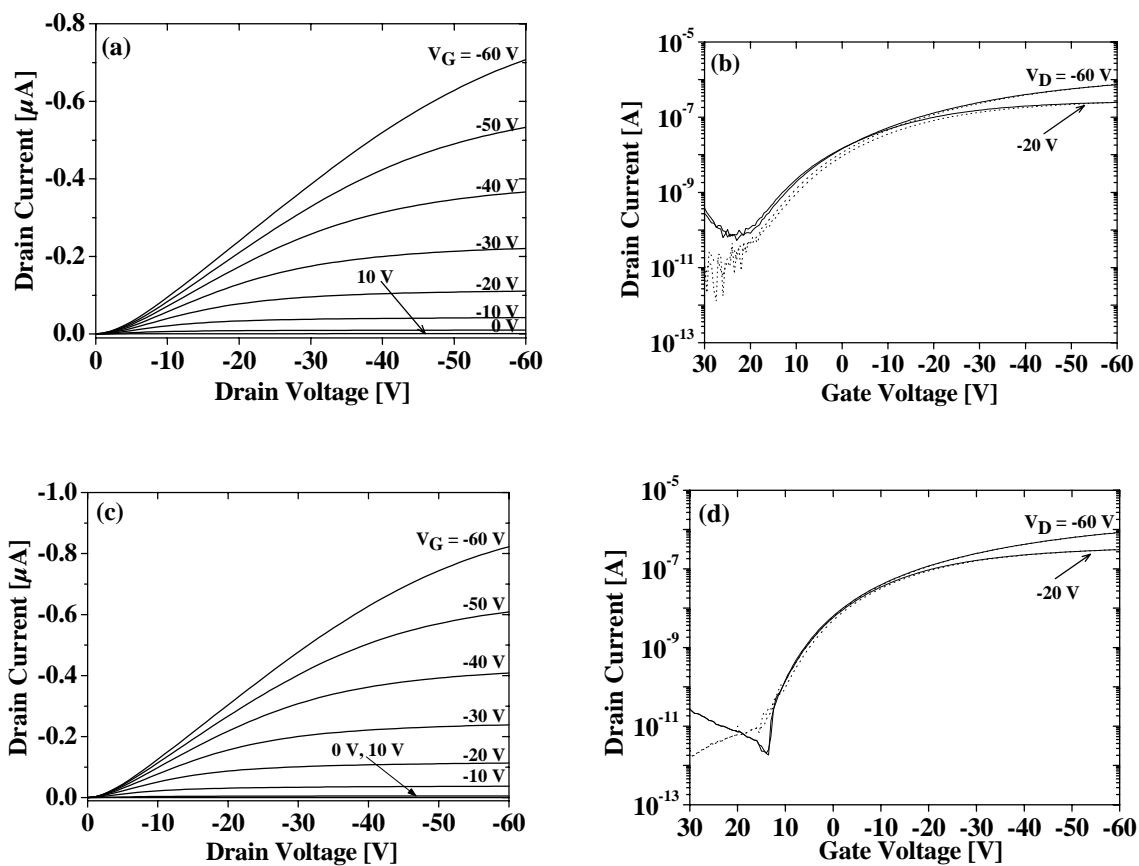
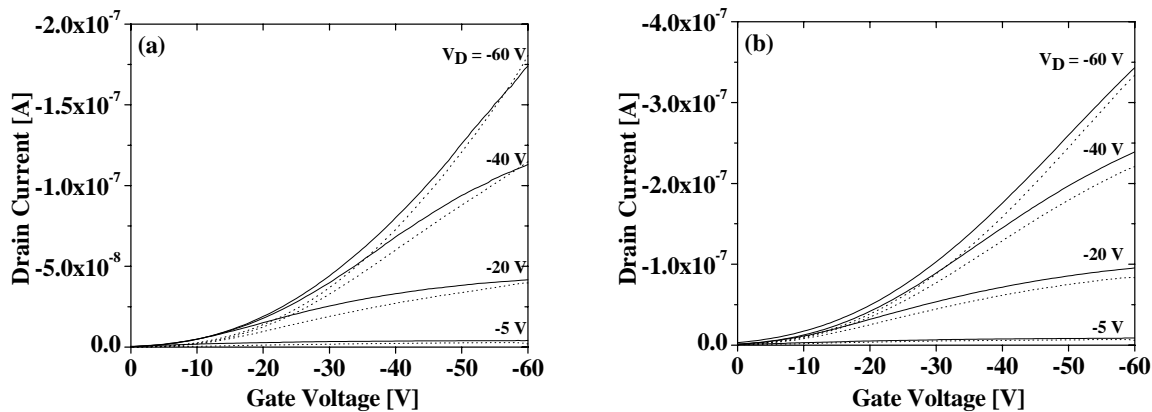


Figure 6.24. Output and transfer characteristics of a Spiro-TTB FET, which was measured after the sample was stored in ambient atmosphere and at RT for 4 months,  $W = 5$  mm,  $L = 10$   $\mu\text{m}$ ,  $C_i = 17.3$  nF/cm<sup>2</sup>. (a). Output characteristics measured in air, (b). Transfer characteristics measured in air, (c). Output characteristics measured in vacuum, and (d). Transfer characteristics measured in vacuum.



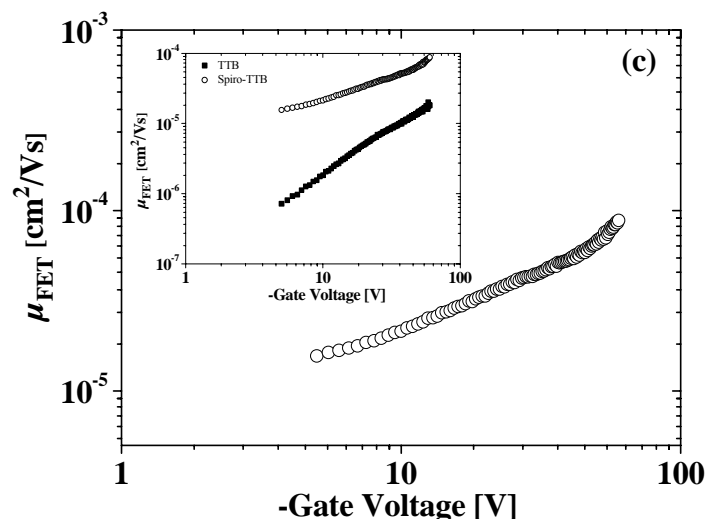


Figure 6.25. Hysteresis characteristics of a Spiro-TTB FET ( $W = 2 \text{ mm}$ ,  $L = 5 \mu\text{m}$ ,  $C_i = 17.3 \text{ nF/cm}^2$ ) measured at RT and in air (a) and in vacuum (b). (c). Variation of the hole mobility of a Spiro-TTB thin film as a function of gate bias at 294 K. The inset shows gate-voltage dependent mobility of TTB (from Figure 6.21(c)) and Spiro-TTB based-field-effect transistors measured at 294 K.

The saturated drain current obtained from the transfer characteristic among the FETs based on spiro-linked compounds are compared. For Spiro-TTB FET, the drain current maximum (at  $V_D = V_G = -60 \text{ V}$ ) measured in vacuum was increased by 38 % with respect to the measurement carried out in air, which is only ca. 10 % for Spiro-TAD or Spiro-TPD. Furthermore, the hysteresis in the transfer characteristics was clearly observed, as displayed in Figure 6.25(a) and 6.25(b). It did not only occur under operation in air but also under operation in vacuum. Furthermore, Figure 6.25(c) shows the dependency of the field-effect mobility in a Spiro-TTB thin film on the gate bias. The mobility in a Spiro-TTB FET is linearly dependent on the gate bias. The mobility increases from  $1.6 \times 10^{-5} \text{ cm}^2/\text{Vs}$  at a gate bias of  $-5 \text{ V}$  to  $8.8 \times 10^{-5} \text{ cm}^2/\text{Vs}$  at a gate bias of  $-60 \text{ V}$ . In contrast, the mobility of holes in a TTB FET increases from very low values ( $7.2 \times 10^{-7} \text{ cm}^2/\text{Vs}$  at a gate bias of  $-5 \text{ V}$ ) to  $1.8 \times 10^{-5} \text{ cm}^2/\text{Vs}$  at a gate bias of  $-60 \text{ V}$ . In conclusion, the mobility of holes in a TTB thin film is much lower than that in a Spiro-TTB thin film, as shown in the inset of Figure 6.25(c).

In the next discussion, the transistor data of Spiro-TTB from two different treatments of the raw materials are presented. First, the Spiro-TTB was used after chemical purification. Second, Spiro-TTB was used after chemical purification and with two additional thermal sublimations. In order to make the analysis easier, both transistors used the same geometry and the capacitance of the gate dielectric. In addition, the thickness of Spiro-TTB in both devices was 130 nm. In this experiment, the channel length and channel width were  $10 \mu\text{m}$

and 2 mm, respectively, and the capacitance per unit area of the gate dielectric was 17.3 nF/cm<sup>2</sup>.

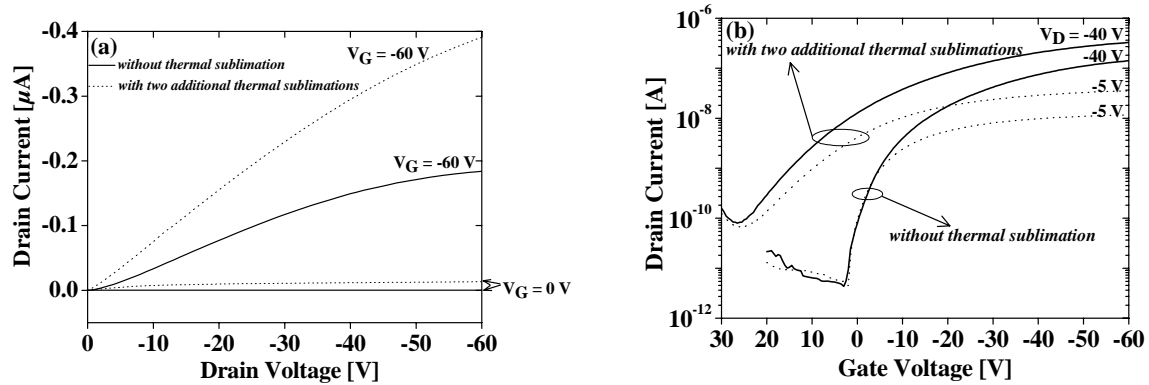


Figure 6.26. Output and transfer characteristics of Spiro-TTB FETs. Two Spiro-TTB FETs were fabricated. First, transistor utilized chemical purified Spiro-TTB which used *without additional thermal sublimation*. Second, transistor utilized Spiro-TTB *with two additional thermal sublimations*.

The transistor based on Spiro-TTB *with two additional sublimations* exhibited large *OFF* current (current at zero gate bias). The ratio of *OFF* current between FETs based on Spiro-TTB *with two additional thermal sublimations* and *without thermal sublimation* was 42 (see Figure 6.26(a)). At high gate biases (for instance  $V_G = -60\text{ V}$ ), however, the drain current of the transistor-based on Spiro-TTB *with two additional thermal sublimations* was only twice higher than that *without thermal sublimation*. The transfer characteristics of the corresponding films are shown in Figure 6.26(b). The switch-on voltage  $V_{so}$  of the device based on Spiro-TTB *without thermal sublimation* was around +2 V. In contrast, the  $V_{so}$  of the device based on Spiro-TTB *with two additional thermal sublimations* was around +24 V. Additionally, the fitted threshold voltage is +2.7 V for device *without thermal sublimation* and is +21.2 V for device based on Spiro-TTB *with two additional thermal sublimations*. However, the field-effect mobility remains relatively unaffected,  $2.25 \times 10^{-5}\text{ cm}^2/\text{Vs}$  for device based on Spiro-TTB *without thermal sublimation* and  $3.05 \times 10^{-5}\text{ cm}^2/\text{Vs}$  for device based on Spiro-TTB *with two additional thermal sublimations*. The shift of the fitted threshold voltage or the switch on voltage can be originated by material defects in Spiro-TTB with *two additional thermal sublimations*. The sublimation was carried out in high vacuum and at temperatures higher than the  $T_g$ . Therefore, after the process the material is probably changed, in which Spiro-TTB is possibly not pure anymore.

### 6.7. *N,N'*-Diphenyl-*N,N'*-bis(1-naphthyl)-1,1'-biphenyl-4,4'-diamine ( $\alpha$ -NPB)

The output and transfer characteristics of an  $\alpha$ -NPB FET measured in air and in vacuum is shown in Figure 6.27. Figure 6.27(a) and 6.27(b) show the output and transfer characteristics of an  $\alpha$ -NPB FET measured in air and at RT. The saturated drain current measured in air was  $0.49 \mu\text{A}$ . *ON/OFF* ratios of  $7.7 \times 10^4$  ( $V_D = -20 \text{ V}$ ) and  $2.5 \times 10^5$  ( $V_D = -60 \text{ V}$ ) were obtained as the gate bias is being swept from 0 V to -60 V. The hole mobility in  $\alpha$ -NPB thin film extracted in the linear regime was  $2.4 \times 10^{-5} \text{ cm}^2/\text{Vs}$ . In the saturation regime, the hole mobility is slightly higher than that extracted in the linear regime. A mobility value of  $4.1 \times 10^{-5} \text{ cm}^2/\text{Vs}$  and a fitted threshold voltage of -6.7 V can be obtained. However, the device turns on or off at -4 V.

Figure 6.27(c) shows the output characteristics measured in vacuum and at RT. The saturated drain current increased by 53 % with respect to the measurement carried out in air. Figure 6.27(d) clearly shows that the *OFF* current of  $\alpha$ -NPB FET measured in vacuum ( $I_{OFF} \sim 0.2 \text{ nA}$ ) was higher than the values measured in air ( $I_{OFF} \sim 2 \text{ pA}$ ). As a result, the measurements performed in vacuum gave *ON/OFF* ratios of  $1.4 \times 10^3$  ( $V_D = -20 \text{ V}$ ) and  $3.5 \times 10^3$  ( $V_D = -60 \text{ V}$ ) as the gate bias is being scanned from 0 V to -60 V, which are lower than the values measured in air. This result implies that even if the sample was stored in a continuous evacuated chamber for 24 hours, the aging of the corresponding thin films could not be prohibited. Moreover, it is possible that device aging already takes place after the deposition of  $\alpha$ -NPB. The hole mobilities were  $3.5 \times 10^{-5} \text{ cm}^2/\text{Vs}$  for linear regime operation and  $6.1 \times 10^{-5} \text{ cm}^2/\text{Vs}$  for saturation regime operation. The fitted threshold voltage extracted in the saturation regime was -4.4 V.

Von Malm [102] previously reported that the field-effect mobility of holes in an  $\alpha$ -NPB thin film utilizing a bottom-contact field-effect transistor was  $4.58 \times 10^{-5} \text{ cm}^2/\text{Vs}$  ( $W = 20 \text{ cm}$ ,  $L = 5 \mu\text{m}$ ,  $C_i = 15 \text{ nF}/\text{cm}^2$ ). Therefore, this result agrees very well with the results obtained in this experiment. Other results were also reported by other groups by means of TOF techniques, bottom-contact FET methods and transient electroluminescence measurements. Chen *et.al* measured the hole mobility in thin films of  $\alpha$ -NPB by utilizing TOF methods with  $\alpha$ -NPB thickness of  $1 \mu\text{m}$  and at an electric field of  $10^5 \text{ V}/\text{cm}$  [103]. They reported a mobility of  $5.1 \times 10^{-4} \text{ cm}^2/\text{Vs}$ . Sizuka *et al.* also reported the field-effect mobility of hole in  $\alpha$ -NPB thin films using a bottom-contact FET ( $W = 116 \text{ mm}$ ,  $L = 100 \mu\text{m}$ ,  $C_i = 17.3 \text{ nF}/\text{cm}^2$ ) and the temperature of substrate during thermal evaporation was



kept constant at 80 °C [104]. A hole mobility of  $9.3 \times 10^{-8} \text{ cm}^2/\text{Vs}$  was reported. This value is in contrast with the values obtained in this thesis. The difference in mobility values is caused by different substrate temperature during thermal evaporation at which the substrate temperature in this experiment was 25 °C. On the other hand, the hole mobility values obtained from the FET technique is one order of magnitude lower than the values obtained from the TOF technique. Kovac *et al.* utilized transient electroluminescence (TEL) measurements to extract the hole mobility in  $\alpha$ -NPB thin films [105]. They found a mobility of  $(1 - 3) \times 10^{-4} \text{ cm}^2/\text{Vs}$ , which is similar to the values obtained from the TOF technique. Table 6.3 displays the hole mobilities in  $\alpha$ -NPB thin films extracted from the TOF and FET techniques.

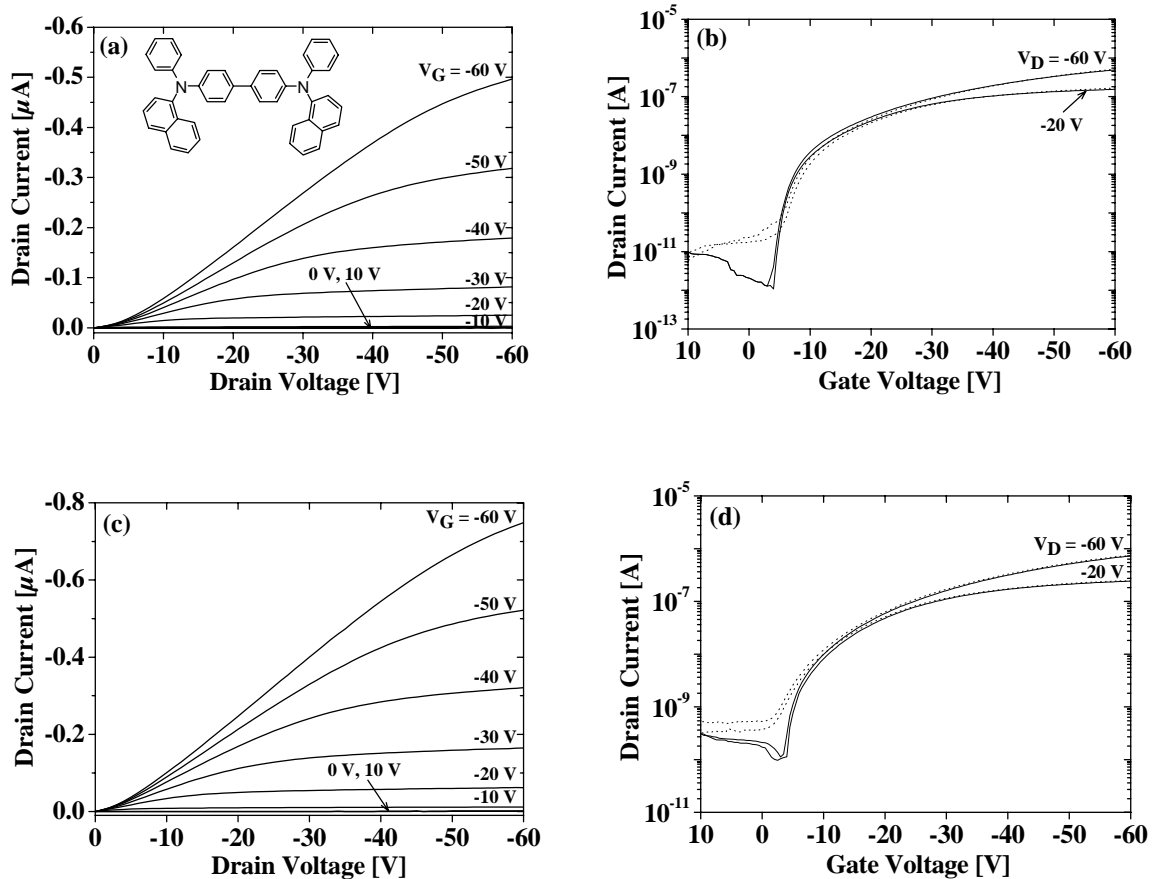


Figure 6.27. Output and transfer characteristics of an  $\alpha$ -NPB FET,  $W = 2 \text{ mm}$ ,  $L = 5 \text{ }\mu\text{m}$ ,  $C_i = 17.3 \text{ nF/cm}^2$ . (a). Output characteristics measured in air. The inset depicts the chemical structure of  $\alpha$ -NPB, (b). Transfer characteristics measured in air, (c). Output characteristics measured in vacuum, and (d). Transfer characteristics measured in vacuum.

Table 6.3. Hole mobilities in  $\alpha$ -NPB thin films extracted from the FET, TOF and TEL techniques.

Device and Material	Field-effect mobility $\mu$ [cm <sup>2</sup> /Vs]	Reference
FET $\alpha$ -NPB	$4.58 \times 10^{-5}$	102
TOF $\alpha$ -NPB	$5.1 \times 10^{-4}$	103
FET $\alpha$ -NPB	$9.3 \times 10^{-8}$	104
FET $\alpha$ -NPB	$(4 - 6) \times 10^{-5}$	This Work
TEL $\alpha$ -NPB	$(1 - 3) \times 10^{-4}$	105

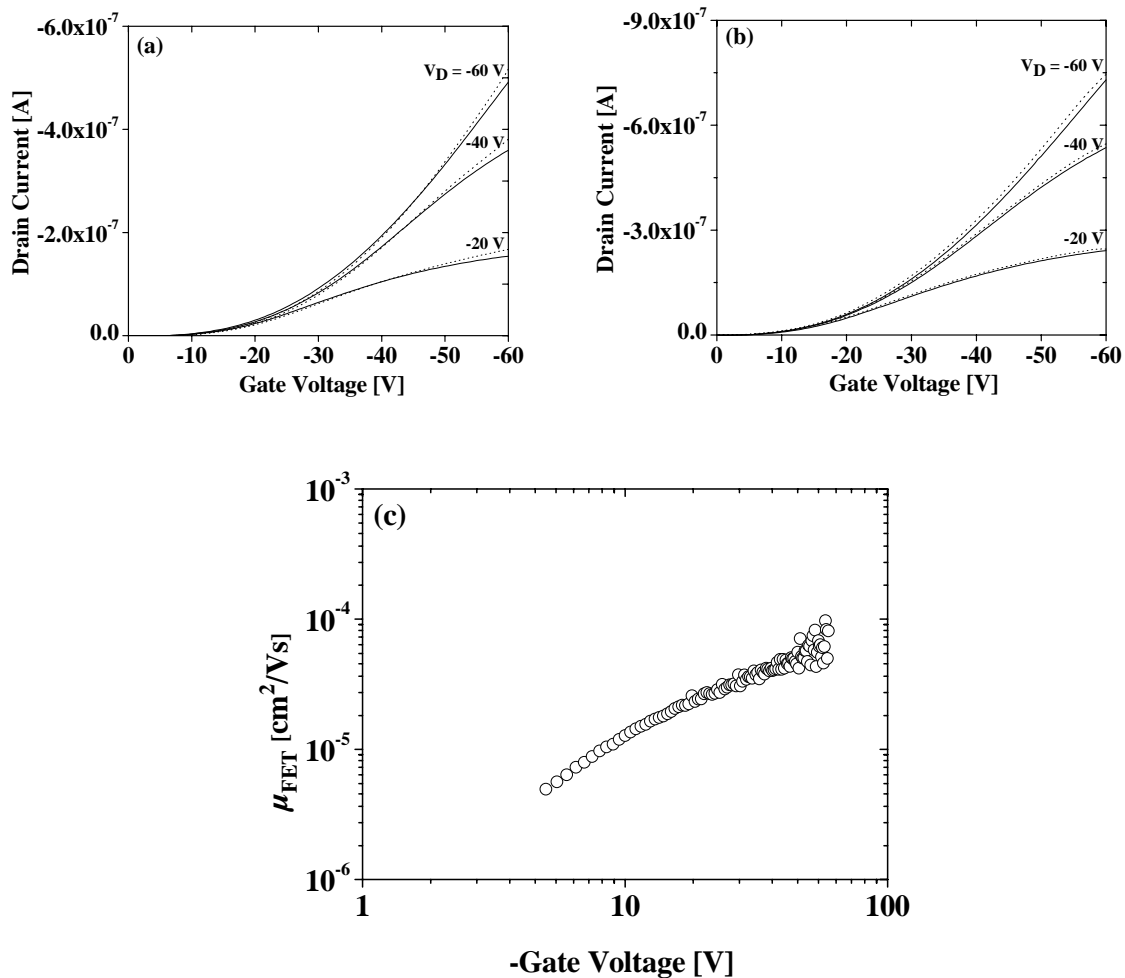


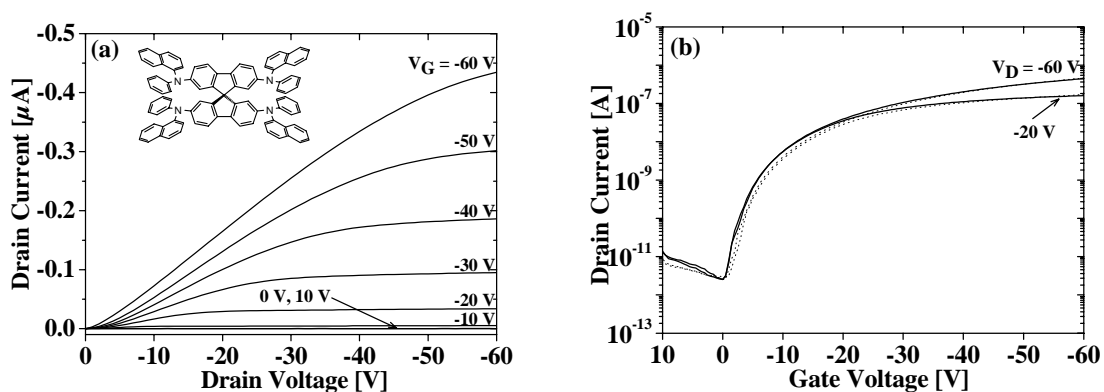
Figure 6.28. Hysteresis characteristics of an  $\alpha$ -NPB FET ( $W = 2$  mm,  $L = 5$   $\mu$ m,  $C_i = 17.3$  nF/cm<sup>2</sup>) measured at RT and in air (a) and in vacuum (b). (c). Variation of the hole mobility of an  $\alpha$ -NPB thin film as a function of gate bias at 294 K.

Figure 6.28(a) and 6.28(b) show the transfer characteristic of an  $\alpha$ -NPB FET measured in air and in vacuum, respectively. The drain current is clearly dependent on the environment, where measurement performed in vacuum exhibited higher drain current than that performed in air. The measurements performed in air involve moisture, which acts as a trap, and thus

limits the current between the source and drain electrodes. Figure 6.28(c) shows the variation of the field-effect mobility in an  $\alpha$ -NPB thin film for different gate biases. A variation of the hole mobility in the range of one order of magnitude was obtained as the gate bias is being scanned from -5 V to -60 V. The variation of the mobility value in  $\alpha$ -NPB films for varying gate voltages is the smallest value among the corresponding parent compounds. The mobility increases from  $5 \times 10^{-6} \text{ cm}^2/\text{Vs}$  at a gate bias of -5 V to  $8 \times 10^{-5} \text{ cm}^2/\text{Vs}$  at a gate bias of -60 V.

### 6.8. 2,2',7,7'-Tetra-(*N*-phenyl-1-naphthylamine)-9,9'-spirobifluorene (Spiro $\alpha$ -NPB)

Figure 6.29 and 6.30 show the output and transfer characteristics of a Spiro  $\alpha$ -NPB FET for a fresh sample and after the sample was stored in ambient atmosphere and at RT for 3 months. At low drain biases ( $V_D < -5 \text{ V}$ ), a nonlinear behavior of the drain currents versus drain bias was observed, which could be attributed to the non-ohmic contacts behavior between the gold electrodes and Spiro  $\alpha$ -NPB. There is a potential barrier ( $\sim 0.1 \text{ eV}$ ) for charge injection from the gold electrodes to Spiro  $\alpha$ -NPB. However, the field-effect mobility of holes measured upon exposure to air were  $1.5 \times 10^{-5} \text{ cm}^2/\text{Vs}$  extracted in the linear regime and  $2.9 \times 10^{-5} \text{ cm}^2/\text{Vs}$  extracted in the saturation regime. The fitted threshold voltages were -8.6 V for linear regime operation and -4.2 V for saturation regime operation. In contrast, the switch-on voltage of the device was 0 V, as shown in Figure 6.29(b). Moreover, *ON/OFF* ratios of typically  $6.4 \times 10^4$  for  $V_D = -20 \text{ V}$  and  $1.8 \times 10^5$  for  $V_D = -60 \text{ V}$  can be obtained from the transfer characteristics when the  $V_G$  is being scanned from 0 V to -60 V.



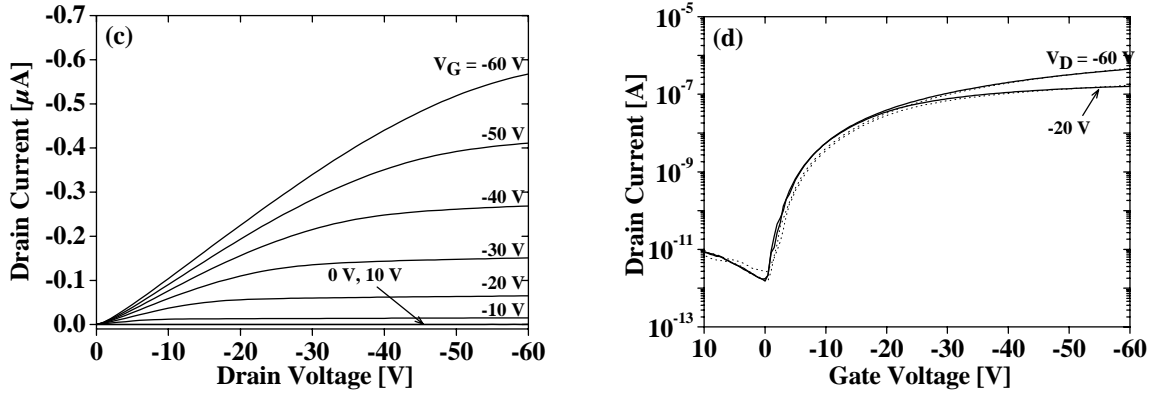
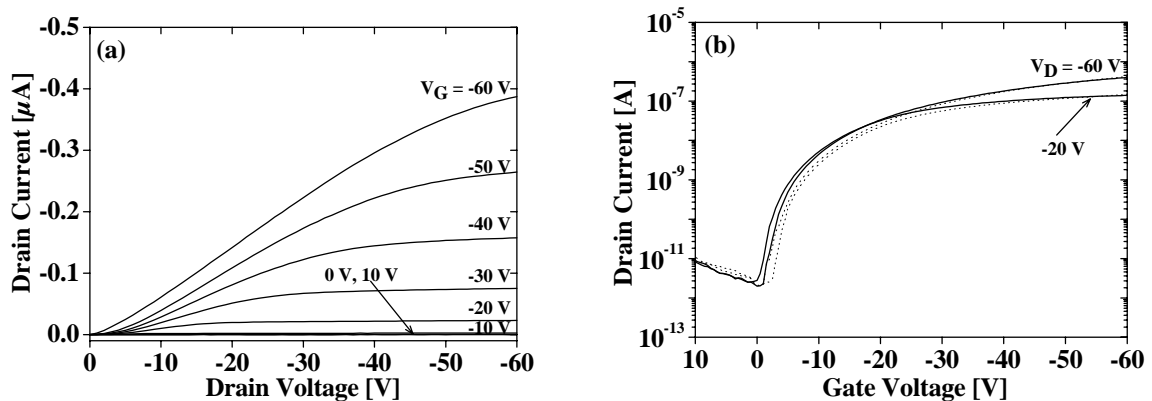


Figure 6.29. Output and transfer characteristics of a Spiro  $\alpha$ -NPB FET,  $W = 5$  mm,  $L = 10$   $\mu\text{m}$ ,  $C_i = 19.9$  nF/cm<sup>2</sup>. (a). Output characteristics measured in air. The inset depicts the chemical structure of Spiro  $\alpha$ -NPB, (b). Transfer characteristics measured in air, (c). Output characteristics measured in vacuum and (d). Transfer characteristics measured in vacuum. All measurements were performed after thermal evaporation of Spiro  $\alpha$ -NPB.

Figure 6.29(c) and 6.29(d) show the output and transfer characteristics measured in vacuum and at RT. The saturated drain current measured in vacuum was 30 % higher than the values measured in air. The fitted threshold voltage was -10.4 V extracted in the linear regime and -4.2 V extracted in the saturation regime. Hole mobilities were  $2.55 \times 10^{-5}$  cm<sup>2</sup>/Vs extracted in the linear regime and  $4.3 \times 10^{-5}$  cm<sup>2</sup>/Vs extracted in the saturation regime. These values were higher than those values obtained from the measurement performed in air. Comparing the measurement performed in air and under vacuum, the *ON/OFF* ratios of device measured in vacuum increased to  $1.1 \times 10^5$  for  $V_D = -20$  V and  $2.6 \times 10^5$  for  $V_D = -60$  V as the gate bias is being swept from 0 V to -60 V.



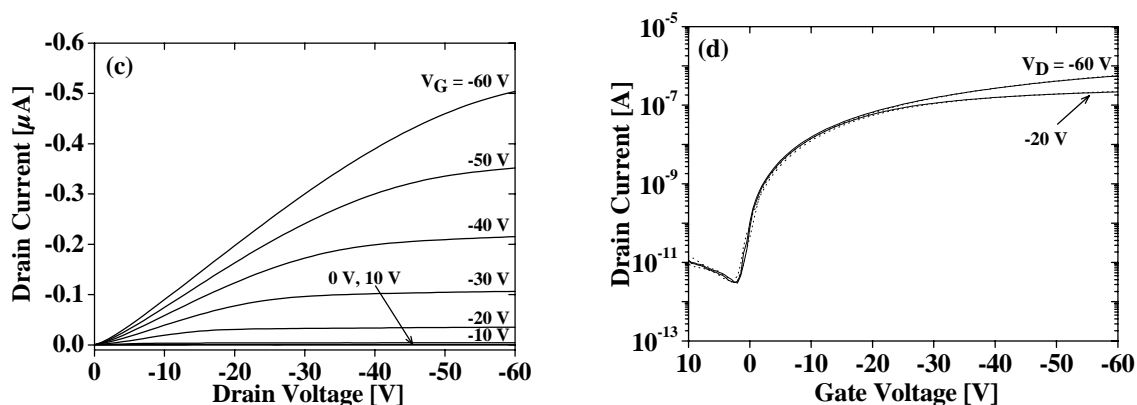


Figure 6.30. Output and transfer characteristics of a Spiro  $\alpha$ -NPB FET, which was measured after the sample was stored in ambient atmosphere for 3 months,  $W = 5$  mm,  $L = 10$   $\mu$ m,  $C_i = 19.9$  nF/cm<sup>2</sup>. (a). Output characteristics measured in air, (b). Transfer characteristics measured in air, (c). Output characteristics measured in vacuum, and (d). Transfer characteristics measured in vacuum.

The same device was then stored at RT and in ambient atmosphere for 3 months. After that, the transistor characteristics were measured again. It was found that after 3 months the saturated drain current decreased by 11 % and the hole mobility decreased by 4 %. Spiro  $\alpha$ -NPB thin films were relatively stable under operation in air and not influenced by moisture. These results are similar with the results obtained for Spiro-TAD or Spiro-TPD transistors in which the hole mobility decreased by ca.2 % after the sample was stored in ambient atmosphere and at RT for 9 months. On the other hand, the transistor turns on at 0 V and slightly shifts toward positive bias after 3 months ( $V_{so} \approx 1 - 2$  V). Similar result were also obtained for the fitted threshold voltage, which shifts from -4.2 V to -4.8 V for in air operation, after the sample was stored for 3 months in ambient atmosphere and at RT. Moreover, *ON/OFF* ratios of  $5 \times 10^4$  for  $V_D = -20$  V and  $2 \times 10^5$  for  $V_D = -60$  V can be obtained as the gate bias is being scanned from +1 V to -60 V and measured in air. The measurement carried out in vacuum gave *ON/OFF* ratios of  $7.2 \times 10^4$  for  $V_D = -20$  V and  $1.9 \times 10^5$  for  $V_D = -60$  V as the gate bias is being swept from +2 V to -60 V, which are lower than those measured for a fresh device.

Figure 6.31(a) and 6.31(b) show the hysteresis in the transfer characteristics of a Spiro  $\alpha$ -NPB FET measured in vacuum and in air. The drain current maximum measured in vacuum was 50% higher than the values measured in air. Furthermore, Figure 6.31(c) shows the dependency of the field-effect mobility on the geometry of devices. It is clear that the field-effect mobility of holes is not influenced by the geometry of devices as also observed for other spiro-linked compounds. Figure 6.32 shows the dependency of the field-effect mobility in a Spiro  $\alpha$ -NPB thin film on the gate bias. The mobility of hole in Spiro  $\alpha$ -NPB FET was

linearly dependent on the gate bias. Moreover, the mobility of hole in  $\alpha$ -NPB thin films is higher than that in Spiro  $\alpha$ -NPB thin films, as shown in the inset of Figure 6.32. For Spiro  $\alpha$ -NPB, the mobility increases from  $4.3 \times 10^{-6} \text{ cm}^2/\text{Vs}$  at  $V_G = -5 \text{ V}$  to  $3 \times 10^{-5} \text{ cm}^2/\text{Vs}$  at  $V_G = -60 \text{ V}$ . In contrast, the mobility increases from  $5 \times 10^{-6} \text{ cm}^2/\text{Vs}$  at  $V_G = -5 \text{ V}$  to  $8 \times 10^{-5} \text{ cm}^2/\text{Vs}$  at  $V_G = -60 \text{ V}$  for  $\alpha$ -NPB FETs.

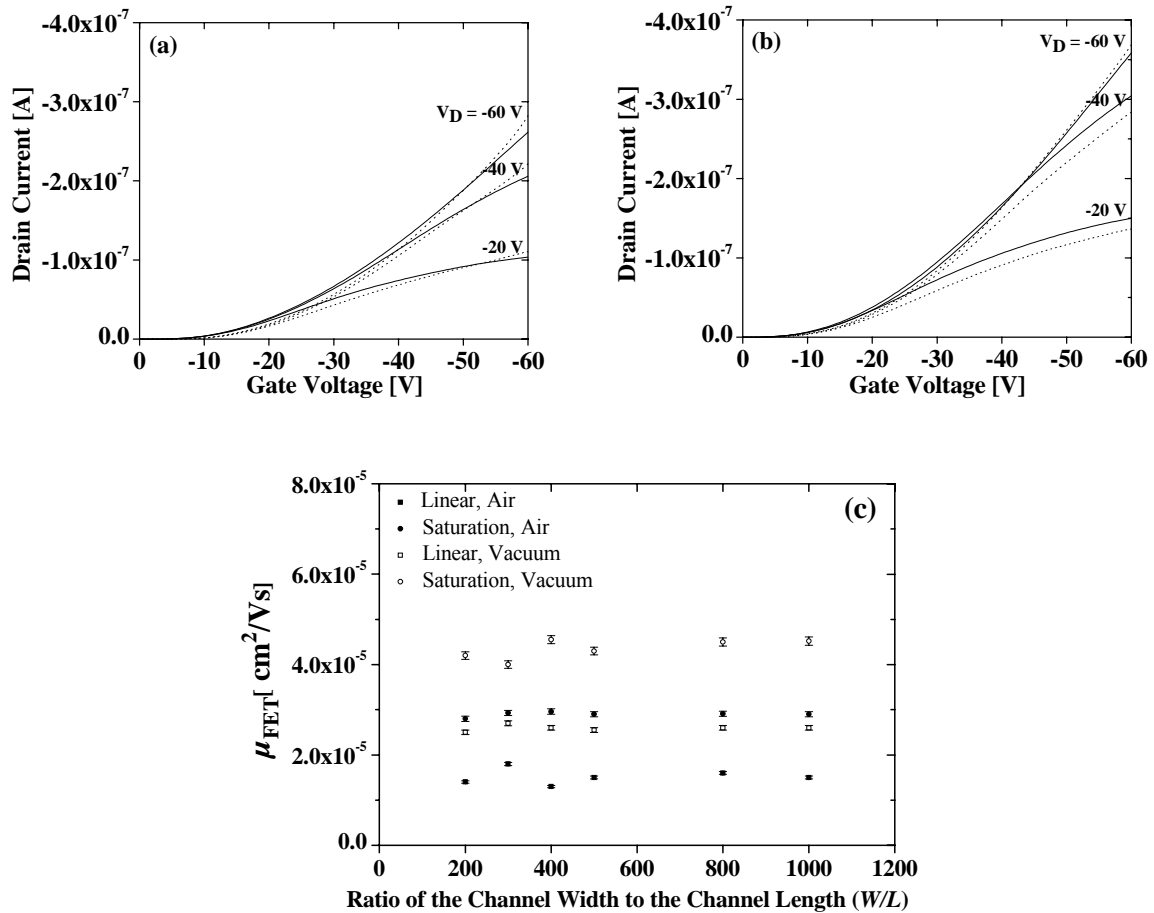


Figure 6.31. Hysteresis characteristics of a Spiro  $\alpha$ -NPB FET ( $W = 3 \text{ mm}$ ,  $L = 10 \text{ }\mu\text{m}$ ,  $C_i = 19.9 \text{ nF/cm}^2$ ) measured at RT and in air (a) and in vacuum (b). (c) The field-effect mobility of charge carriers in Spiro  $\alpha$ -NPB thin films at different ratios of the channel width to the channel length ( $W/L$ ).

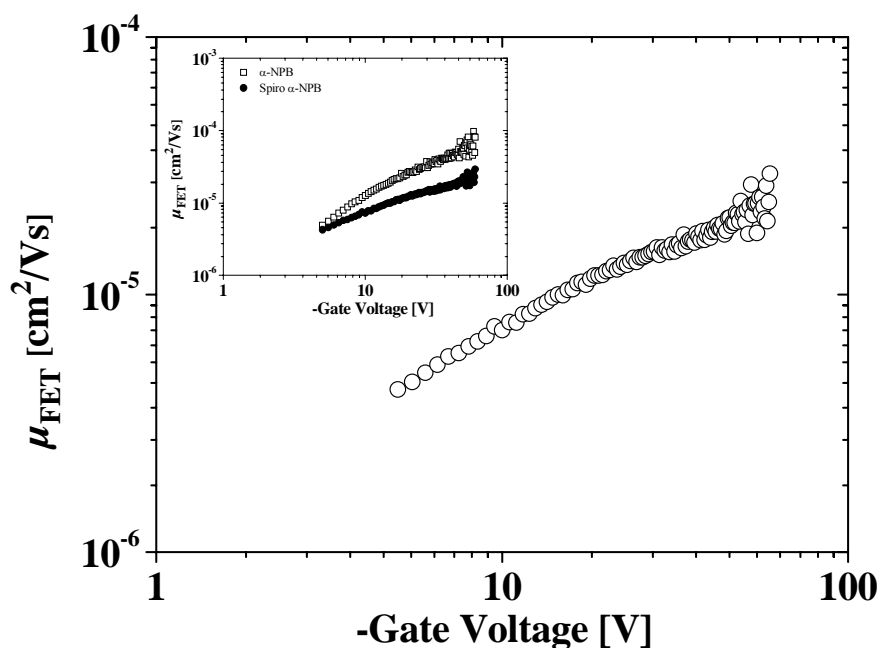


Figure 6.32. Variation of the hole mobility of a Spiro  $\alpha$ -NPB thin film as a function of gate bias at 294 K. The inset shows gate-voltage dependent mobility of  $\alpha$ -NPB (from Figure 6.28(c)) and Spiro-TTB based-field-effect transistors measured at 294 K.

### 6.9. The Influence of a methyl group in symmetrically spiro-linked compounds

In the last section of this chapter, the influence of methyl group on *para* or *meta* positions in spiro-linked compounds is presented. Three materials were used, namely Spiro-TAD, Spiro-TPD, and Spiro-TTB. In order to compare their charge transport, the same geometry of the FETs was used. The channel width was 3 mm and the channel length was 5  $\mu\text{m}$ . In addition, all devices have the same capacitance of the gate dielectric.

At low drain biases, Spiro-TAD transistors exhibited a *near* ohmic contact with the gold electrodes. On the contrary, Spiro-TPD and Spiro-TTB showed a nonlinear behavior especially at drain biases of lower than -5 V, as shown in Figure 6.33. This behavior can be explained by utilizing the metal-semiconductor theory, which is adopted from conventional MOSFET theory. The HOMO level of Spiro-TAD, Spiro-TPD, and Spiro-TTB laid at -5.00 eV, -4.97 eV, and -4.875 eV.

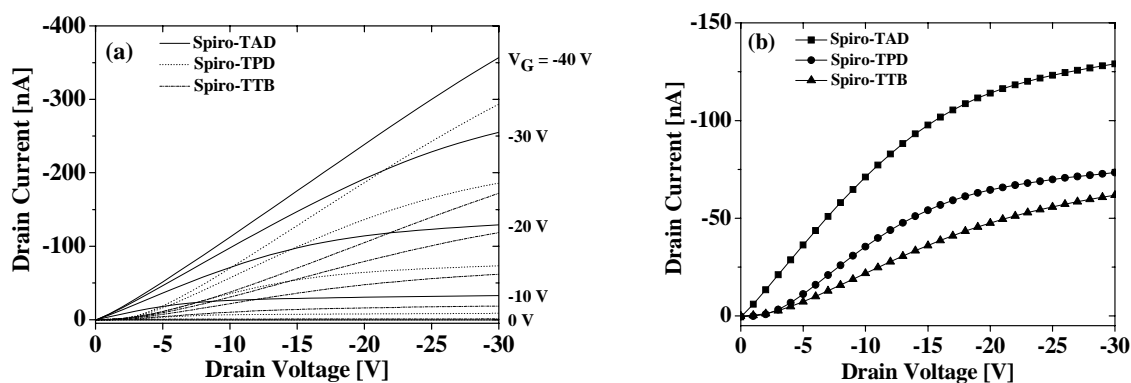


Figure 6.33.(a).Output characteristics of Spiro-TAD, Spiro-TPD, and Spiro-TTB transistors with a channel length of  $5 \mu\text{m}$  and a channel width of  $3 \text{ mm}$ . All devices have the same capacitance per unit area of the gate dielectric. (b).The output characteristic was plotted only at a gate bias of  $-20 \text{ V}$ .

Figure 6.34 shows the visualization of the *energy “band” diagrams* of the gold electrodes-spiro-linked compounds contacts. In this context, the smallest potential barrier ( $\sim 0.1 \text{ eV}$ ) is obtained for charge injection from the gold electrodes to Spiro-TAD. In contrast, Spiro-TTB builds a potential barrier of  $0.225 \text{ eV}$  for charge injection with respect to the gold electrodes, which is the largest potential barrier for charge injection among the spiro-linked compounds. Therefore, the charge injection between the gold electrodes and Spiro-TAD is more efficient than that between the gold electrodes and Spiro-TPD or Spiro-TTB. Introducing methyl groups either in *para* or *meta* positions will decrease the HOMO level of the corresponding compounds with respect to the vacuum level. However, a relative large potential barrier will exist with respect to the work function of the gold electrode. A potential barrier between the metal and the active material does not solely determine the current injection. A nonlinear behavior in the output characteristics of a FET was also reported by CNRS group (France). They addressed the effects of the non-ohmic contacts to a series resistance between the organic layer and the gold contacts [23]. On the other hand, ultraviolet photoelectron spectroscopy (UPS) study revealed the existence of electron and hole barriers for several materials [106,107]. These barriers can be attributed to a dipole layer between the metal electrode and the first layer of the active materials. Consequently, the charge injection will be limited. However, the nonlinearity in the output characteristics is not fully understood yet.



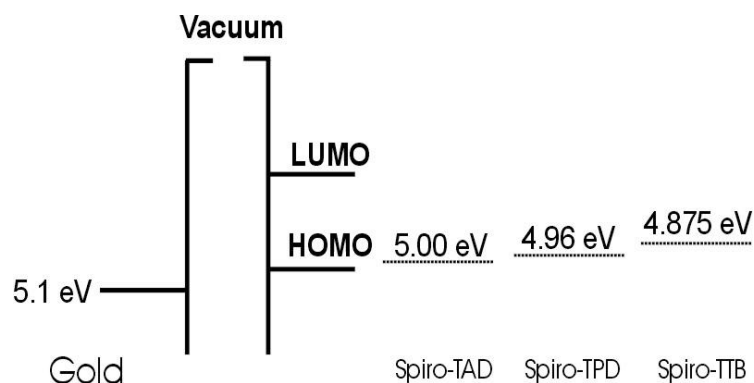


Figure 6.34. Visualization of the energy “band” diagrams of Metal-Semiconductor contacts.

## 6.10. Summary of chapter 6

The hole mobilities in TAD, TPD, TTB,  $\alpha$ -NPB, Spiro-TAD, Spiro-TPD, Spiro-TTB, and Spiro  $\alpha$ -NPB thin films have been extracted by utilizing field-effect transistors methods. Table 6.4 shows the average values of the hole mobilities in corresponding thin films extracted in the linear regime and in the saturation regime. The measurements were also performed in air and in vacuum. The hole mobilities in the linear regime are slightly lower than the values measured in the saturation regime. Moreover, the hole mobilities measured in vacuum are larger than those measured upon exposure to air. It indicates that oxygen or moisture acts as a dopant, prohibiting the hopping transport of positive charges, which form radical cations when sitting on a molecule.

The hole mobilities in thin films of Spiro-TAD and Spiro TTB are higher than the hole mobilities in their corresponding parent compound TAD and TTB. In contrast, the hole mobilities in TPD and  $\alpha$ -NPB thin films are higher than the hole mobilities in Spiro-TPD and Spiro  $\alpha$ -NPB. However, the field-effect mobilities of charge carriers in spiro-linked compounds and their corresponding parent compounds are in the same order of magnitude ( $\sim 10^{-5}$  cm<sup>2</sup>/Vs). Spiro-linked compounds have formed morphologically very stable thin amorphous films. Moreover, the hole mobilities in these thin films did not significantly change after the samples were stored in ambient atmosphere and at RT up to nine months. In contrast, the hole mobilities in thin films of the corresponding parent compounds decreased with increasing time of exposure to air as well as when the samples were kept under vacuum, resulting in a complete loss of FET performance. In conclusion, the introduction of a spiro center between two identical hole transport moieties strongly improves the thermal stability of

the amorphous state, without substantially changing the mobilities of positive charges. Despite the mobilities of charge carrier of both classes being in the same order of magnitude, spiro-linked compounds thin film transistors are more stable under operation in air than thin film transistors based on their corresponding parent compounds.

Table 6.4. Hole mobilities in hole transporters extracted from FET measurements.

Material	Hole Mobility Linear regime, in air [ $10^{-5}$ cm <sup>2</sup> /Vs]	Hole Mobility Saturation regime, in air [ $10^{-5}$ cm <sup>2</sup> /Vs]	Hole Mobility Linear regime, in vacuum [ $10^{-5}$ cm <sup>2</sup> /Vs]	Hole Mobility Saturation regime, in vacuum [ $10^{-5}$ cm <sup>2</sup> /Vs]	Stability
TAD	1.7	4.4	2.9	6.7	Not stable in air, transistor effect vanished after 175 hours stored under vacuum
Spiro-TAD	3.3	5.7	4	7	Stable in air up to 9 months, mobility decreased by 2 %
TPD	5.6	7.4	6.3	8.5	Stable in air for One week
Spiro-TPD	2.5	5.2	3.7	7	Stable in air up to 9 months, mobility decreased by 3 %
TTB	0.63	1.12	1.4	1.8	Not stable in air
Spiro-TTB	2.3	3.2	4	5.9	Stable in air up to 4 months, mobility decreased by 13 %
$\alpha$ -NPB	2.4	4.1	3.5	6.1	Not stable in air
Spiro $\alpha$ -NPB	1.5	2.9	2.55	4.3	Stable in air up to 3 months, mobility decreased by 4 %

## Chapter 7

# Temperature-Dependence in Low Molecular Amorphous Thin Films

In this chapter, the characteristic features of temperature dependent behavior for all materials used in this study are presented. The materials used in this study are amorphous, as described in chapter 5. However, the mobility value of charge carriers in amorphous materials obtained from field-effect transistor methods is too small to be described by band transport. Hence, it has been generally accepted that the charge transport takes place by hopping between localized states. As presented in the previous chapters, the materials used in this study are *p*-type semiconductors. Consequently, the charge transport is governed by positive charges (holes), which form radical cations when located on a molecule. Generally, hole or electron transport occurs by the transfer of charges from states associated with the donor or acceptor functionalities. For hole transport, molecules (or polymers) are initially positively charged (radical cation). Under an applied electric field, neutral molecules will transfer electrons to the radical cation, this process results in the motion of positive charge. This occurs only if the molecules behave donor-like in their neutral state. For electron transport, electrons are displaced from the anion radicals to neutral molecules, which require that the functionalities be acceptor-like in the neutral state [59].

A few models have been proposed to explain temperature and electric dependencies of the mobility of charge carriers in amorphous materials, which include the Arrhenius model [58] and the Gaussian disorder formalism [52,59]. First, the Arrhenius model describes the hopping transport as resulting from a single level of traps or an activation energy arising from polaron relaxation and is described by the expression in equation 2.24 [58]. Second, the Gaussian disorder (GD) model or Bässler model uses the notion that both the energy levels and intersite distance of the transport sites are subject to a distribution in an amorphous solid medium. The authors assume a Gaussian distribution for both the energetic and the positional disorder supported by the fact that the absorption profiles of amorphous materials generally feature Gaussian line shapes. Monte Carlo simulations are based on the Miller-Abrahams

jump rates of hopping process from within a Gaussian distribution of localized states, which results in equation 2.18.

In this chapter, hysteresis in the transfer characteristics is defined as the difference in the current-bias curve, when during a measurement the bias (gate or drain bias) is swept from *OFF* state (low bias) to *ON* state (high bias), the advancing curve, and vice versa, the receding curve. The transfer curve presented here was swept from *ON* state to *OFF* state (dotted line), advancing curve, and vice versa (solid line), receding curve.

### 7.1. *N,N,N',N'*-Tetraphenylbenzidine (TAD)

*N,N,N',N'*-Tetraphenylbenzidine (TAD) thin films showed a lack of morphological stability as presented previously in chapter 5 so that it significantly influences the transistor performances. Figure 7.1(a) shows the hysteresis in the transfer curves of a TAD field-effect transistor (FET) measured in vacuum and at different temperatures, whereas the drain bias was kept constant at -60 V. It has been shown in Figure 7.1(a) that the magnitude of the hysteresis strongly decreases with decreasing temperature, so only at relatively high temperatures the measurements will be negatively affected. The hysteresis of the curve measured near room temperatures (RT) was small and the hysteresis was completely absent at lower temperatures. This is probably due to the number of charge carriers obtained between the advancing and the receding curve being similar. In contrast, the hysteresis was clearly observed at high temperatures, which could be attributed to the fact that the number of charge carriers from the receding measurement (dotted lines) is smaller than the values obtained from the advancing measurement (solid lines). Some possible causes are charge trapping at the interface between the active layer and the SiO<sub>2</sub>-gate dielectric layer [108,109], defect sites in the active layer [110,111], oxygen and water vapor [94,95]. However, the origin of this effect is not understood at this time and is a very interesting subject for further studies, especially from the application point of view.

Along with the hysteresis in the transfer characteristics, the fitted threshold voltages shift towards small bias with increasing temperatures, as shown in Figure 7.1(b). Similar results were also observed for FETs based on pentacene, quaterthiophene, and sexithiophene [112,113]. The threshold voltage in organic transistors is indicative of the trap density. When the magnitude of trapped charge is high, the threshold voltage is large in magnitude and when the extent of trapping is low, the threshold voltages and changes in threshold voltage with

temperature are relative small [114]. Figure 7.1(b) shows that the threshold voltages shift towards small bias with increasing temperature. It implies that the charge transport is thermally activated. As the temperature is increased, the charges have more thermal energy to hop from one molecule to the next. Therefore, the number of trapped charges also gets lower with increasing temperature. This agrees with the shift of the threshold voltage towards small bias with increasing temperature, as shown in Figure 7.1(b).

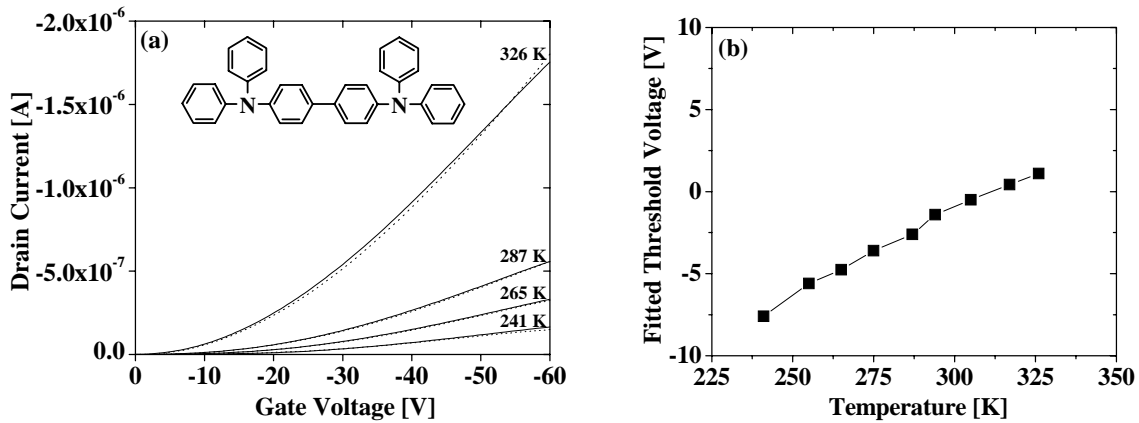


Figure 7.1.(a).Hysteresis characteristics of a TAD FET measured at different temperatures. The drain bias was kept constant at -60 V. The inset shows the chemical structure of TAD. (b).The fitted threshold voltages are linearly plotted against temperatures.

Figure 7.2(a) and 7.2(b) show the mobility of charge carriers in TAD thin films as a function of temperature. The dependency of the field-effect mobility on the temperatures is shown in two representations, namely a reciprocal of temperature in the Arrhenius representation and an inverse square of temperature in the GD Model. The Arrhenius model fits the data better than the GD model, as indicated by standard deviation of the fitting. The standard deviation of the fitting for the Arrhenius model is 0.02. In contrast, the standard deviation of the fitting for the GD model is 0.05. Furthermore, the residual values, which are defined as the difference between the experimental data and the fitted line, are also displayed in Figure 7.2(c) and 7.2(d). The fluctuation of the residual values in the Arrhenius model is smaller than the fluctuation in the GD model. Furthermore, prefactor mobilities of  $7.6 \times 10^{-2} \text{ cm}^2/\text{Vs}$  and  $4.4 \times 10^{-3} \text{ cm}^2/\text{Vs}$  were obtained from the Arrhenius and the GD Model, respectively. The Arrhenius plot yields an activation energy for the hole mobility of 0.22 eV, which corresponds to shallow trapping sites. The relation between the activation energy  $E_a$  and the width of the energetic disorder distribution  $\sigma$  is given by equation 2.21 [52]. If the value of the activation energy is inserted in equation 2.21, a value of 0.080 eV was obtained

for  $\sigma$ . On the other hand, the GD model gave a width of the energetic disorder distribution  $\sigma$  of 0.077 eV, which has a corresponding  $T_o$  of 596 K ( $T_o = 2\sigma/3k$ ). The  $\sigma$  values obtained from both methods gave a difference of 0.003 eV, which is a very small value and can be neglected. From the GD model, an  $E_a$  value of 0.203 eV was obtained, which is 0.017 eV lower than the value obtained from the Arrhenius model.

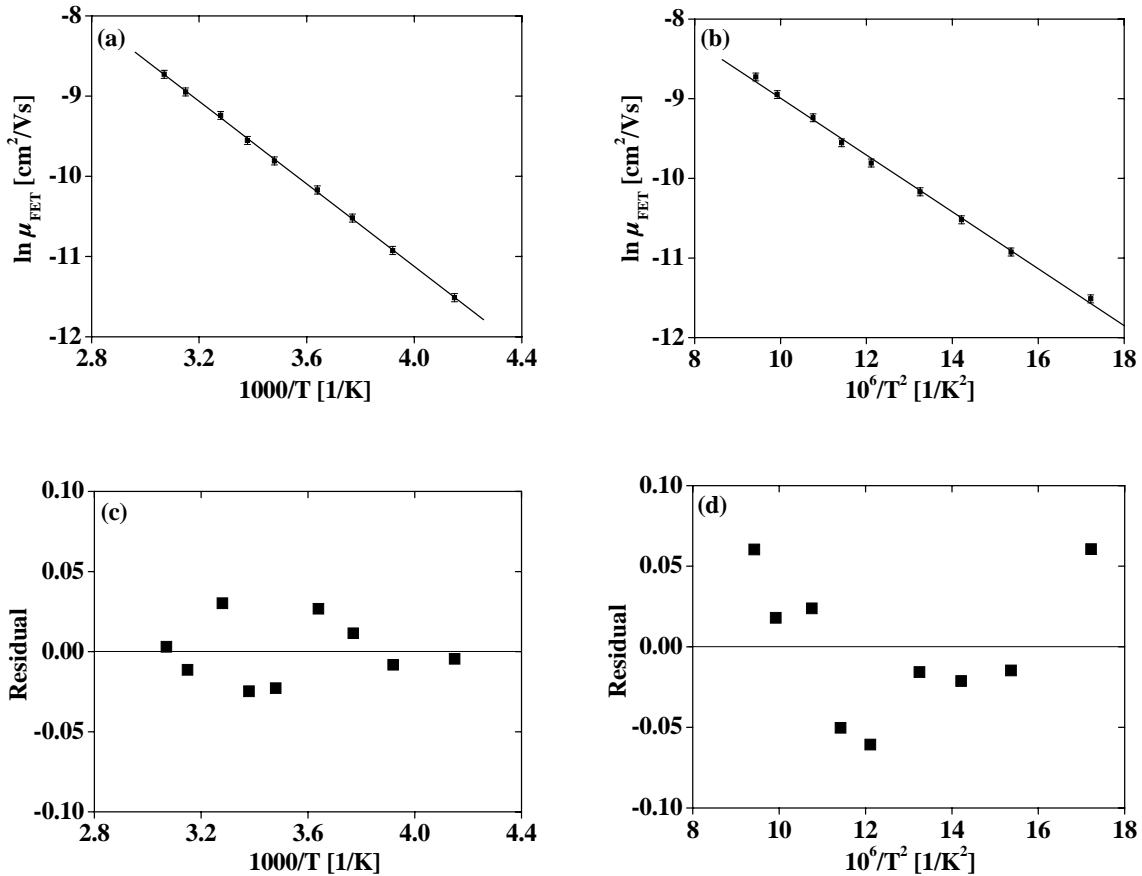


Figure 7.2. Field-effect mobilities of charge carriers in a TAD thin film against (a) The reciprocal of the temperature in the Arrhenius representation, and (b) The inverse square of the temperature in the GD Model. The residual is plotted versus (c) the inverse of the temperature, and (d) the inverse square of the temperature.

Figure 7.3 shows the gate bias dependence of the field-effect mobility in a TAD FET at different temperatures. The mobilities were calculated as described previously in chapter 2. The dependence of the field-effect mobility on the gate bias was quasi-linear for different temperatures. When the data, as shown in Figure 7.3, is fitted to  $\mu(V_G) \propto \text{const.} \times V_G^\lambda$ , then it yields  $\lambda$  of  $0.68 \pm 0.05$ ,  $0.94 \pm 0.02$ ,  $1.03 \pm 0.01$ , and  $1.11 \pm 0.01$  for 241 K, 275 K, 294 K, and 326 K, respectively. The coefficient  $\lambda$  describes how fast the mobility increases with increasing gate bias. If  $\lambda$  is large, the mobility strongly depends on the gate bias. On the other hand, if  $\lambda$  is small, it implies that the mobility is weakly dependent on the gate bias. As shown

in Figure 7.3, the  $\lambda$  values increase with increasing temperature. This implies that at low temperatures the mobility of holes is weakly gate dependent with respect to the mobility at high temperatures. At low temperatures, the weak gate dependence of the mobility is due to low thermal energy for charge carriers to hop from one molecule to the adjacent. As a result, the mobility is weakly dependent on the gate bias and a high threshold voltage is obtained at low temperatures.

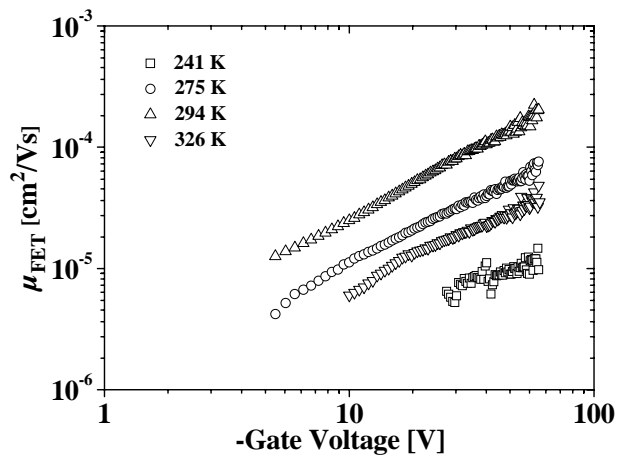


Figure 7.3. Gate bias and temperature dependence of the field-effect mobility of charge carriers in a TAD FET ( $W = 2$  mm,  $L = 5$   $\mu$ m,  $C_i = 17.3$  nF/cm<sup>2</sup>). The curve is plotted as a function of the gate bias for various temperatures ( $T = 241$  K, 275 K, 294 K, 326 K).

## 7.2. 2,2',7,7'-Tetrakis-(diphenylamino)-9,9'-spirobifluorene (Spiro-TAD)

Figure 7.4 (a) shows the hysteresis in the transfer characteristics of a Spiro-TAD FET measured in vacuum and at different temperatures. The magnitude of hysteresis in the transfer characteristics was clearly observed with increasing temperature. The fitted threshold voltage also increases toward positive bias with increasing temperature, as shown in Figure 7.4(b). Both effects have been described in the previous sub-chapter. Figure 7.5(a) and 7.5(b) represent the field-effect mobilities presented in the Arrhenius and the GD model, respectively. The fitted line in Figure 7.5(a) and 7.5(b) satisfy the corresponding model, the Arrhenius and the GD model, quite well. However, the fitted line in the Arrhenius model is better than that in the GD model. The standard deviation of the fitting in the Arrhenius model is 0.03 and is 0.13 in the GD model. Moreover, Figure 7.5(c) and 7.5(d) represent the residual values plotted against  $1/T$  and  $1/T^2$ , respectively. The fluctuation of the residual values in the

Arrhenius model is more distributed around the middle (residual value = 0) than that in the GD model.

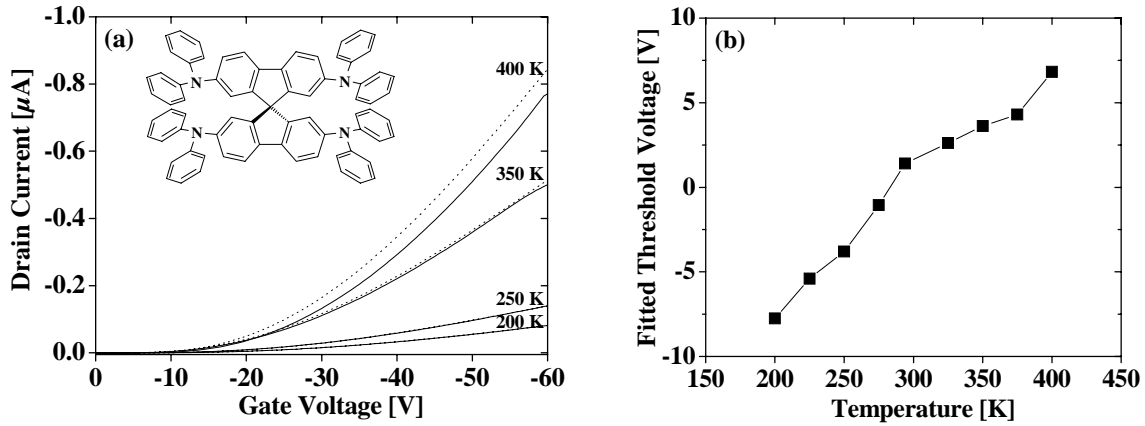


Figure 7.4.(a).Hysteresis characteristics of a Spiro-TAD FET measured at different temperatures. The drain bias was kept constant at -60 V. The inset shows the chemical structure of Spiro-TAD. (b).The fitted threshold voltages are linearly plotted against temperature.

The Arrhenius model gave a prefactor mobility  $\mu_o$  of  $4.0 \times 10^{-3} \text{ cm}^2/\text{Vs}$  and an activation energy of 0.110 eV. If equation 2.21 was used, a value of  $\sigma_{ar} = 0.057 \text{ eV}$  was obtained. The notation  $\sigma_{ar}$  and  $\sigma_{gd}$  denote the width of the energetic disorder distribution obtained from the Arrhenius and the GD model, respectively. On the other hand, the GD model gave a prefactor mobility of  $4.0 \times 10^{-4} \text{ cm}^2/\text{Vs}$  and a  $\sigma_{gd}$  of 0.057 eV ( $T_o = 441 \text{ K}$ ). If the  $\sigma_{gd}$  is inserted in equation 2.21, the activation energy of 0.111 eV was obtained, which agrees very well with the values obtained from the Arrhenius model. These values were lower than the values obtained from the TOF technique, as reported by Bach *et al.* [73]. A prefactor mobility of  $1.6 \times 10^{-2} \text{ cm}^2/\text{Vs}$  and a width of Gaussian distribution  $\sigma$  of 0.080 eV were reported. The  $\mu_o$  obtained from the TOF technique is 1 – 2 orders of magnitude higher than that obtained from the FET technique. Moreover, the width of density of states (DOS) obtained from the TOF technique is also higher than that obtained from the FET method. However, the origin of this discrepancy is not understood at this time. Additionally, a similar spiro-compound, namely 2,2',7,7'-tetrakis-(*N,N*-di-*p*-methoxyphenylamino)-9,9'-spirobi-fluorene (Spiro-OMeTAD) has a prefactor mobility of  $4.7 \times 10^{-2} \text{ cm}^2/\text{Vs}$  and an energetic disorder of 0.101 eV [89].



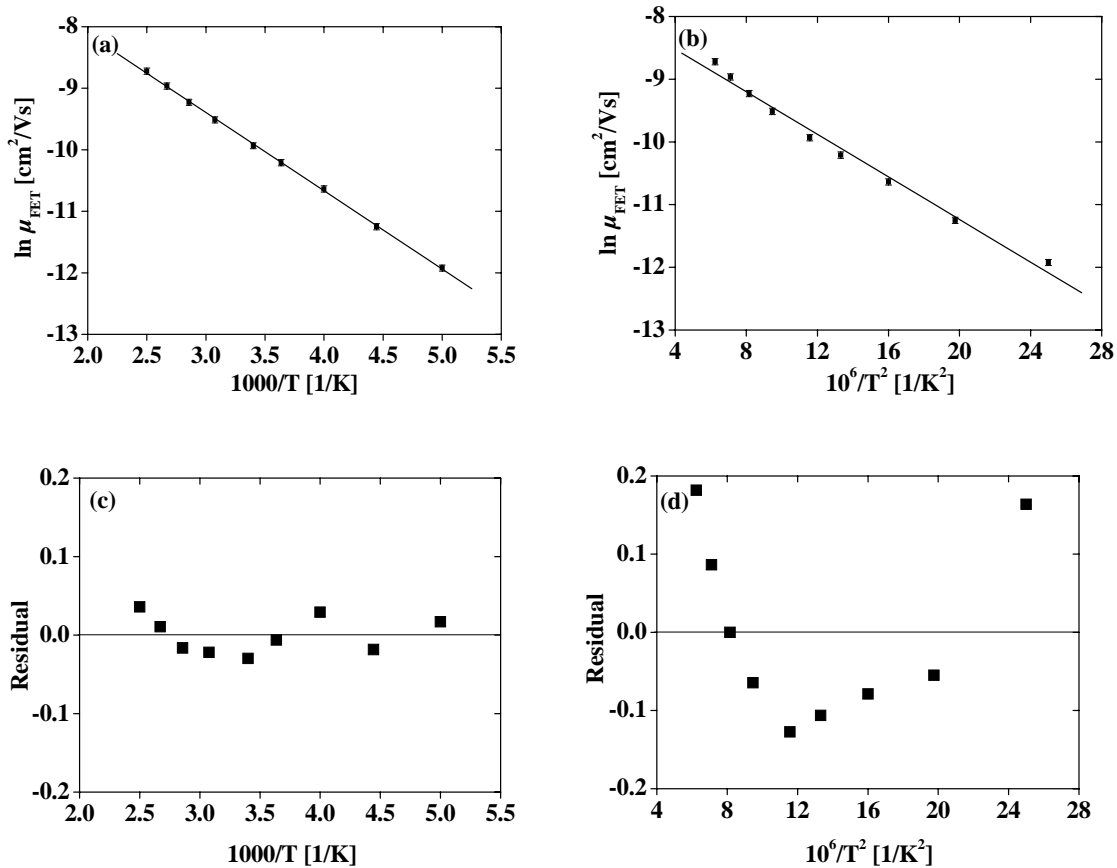


Figure 7.5. Field-effect mobilities of charge carriers in a Spiro-TAD thin film against (a). The reciprocal of the temperature in the Arrhenius representation, and (b). The inverse square of the temperature in the GD Model. The residual is plotted versus (c) the inverse of the temperature, and (d) the inverse square of the temperature.

The field effect mobilities of charge carriers in thin films of TAD and Spiro-TAD were already presented. First, in the Arrhenius models the prefactor mobility of both materials is different by a factor of 19. The prefactor mobility of TAD is higher than that of Spiro-TAD. Second, the activation energy of Spiro-TAD is exactly a half of the activation energy of TAD. On the contrary, the width of DOS of TAD is much larger than that of Spiro-TAD. It can be understood that the width of DOS describes the fluctuation of hopping site energy. Moreover, it arises from the superposition between intermolecular and intramolecular contributions [52,115]. Intermolecular contribution arises from the fluctuation of polarization energy due to charge-dipole and Van-der-Waals interactions. In contrast, intramolecular contribution arises from the variation of the molecular geometry due to bond rotation. As a result, the difference in the variation of molecular geometry may also lead to the difference in the fluctuation of the polarization energy. Therefore, the variation of the molecular geometry of Spiro-TAD is probably smaller than TAD or TPD due to the rigid structure of the spiro-linked compound. It suggests that decreasing the variation of molecular geometry by restricting the internal

rotation or by increasing the symmetry of the compound results in the decrease of the width of the DOS like what we obtained for spiro-linked compound. However, the field-effect mobilities of charge carriers in both thin films are in the same order of magnitude. This implies that the spiro junction does not significantly influence the effective mobility, but rather gives a narrow DOS caused by two perpendicular TAD molecules linked by a spiro center. It is well known that the DOS is determined by dipole moments of constituents. Furthermore, the prefactor mobility is also dependent on the dipole moment of the molecules which decreases with increasing dipole moment.

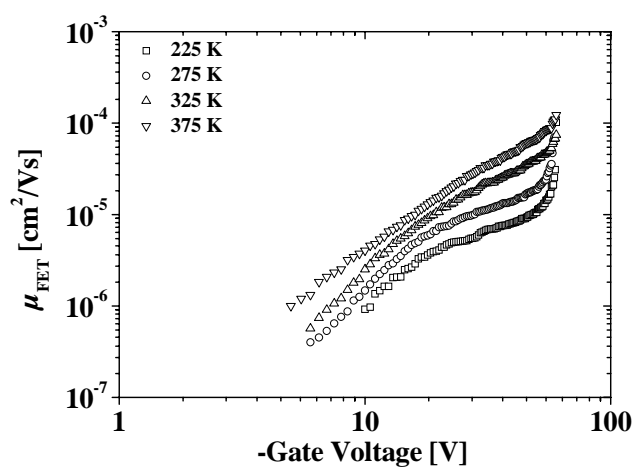


Figure 7.6. Gate bias and temperature dependence of the field-effect mobility of charge carriers in a Spiro-TAD FET ( $W = 2$  mm,  $L = 10$   $\mu\text{m}$ ,  $C_i = 19.9$  nF/cm<sup>2</sup>). The curve is plotted as a function of the gate bias for various temperatures ( $T = 225$  K, 275 K, 325 K, 375 K).

Figure 7.6 shows the gate bias dependence of the field-effect mobility in a Spiro-TAD FET at different temperatures. At  $|V_G| < 40$  V, the dependence of the field-effect mobility on the gate bias was quasi-linear for different temperatures. However, the mobility goes over to a super-linear increase for  $|V_G| > 40$  V. It can be understood by observing the output characteristic of the corresponding transistors, as shown previously in chapter 6. At large gate biases and at a given drain bias (for instance  $V_D = -10$  V), the transconductance  $g_m$  (see equation 2.13) was small because the drain current saturated. This is due to non-ohmic contact behavior between the materials and the gold electrodes. As a result, the mobility is large as the  $g_m$  is small according to equation 2.14. When the data (for  $|V_G| < 40$  V) in Figure 7.6 is fitted to  $\mu(V_G) \propto \text{const.} \times V_G^\lambda$ , then it yields  $\lambda = 1.30 \pm 0.04$ ,  $1.70 \pm 0.05$ ,  $1.87 \pm 0.04$ , and  $1.82 \pm 0.01$  for 225 K, 275 K, 325 K, and 375 K, respectively. The coefficient  $\lambda$  decreased at a temperature of 375 K, which can be possibly caused by a dynamic process in thin films near

the glass temperature ( $T_g$ ) of Spiro-TAD. The coefficient  $\lambda$  obtained for Spiro-TAD is slightly higher than that obtained for TAD. This implies that the mobility of hole in Spiro-TAD is stronger dependent on the gate bias than that in TAD.

### 7.3. *N-N'*-Bis(3-methylphenyl)-(1,1'-biphenyl)-4,4'-diamine (TPD)

Figure 7.7(a) shows the transfer characteristics of a TPD FET measured at different temperatures. No hysteresis has been observed. The fitted threshold voltage was also linearly plotted against temperature, as shown in Figure 7.7(b). The fitted threshold voltage change in field-effect transistors (FETs) of TPD is smaller than those in FETs of TAD and Spiro-TAD. This implies a small bias is required, especially at high temperatures, to fill the lower-lying state of the active layers. Furthermore, Figure 7.8 shows the field-effect mobilities of charge carriers are plotted in the Arrhenius and the GD model, whereas the fitting in the Arrhenius model was better than that in the GD model. The standard deviation of the fitting for the Arrhenius model is 0.5 and is 1.0 for the GD model. In addition, the fluctuation of the residual values in the Arrhenius model is smaller than that in the GD model, as shown in Figure 7.8(c) and 7.8(d). Prefactor mobilities of  $8.0 \times 10^{-4} \text{ cm}^2/\text{Vs}$  and  $2.0 \times 10^{-4} \text{ cm}^2/\text{Vs}$  were obtained from the Arrhenius and the GD model, respectively. A width of DOS of 0.045 eV ( $T_o = 348 \text{ K}$ ) was obtained from the GD model, which is the smallest DOS in thin films of low molecular amorphous. In contrast, the width of DOS obtained from the TOF technique gave a value of 0.077 eV [87,92]. Additionally, the width of DOS obtained for TPD is smaller than that obtained for TAD. The temperature dependence of the mobility follows an Arrhenius-like law with an apparent activation energy of 0.057 eV, which is much lower than the value obtained from the TOF technique ( $E_a = 0.120 \text{ eV}$ ) [91]. The origin of discrepancies in both models is not fully understood.

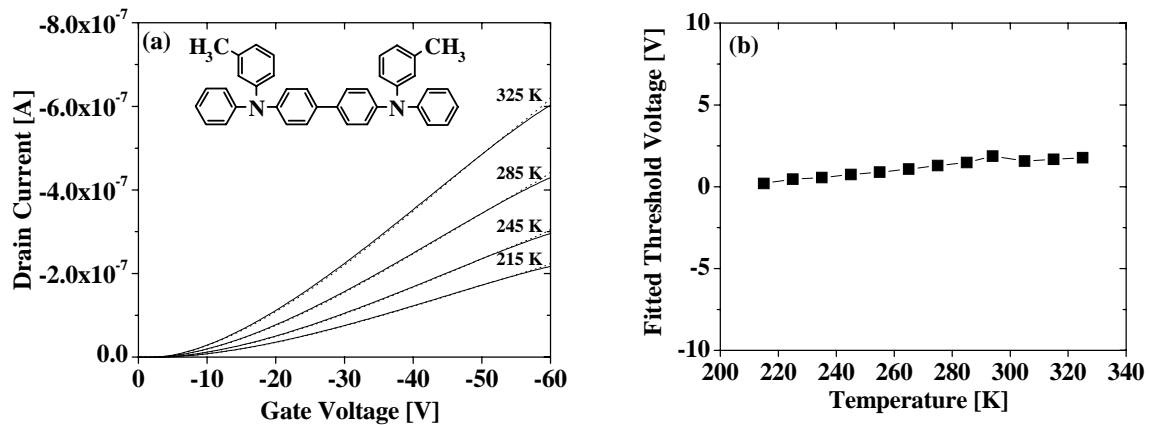


Figure 7.7.(a).Hysteresis characteristics of a TPD FET measured at different temperatures. The drain bias was kept constant at -60 V. The inset shows the chemical structure of TPD. (b).The fitted threshold voltages are linearly plotted against temperature.

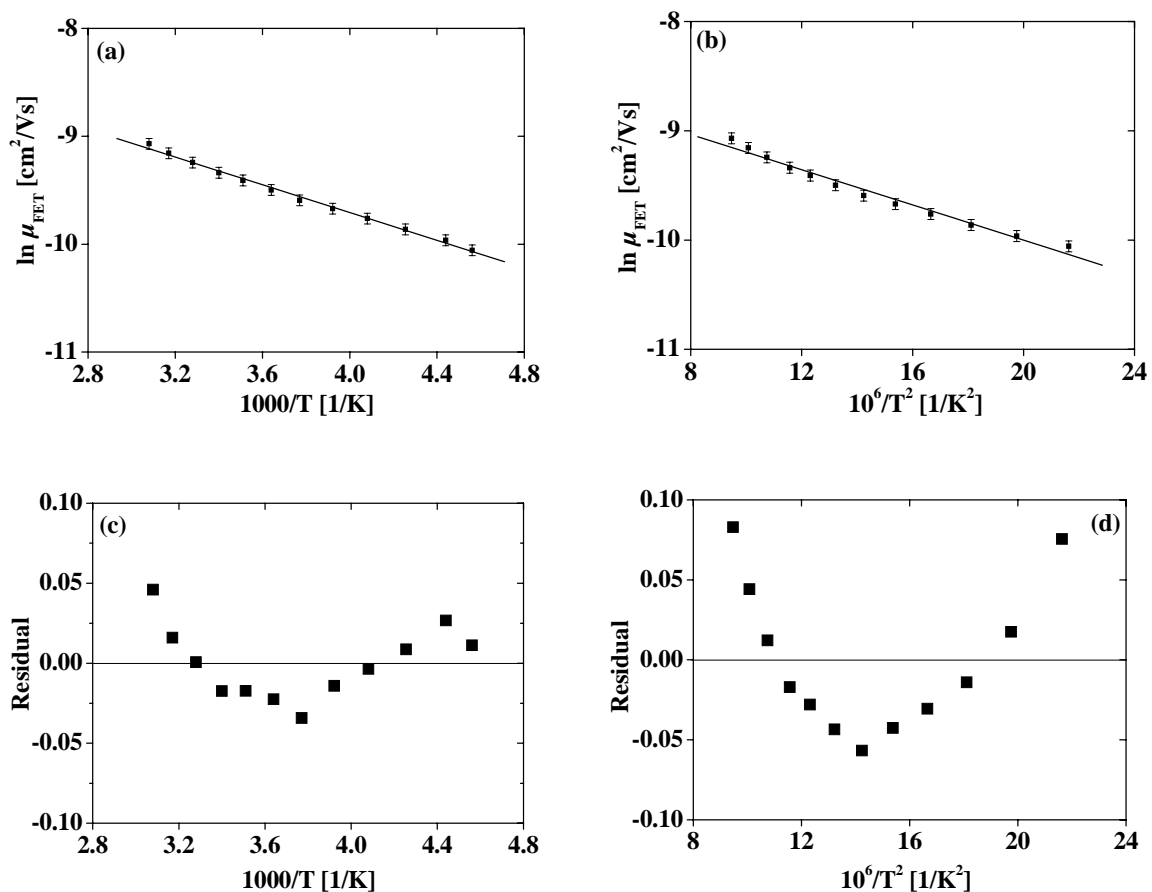


Figure 7.8.Field-effect mobilities of charge carriers in a TPD thin film against (a).The reciprocal of the temperature in the Arrhenius representation, and (b).The inverse square of the temperature in the GD Model. The residual is plotted versus (c) the inverse of the temperature, and (d) the inverse square of the temperature.

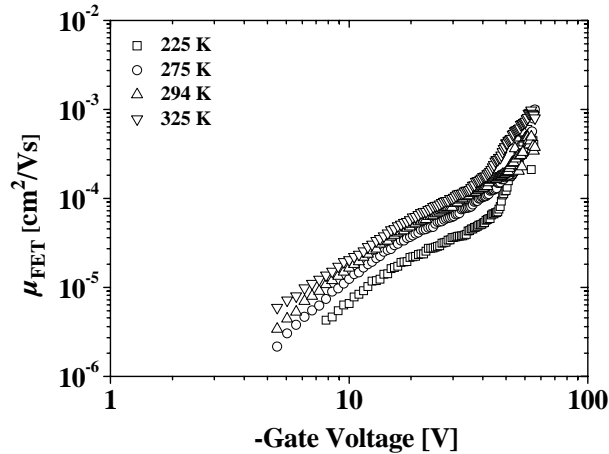


Figure 7.9. Gate bias and temperature dependence of the field-effect mobility of charge carriers in a TPD FET ( $W = 2$  mm,  $L = 10$   $\mu\text{m}$ ,  $C_i = 19.9$  nF/cm<sup>2</sup>). The curve is plotted as a function of the gate bias for various temperatures ( $T = 225$  K, 275 K, 294 K, and 325 K).

Figure 7.9 shows the gate bias dependence of the field-effect mobility in a TPD FET at different temperatures. The dependence of the field-effect mobility at  $|V_G| < 30$  V was quasi-linear for different temperatures. In contrast, the mobility is a super-linear increase for  $|V_G| > 30$  V. This result is similar with the result obtained for Spiro-TAD. The origin of this effect is due to a non-ohmic contact between TPD and the gold electrodes, resulting in saturation of drain current at high gate biases and at a given drain bias ( $V_D = -10$  V). When the data (for  $|V_G| < 30$  V), as shown in Figure 7.9, is fitted to  $\mu(V_G) \propto \text{const.} \times V_G^\lambda$ , then it yields  $\lambda = 1.58 \pm 0.03$ ,  $1.79 \pm 0.03$ ,  $1.75 \pm 0.02$ , and  $1.63 \pm 0.01$  for 225 K, 275 K, 294 K, and 325 K, respectively. The coefficient  $\lambda$  was also decreased at a temperature of 325 K which can be attributed to dynamic process in thin films near the  $T_g$  of TPD ( $T_g = 333$  K). The coefficient  $\lambda$  obtained for TPD is larger than that obtained for TAD. This result indicates that the mobility of charge carriers in thin films of TPD is stronger dependent on the gate-induced charge density than that in thin films of TAD.

#### 7.4. 2,2',7,7'-Tetra-(*m*-tolyl-phenylamino)-9,9'-spirobifluorene (Spiro-TPD)

Figure 7.10(a) shows the hysteresis in the transfer characteristic of a Spiro-TPD FET measured at different temperatures,  $T = 200$  K, 250 K, 298 K, 350 K, and 400 K. The hysteresis was clearly observed at high temperatures. Figure 7.10(b) shows the fitted threshold voltage was plotted against temperature. The fitted threshold voltage also increases

with increasing temperature, which is similar with the results obtained for TAD, Spiro-TAD, and TPD. However, the fitted threshold voltage change (between +1 V and +5 V) in the range of 200 K and 400 K was smaller with respect to the results obtained for Spiro-TAD (between -8V and +7 V) and TAD (between -8 V and +1 V). In contrast, this result was higher than that obtained for FETs based on TPD, which the threshold voltage change was between 0 V and +2 V. Furthermore, Figure 7.11(a) and 7.11(b) shows the field-effect mobilities of charge carriers are plotted in the Arrhenius and the GD model. The Arrhenius model fits the data better than the GD model. The standard deviation of the fitting for the Arrhenius model was 0.3. In contrast, the standard deviation of the fitting for the GD model was 1.4. Figure 7.11(c) and 7.11(d) represent the residual values plotted against  $1/T$  and  $1/T^2$ . The fluctuation of the residual values in the Arrhenius model is smaller than that in the GD model. Prefactor mobilities of  $8.0 \times 10^{-4} \text{ cm}^2/\text{Vs}$  and  $2.0 \times 10^{-4} \text{ cm}^2/\text{Vs}$  were obtained from the Arrhenius and the GD model, respectively. However, the width of DOS was 0.051 eV, which is similar with the result obtained for TPD ( $\sigma = 0.045 \text{ eV}$ ). The corresponding  $T_0$  for Spiro-TPD is 394 K and the activation energy is 0.071 eV.

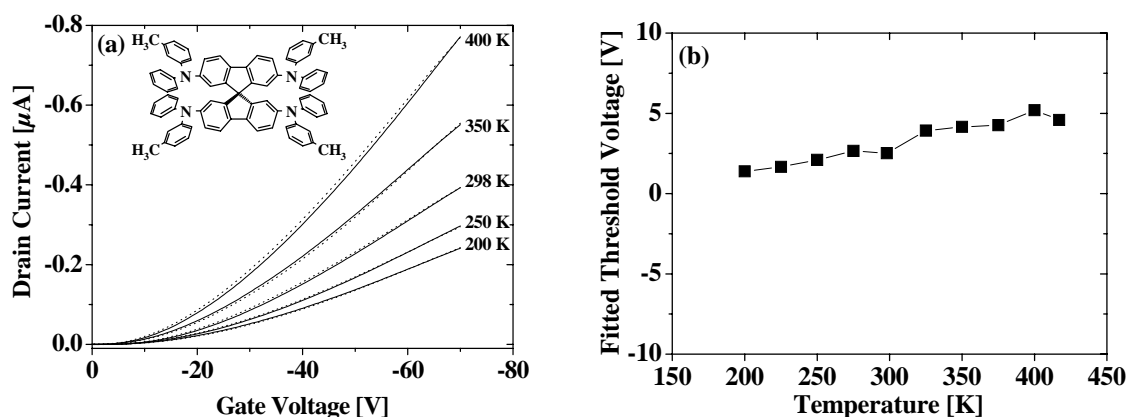


Figure 7.10.(a).Hysteresis characteristics of a Spiro-TPD FET measured at different temperatures. The drain bias was kept constant at -60 V. The inset shows the chemical structure of Spiro-TPD. (b).The fitted threshold voltages are linearly plotted against temperature.

The experimental results revealed that the field effect mobilities in Spiro-TPD thin films are minor affected by temperature. Therefore, the width of DOS of Spiro-TPD is the smallest among thin films of low molecular amorphous spiro-linked compounds. This value is near the value of organic glass polytriarylamine obtained by TOF techniques at which a value of 0.057 eV was obtained [116]. However, the activation energy of TPD is smaller than that of Spiro-TPD. A similar result was also obtained for the width of DOS. Additionally, the

prefactor mobility obtained from the Arrhenius and the GD model for Spiro-TPD and TPD is the same.

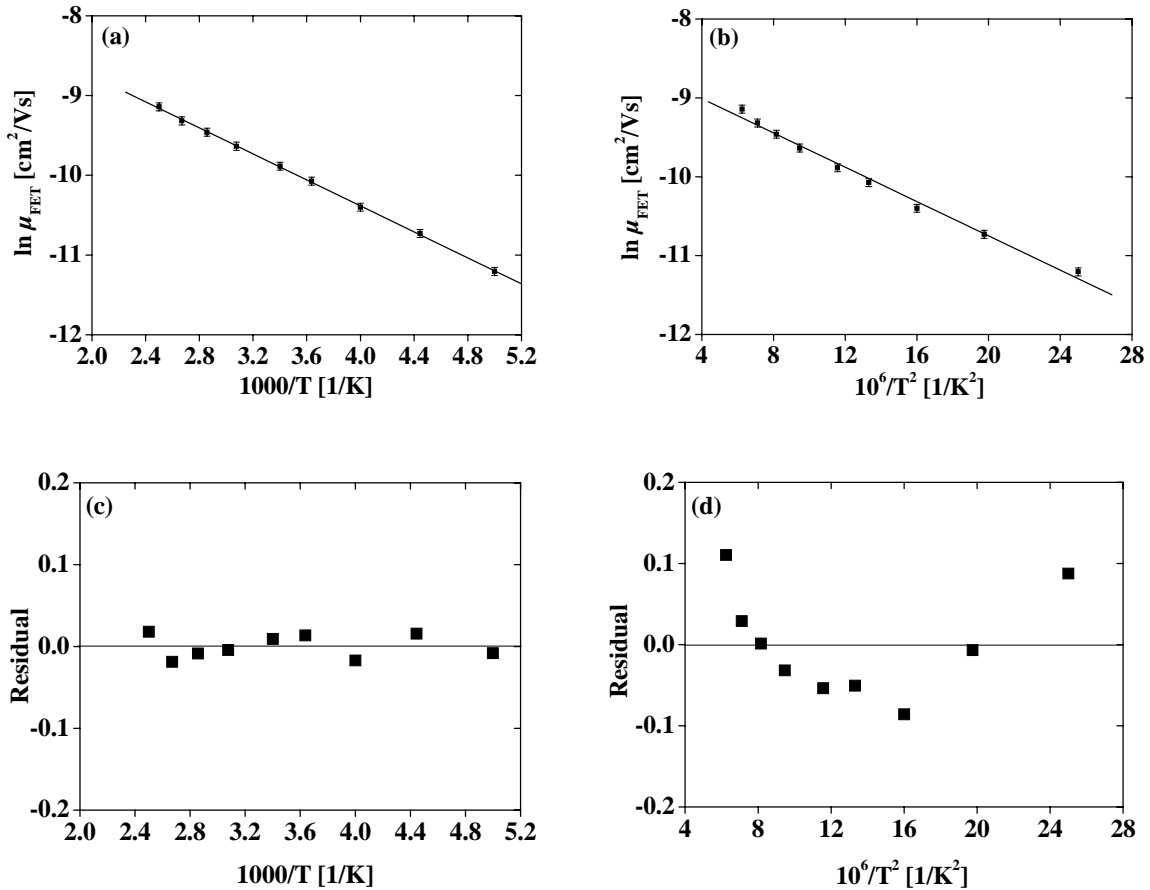


Figure 7.11. Field-effect mobilities of charge carriers in a Spiro-TPD thin film against (a) The reciprocal of the temperature in the Arrhenius representation, and (b) The inverse square of the temperature in the GD Model. The residual is plotted versus (c) the inverse of the temperature, and (d) the inverse square of the temperature.

Figure 7.12 shows the gate bias dependence of the field-effect mobility in a Spiro-TPD FET at different temperatures. The dependence of the field-effect mobility on the gate bias ( $|V_G| < 40$  V) was quasi-linear for different temperatures. However, the mobility goes over to a super-linear increase for  $|V_G| > 40$  V. This result is similar with the results obtained for TPD and Spiro-TAD. The origin of this effect is due to a non-ohmic contact between Spiro-TPD and the gold electrodes, resulting in saturation of drain current at high gate biases and at a given drain bias (in this case  $V_D = -10$  V). When the data (for  $|V_G| < 40$  V) is fitted to  $\mu(V_G) \propto \text{const.} \times V_G^\lambda$ , then it yields  $\lambda = 0.81 \pm 0.01$ ,  $0.89 \pm 0.01$ , and  $0.93 \pm 0.01$ , for 225 K, 275 K, and 350 K, respectively. The coefficient  $\lambda$  obtained for Spiro-TPD is comparable to the values obtained for TAD but much lower than the values obtained for TPD and Spiro-TAD.

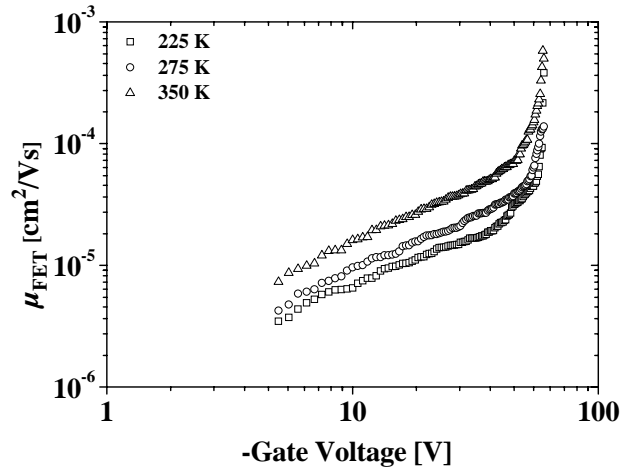


Figure 7.12. Gate bias and temperature dependence of the field-effect mobility of charge carriers in a Spiro-TPD FET ( $W = 2 \text{ mm}$ ,  $L = 10 \text{ }\mu\text{m}$ ,  $C_i = 19.9 \text{ nF/cm}^2$ ). The curve is plotted as a function of the gate bias for various temperatures ( $T = 225 \text{ K}$ ,  $275 \text{ K}$ , and  $350 \text{ K}$ ).

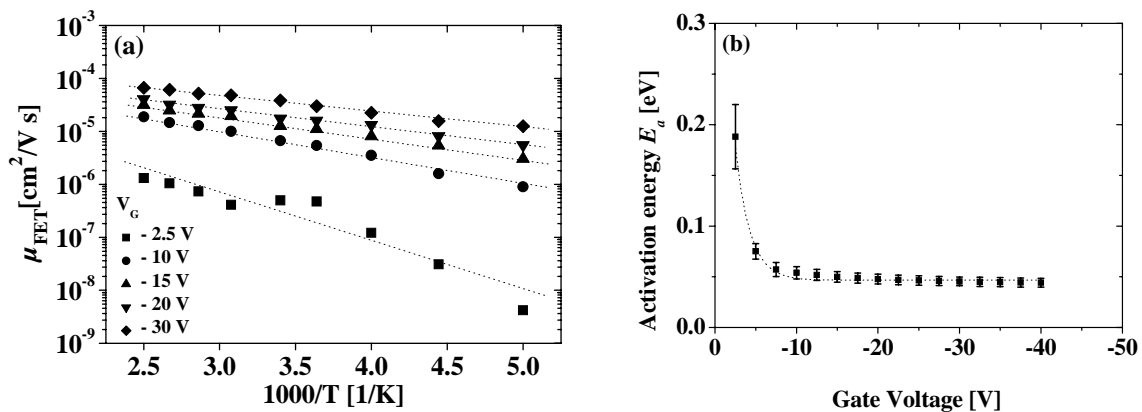


Figure 7.13.(a). Temperature dependence of field-effect mobility for a Spiro-TPD at gate biases of  $-2.5 \text{ V}$ ,  $-10 \text{ V}$ ,  $-15 \text{ V}$ ,  $-20 \text{ V}$ , and  $-30 \text{ V}$ . (b). The activation energy of field-effect mobility plotted against gate voltage.

Figure 7.13(a) shows the temperature dependence of the field-effect mobility for a Spiro-TPD FET at different gate biases ( $V_G = -2.5 \text{ V}$ ,  $-10 \text{ V}$ ,  $-15 \text{ V}$ ,  $-20 \text{ V}$ , and  $-30 \text{ V}$ ). The dotted lines are least-squares fits used to extract the activation energy. Figure 7.13(b) shows that the mobility is simply thermally activated. Error bars are included to show the improved linear fits. The dependence is Arrhenius-like with the apparent activation energy decreasing with increasing gate biases. At high gate biases, the activation energy saturates at a value of  $0.050 \text{ eV}$ . Therefore, the mobility increases with the gate bias as the activation energy decreases. The decrease of the activation energy with increasing absolute gate bias value is



probably a result of accumulated charges filling the lower-lying states. Therefore, any additional charge carriers will occupy sites with a higher energy and less energy will be required to jumping to neighboring sites [27,60,61].

### 7.5. *N,N,N',N'*-Tetrakis(4-methylphenyl)-benzidine (TTB)

Figure 7.14(a) shows the transfer characteristics of a TTB FET measured at various temperatures. However, no hysteresis in the transfer characteristics has been observed for different temperatures. Figure 7.14(b) shows that the fitted threshold voltage increases toward positive bias with increasing temperature. The temperature-dependence measurements were taken after the sample stored in a continuously evacuated chamber for ca. 20 hours. If the chamber is continuously evacuated for more than 48 hours, a decreasing in the drain current is observed. Consequently, a reduction in the mobility of holes is obtained.

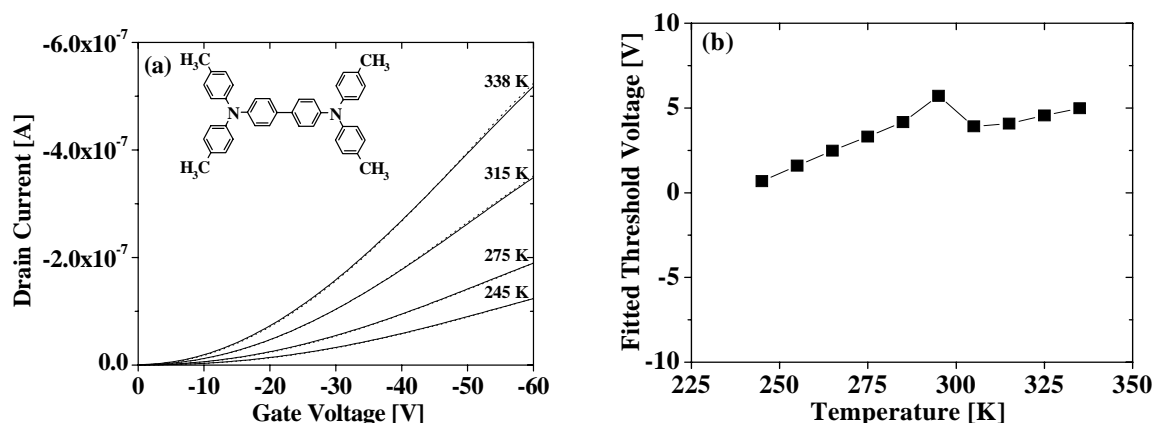


Figure 7.14.(a).Hysteresis characteristics of a TTB FET measured at different temperatures. The drain bias was kept constant at -60 V. The inset shows the chemical structure of TTB. (b).The fitted threshold voltages are linearly plotted against temperature.

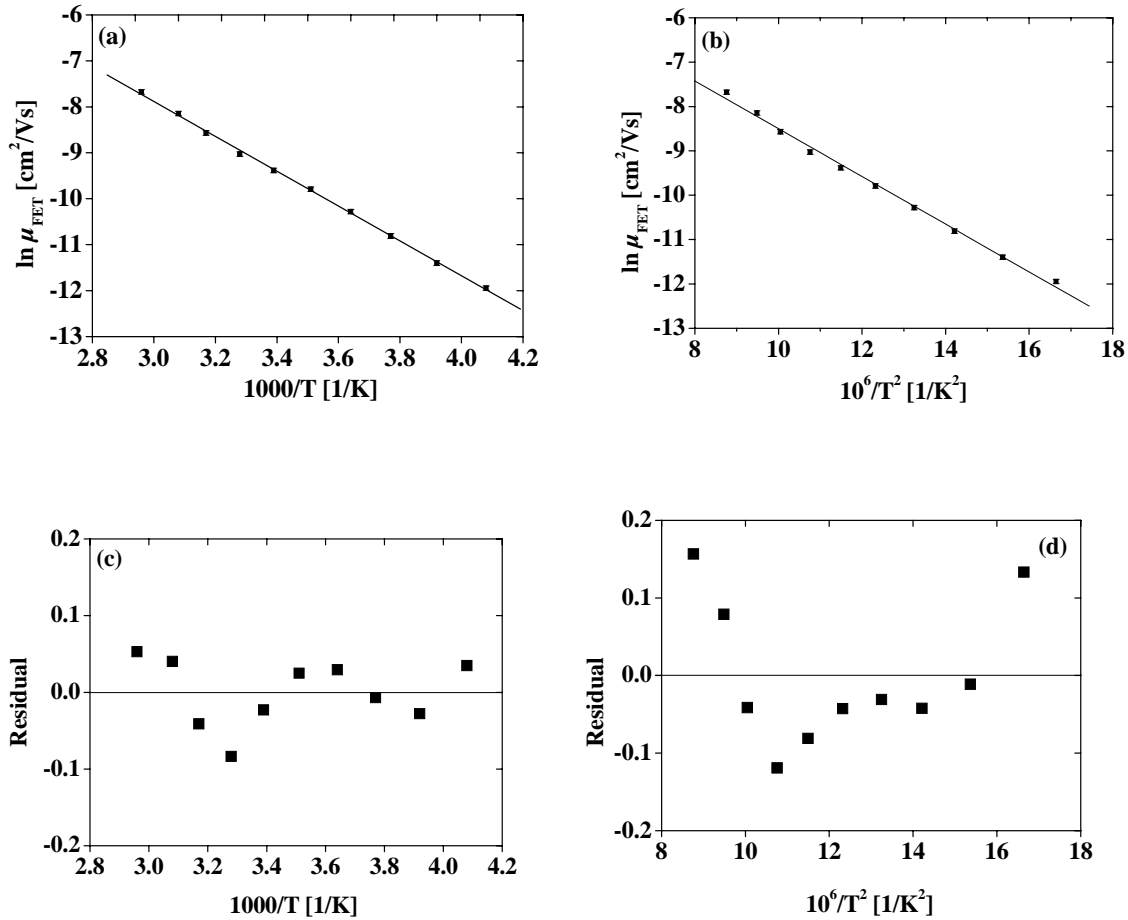


Figure 7.15. Field-effect mobilities of charge carriers in TTB thin films against (a) The reciprocal of the temperature in the Arrhenius representation, and (b) The inverse square of the temperature in the GD Model. The residual is plotted versus (c) the inverse of the temperature, and (d) the inverse square of the temperature.

Figure 7.15 shows that both representations of the mobility, the Arrhenius and the GD model, are well fitted. However, it is clear that the temperature dependence behavior follows the Arrhenius model rather than the GD model. The fitting of the data represented in the Arrhenius model and the GD model gave a standard deviation of 0.9 and 1.9, respectively. Moreover, the fluctuation of the residual values in the Arrhenius model is more distributed around the middle (residual value = 0) than the fluctuation in the GD model, as shown in Figure 7.15(c) and 7.15(d).

The GD model gave a width of the DOS of 0.092 eV ( $T_o = 711$  K), which is 0.014 – 0.023 eV higher than the value obtained from the TOF method [91,101]. In addition, the prefactor mobility of  $4.5 \times 10^{-2}$  cm<sup>2</sup>/Vs was obtained from the GD model, which is a physically meaningful for a low molecular amorphous film. This value is also in the same order of magnitude with the value obtained from the TOF technique. The TOF measurements gave a prefactor mobility of  $3 \times 10^{-2}$  cm<sup>2</sup>/Vs for the GD model [87]. In 1993 Borsenberger

and Fitzgerald also showed that prefactor mobilities of  $2 \times 10^{-2} \text{ cm}^2/\text{Vs}$  and  $1.4 \text{ cm}^2/\text{Vs}$  were obtained from the GD and the Arrhenius model, respectively [101]. In addition, the activation energy of 0.190 eV extracted from the Arrhenius model was also reported.

In contrast, the prefactor mobility obtained from FET methods for the Arrhenius model was  $33 \text{ cm}^2/\text{Vs}$ , which is unrealistic for a non-crystalline material. This value is the highest values among materials used in this study. In addition, an activation energy of 0.330 eV was obtained from the FET method.

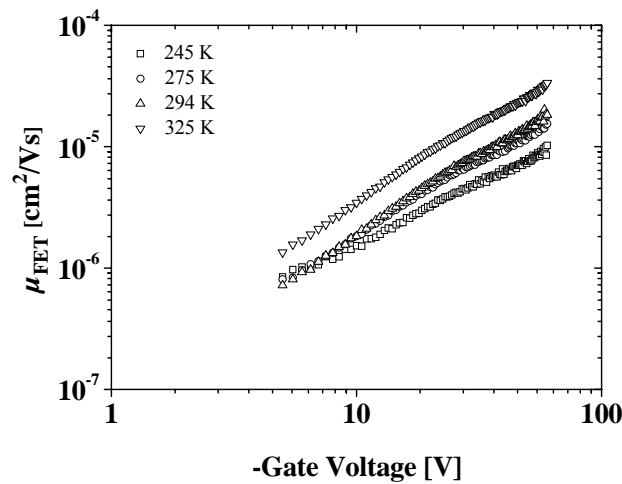


Figure 7.16. Gate bias and temperature dependence of the field-effect mobility of charge carriers in a TTB FET ( $W = 2 \text{ mm}$ ,  $L = 5 \text{ }\mu\text{m}$ ,  $C_i = 17.3 \text{ nF/cm}^2$ ). The curve is plotted as a function of the gate bias for various temperatures ( $T = 245 \text{ K}$ ,  $275 \text{ K}$ ,  $294 \text{ K}$  and  $325 \text{ K}$ ).

Figure 7.16 shows the gate bias dependence of the field-effect mobility in a TTB FET at different temperatures. The dependence of the field-effect mobility on the gate bias was linear for different temperatures. This result is similar with the result obtained for TAD. It can be understood by observing the output characteristic of the corresponding thin films, as shown previously in sub-chapter 6.5. At large gate biases and at a given drain bias (for instance  $V_D = -10 \text{ V}$ ), the transconductance  $g_m$  (see equation 2.13) increases and not saturated. As a result, the mobility increases as the inverse of  $g_m$  decreases, according to equation 2.14. When the data, as shown in Figure 7.16, is fitted to  $\mu(V_G) \propto \text{const.} + V_G^\lambda$ , then it yields  $\lambda = 0.99 \pm 0.01$ ,  $1.17 \pm 0.01$ ,  $1.27 \pm 0.01$ , and  $1.24 \pm 0.01$  for  $245 \text{ K}$ ,  $275 \text{ K}$ ,  $294 \text{ K}$ , and  $325 \text{ K}$ , respectively. The coefficient  $\lambda$  obtained for TTB is higher than that obtained for TAD but lower than that obtained for TPD.

### 7.6. 2,2',7,7'-Tetrakis-(*N,N'*-di-*p*-methylphenylamino)-9,9'-spirobifluorene (Spiro-TTB)

Figure 7.17(a) shows the hysteresis in the transfer curves of a Spiro-TTB FET measured at different temperatures, whereas the drain bias was kept constantly at -60 V. In addition, this effect was accompanied by a shift in the fitted threshold voltage toward positive gate bias with increasing temperature, as shown in Figure 7.17(b). However, the threshold voltage near RT is immensely shifted to positive bias. The origin of this effect is not understood yet. Figure 7.18(a) and 7.18(b) show the mobility of charge carriers in Spiro-TTB thin films as a function of temperature. The dependency of the field-effect mobility on the temperatures is shown in two representations, namely a reciprocal of the temperature in the Arrhenius model and an inverse square of the temperature in the GD model.

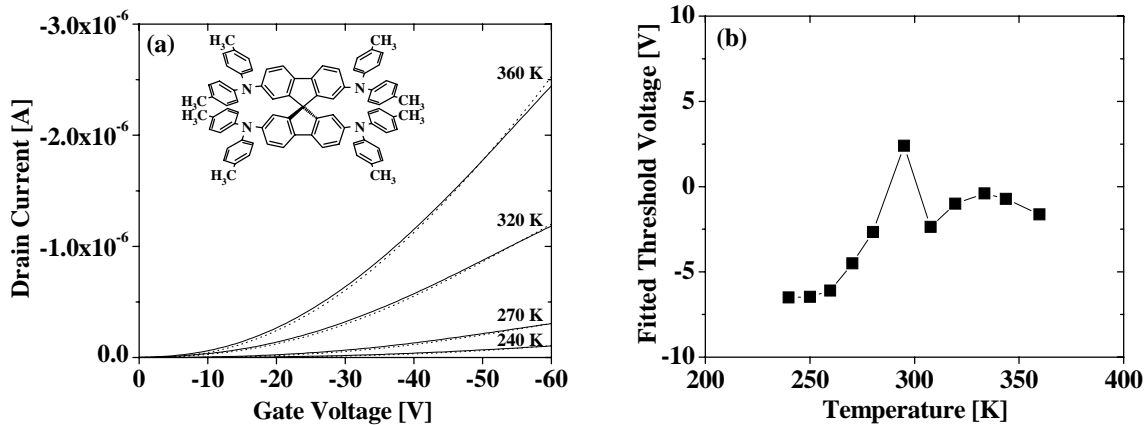


Figure 7.17.(a).Hysteresis characteristics of a Spiro-TTB FET measured at different temperatures. The drain bias was kept constant at -60 V. The inset shows the chemical structure of Spiro-TTB. (b).The fitted threshold voltages are linearly plotted against temperature.

The Arrhenius model is more suitable than the GD model, as indicated by standard deviation of the fitting. The standard deviation of the fitting for the data represented in the Arrhenius model is 0.47. In contrast, the standard deviation of the fitting for the data represented in the GD model is 1.48. Furthermore, the residual values are also displayed in Figure 7.18(c) and 7.18(d). The fluctuation of the residual values in the Arrhenius model is smaller than that in the GD model.

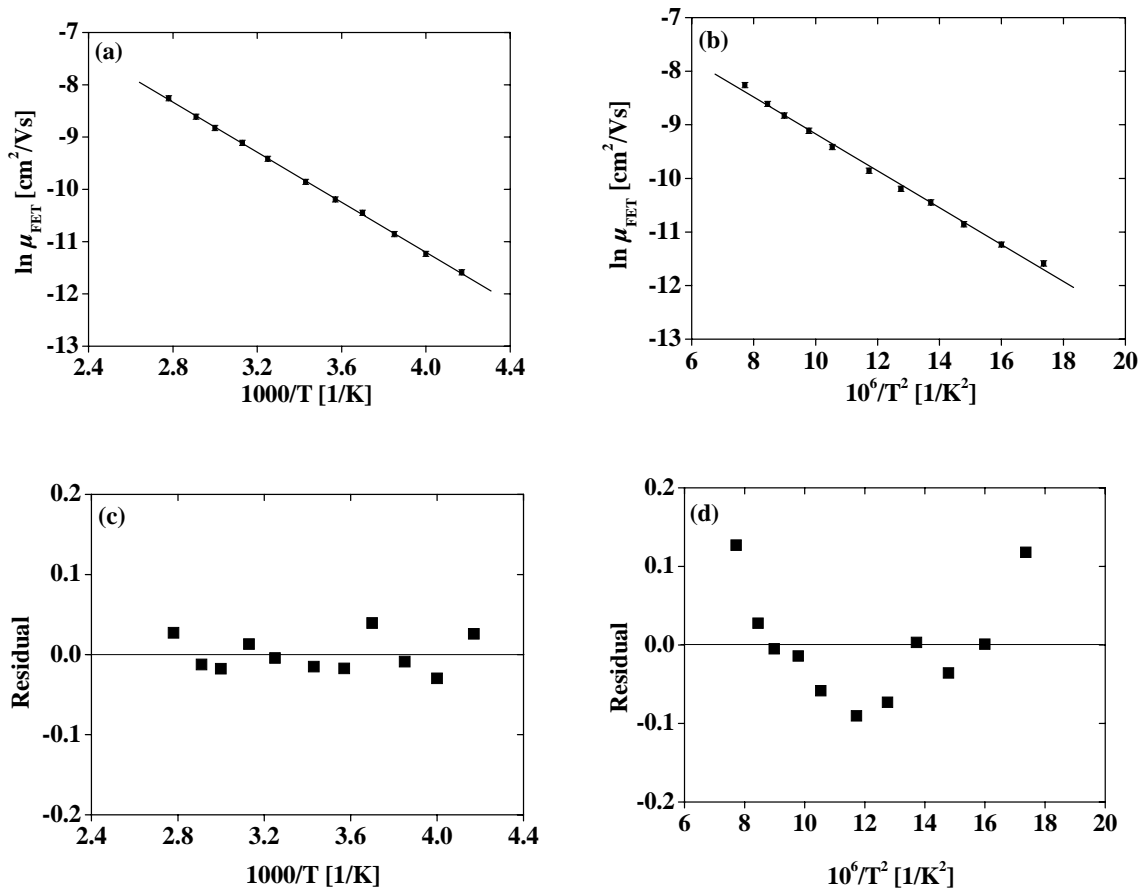


Figure 7.18. Field-effect mobilities of charge carriers in Spiro-TTB thin films against (a). The reciprocal of the temperature in the Arrhenius representation, and (b). The inverse square of the temperature in the GD Model. The residual is plotted versus (c) the inverse of the temperature, and (d) the inverse square of the temperature.

Prefactor mobilities of  $0.2 \text{ cm}^2/\text{Vs}$  and  $3.3 \times 10^{-3} \text{ cm}^2/\text{Vs}$  were obtained for Arrhenius and GD model, respectively. The prefactor mobility extracted from the Arrhenius model for Spiro-TTB is the highest value among spiro-linked compounds. In the previous sub-chapter, a prefactor mobility of  $33 \text{ cm}^2/\text{Vs}$  was obtained for TTB by extracting from the Arrhenius model. Both prefactor mobilities, TTB and Spiro-TTB, obtained from the Arrhenius model are unrealistic for a non-crystalline material. Hence, the Arrhenius model is not applicable to describe the charge transport in TTB and Spiro-TTB. However, it is really difficult to understand why the charge transport of some materials can be described by the Arrhenius model and the others can not be. This issue is not understood yet and needs to be investigated in future.

A width of DOS of  $0.076 \text{ eV}$  ( $T_o = 587 \text{ K}$ ) was obtained by using the GD model for Spiro-TTB, which agrees very well with the value of TTB thin films obtained from the TOF technique [87]. The activation energy obtained from the Arrhenius model was  $0.206 \text{ eV}$ . This value is smaller than that obtained for TTB. In addition, Bach *et al.* [73] reported TOF

measurement for Spiro-*m*-TTB, which a prefactor mobility of  $1.6 \times 10^{-2} \text{ cm}^2/\text{Vs}$  and a width of DOS of 0.080 eV were obtained. The prefactor mobility obtained for Spiro-*m*-TTB was five times higher than that obtained for Spiro-TTB. However, a similar width of DOS was obtained for both materials.

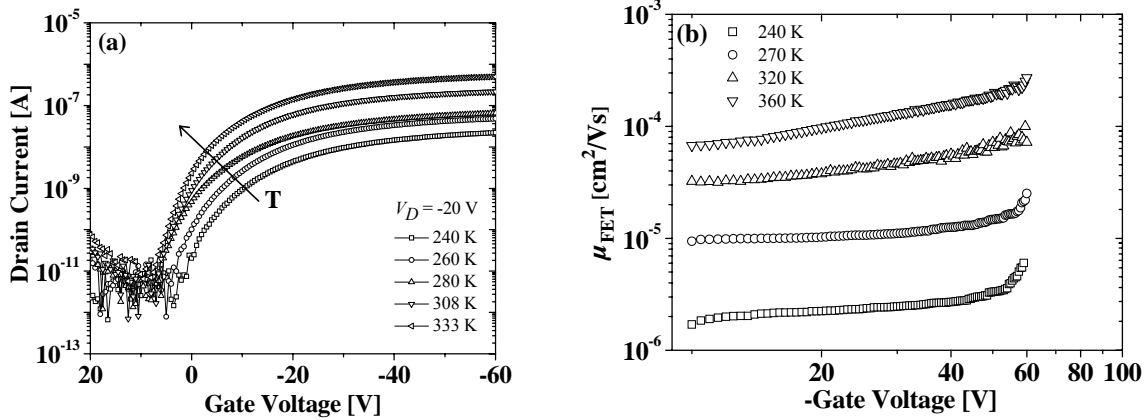


Figure 7.19.(a). Transfer characteristics of a Spiro-TTB FET measured at different temperatures and a drain bias of -20 V. (b). Gate bias and temperature dependence of the field-effect mobility of charge carriers in a Spiro-TTB FET ( $W = 2 \text{ mm}$ ,  $L = 5 \mu\text{m}$ ,  $C_i = 17.3 \text{ nF/cm}^2$ ). The curve is plotted as a function of the gate bias for various temperatures ( $T = 240 \text{ K}$ ,  $270 \text{ K}$ ,  $320 \text{ K}$  and  $360 \text{ K}$ ).

The transfer characteristics of a Spiro TTB FET measured at different temperatures were also shown in Figure 7.19(a). The switch-on voltages shift towards positive gate bias with decreasing temperatures. As the temperature is decreased, the *ON* current is reduced. Consequently, the mobility is decreased with decreasing temperature. The threshold voltage appears to become more negative with decreasing temperature, as shown in Figure 7.17(b). As a consequence, the amount of charge in the channel is determined by gate voltage and the switch on voltage and is dependent on the temperature. Figure 7.19(b) shows the gate bias dependence of the field-effect mobility in a Spiro-TTB FET for different temperatures. The field-effect mobility was quite independent of the gate bias for different temperatures. When the data for  $|V_G| < 45 \text{ V}$ , as shown in Figure 7.19(b), is fitted to  $\mu(V_G) \propto \text{const.} + V_G^\lambda$ , then it yields  $\lambda = 0.21 \pm 0.01$ ,  $0.27 \pm 0.01$ ,  $0.45 \pm 0.01$ , and  $0.67 \pm 0.01$  for 240 K, 270 K, 320 K, and 360 K, respectively. The factor  $\lambda$  obtained for Spiro-TTB is the smallest among the materials used in this study. This implies that the mobility of charge carriers in Spiro-TTB films is relative unaffected by gate-induced charge carriers, which is in contrast with generally observed in organic transistors. This characteristic has a great advantage because one needs the mobility of charge carriers in devices remains constant as the bias is being

applied during device operation. Therefore, Spiro-TTB is a good material as hole transport layer in organic devices due to relatively weak gate dependence of the mobility of charge carriers with respect to other materials such as Spiro-TAD, Spiro-TPD, Spiro  $\alpha$ -NPB or the parent compounds, TAD, TPD, TTB, and  $\alpha$ -NPB.

### 7.7. *N,N'*-Dipheyl-*N,N'*-bis(1-naphthyl)-1,1'-biphenyl-4,4'-diamine ( $\alpha$ -NPB)

Figure 7.20(a) shows that the hysteresis of the transfer characteristics of an  $\alpha$ -NPB FET, which were measured at a drain bias of -60 V. There is no significant hysteresis in the transfer characteristics over a wide range of temperature. Moreover, the fitted threshold voltage increases toward positive bias with increasing temperature, as shown in Figure 7.20(b). The threshold voltage change is also small (between -5 V and -2 V) over a wide range of temperature (250 K < T < 350 K).

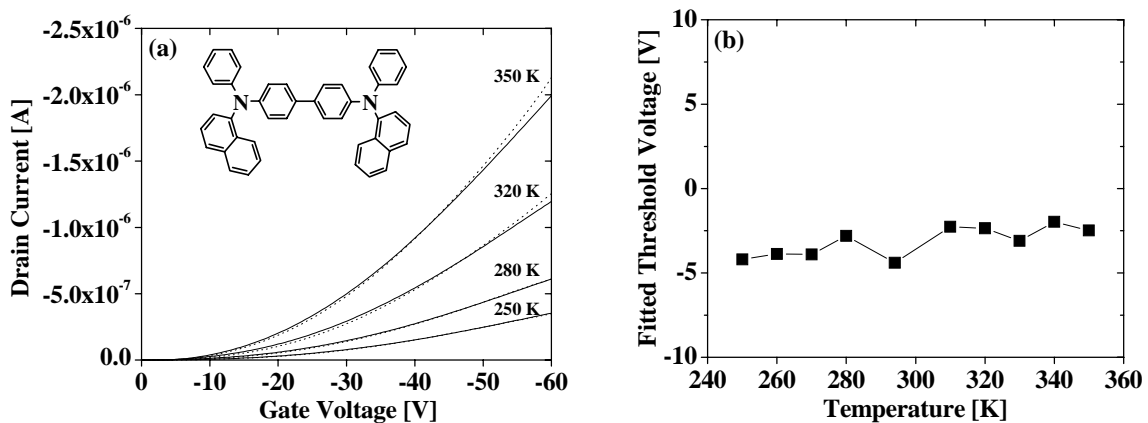


Figure 7.20.(a).Hysteresis characteristics of an  $\alpha$ -NPB FET measured at different temperatures. The drain bias was kept constant at -60 V. The inset shows the chemical structure of  $\alpha$ -NPB. (b).The fitted threshold voltages are linearly plotted against temperature.

Figure 7.21(a) and 7.21(b) show the field-effect mobilities presented in the Arrhenius and the GD model, respectively. The fitted line in Figure 7.21(a) is better than that in Figure 7.21(b). Therefore, the temperature-dependence follows the Arrhenius model rather than the GD model. The standard deviation of the fitting in the Arrhenius model is 0.01 and is 0.04 in the GD model. Moreover, Figure 7.21(c) and 7.21(d) represent the residual values plotted against the inverse of the temperature and the inverse square of the temperature. The

fluctuation of the residual values in the Arrhenius model is more distributed around the middle (residual value = 0) than that in the GD model.

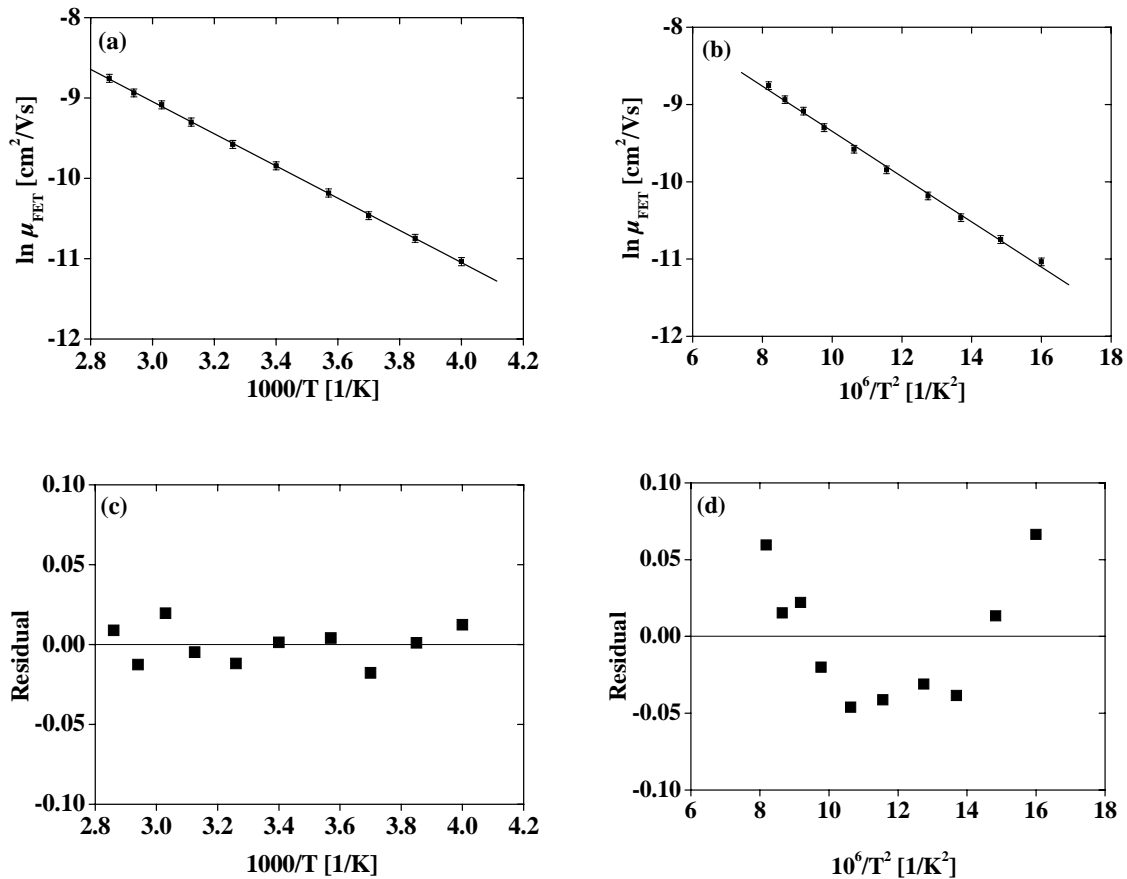


Figure 7.21. Field-effect mobilities of charge carriers in  $\alpha$ -NPB thin films against (a) The reciprocal of the temperature in the Arrhenius representation, and (b) The inverse square of the temperature in the GD Model. The residual is plotted versus (c) the inverse of the temperature, and (d) the inverse square of the temperature.

A width of DOS of 0.071 eV was obtained from the GD model, which relates to a  $T_0$  of 549 K. This results agree very well with the results obtained from the TOF technique ( $\sigma = 0.073$  eV) [117]. Prefactor mobilities of  $5 \times 10^{-2} \text{ cm}^2/\text{Vs}$  and  $2 \times 10^{-3} \text{ cm}^2/\text{Vs}$  were obtained for the Arrhenius and the GD model, respectively. The TOF data gave a prefactor mobility of  $0.35 \text{ cm}^2/\text{Vs}$  for the GD model [117]. Moreover, an activation energy of 0.174 eV was obtained from the Arrhenius model.

Figure 7.22(a) shows the transfer characteristic of a Spiro  $\alpha$ -NPB FET measured at different temperatures. The drain current increases with increasing temperature. The switch-on voltage is relatively unaffected by decreasing or increasing temperature. As a consequence, the amount of charge in the channel is determined only by gate voltage and is independent of



the temperature. This result corresponds very well with other materials-based field-effect transistors such as poly(2,5-thienylene vinylene) (PTV) and poly(3-hexylthiophene) (P3HT), reported by Philips groups [22]. They reported that the  $V_{so}$  for PTV, pentacene, and P3HT were +1 V, +1 V, and +2.5 V, respectively. Furthermore,  $V_{so}$  is temperature independent. In  $\alpha$ -NPB FETs, the  $V_{so}$  is -1.5 V, which does not depend on the temperature as well.

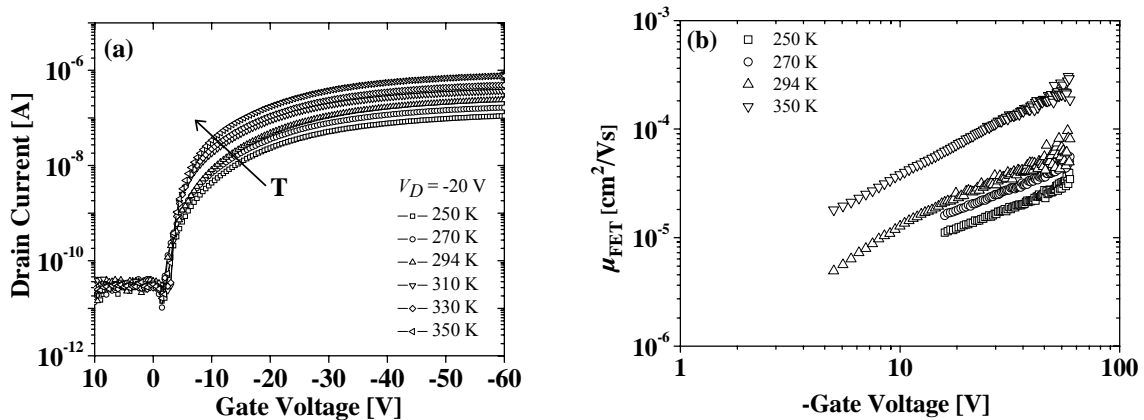


Figure 7.22.(a). Transfer characteristics of an  $\alpha$ -NPB FET measured at different temperatures and a drain bias of -20 V. (b). Gate bias and temperature dependence of the field-effect mobility of charge carriers in a Spiro-TTB FET ( $W = 2$  mm,  $L = 5$   $\mu\text{m}$ ,  $C_i = 17.3$  nF/cm<sup>2</sup>). The curve is plotted as a function of the gate bias for various temperatures ( $T = 250$  K, 270 K, 294 K and 350 K).

Figure 7.22(b) shows the gate bias dependence of the field-effect mobility in an  $\alpha$ -NPB FET at different temperatures. The dependence of the field-effect mobility on the gate bias was linear for different temperatures. When the data for  $|V_G| < 50$  V, as shown in Figure 7.22(b), is fitted to  $\mu(V_G) \propto \text{const.} + V_G^\lambda$ , then it yields  $\lambda = 0.84 \pm 0.01$ ,  $0.87 \pm 0.01$ ,  $0.95 \pm 0.02$ , and  $1.05 \pm 0.01$  for 250 K, 270 K, 294 K, and 350 K, respectively. The coefficient  $\lambda$  obtained for  $\alpha$ -NPB is the lowest value among the parent compounds such as TAD, TPD and TTB.

### 7.8. 2,2',7,7'-Tetra-(*N*-phenyl-1-naphthylamine)-9,9'-spirobifluorene (Spiro $\alpha$ -NPB)

Figure 7.23(a) shows that the hysteresis in the transfer characteristics of a Spiro  $\alpha$ -NPB FET, measured at a drain bias of -60 V and at various temperatures. The hysteresis was clearly observed with increasing temperature. The magnitude of the hysteresis strongly decreases with decreasing temperature, so only at relatively high temperatures the

measurements will be negatively affected. The hysteresis in the curve measured near RT was small and the hysteresis was completely absent at low temperatures. The fitted threshold voltages also increase toward positive bias with increasing temperatures, as shown in Figure 7.23(b).

Figure 7.24(a) and 7.24(b) represent the field-effect mobilities presented in the Arrhenius and GD model, respectively. The fitted line in Figure 7.24(a) and 7.24(b) satisfy the corresponding model, the Arrhenius and the GD model, quite well. However, the fitted line in the Arrhenius model is better than in the GD model. The standard deviation of the fitting in the Arrhenius model is 0.04 and is 0.07 in the GD model. Moreover, Figure 7.24(c) and 7.24(d) represent the residual values plotted against the inverse of the temperature and the inverse square of the temperature. The fluctuation of the residual values in the Arrhenius model is smaller than that in the GD model. Prefactor mobilities of  $8 \times 10^{-2} \text{ cm}^2/\text{Vs}$  and  $3 \times 10^{-3} \text{ cm}^2/\text{Vs}$  were obtained for the Arrhenius and GD model, respectively. These values are in the same order of magnitude with the value obtained for  $\alpha$ -NPB FET ( $\mu_o = 2 \times 10^{-3} \text{ cm}^2/\text{Vs}$ ). However, this value is lower than the value for  $\alpha$ -NPB obtained from the TOF technique ( $\mu_o = 0.35 \text{ cm}^2/\text{Vs}$ ) [117]. A width of distribution  $\sigma$  of 0.077 eV was obtained, which agrees very well with the results obtained from the TOF technique ( $\sigma = 0.073 \text{ eV}$ ) [117] and FET techniques ( $\sigma = 0.071 \text{ eV}$ ). The corresponding  $T_o$  and the activation energy of Spiro  $\alpha$ -NPB are 596 K and 0.205 eV, respectively.

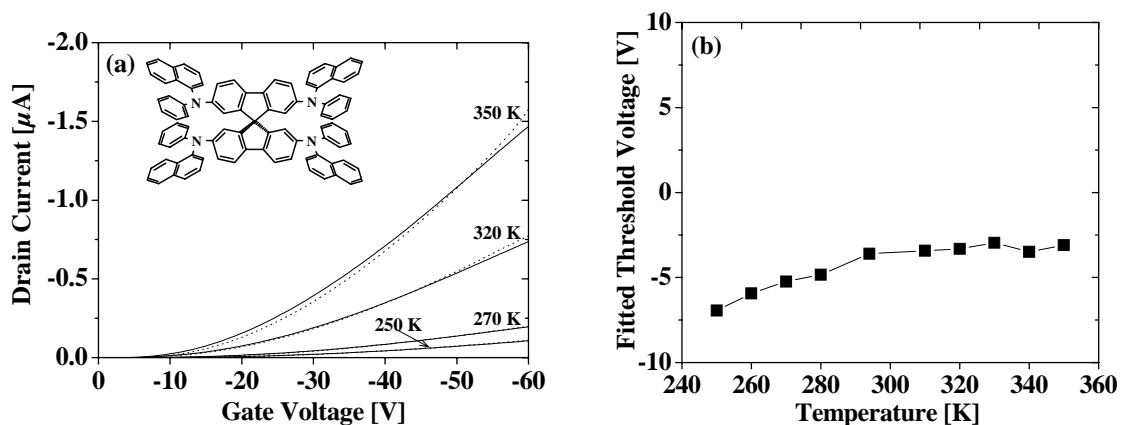


Figure 7.23.(a).Hysteresis characteristics of a Spiro  $\alpha$ -NPB FET measured at different temperatures. The drain bias was kept constant at -60 V. The inset shows the chemical structure of Spiro  $\alpha$ -NPB. (b).The fitted threshold voltages are linearly plotted against temperature.

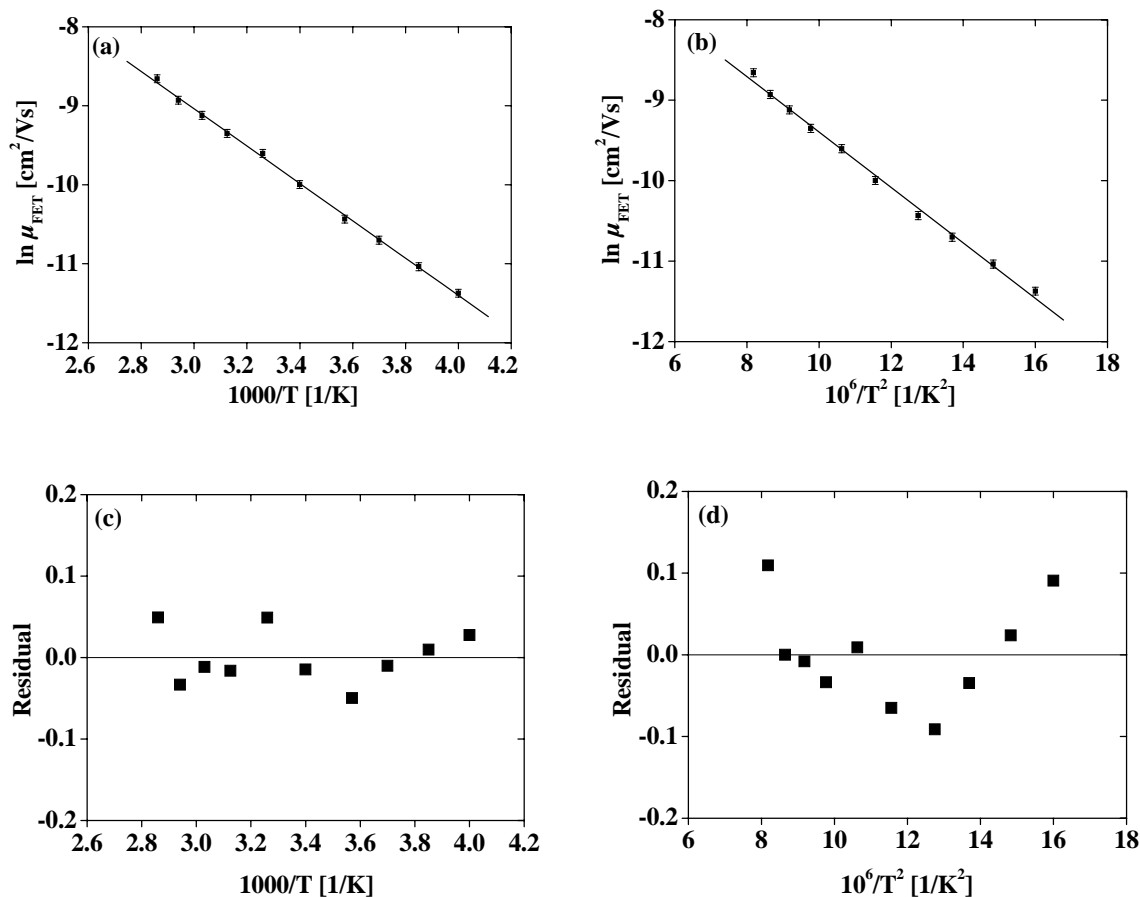


Figure 7.24. Field-effect mobilities of charge carriers in Spiro  $\alpha$ -NPB thin films against (a) The reciprocal of the temperature in the Arrhenius representation, and (b) The inverse square of the temperature in the GD Model. The residual is plotted versus (c) the inverse of the temperature, and (d) the inverse square of the temperature.

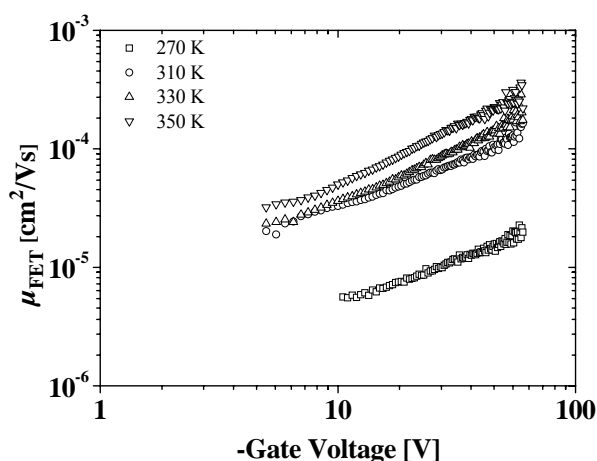


Figure 7.25. Gate bias and temperature dependence of the field-effect mobility of charge carriers in a Spiro  $\alpha$ -NPB FET ( $W = 3 \text{ mm}$ ,  $L = 10 \text{ }\mu\text{m}$ ,  $C_i = 19.9 \text{ nF/cm}^2$ ). The curve is plotted as a function of the gate bias for various temperatures ( $T = 270 \text{ K}$ ,  $310 \text{ K}$ ,  $330 \text{ K}$  and  $350 \text{ K}$ ).

Figure 7.25 shows the gate bias dependence of the field-effect mobility in a Spiro-TTB FET at different temperatures. The dependence of the field-effect mobility on the gate bias was quasi-linear for different temperatures. When the data for  $|V_G| < 50$  V, as shown in Figure 7.25, is fitted to  $\mu(V_G) \propto \text{const.} + V_G^\lambda$ , then it yields  $\lambda = 0.77 \pm 0.01$ ,  $0.79 \pm 0.01$ ,  $0.92 \pm 0.01$ , and  $0.95 \pm 0.01$  for 270 K, 310 K, 330 K, and 350 K, respectively. The coefficient  $\lambda$  obtained for Spiro  $\alpha$ -NPB is smaller than those obtained for  $\alpha$ -NPB, Spiro-TAD and TPD but higher than that obtained for Spiro-TTB. In addition, the  $\lambda$  values of Spiro  $\alpha$ -NPB are similar with the values obtained for Spiro-TPD.

## 7.9. Summary of chapter 7

The temperature dependencies of the mobilities of charge carriers in TAD, TPD, TTB,  $\alpha$ -NPB, Spiro-TAD, Spiro-TPD, Spiro-TTB and Spiro  $\alpha$ -NPB thin films have been presented in two models, namely the Arrhenius and the Gaussian disorder (GD) model. However, the data presented in the Arrhenius model are better fitted than those in the GD model. The fitting of the data represented in the Arrhenius model gave a lower standard deviation value than that in the GD model. Moreover, the residual values presented in the Arrhenius model were more evenly distributed around the middle (residual value = 0) than those in the GD model. Therefore, the temperature dependence of mobility follows the Arrhenius model rather than the GD model. Moreover, the fitted threshold voltage increases toward positive bias with increasing temperature. Finally, the mobility of charge carriers in spiro-linked compound thin films are relatively unaffected by temperature with respect to their corresponding parent compound. Table 7.1 summarizes all parameters that have been extracted from FET techniques. The TOF data obtained from the literature were also presented.

The prefactor mobilities obtained for TAD and Spiro-TAD were in the range of  $10^{-4}$   $\text{cm}^2/\text{Vs}$  and  $10^{-2}$   $\text{cm}^2/\text{Vs}$ . These values are realistic for low molecular amorphous thin films. However, the prefactor mobilities obtained for TAD were one order of magnitude higher for both models than that obtained for Spiro-TAD. The GD model gave a width of DOS of 0.077 eV for TAD which is 0.020 eV higher than the values obtained for Spiro-TAD. This implies that the width of DOS in Spiro-TAD is smaller than that in TAD. As a consequence, the activation energy of charge carriers to hop from one molecule to the next in TAD was higher than that in Spiro-TAD.

Spiro-TPD and its corresponding parent compound, TPD, have the same prefactor mobilities obtained from both models. The prefactor mobilities were in the range of  $2 \times 10^{-4}$   $\text{cm}^2/\text{Vs}$  and  $8 \times 10^{-4}$   $\text{cm}^2/\text{Vs}$ . Similar results were also obtained for a width of DOS. The GD model gave a value of 0.045 eV and 0.051 eV for TPD and Spiro-TPD, respectively. Notably, the values of the width of DOS obtained for TPD is the smallest among the materials used in this study. In addition, this value was also higher than the value obtained by TOF methods [87,92]. The prefactor mobility obtained from TOF techniques was two orders of magnitude higher than that obtained from FET methods [87,92].

In most studies, the temperature range for which measurements can be performed is sufficiently narrow that an exponential dependence on  $1/T^2$  cannot be readily distinguished from a  $1/T$  relationship. In this study, a  $1/T$  dependence provides a better description of the experimental results. However, the problem concerning the use of an Arrhenius model is the magnitude of the prefactor mobility. For TTB and Spiro-TTB, the Arrhenius plot notoriously overestimates the prefactor mobilities with values typically between 0.2 and 33  $\text{cm}^2/\text{Vs}$  for Spiro-TTB and TTB, respectively. The values obtained for Spiro-TTB ( $\mu_o = 0.2$   $\text{cm}^2/\text{Vs}$ ) is acceptable for low molecular amorphous films, but the values for TTB is really unrealistic (33  $\text{cm}^2/\text{Vs}$ ). In addition, the GD model gave a value of  $4.5 \times 10^{-2}$   $\text{cm}^2/\text{Vs}$  and  $3.3 \times 10^{-3}$   $\text{cm}^2/\text{Vs}$  for TTB and Spiro-TTB, respectively. Furthermore, the width of DOS for TTB is the largest among the materials used in this study.

The prefactor mobilities in  $\alpha$ -NPB and Spiro  $\alpha$ -NPB were in the range of  $10^{-3}$   $\text{cm}^2/\text{Vs}$  and  $10^{-2}$   $\text{cm}^2/\text{Vs}$ , which is a realistic value for low molecular amorphous film. The width of DOS in  $\alpha$ -NPB and Spiro  $\alpha$ -NPB was also similar. Values of 0.071 eV and 0.077 eV were obtained for  $\alpha$ -NPB and Spiro  $\alpha$ -NPB, respectively.

Table 7.1. Transport parameters extracted from the FET and TOF techniques.

Material and Method	Arrhenius model			Gaussian disorder model			Ref.
	$\mu_o$ [cm <sup>2</sup> /Vs]	$E_a$ [eV]	$\sigma$ [eV] Eq.2.21	$\mu_o$ [cm <sup>2</sup> /Vs]	$\sigma$ [eV]	$E_a$ [eV] Eq.2.21	
TAD FET	$7.6 \times 10^{-2}$	0.220	0.080	$4.4 \times 10^{-3}$	0.077	0.203	this work
Spiro-TAD FET	$4.0 \times 10^{-3}$	0.110	0.057	$4.0 \times 10^{-4}$	0.057	0.111	this work
TPD FET	$8.0 \times 10^{-4}$	0.057	0.041	$2.0 \times 10^{-4}$	0.045	0.069	this work
Spiro-TPD FET	$8.0 \times 10^{-4}$	0.071	0.046	$2.0 \times 10^{-4}$	0.051	0.089	this work
TTB FET	33	0.330	0.098	$4.5 \times 10^{-2}$	0.092	0.289	this work
Spiro-TTB FET	0.2	0.206	0.078	$3.3 \times 10^{-3}$	0.076	0.197	this work
$\alpha$ -NPB FET	$5.0 \times 10^{-2}$	0.174	0.071	$2.0 \times 10^{-3}$	0.071	0.172	this work
Spiro $\alpha$ -NPB FET	$8.0 \times 10^{-2}$	0.205	0.077	$3.0 \times 10^{-3}$	0.077	0.203	this work
TPD TOF	NA	0.203	0.077	$3.2 \times 10^{-2}$	0.077	0.203	87,92
$\alpha$ -NPB TOF	NA	NA	NA	0.35	0.073	0.182	117
TTB TOF	NA	NA	NA	$3.0 \times 10^{-2}$	0.078	0.208	87
TTB TOF	1.4	0.190	0.075	$1.9 \times 10^{-2}$	0.069	0.158	101
Spiro-TAD TOF	NA	NA	NA	$1.6 \times 10^{-2}$	0.080	0.219	73
Spiro- <i>m</i> -TTB TOF	NA	NA	NA	$1 \times 10^{-2}$	0.080	0.219	73
Spiro-MeO-TAD TOF	NA	NA	NA	$4.7 \times 10^{-2}$	0.101	0.349	89

## Chapter 8

# Asymmetrically Spiro-linked Compounds

In chapter 6 the field-effect mobilities of charge carriers in thin films of symmetrically spiro-linked compounds and the corresponding parent compounds have been described. A symmetrically spiro-linked compound is defined as a material consisting of two identical functional groups linked with a spiro carbon center, as shown in Figure 1(a). The functional groups can be associated with a donor, acceptor and emitter molecule. In the case of previous results, the functional groups are donor molecules, for instance TAD, TPD, TTB and  $\alpha$ -NPB. Besides symmetrically spiro-linked compounds, asymmetrically spiro-linked compounds have been already synthesized [17]. In this context, the term asymmetric means that the functional groups in the upper and lower half are not identical; giving a combination of donor and emitter (Figure 1(b)), donor and acceptor (Figure 1(c)), or acceptor and emitter (Figure 1(c)) in asymmetrically spiro-linked compounds.

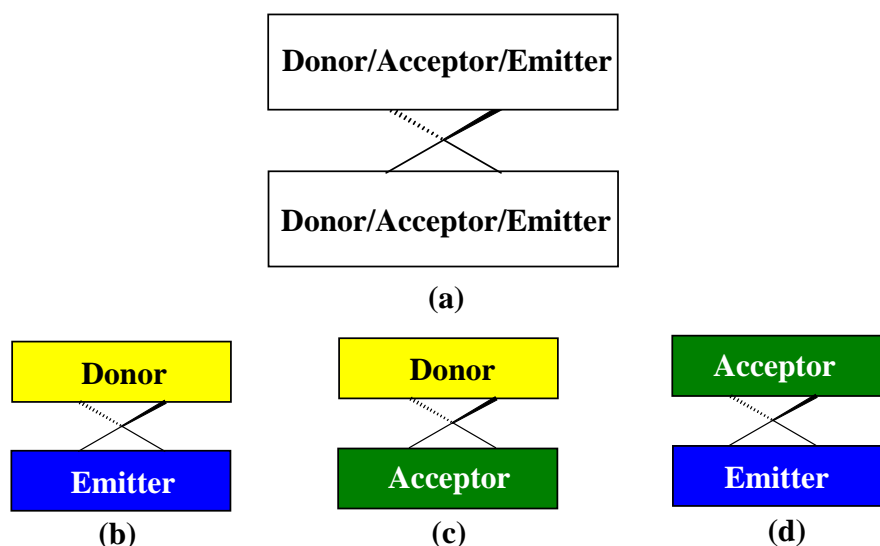


Figure 8.1. Schematic view of the spiro concept; symmetrically spiro-linked compounds (a) and asymmetrically spiro-linked compounds (b,c,d).

In this chapter, the charge transport in an asymmetrically spiro-linked compound will be presented. The method used in this study is still the field-effect transistor. The materials used in this experiment were 2,7-bis-(*N,N'*-diphenylamino)-2',7'-bis(biphenyl-4-yl)-9,9'-

spirobifluorene (Spiro-DPSP) and 2,7-bis-(*N,N'*-diphenylamino)-2',7'-bis(spirobifluorene-2-yl)-9,9'-spirobifluorene (Spiro-DPSP<sup>2</sup>). The synthesis of these materials is described elsewhere [17]. The chemical structures of both materials are shown in Figure 8.2. They belong to the class of asymmetrically spiro-linked compounds in which two different functional chromophores are linked together by a central spiro atom. In this case, the functional units consist of a sexiphenyl/terfluorene-derivative and a bis(diphenylamino)biphenyl moiety. Generally, spiro-compounds are known as glass-forming materials with high glass transition temperatures and a good morphological stability, which makes them well suitable for organic electronic devices. The symmetrically substituted parent compounds of Spiro-DPSP and Spiro-DPSP<sup>2</sup> are 2,2',7,7'-tetrakis(diphenylamino)-9,9'-spirobifluorene (Spiro-TAD), 2,2',7,7'-tetrakis(biphenyl-4-yl)-9,9'-spirobifluorene (Spiro-6Φ), and 2,2',7,7'-tetrakis(9,9'-spirobifluorene-2-yl)-9,9'-spirobifluorene (4-Spiro<sup>2</sup>). The glass transition temperatures of Spiro-DPSP and Spiro-DPSP<sup>2</sup> are 159°C and 210 °C [17], which lie between the glass transition temperatures of Spiro-TAD (133 °C) and 4-Spiro<sup>2</sup> (273 °C) [70,118].

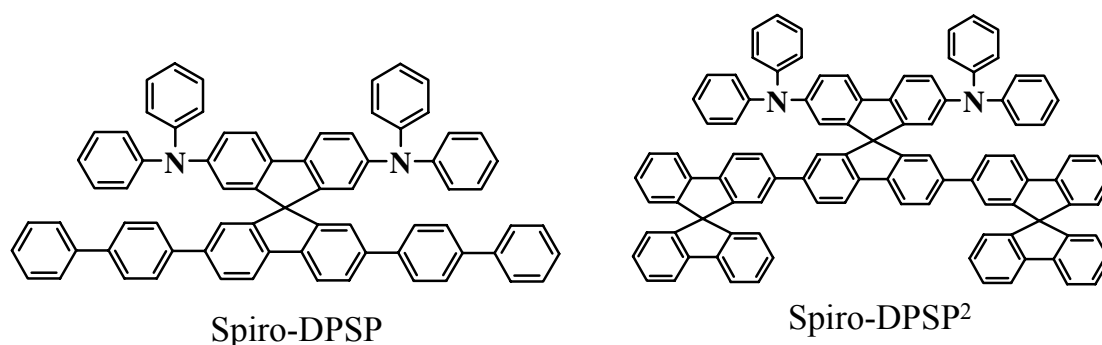


Figure 8.2. The chemical structures of asymmetrically spiro-linked compounds used in this study, Spiro-DPSP and Spiro-DPSP<sup>2</sup>.

### 8.1. Transistor characteristics measured in the dark and surface morphology

The fabrication and characterization of Spiro-DPSP and Spiro-DPSP<sup>2</sup> transistors follow the experimental procedures as described previously in chapter 4. The results are shown in Figure 8.3 and 8.4. The mobilities of charge carriers in the saturation regime were extracted by utilizing equation 2.11. Figure 8.3(a) shows the output characteristics of a Spiro-DPSP field-effect transistor (FET) measured in air, in the dark and at room temperature (RT). The channel currents were plotted against the drain voltage for different gate voltages. The



drain current increases as the gate voltage is increased towards larger negative voltage, which underwent an effective field-effect modulation caused by the variation of the gate bias. The sign of the field-enhanced current ( $I_D < 0$  with  $V_G < 0$ ) is consistent with an accumulation regime. Figure 8.3(b) shows the variation of channel conductivity with varying gate voltage at a drain voltage of -60 V. The channel conductivity rises by a factor of  $2 \times 10^4$  as the gate voltage is being scanned from 0 V to -60 V. The device operates between depletion and accumulation for these gate voltages. No evidence for the formation of an inversion layer has been observed. In the saturation regime ( $V_D = -60$  V), the mobility can be calculated from the slope of the plot of the square-root of the saturated drain current versus  $V_G$ . A fitted threshold voltage of -9 V and a carrier mobility of  $7.6 \times 10^{-6}$  cm<sup>2</sup>/Vs were obtained. The device turns on at -6 V.

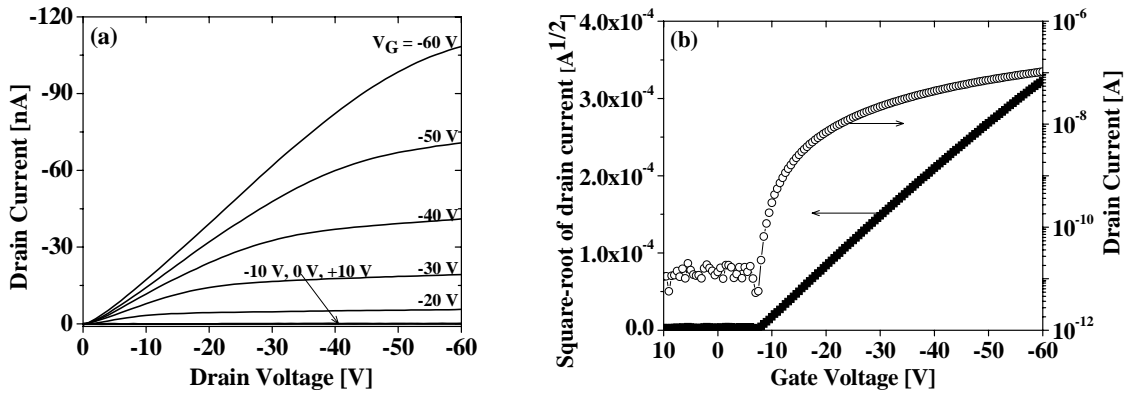


Figure 8.3. Output characteristics (a) and transfer characteristics (b) of a Spiro-DPSP transistor ( $L = 5 \mu\text{m}$ ,  $W = 4 \text{ mm}$ , and  $C_i = 20.93 \text{ nF/cm}^2$ ) measured in air and in the dark. The transfer curve was obtained at drain bias -60 V. The drain current is plotted logarithmically and the square-root of drain current is plotted linearly.

Figure 8.4(a) shows a typical set of drain current of a Spiro-DPSP<sup>2</sup> FET plotted against drain voltage for different gate voltages; measured on a device with a channel length of  $5 \mu\text{m}$  and a channel width of  $5 \text{ mm}$ . The measurement was carried out in air, in the dark and at RT. Although a clear saturation of drain current is observed when the drain voltage exceeds the gate voltage, the onset of the curves is far from being linear. At low drain biases, the output characteristic exhibits some nonlinearities which can be attributed to the non-ohmic contacts between Spiro-DPSP<sup>2</sup> and the gold electrodes. An *ON/OFF* ratio of typically  $4.2 \times 10^3$  can be obtained when the  $V_G$  is being scanned from 0 V to -60 V and  $V_D = -60$  V. The field-effect mobility of charge carriers in Spiro-TAD thin films is  $9.2 \times 10^{-7}$  cm<sup>2</sup>/Vs extracted in the saturation regime. The threshold voltage and the switch-on voltage were -6.7 V and 0 V, respectively.

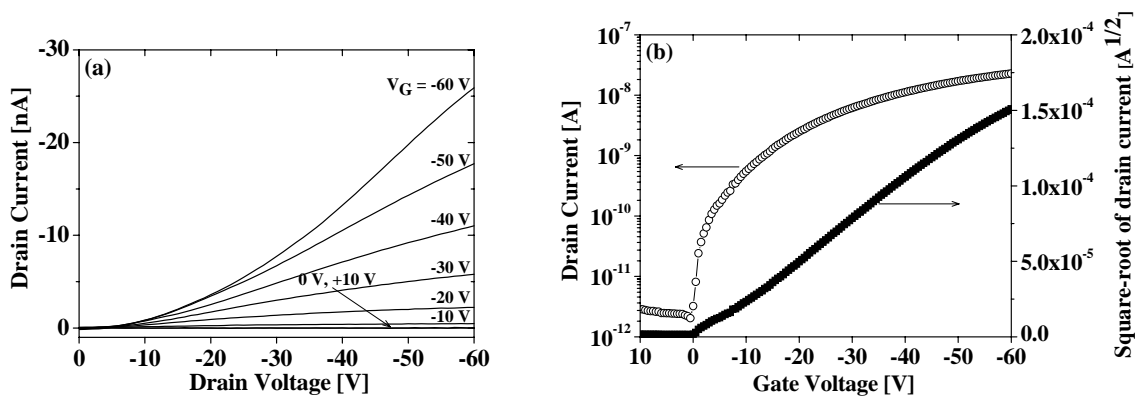


Figure 8.4. Output characteristics (a) and transfer characteristics (b) of a Spiro-DPSP<sup>2</sup> transistor ( $L = 5 \mu\text{m}$ ,  $W = 5 \text{mm}$ , and  $C_i = 17.3 \text{ nF/cm}^2$ ) measured in air and in the dark. The transfer curve was obtained at drain bias  $-60 \text{ V}$ . The drain current is plotted logarithmically and the square-root of drain current is plotted linearly.

The transistor characteristics of Spiro-DPSP and Spiro-DPSP<sup>2</sup> FETs measured in the dark and in air have been already presented. The transistor characteristics of the corresponding symmetrically substituted parent compounds of these materials, 2,2',7,7'-tetrakis(diphenyl-amino)-9,9'-spirobifluorene (Spiro-TAD), 2,2',7,7'-tetrakis(biphenyl-4-yl)-9,9'-spirobi-fluorene (Spiro-6 $\Phi$ ), have been characterized as well. The transistor characteristic of a Spiro-TAD FET has been presented in sub-chapter 6.2. However, no transistor action has been observed on FETs based on Spiro-6 $\Phi$ . A possible cause is a large potential barrier for charge injection from the gold electrodes (work function  $\approx 5.1 \text{ eV}$ ) to the HOMO level of Spiro-6 $\Phi$  ( $E_{\text{HOMO}} \approx 5.9 \pm 0.1 \text{ eV}$ ) [71]. As a result, the charge injection from the gold electrode to spiro-6 $\Phi$  is poor and thus no transistor effect can be observed.

In chapter 5 the surface morphology of symmetrically spiro-linked compounds and the corresponding parent compound have been presented. In order to compare those results, the surface morphology of vacuum-deposited asymmetrically spiro-linked compounds thin film grown on SiO<sub>2</sub>/p-Si substrates will be presented as well. The surface images were obtained by means of tapping-mode atomic force microscopy, as described previously in chapter 5. Figure 8.5 shows the surface morphology of spiro-6 $\Phi$  films grown on a mica substrate. The surface was entirely flat and smooth with a mean roughness of 0.4 nm and a root-mean square roughness of 0.5 nm. A peak-to-valley height of 3.1 nm was obtained from the cross-section analysis. Additionally, the mean roughness of Spiro-TAD films was 1.56 nm and 0.21 nm obtained for the sample grown on a SiO<sub>2</sub>/p-Si substrate and a mica substrate, respectively. The surface morphology of a Spiro-TAD film was described in sub-chapter 5.2. Figure 8.6 shows the surface morphology of Spiro-DPSP thin films grown on HMDS treated SiO<sub>2</sub>/p-Si substrates. The surfaces of the thin film were smooth and flat with a mean roughness of 0.9

nm and a root-mean square roughness of 1.1 nm. The variation of peak and valley of the surface was less than 5 nm, as shown in the cross-section analysis.

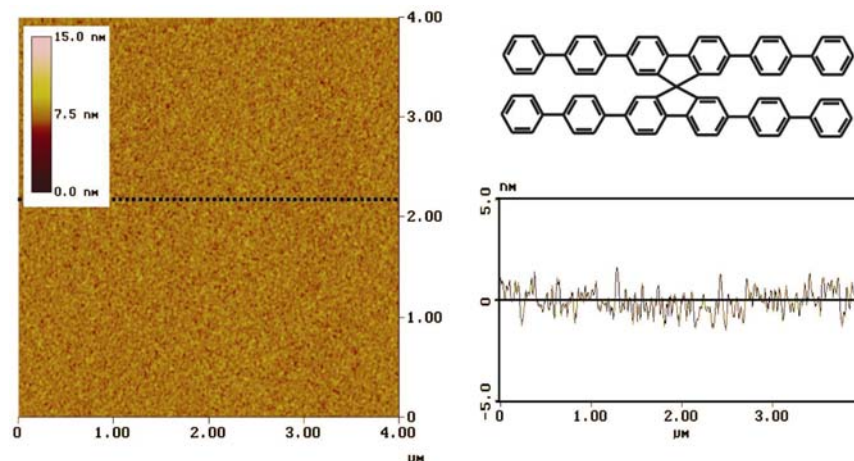


Figure 8.5. AFM topographical image of a Spiro-6 $\Phi$  thin film on a mica substrate. Left side:  $4 \times 4 \mu\text{m}^2$  AFM images, and Right side: Surface height of AFM images and the chemical structure of Spiro-6 $\Phi$ . Dotted lines in AFM image denote the cross-section analysis.

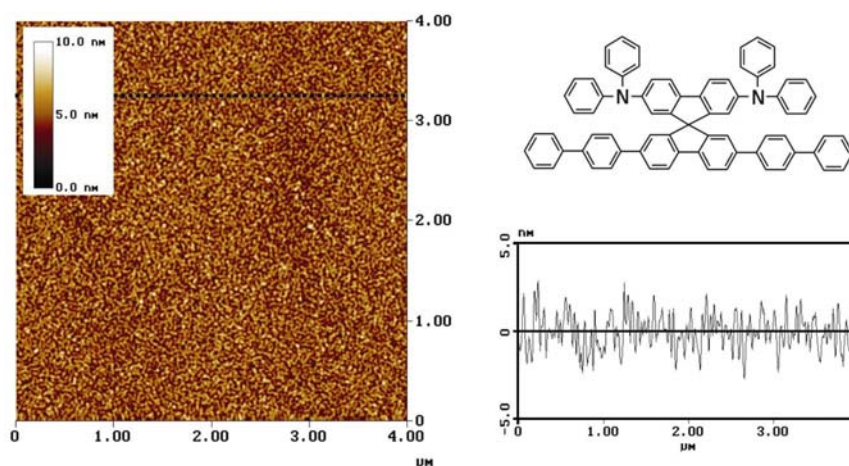


Figure 8.6. AFM topographical image of a Spiro-DPSP thin film on a  $\text{SiO}_2/p\text{-Si}$  substrate. Left side:  $4 \times 4 \mu\text{m}^2$  AFM images, and Right side: Surface height of AFM images and the chemical structure of Spiro-DPSP. Dotted lines in AFM image denote the cross-section analysis.

Figure 8.7 shows the surface morphology of Spiro-DPSP<sup>2</sup> thin films grown on HMDS treated  $\text{SiO}_2/p\text{-Si}$  substrates. The surfaces of the thin films were flat with a mean roughness of 0.27 nm and a root-mean square roughness of 0.33 nm. This value is smaller than the values obtained for Spiro-DPSP, indicating the surface of Spiro-DPSP<sup>2</sup> films is smoother than that of Spiro-DPSP films. The cross-section analysis shows that the variation of peak and valley of

the surface was less than 2 nm. This implies that the surface of Spiro-TAD films is rougher than those of Spiro-DPSP and Spiro-DPSP<sup>2</sup> films.

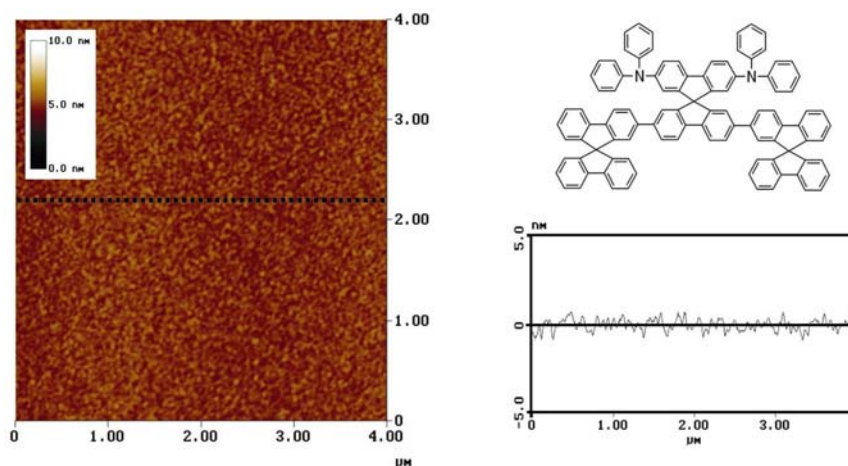


Figure 8.7. AFM topographical images of a Spiro-DPSP<sup>2</sup> thin film as deposited on a SiO<sub>2</sub>/*p*-Si substrate. Left side: 4 × 4 μm<sup>2</sup> AFM images, and Right side: Surface height of AFM images and the chemical structure of Spiro-DPSP<sup>2</sup>. Dotted lines in AFM image denote the cross-section analysis.

A preliminary experiment has shown an intramolecular charge transfer between two constituent moieties in asymmetrically spiro-linked compounds [17]. However, the optoelectronic properties of these materials have not been elucidated. There is a hint from the absorption and emission spectra that a charge transfer takes place in a molecule upon illumination. Therefore, it is a very interesting idea to observe the effect of illumination on the device performance. In the following discussion, the influence of light exposure on organic field-effect transistors based on asymmetrically spiro-linked compounds is presented.

## 8.2. Influence of light exposure on asymmetrically spiro-linked compounds field-effect transistors

### 8.2.1. Device fabrication and characterization

Ultraviolet-Visible and Fluorescence measurements of the active materials were carried out with a Perkin-Elmer Lambda 900 UV/VIS/NIR spectrophotometer and a Hitachi F-4500 fluorescence spectrophotometer, respectively. Device fabrication follows the experimental procedures described in chapter 4. For Spiro-DPSP and Spiro-DPSP<sup>2</sup>, the films

were grown with the following deposition parameters: vacuum of  $2 \times 10^{-6}$  mbar, deposition rate of 0.04 nm/s – 0.06 nm/s and a final thickness of 100 nm.

The influence of light exposure on asymmetrically spiro-linked compounds FETs were carried out in air, inside a light-shield insulating enclosure. The devices were illuminated with a Nichia ultraviolet (UV) LED NSHU 590E ( $\lambda_{\text{max}} = 374$  nm, FWHM = 11 nm) as a light source. The distance between the devices and the light source was 2.2 cm and the illumination area was  $(1.77 \pm 0.10)$  cm<sup>2</sup>. The illumination intensity can be controlled by tuning the bias or current of the Nichia UV LED. The illumination intensity is defined as the ratio of incident optical power to the active illumination area. The incident optical power of the UV LED was recorded with an AP30UV photodiode detector (Scientech) supplied with a H410 display. The accuracy of measurement is 5 %. Since the thickness of the film is 100 nm, it was assumed that the light intensity is relatively constant across the film and the irradiance inside the organic film at the channel is approximately equal to the irradiance at the surface film. This implies that the photons are uniformly absorbed throughout the organic film. Since light is used as a *third* or *additional gate electrode*, we refer to use *organic phototransistor* (OPT) term in the following discussion. A schematic view of an organic phototransistor is shown in Figure 8.8.

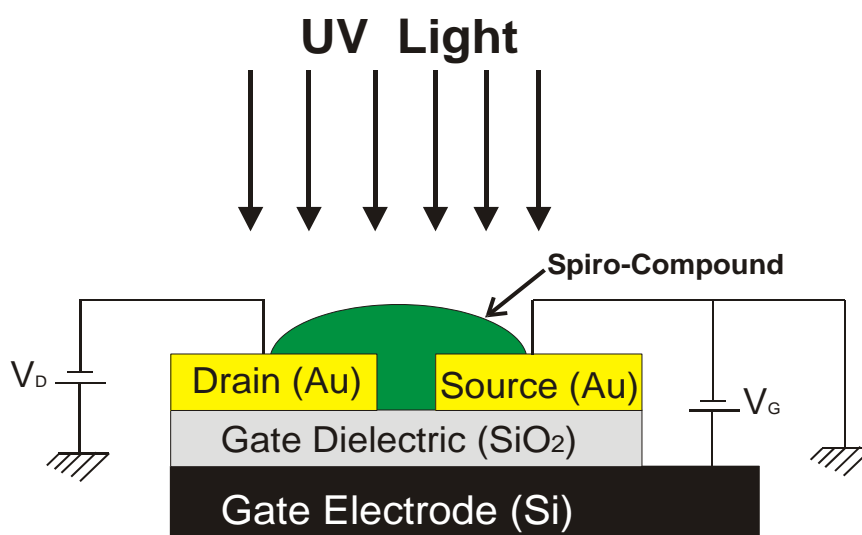


Figure 8.8. Standard bottom-contact structure of organic phototransistor fabricated through conventional lithography where ultraviolet light was used as a *third* or *additional gate electrode*.

### 8.2.2. 2,7-Bis-(*N,N'*-diphenylamino)-2',7'-bis(biphenyl-4-yl)-9,9'-spirobifluorene (Spiro-DPSP)

The spectroscopic properties of Spiro-DPSP in different solvents and in neat films are displayed in Figure 8.9. The absorption primarily takes place in the sexiphenyl chain, which can be deduced by comparison of the spectra and absorption coefficients of Spiro-DPSP, Spiro-6 $\Phi$  and Spiro-TAD. The absorption maximum is between  $\lambda_{\text{max}} = 338$  nm in hexane and  $\lambda_{\text{max}} = 347$  nm in thin films, as shown in Figure 8.9(a). Therefore, the absorption is only weakly influenced by the polarity of the environment, which indicates no interaction between the upper and lower part of the molecule in the ground state. This is different for the emission behavior. There is a large solvatochromic shift of the emission band from 419 nm in hexane to 520 nm in dichloromethane.

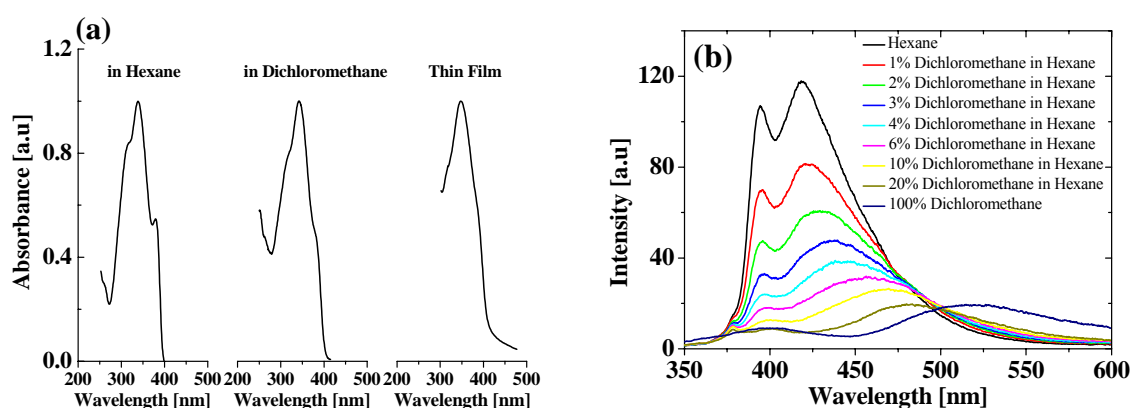


Figure 8.9. Absorption (a) and emission (b) spectra of Spiro-DPSP. The measurements of absorption spectra were carried out for thin films and in solution (hexane and dichloromethane). Emission spectra of Spiro-DPSP were measured with various concentration of dichloromethane in hexane [17].

Figure 8.9(b) shows the shifting of maxima of emission for different ratios of dichloromethane/hexane as solvent. In apolar environments, a direct relaxation under light emission is preferred, while a polar environment favors a charge transfer between the molecular halves, leaving the positive charge in the amine moiety and the negative charge in the sexiphenyl chromophore. Comparable intramolecular charge transfer effects were also found in other spiro-conjugated dyes [119,120] and are related to an overlap of higher molecular orbital of the two halves that have the appropriate symmetry (e.g. two perpendicular nodal planes) [121]. Since hole transport via hopping between the

bis(diphenylamino)biphenyl sites is faster than electron transport on the sexiphenyl units, the material can thus be regarded as an ideal photoconductor in which every excitation center of the one-component system carries its own electron trap. Without the need of a heterojunction for charge separation, this is the ideal prerequisite for applications like photorefractive systems [122] or phototransistors. The shift of the fluorescence maxima upon increasing solvent polarity depends on the difference in permanent dipole moments between ground and excited state. This behavior is also observed in spirobifluorene derivatives where the 2' or 7' position of spirobifluorene center is substituted with a strong electron acceptor such as the 1,3,4-oxadiazole groups {2,7'-bis-(*N,N*-diphenylamino)-2-(5-(4-*tert*-butylphenyl)-1,3,4-oxadiazole-2-yl)-9,9'-spirobifluorene) or Spiro-DPO}[17] or where both of these positions are substituted with 1,3,4-oxadiazole groups [123].

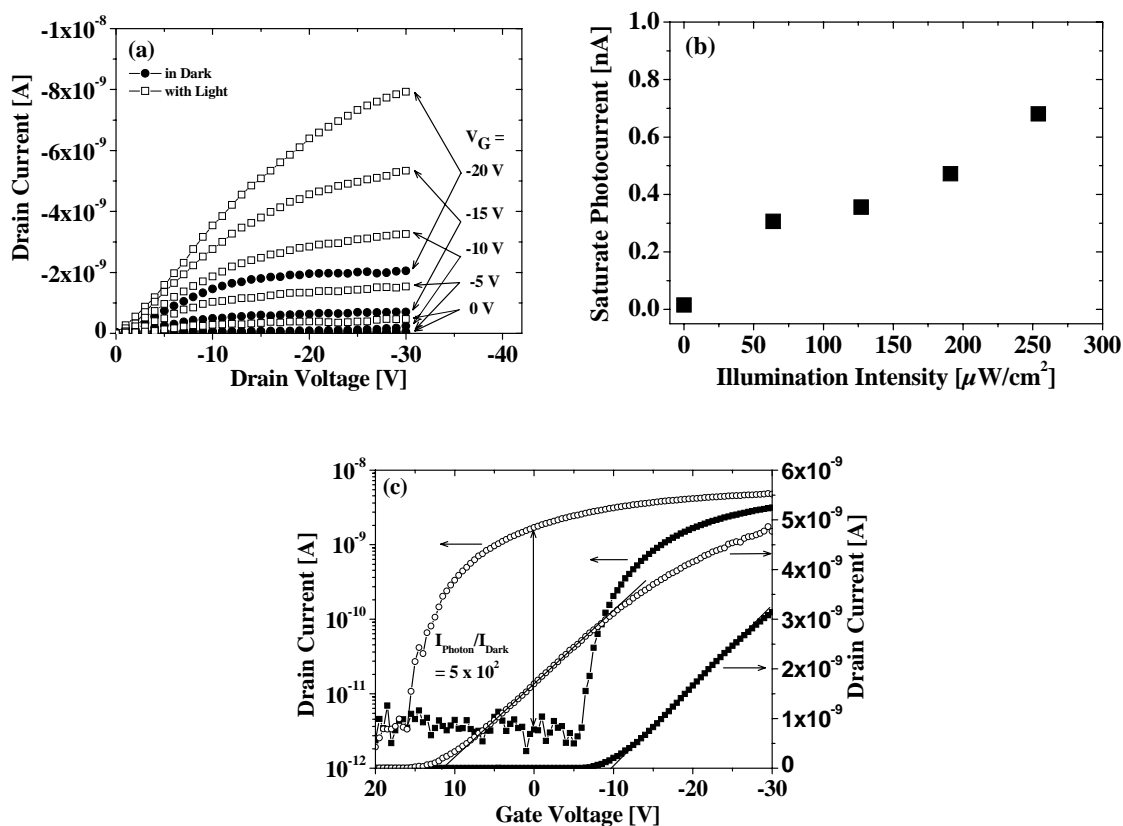


Figure 8.10.(a).Output characteristic of an OPT at different gate voltages in the dark (closed circles) and under illumination with  $191 \mu\text{W}/\text{cm}^2$  (open squares). The channel length of the device was  $10 \mu\text{m}$  and the channel width  $2 \text{ mm}$ , respectively ( $C_i = 20.93 \text{ nF}/\text{cm}^2$ ), (b).Dependency of the saturated photocurrent on the illumination intensity ( $V_D = -30 \text{ V}$  and zero gate bias), and (c).Transfer characteristic at constant drain voltage ( $V_D = -10 \text{ V}$ ) in the dark and under illumination with  $127 \mu\text{W}/\text{cm}^2$ . The drain current is plotted both logarithmically (left side) and linearly (right side). Photoirradiation shifts the transfer curve horizontally towards higher gate voltages. From the slope in the linear plot, the mobility can be obtained [15].

Figure 8.10(a) displays the output characteristics of a Spiro-DPSP phototransistor measured in the dark and under an illumination of  $191 \mu\text{W}/\text{cm}^2$  for different gate voltages. The transistors can be operated as *three terminal* devices with two electrical contacts (source and drain electrodes) and light as the amplifying gate, or as *four terminal* devices with an additional electrical gate, allowing additional biasing of the device by the electrical field-effect. Light works in the devices in a manner similar to the conventional field-effect by increasing the number of mobile charge carriers in the channel. Generally, a clear increase in the drain current was observed under illumination. Without illumination, the drain current is in the order of 10 pA and increases to several nA upon illumination. The dependency of the photocurrent in the saturation region at  $V_D = -30 \text{ V}$  on the irradiation intensity is plotted in Figure 8.10(b). In this case, the gate bias was kept constantly at  $V_G = 0 \text{ V}$ . An increase in irradiation intensity leads to an increase of the photocurrent. The mean sensitivity can be given as  $1.3 \text{ A/W}$ , but there are some deviations from linearity in the sensitivity curve. The mean sensitivity or responsivity is defined as a ratio of the drain photocurrent density to the illumination intensity. This sensitivity is lower than for amorphous silicon ( $300 \text{ A/W}$ ) [124], but higher than for polymer devices ( $1 \text{ A/W}$ ) [125,126,127,128]. The detail behavior of the sensitivity curve is subject to current investigations, but first hints can be obtained from the transfer characteristic.

Figure 8.10(c) shows the transfer characteristic of the OPT in the dark and under illumination with  $127 \mu\text{W}/\text{cm}^2$  for a drain voltage of  $-10 \text{ V}$ . A ratio of photocurrent to dark current as high as  $5 \times 10^2$  can be obtained which is comparable to amorphous silicon phototransistors. The transfer characteristics clearly show that the  $I_D - V_G$  curves are not substantially changed in shape or magnitude but rather displaced by a shift in the fitted threshold voltage (from  $-9 \text{ V}$  in the dark to  $+15 \text{ V}$  at  $127 \mu\text{W}/\text{cm}^2$ ). The threshold voltage for organic field-effect transistors in the accumulation regime is given by [100]

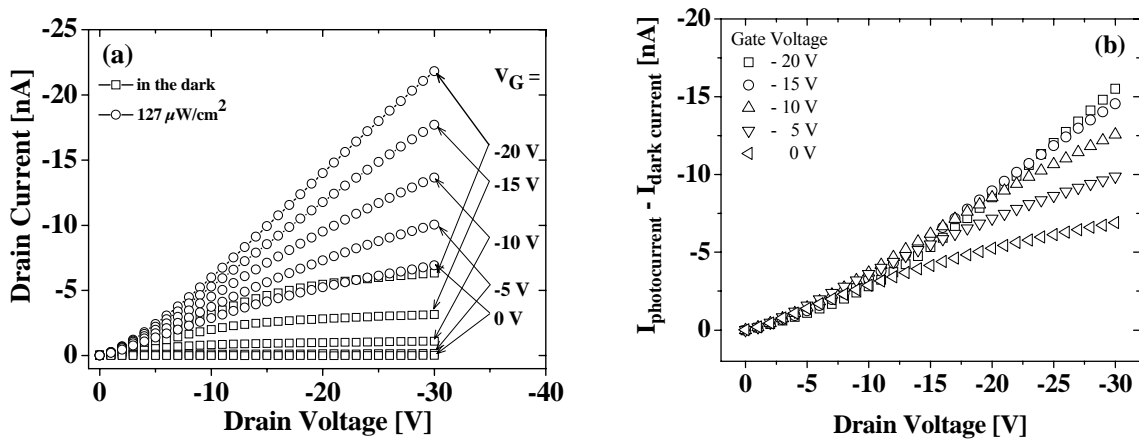
$$V_T = -\frac{qn_0 d}{C_i} + V_{FB} \quad (8.1)$$

where  $V_{FB}$  is the flat band potential,  $q$  the elementary charge, and  $n_0$  the bulk carrier density. Assuming the flat band voltage to be invariant, the charge carrier density is the only parameter that can be changed by illumination, causing the shift in the threshold voltage. From Figure 8.10(c), it becomes clear that low light intensities could not be measured at zero gate voltage. Instead, the optimum working point can be adjusted by choosing a gate bias



directly at the switch-on voltage under dark conditions, in this case at  $-6$  V. The OPT operates in the linear regime according to equation 2.9 and in the saturation regime according to equation 2.11. It allows the extraction of the charge carrier mobility. For Spiro-DPSP transistors, values of  $1.3 \times 10^{-6} \text{ cm}^2/\text{V s}$  and  $7.6 \times 10^{-6} \text{ cm}^2/\text{Vs}$  were obtained for linear and saturation regime, respectively.

Figure 8.11 shows the characteristics of a Spiro-DPSP phototransistor with a different of the channel length, the channel width, and the capacitance of the gate dielectric. The drain photocurrent is significantly increased under illumination with  $127 \mu\text{W}/\text{cm}^2$ , as shown in Figure 8.11(a). Figure 8.11(b) shows the difference between drain photocurrent and drain dark current versus drain bias for different gate voltages. The drain photocurrent upon various illumination intensities and the dark current are given in Figure 8.11(a). The difference between drain photocurrent and dark current seems to be constant at low drain biases for a given gate bias. However, the difference of current is clearly observed at high drain biases. The drain current in the accumulation regime is relatively unaffected by the illumination, as shown in Figure 8.11(c). However, the drain photocurrents at accumulation regime are significantly higher than the dark current. Moreover, the switch-on voltage shifts towards positive gate bias by increasing the incident light intensity. This effect was also observed in amorphous silicon phototransistor [129,130].



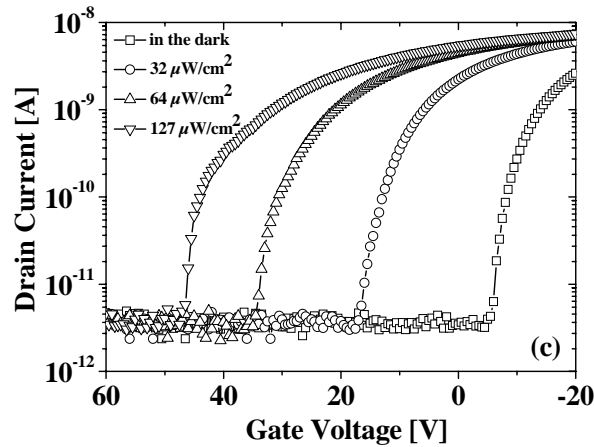


Figure 8.11.(a). Output characteristics of a Spiro-DPSP phototransistor ( $L = 5 \mu\text{m}$ ,  $W = 2 \text{ mm}$ , and  $C_i = 17.27 \text{ nF/cm}^2$ ) at different gate voltages measured in the dark (open squares) and under illumination with  $127 \mu\text{W/cm}^2$  (open circles), and (b). The difference between drain photocurrent and drain dark current is plotted versus the drain bias at different gate biases. These values are obtained from Figure 8.11(a). (c). Transfer characteristics at constant drain voltage ( $V_D = -10 \text{ V}$ ) measured in the dark and under illumination with  $32 \mu\text{W/cm}^2$ ,  $64 \mu\text{W/cm}^2$ , and  $127 \mu\text{W/cm}^2$ . The drain current is plotted semi-logarithmically. Photoirradiation shifts the transfer curve horizontally towards higher gate voltages.

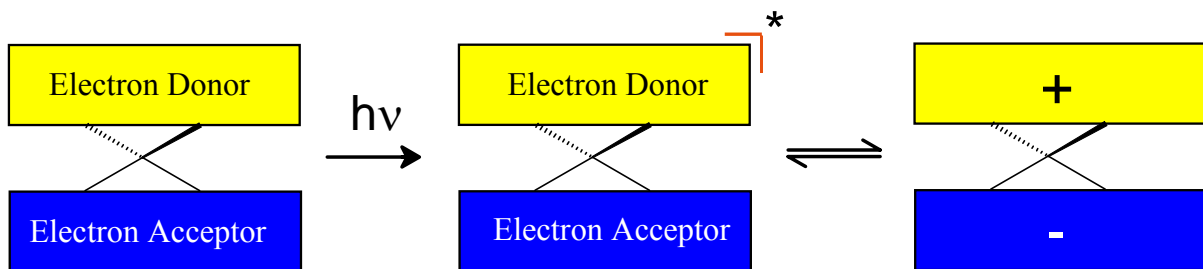


Figure 8.12. Schematic process of light induced current in organic phototransistor based on intramolecular charge transfer between two constituent moieties.

In amorphous silicon phototransistors, the illumination produces a change in the density of deep states, causing the bulk Fermi level to be moved with respect to the conduction band. The photogenerated electrons and holes disturb the balance between diffusion and drift currents that existed in the dark. Furthermore, the photogenerated electron-hole pairs are separated and electrons are swept towards the gate and holes away from the gate. The electron-hole pairs induce a redistribution of the space charge in the localized states. Moreover, the band bending will be reduced and after some time a steady state is reached, in which the bending is reduced by a certain amount and there is no longer a current flow perpendicular to the semiconductor/insulator interfaces [129]. However, this mechanism is difficult to apply in organic phototransistors, whereas the transport in organic semiconductors

is governed by a hopping mechanism. Moreover, light absorption in organic semiconductor results in the formation of exciton, a bound electron-hole pair, rather than the free electron-hole pairs directly produced in inorganic semiconductor.

A blank experiment using Spiro-TAD instead of Spiro-DPSP and Spiro-DPSP<sup>2</sup> as the organic film was performed in order to show how the effect is related to the bipolar character of the material. In that case, no photocurrent was observed. This observation suggests that the underlying mechanism can be sufficiently explained by photoinduced charge transfer between bis(diphenylamino)biphenyl and sexiphenyl sites upon illumination, as shown in Figure 8.12, and not an improved charge injection at the organic/metal electrode interface, as it was suggested in the case of photocurrent multiplication in other materials [131].

Generally, organic transistors operate in the accumulation mode and a strong inversion has not been observed yet. Since in classical MOSFET the threshold voltage refers to the onset bias of the strong inversion, the threshold voltage in organic transistor is merely a fit parameter and so the concept of the threshold voltage has no physical meaning in OFET. Therefore, the term switch-on voltage will be used to obtained physical parameter such as the number of bulk carriers, which have already described in chapter 2.

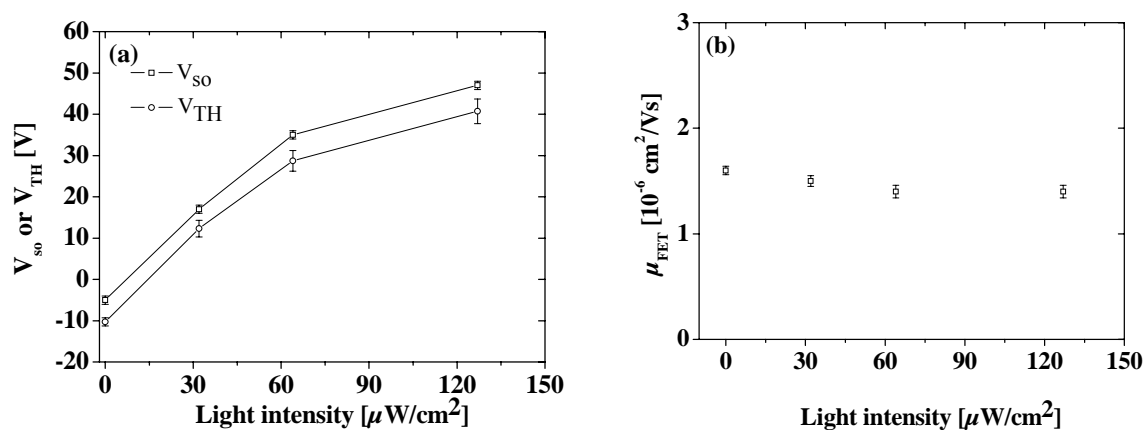


Figure 8.13.(a).Dependence of the switch-on voltage and the fitted threshold voltage on light intensity, and (b).Dependence of the field-effect mobility on light intensity.

Based on the model that Meijer *et.al* proposed [22], the  $V_{so}$  is increased toward high positive bias by increasing the incident light intensity. For instance,  $V_{so}$  is -5 V for condition in the dark, +17 for illumination of  $32 \mu\text{W}/\text{cm}^2$ , +35 V for illumination of  $64 \mu\text{W}/\text{cm}^2$  and +47 V for illumination of  $127 \mu\text{W}/\text{cm}^2$  (Figure 8.13(a)). For simplicity, the shift of  $V_{so}$  or the fitted threshold voltage could be attributed to the increase in conductivity or the number of charge carriers upon increasing incident light intensity. Figure 8.13(a) also shows that the

switch-on voltage or the fitted threshold voltage shifts as far as 50 V upon illumination. However, the mobility of charge carriers is relatively unaffected by the illumination, as shown in Figure 8.13(b).

In inorganic field-effect phototransistor structures the illumination is directly performed on the gate electrode, where the internal photoemission of charge carriers from the gate electrode into the channel as observed in GaAs field-effect phototransistors can not be neglected [132]. In organic phototransistors the illumination directly performed on the active materials. As a result, such an internal photoemission effect can be neglected.

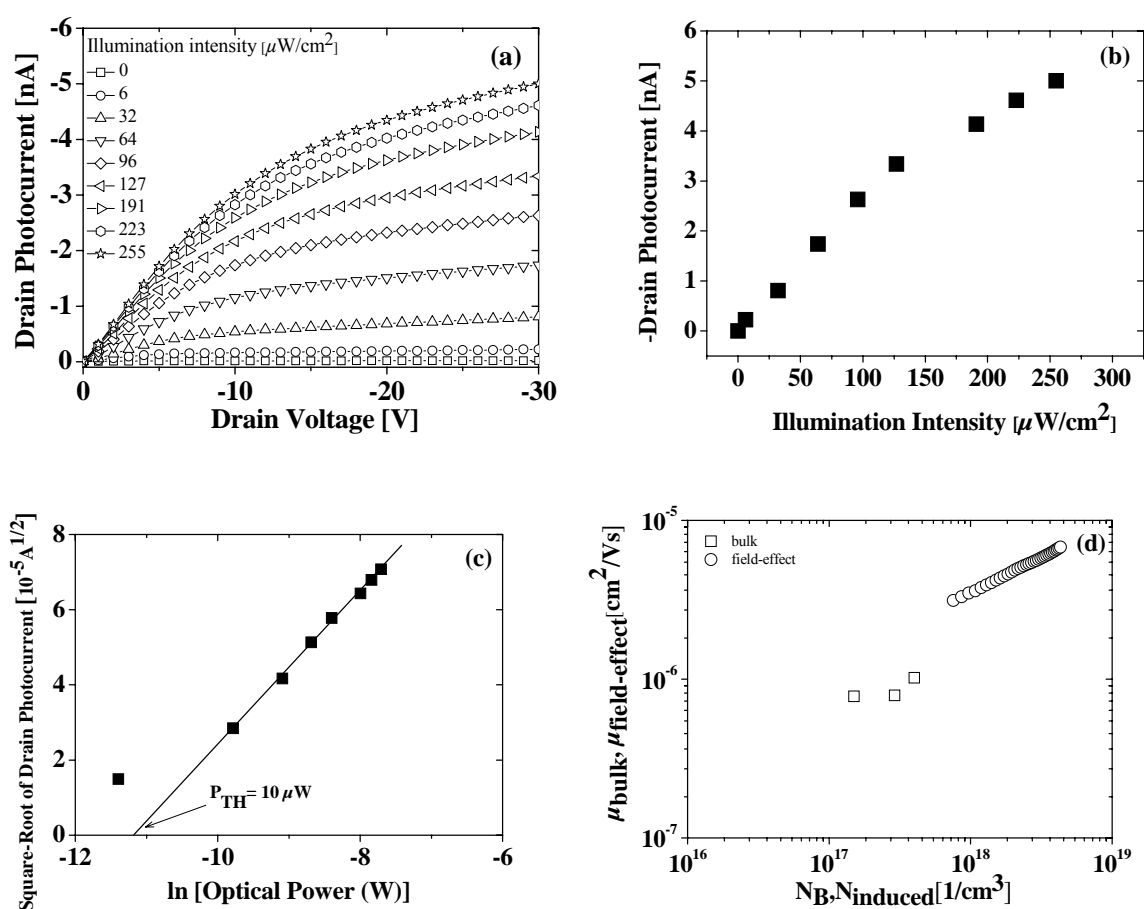


Figure 8.14.(a).Drain photocurrent is plotted versus drain bias at different illumination intensities and the gate bias is being zero, (b).Saturated drain photocurrent (at  $V_D = -30$  V) is plotted versus the illumination intensity, (c).Square-root of the drain photocurrent is plotted versus natural logarithmic of the incident optical power, and (d).The bulk charge carriers mobility in Spiro-DPSP due to the illumination versus the number of bulk charge carriers  $N_B$ . For comparison, the field effect mobility as a function of induced charge is given.

Organic phototransistors based on spiro-linked compounds show that the UV light can completely serve as the *third electrode*, as shown in Figure 8.14(a). An interesting characteristic is the transistor characteristic was observed as the gate bias is being zero. The

channel and bulk conductivity can be tuned by varying the illumination intensity. This indicates that the gate electric function can be replaced optically. Furthermore, the presence of the saturation regime as shown in Figure 8.14(a) implies that the drain photocurrent under illumination is also channel restricted. From Figure 8.14(a), the ratio of the drain photocurrent to the dark drain current at a drain bias of -30 V is  $1.5 \times 10^3$ . This value is comparable to amorphous silicon phototransistor which has a ratio of  $3.5 \times 10^3$  at  $V_G = V_D = 10$  V under illumination of 10000 lx [133]. High current ratios originate from the very low *OFF* current, the drain current at zero gate bias which is in the range of pA. High purity materials endowed with amorphous character give very low *OFF* current. Indeed, most spiro-linked compound thin films are not influenced by moisture, even though the sample was stored in ambient atmosphere up to nine months as described previously in chapter 6.

The saturated drain photocurrent in a floating gate scheme depends on incident light power as described for inorganic phototransistors based on GaAs, which is given by [132]

$$\sqrt{I_D} \propto \ln(P) \quad (8.2)$$

where  $P$  is the incident light power. Figure 8.14(b) shows the drain photocurrent is linearly plotted versus the illumination intensity. However, the drain photocurrents do not increase linearly with increasing illumination intensity. Figure 8.14(c) shows a plot of the square-root of the saturated drain photocurrent versus natural logarithmic of the incident light power. The fitted line in Figure 8.14(c) satisfies equation 8.2 quite well. There is a deviation at low light intensities, for instance at a light intensity of  $6 \mu\text{W}/\text{cm}^2$ . However, the square-root of drain photocurrent is linearly increased with the natural logarithmic of light intensity at light intensities larger than  $30 \mu\text{W}/\text{cm}^2$ .

The threshold of incident optical power  $P_{TH}$  is derived from the intersection of the linear fit of the square-root of the saturated drain photocurrent versus natural logarithmic of the incident optical power with the abscissa. A value of  $14 \mu\text{W}$  is obtained for Spiro-DPSP phototransistor. A threshold optical power in the context of organic phototransistors could be regarded as the minimum optical power to cause a photoelectric effect. Below  $P_{TH}$ , the material is insensitive and, therefore, no light can be detected. Furthermore, the fitted threshold voltage is increased by increasing the illumination intensity. Therefore, the number of the bulk carrier is also increased by increasing the illumination intensity according to equation 8.1. Figure 8.14(d) shows the dependency of the bulk carriers on the number of bulk charge carrier, which is estimated using equation 8.7 and 8.8. The dependency of the induced

carrier density on the field-effect mobilities is also provided. The contribution of bulk carrier mobility can be negligible to the total mobility in devices, even though the number of bulk carriers is a half lower than the number of field-induced charge in the active channel. However, the bulk carriers dominate the behavior in the depletion mode whereas the field-induced charge in the active channel does not exist yet. That is the reason why the threshold voltage or the switch-on voltage shifts toward positive gate bias with increasing illumination intensity. In the following text, the number of the bulk carriers due to the illumination from a well-known method in organic/inorganic semiconductors is derived [28]. For a small drain bias, the depletion layer width is given by equation 2.15. Furthermore, the gate dielectric capacitance per unit area is given by

$$C_i = \frac{\epsilon_o \epsilon_{ins}}{d_{ins}} \quad (8.3)$$

and the semiconductor layer capacitance is given by

$$C_{sem} = \frac{\epsilon_o \epsilon_{sem} A}{d_{sem}} \quad (8.4)$$

where  $\epsilon_o$  is the permittivity of vacuum ( $8.85 \times 10^{-14}$  C/(J cm)),  $\epsilon_{ins}$  the relative dielectric constant of the gate insulator,  $\epsilon_{sem}$  the relative dielectric constant of the active layer,  $d_{ins}$  the thickness of the insulator,  $d_{sem}$  the thickness of the active layer, and  $A$  the active area of the transistors ( $L \times W$ ). Then, the depletion layer width (Equation 2.15) for the pinch-off condition can be calculated (the pinch-off voltage is the voltage at which the FET is driven far enough into depletion, eventually the entire film will be depleted of mobile charge and no more current will flow);  $V_{pinch} = V_{S'} - V_{so}$ . This is the case in which the depletion layer is equal to the semiconductor layer thickness. By inserting  $W_d$  is equal to  $d_{sem}$ , equation 8.3 and equation 8.4 to equation 2.15, the number of the bulk carrier  $N_B$  was obtained as

$$N_B = \frac{2 \epsilon_o V_{pinch}}{q \left( \frac{d_{sem}^2}{\epsilon_{sem}} + \frac{2 d_{sem} d_{ins}}{\epsilon_{ins}} \right)} \quad (8.5)$$

For calculating  $N_B$ ,  $\epsilon_{sem} \approx 3.18$ ,  $d_{sem} = 100$  nm,  $d_{ins} = 200$  nm,  $\epsilon_{ins} \approx 3.9$ , and  $V_{pinch} = V_{S'} - V_{so}$  were substituted to equation 8.5.  $V_{so}$  is the switch-on voltage of the phototransistor without illumination, and  $V_{S'}$  is the corresponding switch-on voltage upon illumination. Finally, the bulk charge carriers mobilities is calculated by using equation 8.6 [28]

$$\mu_{bulk} = \frac{L I_d}{N_B q W d_{sem} V_D} \Big|_{V_G = V_{so}} \quad (8.6)$$

where  $W$  is the channel width, and  $L$  the channel length. The result of those calculations is shown in Figure 8.14(d).

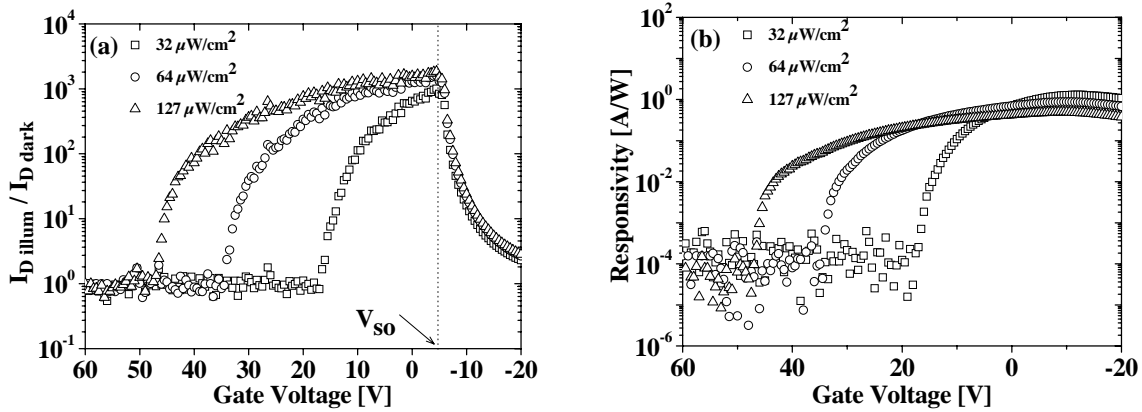


Figure 8.15.(a).Ratio of drain photocurrent to drain dark current is plotted against gate biases. The dotted lines indicate the switch-on voltage, and (b).The responsivity is plotted against gate biases.

Figure 8.15(a) shows the ratio of drain photocurrent to dark current at different gate biases. A maximum ratio of  $1.9 \times 10^3$  is obtained at the switch on voltage. However, the ratio of drain photocurrent to drain dark current decreased and reached the ratio of ca.3 when the gate bias is being larger than the switch-on voltage. This happened because the channel current at  $V_G < V_{so}$  becomes significant with respect to the bulk current. Thus, the current at  $V_G < V_{so}$  was a contribution of the channel current due to the field-effect and the current from the illumination effect. Consequently, the ratio of drain photocurrent to drain dark current is optimum at  $V_G > V_{so}$ . However, this ratio also depends on the illumination intensity, as shown in Figure 8.15(a).

Figure 8.15(b) shows the operational responsivity of Spiro-DPSP phototransistors at different gate biases and illumination intensities. The maximum operational responsivity of

Spiro-DPSP phototransistors is 1.3 A/W at  $V_G = -12$  V. However, the ratio of drain photocurrent to dark current at that point is 10, which is very low for photosensing application. The optimal responsivity of 1.1 A/W can be obtained at the switch-on voltage ( $V_G = -6$  V); giving a ratio of drain photocurrent to dark current of  $1.9 \times 10^3$ . At  $V_G = 0$  V, a ratio of photocurrent to dark current of  $1.6 \times 10^3$  and a responsivity of 0.7 A/W can be obtained. However, this responsivity is still lower than the responsivity of single crystal silicon (300 A/W) [124], but higher than polymer photoresponsive [125,126,127,128]. Notably, the operational responsivity is defined as  $\Delta J_D/P_{inc}$ , where  $\Delta J_D \equiv J_{D,ph} - J_{D,dark}$ .  $P_{inc}$  is the incident light intensity,  $J_{D,dark}$  is the current density in the dark, and  $J_{D,ph}$  is the current density upon illumination. Moreover, the responsivity covers a broad range of the gate bias with increasing the illumination intensity. For instance at a light intensity of  $127 \mu\text{W}/\text{cm}^2$ , an operational responsivity of larger than 0.01 A/W can be obtained in the range of the gate biases between +40 V and -20 V.

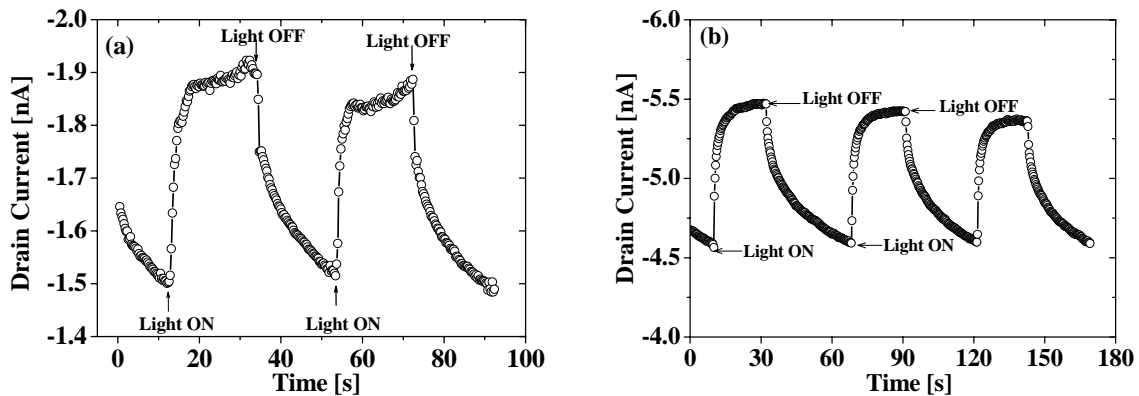


Figure 8.16.(a).Time-resolved response of Spiro-DPSP phototransistor ( $W = 2$  mm,  $L = 10 \mu\text{m}$ ,  $C_i = 20.93$  nF/cm<sup>2</sup>) upon irradiation with  $191 \mu\text{W}/\text{cm}^2$  at  $V_G = V_D = -10$  V. The photoswitching of the drain current is reversible with a relaxation time of 10.3 s [15]. (b).Time-resolved response of the phototransistor ( $W = 2$  mm,  $L = 5 \mu\text{m}$ ,  $C_i = 17.27$  nF/cm<sup>2</sup>) upon irradiation with  $127 \mu\text{W}/\text{cm}^2$  at  $V_G = -20$  V, and  $V_D = -10$  V. The photoswitching of the drain current is reversible with a relaxation time of 10 s.

The time-resolved response of the phototransistor are also measured, as shown in Figure 8.16(a) and Figure 8.16(b). Figure 8.16(a) shows that the response cannot be described by a single response time but rather as a combination of a fast increase of photocurrent at the beginning and a second, slower process in the order of tens of seconds. For the fast response, the time constant is approximately 1.5 seconds in this case, but depends on irradiation intensity and wavelength. The relaxation after switching the light off can be fitted by a single exponential decay quite well, giving a rather long time constant of 10.3 seconds. Since this



relaxation time is related to the recombination of the photoseparated charges, it can be improved by an appropriate material design, thus allowing faster detection speeds. Figure 8.16(b) shows that the drain photocurrent reached 90% of maximum current in less than 3 seconds.

As mentioned previously, Spiro-DPSP consists of a sexiphenyl and a bis(diphenylamino)biphenyl moiety. Both functional molecules are linked by a spiro carbon atom. However, what would happen if two functional molecules were simultaneously evaporated. Could a phototransistor effect be also observed? Regarding this question, an organic phototransistor was made at which the active layer was deposited by co-evaporating Spiro-TAD and Spiro-6 $\Phi$  (Spiro-TAD : Spiro-6 $\Phi$  = 1:1). Spiro-TAD and Spiro-6 $\Phi$  are the symmetrically substituted parent compounds of Spiro-DPSP. The absorption spectrum of Spiro-TAD : Spiro-6 $\Phi$  (1:1) thin films indicates the absorption ( $\lambda_{\text{max}} = 346$  nm) takes place in spiro-6 $\Phi$ . Figure 8.17 shows the phototransistor characteristic based on Spiro-TAD : Spiro-6 $\Phi$  (1:1). The co-evaporated thin film is also light sensitive like Spiro-DPSP. The field-effect mobility of hole in the linear regime is  $2.6 \times 10^{-7}$  cm<sup>2</sup>/Vs, which is five times smaller than the hole mobility in Spiro-DPSP. The drain current at  $V_D = -30$  V and  $V_G = -20$  V is 1.3 nA measured in the dark and 5.1 nA measured upon illumination with  $127 \mu\text{W}/\text{cm}^2$ . Figure 8.17(a) also shows that there is a current of 0.7 nA at  $V_D = V_G = 0$  upon illumination, which is higher than the dark current ( $\sim 0.01$  nA). The origin of this effect is not understood yet.

Figure 8.17(b) shows the transfer characteristic measured in the dark and under illumination with 32 and  $64 \mu\text{W}/\text{cm}^2$ . The switch-on voltage also shifts toward positive gate bias with increasing the illumination intensities. A similar result was also reported for Spiro-DPSP phototransistor. Moreover, the mobility of holes is also not affected by the illumination. The drain photocurrent of co-evaporation thin films is also five times smaller than the drain photocurrent of Spiro-DPSP phototransistor. The origin of this effect is due to the fact that the co-evaporation process does not exhibit homogeneous distribution of Spiro-TAD and Spiro-6 $\Phi$  in thin films as is the case with bis(diphenylamino)biphenyl and sexiphenyl sites in Spiro-DPSP. A maximum operational responsivity of 0.17 A/W can be obtained at the switch-on voltage ( $V_G = -3$  V), which is one order of magnitude lower than the value obtained for Spiro-DPSP phototransistors. A maximum ratio of drain photocurrent to dark current of 60 can be obtained at the switch-on voltage. This value is much lower than the value obtained for Spiro-DPSP phototransistor. At  $V_G = 0$  V, the ratio of photocurrent to dark current of 26 and the responsivity of 0.13 A/W can be obtained. Based on this result, the charge transfer does not only take place in Spiro-DPSP, but also in co-evaporation of Spiro-TAD and Spiro-6 $\Phi$ .

This result supports the concept of intramolecular charge transfer mechanism in Spiro-DPSP phototransistors. However, the charge transfer is more effective in Spiro-DPSP than that in Spiro-TAD : Spiro-6 $\Phi$  (1:1).

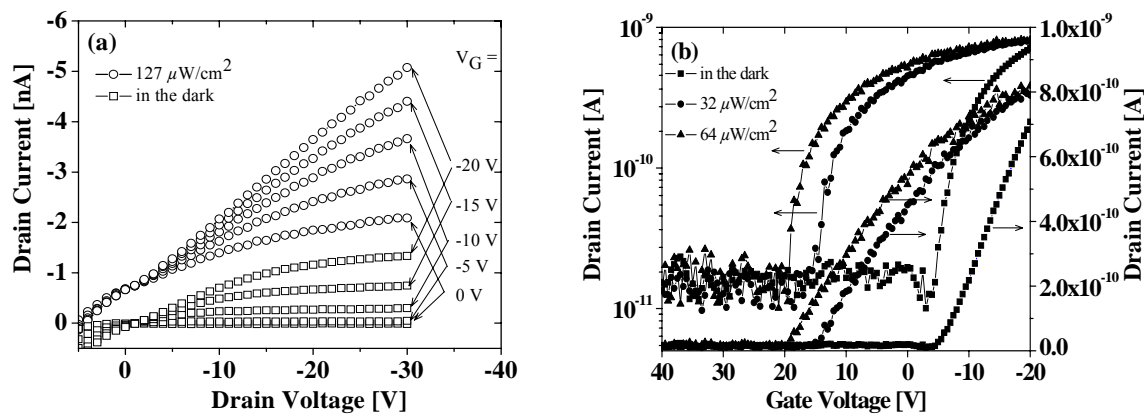


Figure 8.17.(a).Output characteristic of Spiro-TAD : Spiro-6 $\Phi$  (1:1) phototransistors ( $L = 5 \mu\text{m}$ ,  $W = 2 \text{mm}$ , and  $C_i = 17.27 \text{ nF/cm}^2$ ) at different gate voltages in the dark (open squares) and under illumination with  $127 \mu\text{W/cm}^2$  (open circles). (b).Transfer characteristic at constant drain voltage ( $V_D = -10 \text{ V}$ ) in the dark and under illumination with  $32 \mu\text{W/cm}^2$ , and  $64 \mu\text{W/cm}^2$ . The drain current is plotted semi-logarithmically (left side) and linearly (right side). Photoirradiation shifts the transfer curve horizontally towards higher gate voltages.

### 8.2.3. 2,7-Bis-(*N,N'*-diphenylamino)-2',7'-bis(spirobifluorene-2-yl)-9,9'-spirobifluorene (Spiro-DPSP<sup>2</sup>)

Another photosensitive asymmetrically spiro-linked compound is 2,7-bis-(*N,N'*-diphenylamino)-2',7'-bis(spirobifluorene-2-yl)-9,9'-spirobifluorene (Spiro-DPSP<sup>2</sup>). It belongs to the class of asymmetrically spiro-linked compounds in which two different functional chromophores are linked together by a central spiro atom. In this case, the functional units consist of a terfluorene-derivative and a bis(diphenylamino)biphenyl moiety. Figure 8.18(a) shows the absorption of Spiro-DPSP<sup>2</sup> in thin films and in solution (hexane and dichloromethane). The absorption maximum is at  $\lambda_{\text{max}} = 354 \text{ nm}$  in solution and in thin films. There is no shift in absorption maxima as observed in Spiro-DPSP. Therefore, the absorption is not influenced by the polarity of the environment. The emission behavior exhibits a large solvatochromic shift. The emission maximum  $\lambda_{\text{em}}$  shifts from 415 nm measured in hexane to 544 nm measured in dichloromethane. Similar to Spiro-DPSP, a direct relaxation under light emission is preferred in apolar environments, while polar environment favors a charge

transfer between the molecular halves, leaving the positive charge in the amine moiety and the negative charge in the terfluorene-derivative chromophores.

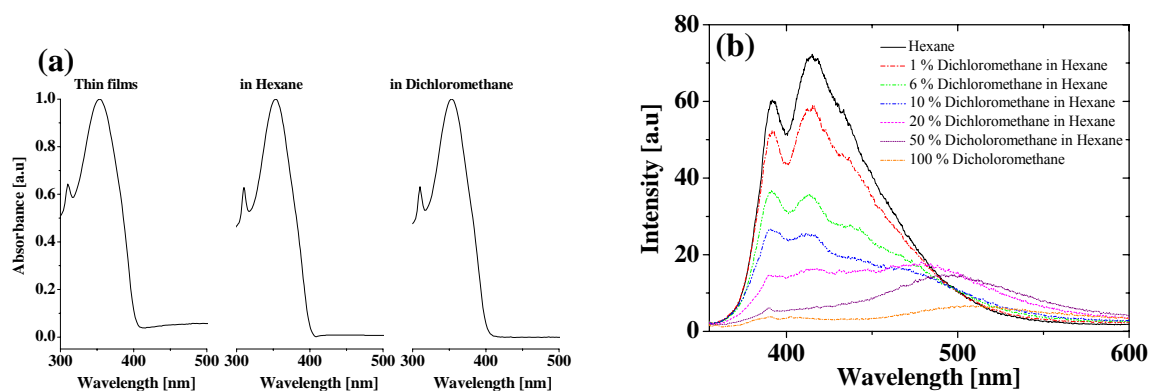


Figure 8.18. Absorption (a) and emission (b) spectra of Spiro-DPSP<sup>2</sup>. The measurements of absorption spectra were carried out for thin films and in solution (hexane and dichloromethane). Emission spectra of Spiro-DPSP<sup>2</sup> were measured with various concentration of dichloromethane in hexane.

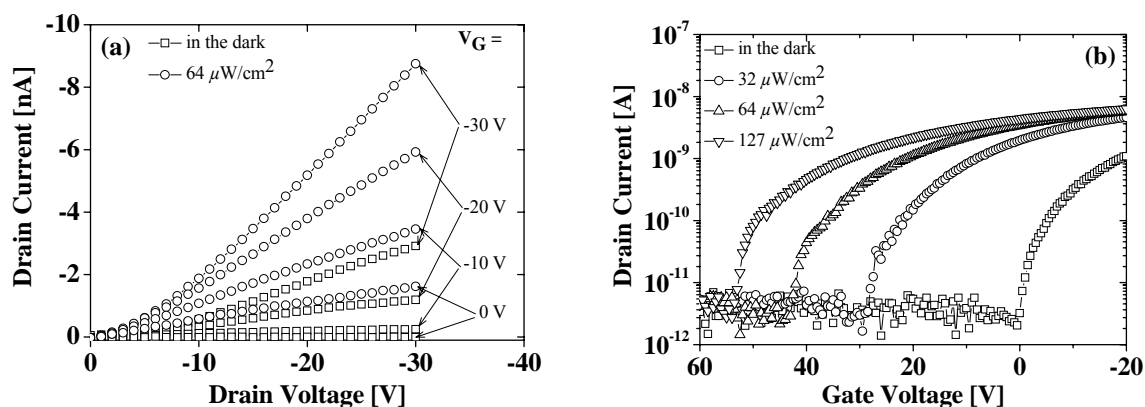


Figure 8.19. (a). Output characteristics of a Spiro-DPSP<sup>2</sup> phototransistor ( $L = 5 \mu\text{m}$ ,  $W = 5 \text{mm}$ , and  $C_i = 17.27 \text{nF}/\text{cm}^2$ ) at different gate voltages measured in the dark and under illumination with  $64 \mu\text{W}/\text{cm}^2$ . (b). Transfer characteristics at constant drain voltage ( $V_D = -20 \text{V}$ ) measured in the dark and under illumination with  $32 \mu\text{W}/\text{cm}^2$ ,  $64 \mu\text{W}/\text{cm}^2$  and  $127 \mu\text{W}/\text{cm}^2$ . The drain current is plotted semi-logarithmically. Photoirradiation shifts the transfer curve horizontally towards higher gate voltages.

Figure 8.19(a) shows the output characteristic of Spiro-DPSP<sup>2</sup> phototransistor measured in air and in two conditions: in the dark and under illumination with  $64 \mu\text{W}/\text{cm}^2$ . The drain current significantly increased upon illumination as also observed for Spiro-DPSP phototransistors. The drain current at  $V_G = V_D = -30 \text{V}$  was  $2.9 \text{nA}$  measured in the dark and increased to  $8.7 \text{nA}$  measured under illumination with  $64 \mu\text{W}/\text{cm}^2$ . However, the output characteristic exhibits some nonlinearities at low drain biases, which can be attributed to the

non-ohmic contacts between Spiro-DPSP<sup>2</sup> and the gold electrodes. In addition, UV light did not improve the charge injection. This argument was supported by evidence that the drain current at low drain biases did not increase significantly upon illumination.

Figure 8.19(b) shows the transfer characteristics ( $V_D = -20$  V) measured in the dark and under illumination with 32, 64 and 127  $\mu\text{W}/\text{cm}^2$ . The drain current at accumulation regime is slightly affected by the illumination. The drain current at  $V_G = -20$  V measured in the dark was 1.1 nA. The drain current increased to 4.6 nA, 5.7 nA and 6.3 nA under illumination with 32, 64 and 127  $\mu\text{W}/\text{cm}^2$ , respectively. This implies that the channel conductivity was controlled by gate biases and light intensities. The switch-on voltage shifts toward positive gate bias as the light intensities impinged on the surface increase.

Another feature is a shift of the switch-on voltage towards more positive gate bias by increasing illumination intensity. Figure 8.20(a) shows that the switch-on voltage or the fitted threshold voltage shifts as far as 50 V upon illumination. A fitted threshold voltage or switch-on voltage corresponds with a number of charge carriers in thin films according to equation 8.1. The field-effect mobility of hole measured in the linear regime was  $2.7 \times 10^{-7} \text{ cm}^2/\text{Vs}$ . The hole mobilities measured in air are the same as the values measured in vacuum. Furthermore, the field-effect mobility of charge carriers is independent of the illumination intensity, as shown in Figure 8.20(b).

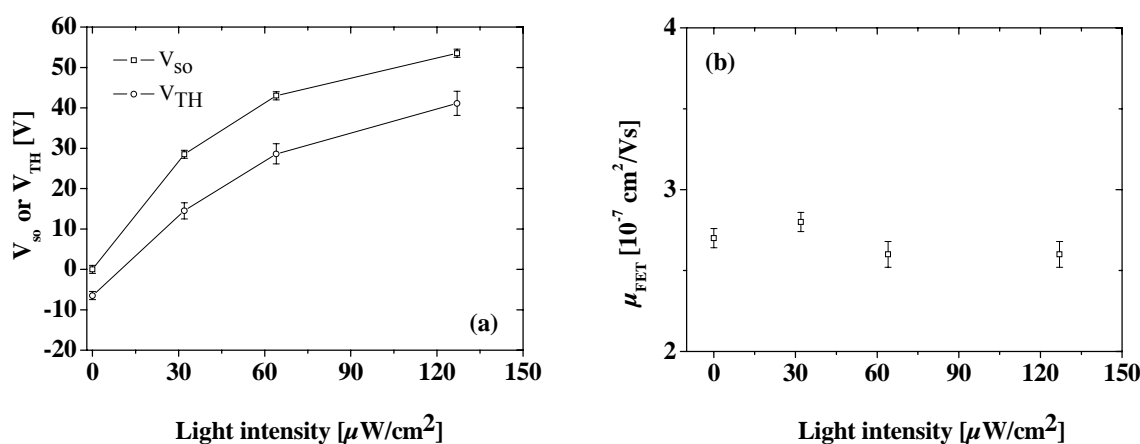


Figure 8.20.(a).Dependence of the switch-on voltage and the fitted threshold voltage on light intensity, and (b).Dependence of the field-effect mobility, extracted in the linear regime, on light intensity.

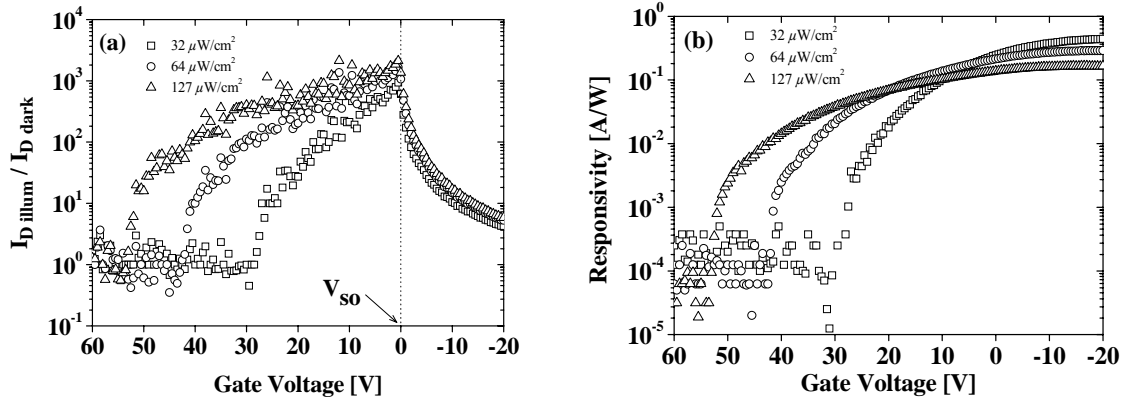


Figure 8.21.(a).Ratio of the current upon illumination to the dark current is plotted against gate biases. The dotted lines indicate the switch-on voltage, and (b).The responsivity is plotted against gate biases.

Figure 8.21(a) shows a ratio of the drain current upon illumination to the dark current at different gate biases. A maximum ratio of  $2.1 \times 10^3$  can be obtained at the switch-on voltage. This value is similar with the value obtained for Spiro-DPSP phototransistor. It is also clear that the ratio of drain photocurrent to the dark current depends on the illumination intensity and the gate biases. Moreover, the ratio of drain photocurrent to the dark current decreases as the gate bias is being swept towards more negative gate biases ( $V_G < V_{so}$ ). This evidence caused by the fact that the channel current (due to field-effect) becomes significant at  $V_G < V_{so}$ . As a result, the ratio of drain photocurrent to dark current decreases as the gate bias increases toward more negative biases.

Figure 8.21(b) shows the operational responsivity at different gate biases and illumination intensities. The shape of responsivity is similar with the transfer characteristics. The maximum operational responsivity of Spiro-DPSP<sup>2</sup> phototransistors is 0.44 A/W at  $V_G = -20$  V. This value is three times lower than the value obtained for Spiro-DPSP phototransistor. However, at that point ( $V_G = -20$  V) the ratio of drain photocurrent to dark current is 6, which is very low for photodetector application. The optimal value is at switch-on voltage ( $V_{so} = 0$  V). A responsivity of 0.24 A/W and a ratio of drain photocurrent to dark current of  $2.1 \times 10^3$  can be obtained at that point. Additionally, a responsivity of 1.1 A/W and a ratio of drain photocurrent to dark current of  $1.9 \times 10^3$  can be obtained at the switch-on voltage for Spiro-DPSP phototransistor.

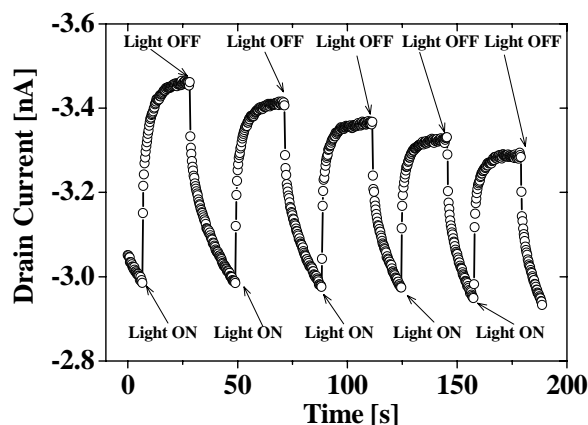
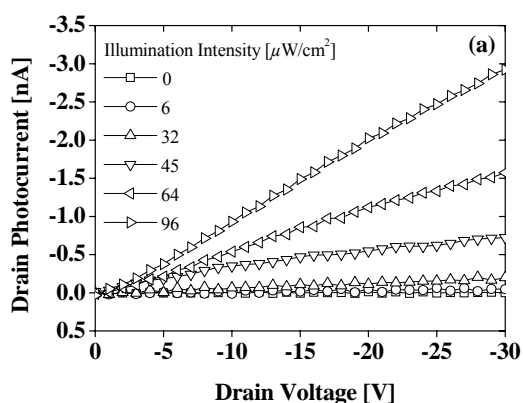


Figure 8.22. Time-resolved response of Spiro-DPSP<sup>2</sup> phototransistors ( $W = 5 \text{ mm}$ ,  $L = 5 \text{ }\mu\text{m}$ ,  $C_i = 17.27 \text{ nF/cm}^2$ ) upon irradiation with  $64 \text{ }\mu\text{W/cm}^2$  at  $V_G = V_D = -20 \text{ V}$ .

Figure 8.22 shows the time-resolved response of Spiro-DPSP<sup>2</sup> phototransistors measured at  $V_D = V_G = -20 \text{ V}$ . The photocurrent reached its maximum in 3 seconds and the relaxation needs more than 15 seconds. It is clear that the response time of Spiro-DPSP<sup>2</sup> phototransistor is slower than of Spiro DPSP phototransistor. One interesting feature revealed in the time-resolve response is the drain photocurrent maximum decreased with increasing time which is not observed in Spiro-DPSP phototransistors. This result is not fully understood yet.



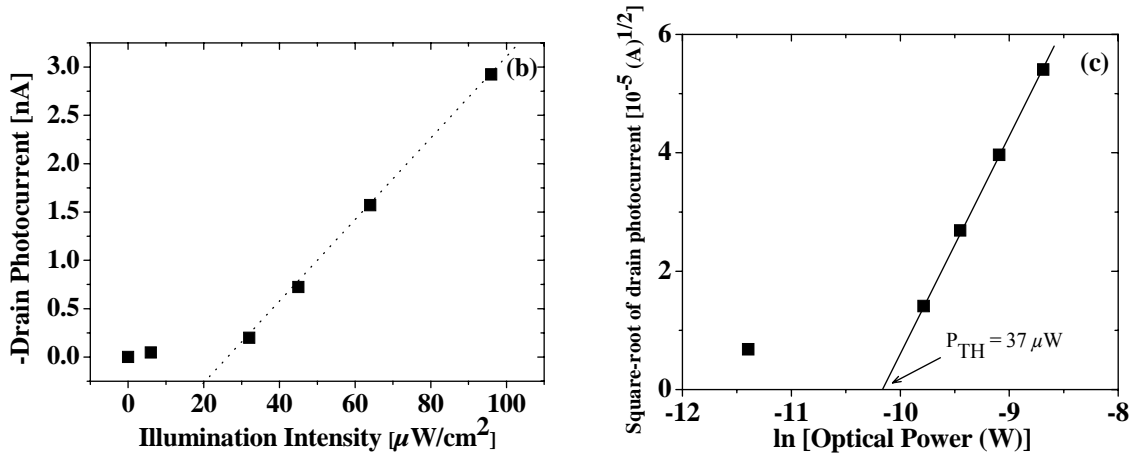


Figure 8.23.(a).Drain photocurrent is plotted against drain bias at different illumination intensity, the gate bias being zero, (b).Saturated drain photocurrent of Spiro-DPSP<sup>2</sup> phototransistors (at  $V_D = -30$  V) is plotted against illumination intensity. Dotted line is a visual guide for the eye. (c).Square-root of saturated photocurrent is plotted against natural logarithmic of the incident optical power.

Figure 8.23(a) shows the drain photocurrents are plotted versus drain bias as the gate bias is being zero. The drain photocurrent increases linearly against drain bias with increasing illumination intensities. An interesting feature revealed in the output characteristics is the linearity of the drain photocurrent versus drain bias. This implies no barrier exists between the electrode and Spiro-DPSP<sup>2</sup> upon illumination. A plausible cause is the charge is injected from the gold electrode with increasing gate bias ( $V_G < 0$ ) and drain bias ( $V_D < 0$ ). In contrast, the charge is already present in films (bulk and channel) upon illumination and then the drain bias drives the charge between the source and drain electrodes. This indicates that the charges have no barrier since the charges are not injected, but already present due to photoinduced charge transfer upon illumination. Therefore, these are two different situations. It was also found that no clear saturation of drain photocurrent was observed. Additionally, the drain photocurrent of 2.9 nA can be obtained at  $V_D = -30$  V and with illumination of  $96 \mu\text{W}/\text{cm}^2$ . Figure 8.23(b) shows the drain photocurrent is plotted linearly against illumination intensity. Two regimes have been observed in this figure, i.e.  $I_{\text{illu}} < 30 \mu\text{W}/\text{cm}^2$  and  $I_{\text{illu}} > 30 \mu\text{W}/\text{cm}^2$ . At  $I_{\text{illu}} < 30 \mu\text{W}/\text{cm}^2$ , the drain photocurrent slowly increased with increasing illumination intensity. In contrast, the drain photocurrent greatly increased with increasing illumination intensity at  $I_{\text{illu}} > 30 \mu\text{W}/\text{cm}^2$ . Therefore, there is a boundary between these regimes which is the so called threshold point ( $I_{\text{illu, threshold}} \approx 20 \mu\text{W}/\text{cm}^2$ ). In addition, Figure 8.23(c) shows a plot of the square-root of the drain photocurrent is plotted against the natural logarithm of the incident optical power. A threshold of incident optical power of  $37 \mu\text{W}$  is obtained according to

equation 8.2, which is higher than the values obtained for Spiro-DPSP. This implies that Spiro-DPSP is better than Spiro-DPSP<sup>2</sup> in term of sensitivity to UV light.

### 8.3. Summary of chapter 8

In summary, organic phototransistors based on asymmetrically spiro-linked compounds 2,7-bis-(*N,N'*-diphenylamino)-2',7'-bis(biphenyl-4-yl)-9,9'-spirobifluorene (Spiro-DPSP) and 2,7-bis-(*N,N'*-diphenylamino)-2',7'-bis(spirobifluorene-2-yl)-9,9'-spirobifluorene (Spiro-DPSP<sup>2</sup>) have been demonstrated. Intramolecular charge transfer between a sexiphenyl/terfluorene-derivative and a bis(diphenylamino)biphenyl moiety leads to an increase in the charge carrier density upon illumination, providing the amplification effect. The *OFF* current is significantly increased by a factor which is comparable with devices based on amorphous silicon. Upon illumination, the drain current in the accumulation regime remains relatively unaffected by the illumination and the charge carrier mobility is relatively constant. Furthermore, the illumination strongly shifts the threshold voltage or the switch-on voltage toward more positive gate bias. Based on these results, single layer amorphous organic semiconductors based on Spiro-DPSP and Spiro-DPSP<sup>2</sup> seem to be very attractive for low-cost ultraviolet photodetector application. Another possible application could be non-volatile memory devices. The stored charge affects the threshold voltage or switch-on voltage. For erasing the stored charge and returning the device to a *lower threshold or switch-on voltage* state, ultraviolet light can be used [18,134,135].



## Conclusions

A comparison between the charge transport properties in low molecular amorphous spiro-linked compound thin films such as 2,2',7,7'-tetrakis-(diphenylamino)-9,9'-spirobifluorene (Spiro-TAD), 2,2',7,7'-tetra-(*m*-tolyl-phenylamino)-9,9'-spirobifluorene (Spiro-TPD), 2,2',7,7'-tetrakis-(*N,N'*-di-*p*-methylphenylamino)-9,9'-spirobifluorene (Spiro-TTB), and 2,2',7,7'-tetra-(*N*-phenyl-1-naphthylamine)-9,9'-spirobifluorene (Spiro  $\alpha$ -NPB) and the corresponding parent compound thin films such as *N,N,N',N'*-tetraphenylbenzidine (TAD), *N,N'*-bis(3-methylphenyl)-(1,1'-biphenyl)-4,4'-diamine (TPD), *N,N,N',N'*-tetrakis(4-methylphenyl)benzidine (TTB), and *N,N'*-diphenyl-*N,N'*-bis(1-naphthyl)-1,1'-biphenyl-4,4'-diamine ( $\alpha$ -NPB), has been demonstrated. Finally, organic thin film phototransistors (OPTs) based on asymmetrically spiro-linked compound thin films have been demonstrated for the first time. The photoresponsive material applied in OPTs were 2,7-bis-(*N,N'*-diphenylamino)-2',7'-bis(biphenyl-4-yl)-9,9'-spirobifluorene (Spiro-DPSP) and 2,7-bis-(*N,N'*-diphenylamino)-2',7'-bis(spirobifluorene-2-yl)-9,9'-spirobifluorene (Spiro-DPSP<sup>2</sup>).

Thin films based on these materials were fabricated by thermal evaporation and the surface morphology was characterized by means of atomic force microscopy and optical microscopy techniques. All films were amorphous, smooth and flat. Directly after deposition the spiro-linked compound films showed very smooth surfaces with mean roughnesses of less than 1.6 nm and peak-to-valley heights of less than 10 nm. After the samples were left in ambient atmosphere for a certain time, the quality of the surface did not change significantly. Mean roughnesses of less than 1.9 nm and the peak-to-valley heights of less than 12 nm were obtained after the samples have been left in ambient atmosphere and at room temperature for several months. In contrast, the films based on the corresponding parent compounds crystallized easily after the samples were left in ambient atmosphere/in vacuum for a few days. Initially, the parent compound films have a maximum mean roughness of 1.06 nm and peak-to valley height of less than 7 nm. However, a mean roughness of up to 39 nm and a peak-to-valley height of up to 233 nm were obtained after the samples have been left in ambient atmosphere and at room temperature for a few days. The resulting crystal heights were much higher than the thicknesses of thin films themselves. This implies that the substrates were revealed by crystallization. Based on these results, the surface morphological stability of the spiro-linked compound thin films is better than those of their corresponding parent compounds thin films.

The field-effect mobilities of charge carriers in parent compound thin films are slightly higher than those in their corresponding spiro-linked compound thin films. However, both mobilities are in the same order of magnitude ( $\sim 10^{-5} \text{ cm}^2/\text{Vs}$ ). The transistor characteristics of spiro-linked compound field-effect transistors (FETs) were measured for fresh devices and after the devices have been stored for a certain time. The hole mobilities in spiro-linked compound thin films decreased typically by 2 % after the samples have been stored in ambient atmosphere and at room temperature for 9 months. In contrast, organic FETs based on the parent compound thin films degraded after the devices have been left for a few days in ambient atmosphere/vacuum.

Generally, it was found that the measurements performed under vacuum give less hysteresis in the transfer/output characteristics than those performed in air. The hysteresis in the transfer curve is also gate bias and temperature dependent. The hysteresis is clearly observed at high gate biases and high temperatures. This effect could be ascribed to either charge trapping effect or defects in the active layers. Comparing spiro-linked compounds and their parent compound-based FETs, the mobility of holes in spiro-linked compound thin films are relatively unaffected by temperature with respect to their corresponding parent compound thin films. Furthermore, temperature dependence of the mobility was analyzed in two models, namely the Arrhenius model and the Gaussian Disorder model. The Arrhenius model tends to give a high value of the prefactor mobility. However, it is difficult to distinguish whether the temperature behaviors of the material under consideration follows the Arrhenius model or the Gaussian Disorder model due to the narrow accessible range of the temperatures.

Organic phototransistors based on asymmetrically spiro-linked compounds, Spiro-DPSP and Spiro-DPSP<sup>2</sup>, have been demonstrated. Intramolecular charge transfer between a sexiphenyl/terfluorene-derivative and a bis(diphenylamino)biphenyl moiety leads to an increase in the charge carrier density upon illumination, providing the amplification effect. The *OFF* current is significantly increased by a factor which is comparable to devices based on amorphous silicon. Upon illumination, the drain current in the accumulation regime is relatively unaffected by the illumination and the charge carriers mobility is relatively constant. However, the illumination strongly shifts the threshold voltage. Remarkably, the phototransistor can work in two terminal devices (source and drain) and with the incident UV light acting as an *optical gate electrode*. Therefore, employing a single layer amorphous organic semiconducting device seems to be very attractive for low-cost ultraviolet photodetector applications.

## References

- [1] BCC Inc., *Materials Today* **5**, 18 (February 2002).
- [2] M. Pope, H. P. Kallmann, and P. Magnante, *J. Chem. Phys.* **38**, 2042 (1963).
- [3] C. W. Tang and S. A. Van Slyke, *Appl. Phys. Lett.* **51**, 913 (1987).
- [4] J. H. Burroughes, D. D. C. Bradley, A. R. Brown, R. N. Marks, K. Mackay, R. H. Friend, P. L. Burn, and A. B. Holmes, *Nature (London)* **357**, 539 (1990).
- [5] E.-M. Han, L.-M. Do, M. Fujihara, H. Inada, and Y. Shirota. *J. Appl. Phys.* **80**, 3297 (1996).
- [6] Y. Qiu and J. Qiao, *Thin Solid Films* **372**, 265 (2000).
- [7] H. Sirringhaus, N. Tessler, and R. H. Friend, *Science* **280**, 1741 (1998).
- [8] B. Crone, A. Dodabalapur, Y. Y. Lin, R. W. Filas, Z. Bao, A. LaDuca, R. Sarpeshkar, H. E. Katz, and W. Li, *Nature (London)* **403**, 251 (2000).
- [9] G. H. Gelinck, H. E. A. Huitema, E. Van Veenendaal, E. Cantatore, L. Schrijnemakers, J. B. P. H. Van Der Putten, T. C. T. Geuns, M. Beenhakkers, J. B. Giesbers, B.-H. Huisman, E. J. Meijer, E. M. Benito, F. J. Touwslager, A. W. Marsman, B. J. E. Van Rens, and D. M. De Leeuw, *Nature Materials* **3**, 106 (2004).
- [10] J. Salbeck, in *Proc. Symp. Inorg. Org. Electroluminescence (EL 1996)*, *Eds : R H Mauch, H E Gumlich*, Wissenschaft und Technik Berlin, **243** (1996).
- [11] U. Bach, D. Lupo, P. Compte, J. E. Moser, F. Weissörtel, J. Salbeck, H. Spreitzer, and M. Gratzel, *Nature (London)* **395**, 583 (1998).
- [12] J. Salbeck, N. Yu, J. Bauer, F. Weissörtel, and H. Bestgen, *Synth. Met.* **91**, 209 (1997).
- [13] F. Steuber, J. Staudigel, M. Stössel, J. Simmerer, A. Winnacker, H. Spreitzer, F. Weissörtel, and J. Salbeck, *Adv. Mat.* **12**, 130 (2000).
- [14] T. P. I. Saragi, R. Pudzich, Th. Fuhrmann, and J. Salbeck, *Mater. Res. Soc. Symp. Proc.* **725**, 89 (2002).
- [15] T. P. I. Saragi, R. Pudzich, Th. Fuhrmann, and J. Salbeck, *Appl. Phys. Lett.* **84**, 2334 (2004).
- [16] J. Salbeck, M. Schörner, and Th. Fuhrmann, *Thin Solid Films* **417**, 20 (2002).
- [17] R. Pudzich, *Ph.D Thesis*, University of Kassel (2002).
- [18] S. M. Sze, *Physics of Semiconductor Devices* (Wiley, New York, 1981).

- 
- [19] M. Shur, *Introduction to Electronic Devices* (Wiley, New York, 1996).
- [20] M. Shur, M. Hack, and J. G. Shaw, *J. Appl. Phys.* **66**, 3371 (1989).
- [21] M. Shur and M. Hack, *J. Appl. Phys.* **55**, 3831 (1984).
- [22] E. J. Meijer, C. Tanase, P. W. M. Blom, E. van Veenendaal, B.-H. Huisman, D. M. de Leeuw, and T. M. Klapwijk, *Appl. Phys. Lett.* **80**, 3838 (2002).
- [23] G. Horowitz, R. Hajlaoui, D. Fichou, and A. E. Kassimi, *J. Appl. Phys.* **85**, 3202 (1999).
- [24] H. Iishi, K. Sugiyama, E. Ito, and K. Seki, *Adv. Mat.* **11**, 605 (1999).
- [25] D. P. Woodruff and T. A. Delchar, *Modern Techniques of Surface Science* (Cambridge University Press, Cambridge, 1986).
- [26] J. Hoelzel, F. K. Schulte, and H. Wagner, *Solid State Surface Physics* (Springer, Berlin, 1979).
- [27] A. R. Brown, C. P. Jarrett, D. M. de Leeuw, and M. Matters, *Synth. Met.* **88**, 37 (1997).
- [28] E. J. Meijer, C. Detcheverry, P. J. Baesjou, E. van Veenendaal, D. M. de Leeuw, and T. M. Klapwijk, *J. Appl. Phys.* **93**, 4831 (2003).
- [29] Y.-Y. Lin, D. J. Gundlach, S. F. Nelson, and T. N. Jackson, *IEEE Trans. Electron Devices.* **18**, 606 (1997).
- [30] D. Knipp, R. A. Street, B. Krusor, J. Ho, and R. B. Apte, *Mat. Res. Soc. Symp. Proc.* **708**, BB8.10.1 (2002).
- [31] L. L. Kosbar, C. D. Dimitrakopoulos, and D. J. Mascaro, *Mat. Res. Soc. Symp. Proc.* **665**, C10.6.1 (2001).
- [32] D. Knipp, R. A. Street, A. Völkel, and J. Ho, *J. Appl. Phys.* **93**, 347 (2003).
- [33] M. Shtein, J. Mapel, J. B. Benziger, and S. R. Forrest, *Appl. Phys. Lett.* **81**, 268 (2002).
- [34] Z. Bao, A. Dodabalapur, and A. J. Lovinger, *Appl. Phys. Lett.* **69**, 4108 (1996).
- [35] A. Salleo, M. L. Chabinyc, M. S. Yang, and R. A. Street, *Appl. Phys. Lett.* **81**, 4383 (2002).
- [36] H. Sirringhaus, N. Tessler, and R. H. Friend, *Science* **280**, 1741 (1998).
- [37] H. E. Katz, A. J. Lovinger, and J. G. Laquindanum, *Chem. Mater.* **10**, 457 (1998).
- [38] Z. Bao, A. J. Lovinger, and A. Dodabalapur, *Appl. Phys. Lett.* **69**, 3066 (1996).
- [39] X.-C. Li, H. Sirringhaus, F. Garnier, A. B. Holmes, S. C. Moratti, N. Feeder, W. Clegg, S. J. Teat, and R. H. Friend, *J. Am. Chem. Soc.* **120**, 2206 (1998).

- [40] H. Sirringhaus, R. H. Friend, X. C. Li, S. C. Moratti, A. B. Holmes, and N. Feeder, *Appl. Phys. Lett.* **71**, 3871 (1997).
- [41] A. Facchetti, Y. Deng, A. Wang, Y. Koide, H. Sirringhaus, T. J. Marks, and R. H. Friend, *Angew. Chem. Int. Ed.*, **39**, 4547 (2000).
- [42] Z. Bao, A. J. Lovinger, and J. Brown, *J. Am. Chem. Soc.* **120**, 207 (1998).
- [43] R. C. Haddon, A. S. Perel, R. C. Morris, T. T. M. Palstra, A. F. Hebard, and R. M. Fleming, *Appl. Phys. Lett.* **67**, 121 (1995).
- [44] C. D. Dimitrakopoulos and P. R. L. Malenfant, *Adv. Mat.* **14**, 99 (2002).
- [45] H. E. Katz, J. Johnson, A. J. Lovinger, and W. Li, *J. Am. Chem. Soc.* **122**, 7787 (2000).
- [46] P. R. L. Malenfant, C. D. Dimitrakopoulos, J. D. Gelorme, L. L. Kosbar, T. O. Graham, A. Curioni, and W. Andreoni, *Appl. Phys. Lett.* **80**, 2517 (2002).
- [47] K.-D. Rockwitz and H. Bässler, *Chem. Phys.* **70**, 307 (1982).
- [48] R. Jankowiak, K.-D. Rockwitz, and H. Bässler, *J. Phys. Chem.* **87**, 552 (1983).
- [49] J. Friedrich and D. Haarer, *Angew. Chem. Int. Ed.* **23**, 113 (1984).
- [50] A. Elscher and H. Bässler, *Chem. Phys.* **112**, 285 (1987).
- [51] A. Miller and E. Abrahams, *Phys. Rev.* **120**, 745 (1960).
- [52] H. Bässler, *Phys. Status Solidi (b)* **175**, 15 (1993) and references therein.
- [53] G. Schönherr, H. Bässler, and M. Silver, *Phil. Mag. B.* **44**, 47 (1981).
- [54] P. M. Borsenberger, L. Pautmeier, and H. Bässler, *J. Chem. Phys.* **94**, 8276 (1991).
- [55] D. H. Dunlap, P. E. Parris, and V. M. Kenkre, *Phys. Rev. Lett.* **77**, 542 (1996).
- [56] S. V. Novikov, D. H. Dunlap, V. M. Kenkre, P. E. Parris, and A. V. Vannikov, *Phys. Rev. Lett.* **81**, 4472 (1998).
- [57] P. W. M. Blom and M. C. J. M. Vissenberg, *Mat. Sci. Eng. A.* **27**, 53 (2000).
- [58] W. D. Gill, *J. Appl. Phys.* **43**, 5033 (1972).
- [59] P. M. Borsenberger and D. S. Weiss, *Organic Photoreceptors for Imaging Systems* (New York, Marcel Dekker, 1993).
- [60] M. C. J. M. Vissenberg and M. Matters, *Phys. Rev. B.* **57**, 12964 (1998).
- [61] M. C. J. M. Vissenberg, *Ph.D. Thesis*, University of Leiden (1999).
- [62] G. E. Pike and C. H. Seager, *Phys. Rev. B.* **10**, 1421 (1974).
- [63] Y. Shirota, *J. Mater. Chem.* **10**, 1 (2000).
- [64] E.-M. Han, L.-M. Do, N. Yamamoto, and M. Fujihara, *Chem. Lett.* **57** (1995).
- [65] E.-M. Han, L.-M. Do, Y. Niidome, and M. Fujihara, *Chem. Lett.* **969** (1994).

- [66] P. F. Smith, P. Gerroir, S. Xie, A. M. Hor, Z. Popovic, and M. L. Hair, *Langmuir* **14**, 5946 (1998).
- [67] S. A. Van Slyke, C. H. Chen, and C. W. Tang, *Appl. Phys. Lett.* **69**, 2160 (1996).
- [68] D. F. O'Brien, P. E. Burrows, S. R. Forrest, B. E. Koene, D. E. Loy, and M. E. Thompson, *Adv. Mater.* **10**, 1108 (1998).
- [69] D. E. Loy, B. E. Koene, and M. E. Thompson, *Adv. Funct. Mat.* **12**, 245 (2002).
- [70] F. Weissörtel, *Ph.D. Thesis*, University of Regensburg (1999).
- [71] N. Johansson, D. A. dos Santos, S. Guo, J. Cornil, M. Fahlman, J. Salbeck, H. Schenk, H. Arwin, J. L. Brédas, and W. R. Salaneck, *J. Chem. Phys.* **107**, 2542 (1997).
- [72] K. Seki, U. O. Karlsson, R. Engelhardt, E.-E. Koch, and W. Schmidt, *Chem. Phys.* **91**, 459 (1984).
- [73] U. Bach, K. De Cloedt, H. Spreitzer, and M. Grätzel, *Adv. Mat.* **12**, 1060 (2000).
- [74] J. Heinze, *Angew. Chem.* **96**, 823 (1984).
- [75] Th. Fuhrmann and J. Salbeck, in *Advances in Photochemistry*, Vol 27, 83 - 166 (Eds: D. C. Neckers, G. von Büнау, W. S. Jenks, Wiley, 2002).
- [76] J. Pommerehne, H. Westweber, W. Guss, R. F. Mahrt, H. Bässler, M. Porsch, and J. Daub, *Adv. Mat.* **7**, 551 (1995).
- [77] Th. Ebert and J. Salbeck. Unpublished results.
- [78] G. S. May and S. M. Sze, *Fundamentals of Semiconductor Fabrication* (New York, Wiley, 2004).
- [79] AZ 1500 Series, Clariant GmbH, Germany.
- [80] H. Sirringhaus, P. J. Brown, R. H. Friend, M. M. Nielsen, K. Bechgaard, B. M. W. Langeveld-Voss, A. J. H. Spiering, R. A. Janssen, E. W. Meijer, P. T. Herwig, and D. M. de Leeuw, *Nature (London)* **401**, 685 (1999).
- [81] Keithley 4200-SCS Semiconductor Characterization System Reference Manual, (Keithley Instruments, Inc., 2000).
- [82] S. Martin, J.-Y. Nahm, and J. Kanicki, *J. Elec. Mater.* **31**, 512 (2002).
- [83] Handbook of Microscopy Method II, Editors S. Amelinckx, D. van Dyck, J. van Landuyt, and B. van Tendeloo, VCH Weinheim, 1997.
- [84] Y. S. Yang, S. H. Kim, J.-I. Lee, H. Y. Chu, L.-M. Do, H. Lee, J. Oh, T. Zyung, M. K. Ryu, and M. S. Jang, *Appl. Phys. Lett.* **80**, 1595 (2002).
- [85] A. Andreev, G. Matt, C. J. Brabec, H. Sitter, D. Badt, H. Seyringer, and N. S. Sariciftci, *Adv. Mat.* **12**, 629 (2000).
- [86] T. Mori, S. Miyake, and T. Mizutani, *Jpn. J. Appl. Phys.* **34**, L845 (1995).

- [87] S. Heun and P. Borsenberger, *Chem. Phys.* **200**, 245 (1995).
- [88] C. D. Dimitrakopoulos, A. R. Brown, and A. Pomp, *J. Appl. Phys.* **80**, 2501 (1996)
- [89] D. Poplavskyy and J. Nelson, *J. Appl. Phys.* **93**, 341 (2003).
- [90] L. Torsi, A. Dodabalapur, and H. E. Katz, *J. Appl. Phys.* **78**, 1088 (1995).
- [91] M. Stolka, J.F. Yanus, and D. M. Pai, *J. Phys. Chem.* **88**, 4707 (1984).
- [92] H. H. Fong, K. C. Lun, and S. K. So, *Chem. Phys. Lett.* **353**, 407 (2002).
- [93] C. Tanase, E. J. Meijer, P.W.M. Blom, and D. M. de Leeuw, *Phys. Rev. Lett.* **91**, 216601 (2003).
- [94] D. M. Taylor, H. L. Gomes, A. E. Underhill, S. Edge, and P. I. Clemenson, *J. Phys. D: Appl. Phys.*, **24**, 2032 (1991).
- [95] W. Kim, A. Javey, O. Vermesh, Q. Wang, Y. Li, and H. Dai, *Nano Letters* **3**, 193 (2003).
- [96] W. R. Caseri, H. D. Chanzy, K. Feldman, M. Fontana, P. Smith, T. A. Tervoort, J. G. P. Goossens, E. W. Meijer, A. P. H. J. Schenning, I. P. Dolbnya, M. G. Debije, M. P. de Haas, J. M. Warman, A. M. van de Craats, R. H. Friend, H. Sirringhaus, and N. Stutzmann, *Adv. Mat.* **15**, 125 (2003).
- [97] Y. Qiu, Y. Hu, G. Dong, L. Wang, J. Xie, and Y. Ma, *Appl. Phys. Lett.* **83**, 1644 (2003).
- [98] Y. Shirota, S. Nomura, and H. Kageyama, *SPIE Symp. Proc.* **3476**, 132 (1998).
- [99] Y. Y. Lin, D. J. Gundlach, S. F. Nelson and T. N. Jackson, *IEEE Trans. Electron. Devices.* **44**, 1325 (1997).
- [100] G. Horowitz, in *Semiconducting Polymer: Chemistry, Physics and Engineering* (Edited by G. Hadziioannou, and P. F. van Hutten (Wiley-VCH, Weinheim, 1999).
- [101] P. M. Borsenberger and J. J. Fitzgerald, *J. Phys. Chem.* **97**, 4815 (1993).
- [102] N. von Malm, *Ph.D Thesis*, Technischen Universität Darmstadt (2003).
- [103] B. Chen, C.-S. Lee, S.-T. Lee, P. Webb, Y.-C. Chan, W. Gambling, H. Tian, and W. Zhu, *Jpn. J. Appl. Phys.* **39**, 1190, Part 1, No. 3A (2000).
- [104] M. Iizuka, M. Nakamura, K. Kudo, and K. Tanaka, *IEICE Trans. Electron.* **E85-C**, 1311 (2002).
- [105] J. Kovac, T.C. Wong, M.K. Fung, M. W. Liu, V. Kremnican, I. Bello, and S.T. Lee, *Mat. Sci. Eng. B.* **85**, 172 (2001).
- [106] I. G. Hill, A. Rajagopal, and A. Kahn, *Appl. Phys. Lett.* **73**, 662 (1998)
- [107] I. G. Hill and A. Kahn, *J. Appl. Phys.* **84**, 5583 (1998).
- [108] M. J. Powell, C. van Berkel, and J. R. Hughes, *Appl. Phys. Lett.* **54**, 1323 (1989).

- [109] M. J. Powell, *Appl. Phys. Lett.* **43**, 597 (1983).
- [110] M. J. Powell, C. van Berkel, I. D. French, and D. H. Nichols, *Appl. Phys. Lett.* **51**, 1242 (1987).
- [111] A. V. Gelatos and J. Kanicki, *Appl. Phys. Lett.* **57**, 1197 (1990).
- [112] M. Münch, *PhD. Thesis*, University of Stuttgart (2001).
- [113] W. A. Schoonveld, *PhD. Thesis*, University of Groningen (1999).
- [114] L. Torsi, A. Dodabalapur, L. J. Rothberg, A. W. P. Fung, and H. E. Katz, *Phys. Rev. B.* **57**, 572271 (1998).
- [115] S. A. Visser, W. T. Gruenbaum, E. H. Magin, and P. M. Borsenberger, *Chem. Phys.* **240**, 197 (1999).
- [116] J. Veres, S. D. Ogier, S. W. Leeming, D. C. Cupertino, and S. M. Khaffaf, *Adv. Funct. Mat.* **13**, 199 (2003).
- [117] P. M. Borsenberger, E. H. Magin, and J. Shi, *Physica B* **217**, 212 (1996).
- [118] J. Salbeck, F. Weissörtel, and J. Bauer, *Macromol. Symp.* **125**, 121 (1997).
- [119] P. Maslak, M. P. Augustine, and J. D. Burkey, *J. Am. Chem. Soc.*, **112**, 5539 (1990).
- [120] P. Maslak, *Adv. Mat.*, **6**, **405** (1994).
- [121] A. Schweig, U. Weidner, D. Hellwinkel, and W. Krapp, *Angew. Chem.* **85**, 360 (1973)
- [122] K. Meerholz, *Angew. Chemie* **109**, 981 (1997).
- [123] Y.-Y. Chien, K.-T. Wong, P.-T. Chou, and Y.-M. Cheng, *Chem. Comm.* **23**, 2874 (2002).
- [124] N. M. Johnson and A. Chiang, *Appl. Phys. Lett.* **45**, 1102 (1984).
- [125] K. S. Narayan, and N. Kumar, *Appl. Phys. Lett.* **79**, 1891 (2001).
- [126] M. C. Hamilton, S. Martin, and J. Kanicki, *IEEE Trans. Electron Devices* **51**, 877 (2004).
- [127] M. C. Hamilton, S. Martin, and J. Kanicki, *SPIE Symp. Proc.* **5217**, 193 (2003).
- [128] M. C. Hamilton, S. Martin, and J. Kanicki, *Mat. Res. Soc. Symp. Proc.* **771**, L10.17.1 (2003).
- [129] C. van Berkel and M. J. Powell, *J. Appl. Phys.* **60**, 1521 (1986).
- [130] M. J. Powell, B. C. Easton, and D. H. Nicholls, *J. Appl. Phys.* **53**, 5068 (1982).
- [131] M. Hiramoto, A. Miki, M. Yoshida, and M. Yokoyama, *Appl. Phys. Lett.* **81**, 1500 (2002).
- [132] B. Lakshmi, K. Chalapati, A. K. Srivastava, B. M. Arora, S. Subramanian, and D. K. Sharma, *IEEE Trans. on Electron. Dev.* **37**, 1533 (1990).
- [133] Y. Kaneko, N. Koike, K. Tsutsui, and T. Tsukada, *Appl. Phys. Lett.* **56**, 650 (1990).



[134] H. C. Card and A. G. Worrall, *J. Appl. Phys.* **44**, 2326, 1973.

[135] D. Kahng and S. M. Sze, *Bell Syst. Tech. Journal*, **46**, 1288, 1967.



# Acknowledgments

I thank Jesus Christ for His mercy, guiding me through my life, and providing me a peaceful heart. I also wish to thank many people who helped make the work and the writing of my thesis possible.

Primarily, I thank Prof. Josef Salbeck who supported me, gave me an opportunity to work in his group, and also gave me a new perspective of organic electronic devices. Thank you also for helping me with administrative matters.

I thank Prof. Heinz von Seggern for giving the “first experimental lecture” in organic transistors and being my second advisor.

I thank the DAAD for the scholarship.

I thank Prof. Luisa Torsi (University of Bari, Italy) and Dr. Brian Crone (Los Alamos National Laboratory, USA) for helping me in the earlier stages of this thesis.

I thank Dr. Thomas Fuhrmann-Lieker and Dr. Rainer Bausch for giving their valuable time and illuminating discussions.

I thank the late Dr. Robert Pudzich for synthesizing asymmetrically spiro-linked compounds; giving an opportunity to demonstrate for the first time an organic phototransistor. I thank you also for illuminating discussion about intramolecular charge transfer and the spiro concept. May he rest in peace.

I thank Lothar Weißenborn for helping me with some stuff in laboratory such as mask and vacuum evaporation.

For electrochemistry data which is really important in my experiments, I must thank Thomas Ebert and Irina Suske.

I also thank Joscha Londenberg, Kristian Onken, Achim Siebert, and Dr. Michael Fetten for very helpful discussion about general molecular structure and the chemical properties of the spiro-compounds.

My thank goes also to Till Spehr for a critical reading of my thesis. Thanks for correcting my grammar too. I think I have learned more English and you have learned more about transistor, so you are also expert in organic transistors.

I thank Dr. Gerhard Thiel and his family for their hospitality in my first four days in Germany. Thanks also for a very nice Christmas eve.

To Karin Pfaff, thank you for being there when I needed help with administrative matters.

*To people in Institute for Microstructure Technology and Analytic (IMA).*

I thank Dr. Wenzel Scholz for designing and realizing the mask for optical lithography and some discussion about lithography and scanning electron microscopy techniques.

I thank Dr. Georgie Georgiev for helping me to deposit spiro-linked compounds for the first time. Thanks also for being a good colleague during my work in clean room.

My thanks also go to Dr. Michael Müller-Wiegand and Dipl. Phys. Kai Ludolph for being a “good mentor”; for AFM measurement and in general problems in experimental physics.

I thank Dipl. Phys. Dirk Albert and Ina Kommallein for helping me to work effectively in clean room. You know if something does not work properly, I will call you both first. Thank you!

Dipl. Ing. Dietmar Gutermuth, I owe you a beer for depositing the gold on my silicon dioxide substrate. Sorry, honestly I owe you 45 beers since you have deposited the gold on my very precious 45 silicon dioxide substrates.

*To people who always support me:*

I am very grateful for Family M. Kessler, Manfred, Juliana, Maureen, Madeleine, and Marc, for their hospitality, friendship, unfailingly generous words and wise counsel.

I also thank Kerstin Londenberg for being a good friend.

Thank also goes to Retty Paruntu for our friendship and helping me in general matters. My thanks also go to Tito Nugroho, Lauw, Novita, Andrew, Joanna Susilowati, Laura Indradewa for being friendly and supporting me in prayer.

I thank Family Schwarzler for their hospitality and friendship.

Finally, I must thank my parents, Family M. Saragi, for being so supportive, understanding, and tolerance during my PhD in Germany. I thank my brother Parlin, my sisters Sisca, Bertha, and Muri for being the best family that I ever have.

My heartfelt thanks are due to my living joy Eva B.M.T. Tobing, who is always supporting me with a never ending enthusiasm and unflagging support. Thanks honey! Time is up!

Tobat Parasian Irianto Saragi  
Kassel, Germany  
October 2000 - October 2004

## Curriculum Vitae

Name : Tobat Parasian Irianto Saragi

Date/Place of Birth : 29 April 1974, Serui, Indonesia

1989 – 1992 Regina Pacis Senior High School, Bogor, Indonesia

1992 –1996 Bachelor of Science (BSc), Physics, Bandung Institute of Technology, Indonesia

1996 BSc thesis under the supervision of Prof. Dr. M. O. Tjia  
Theme: Fabrication of emeraldine base/polymethyl methacrylate polyblends for optics application

1997 – 2000 Master of Science (MSc), Physics, Bandung Institute of Technology, Indonesia

2000 MSc thesis under the supervision of Prof. Dr. M. O. Tjia  
Theme: Synthesis of poly(*p*-phenylene vinylene) (PPV) and its application for an electroluminescence ITO/PPV/Al device

2000 – 2004 Macromolecular Chemistry and Molecular Materials, Department of Sciences, University of Kassel, Germany – PhD Student under the supervision of Prof. Dr. J. Salbeck.  
Theme: Organic field-effect transistors and phototransistors based on amorphous materials.